Universitat Autònoma de Barcelona

Self-Assembled Monolayers of Electroactive Molecules for the Preparation of Memory Devices

Elena Marchante Rodríguez

Universitat Autònoma de Barcelona

Self-Assembled Monolayers of Electroactive Molecules for the Preparation of Memory Devices

Elena Marchante Rodríguez

Thesis submitted for the award of Ph.D.

PhD Programme in Materials Science

SUPERVISORS

Dr. Marta Mas Torrent and Dr. Núria Crivillers

TUTOR

Dr. Iluminada Gallardo García

Chemistry Department / Science Faculty

Universidad Autònoma de Barcelona 2017

Memoria presentada para aspirar al Grado de Doctor por:

Elena Marchante Rodríguez

Firmado por:

Dr. Marta Mas Torrent   Dr. Núria Crivillers   Dr. Iluminada Gallardo

Bellaterra, 21 de Abril de 2017

La Dr. **Marta Mas**, Investigadora Científica del CSIC en el Instituto de Ciencia de Materiales de Barcelona (ICMAB-CSIC), y la Dr. **Núria Crivillers**, Científica Titular del CSIC en el Instituto de Ciencia de Materiales de Barcelona (ICMAB-CSIC),

CERTIFICAN

Que Elena Marchante Rodríguez, licenciada en Ingeniería Química, ha realizado el trabajo de investigación que tiene como título "*Self-Assembled Monolayers of Electroactive Molecules for the Preparation of Memory Devices*", y que este trabajo se ha desarrollado en el marco del Programa de Doctorado de Ciencia de Materiales del Departamento de Química de la Universidad Autónoma de Barcelona.

Y para que así conste, firman el presente certificado

Dr. Marta Mas Torrent   Dr. Núria Crivillers

Bellaterra, 21 de Abril de 2017

Acknowledgements

Dentro de mi corta experiencia dentro del mundo de la investigación, he atravesado por distintos momentos, tanto buenos como no tan buenos. Dí mis primeros pasos cuando todavía estaba terminando la carrera, gracias a una beca de colaboración, y fue cuando empecé a disfrutar de la magia de la ciencia. Después, me planteé continuar en este mundo, y entonces fui consciente de la importancia del apoyo económico que se necesita para seguir adelante con lo que a uno realmente le gusta. Pero también pude ver que no todas las personas que se dedican a la investigación científica lo hacen por pasión, sino por el propio beneficio económico, lo que me llevo a pensar en tirar la toalla y orientar mi futuro hacia otra dirección. Pero gracias a la oportunidad que tuve de entrar en el ICMAB, de conocer a la gente que lo forma, su forma de trabajar y el apoyo que recibí en todo momento, recuperé esa ilusión inicial que tenía por dedicarme a la investigación.

Por todo esto, quiero agradecer muy especialmente a mis directoras de Tesis, Marta y Núria, por brindarme la oportunidad de seguir en el mundo de la ciencia, por la confianza que habéis depositado en mí, y por vuestro apoyo tanto profesional como personal, que ha hecho que me vuelque de lleno en la investigación. He podido aprender mucho con vuestras aportaciones y orientaciones en la realización de este trabajo, adquiriendo habilidades científicas y progresando profesionalmente. Igualmente, me gustaría agradecer a Jaume y Cun, el apoyo y consejos que me habéis dado a lo largo de estos años de tesis dentro del grupo.

A todos mis compañeros de NANOMOL: Inés, Toni, Francesc, Dolores, Antonio, Davide, Serena, Qiaoming, Lijia, Francesca, Stefano, Sergi, Adrián, José, Cristina, Diego, Simona, Adriana, Luiz, Paula, Edu, Judit Guasch, Lidia, Natascia, Nathaly, Maria Aguado, Primiano, Judit Tomsen, Guillem, Javi Repetto, David, Ramón, Elisabet, Belen, Amable, Arnau, Vega, Pepe, Nora, Santi, Imma, Elena L., Vladimir y Carme, y a los antiguos compañeros que pasaron antes: Rapha, Víctor, Freddy, Dayana, Gonca, Ajay, Mónica, Fernanda, César, Eli, Evelyn, Elena Rojas, Ingrid, José, Witold, Carlos, Manel, Lourdes, Paco Vera, Mary Cano, por todas las experiencias compartidas en el laboratorio y en los despachos, pudiendo contar con su apoyo y ánimos en cada etapa que se pasa a lo largo de estos años de tesis. También quiero agradecer al resto de compañeros del ICMAB, que de manera indirecta me habéis mostrado vuestro apoyo y habéis vivido conmigo la realización de esta tesis doctoral, muy especialmente a Mengdy, Wenjie, Cica, Enrique Irisarri, Juan Antonio, Andrea, Laia, Isa y Begoña.

Igualmente agradecer a Javi Casado, Laura Córcoles, Stamatis, Rafaela y Coco por todo vuestro apoyo, ánimo y colaboración en todo momento, pero sobre todo por vuestra valiosa amistad.

Agradecer hoy y siempre a mi familia, mis padres Sebastián y María Elena, mis hermanos Sebastián y Verónica, mis cuñados Paloma y Rishi, porque a pesar de la distancia, el ánimo, apoyo y alegría que me brindan me dan la fortaleza necesaria para seguir adelante.

Finalmente, quiero dar las gracias a mi futuro marido Andrés, por su apoyo incondicional y su comprensión, por hacerme reflexionar y ver las cosas desde otros puntos de vista.

Abbreviations

SAM	Self-assembled monolayer
ET	Electron transfer
PTM	polychlorotriphenylmethyl radical
OFET	Organic field-effect transistor
IC	Integrated circuit
JFET	Junction field-effect transistor
MOSFET	Metal-oxide-semiconductor field-effect transistor
H_{AB}	Electron coupling between donor and acceptor
Fc	Ferrocene
AQ	Anthraquinone
Q	Quinone
TTF	Tetrathiafulvalene
CV	Cyclic Voltammetry
SERS	Surface-enhanced Raman spectroscopy
TCNQ	Tetracyanoquinodimethane
Me_4TTF	Tetramethyltetrathiafulvalene
TMTSF	Tetramethylselenafulvalene
BEDT-TTF	Bis (ethylenedithio) tetrathiafulvalene
ITO	Indium tin oxide
CP-AFM	Conductive probe atomic force microscopy
EGaIn	Eutectic gallium-indium
SUMO	Single unoccupied molecular orbital
STM- BJ	Scanning tunnelling microscope break junction
MCBJ	Mechanically controllable break junctions
CA	Chronoamperometry
EIS	Electrochemical Impedance Spectroscopy
ILIT	Laser induced temperature jump
ACV	Alternating cyclic voltammetry
EMCS	Electroactive monolayer capacitive spectroscopy
k_{ET}	Electron transfer constant rate
WE	Working electrode
RE	Reference electrode
CE	Counter electrode
GC	Glassy carbon
SCE	Saturated calomel electrode
IL	Ionic liquid

IG	Ion gel
PVdF–HFP	Poly (vinylidene fluoride–co–hexafluoropropylene)
EMIM-TFSI	1–ethyl–3–methylimidazolium bis (trifluoromethylsulfonyl) imide
EMIM-BF_4	1–ethyl–3–methylimidazolium tetrafluoroborate
EMIM-$EtSO_4$	1–ethyl–3–methylimidazolium ethyl sulphate
BMIM-OTf	11-Butyl-3-methylimidazolium trifluoromethanesulfonate
NBu_4PF_6	Tetrabutylammonium hexafluorophosphate
NBu_4ClO_4	Tetrabutylammonium perchlorate
$LiClO_4$	Lithium perchlorate
ACN	Acetonitrile
THF	Tetrahydrofuran
DCM	Dichloromethane
BzN	Benzonitrile
RP1	First reduction process
RP2	Second reduction process
D-A	Donor – acceptor
XPS	X-ray photoelectron spectroscopy
ToF-SIMs	Time-of-flight secondary ion mass spectroscopy
UV	Ultra violet
AFM	Atomic force microscopy
SEM	Scanning electron microscopy
FT-IR	Fourier transform infrared spectroscopy
DSC	Differential scanning calorimetry
RH	Relative humidity
PM-IRRAS	Polarisation modulation IR reflection absorption spectroscopy
HOMO	Highest occupied molecular orbital
LUMO	Lowest unoccupied molecular orbital
CT	Charge transfer
RF-ID	Radio-frequency identification
TFT	Thin film transistor
diF-TES-ADT	2,8-difluoro-5,11-bis(triethylsilylethynyl) anthradithiophene
PS	Polystyrene
PVP	Poly(4-vinylphenol)
PMMA	Poly(methyl methacrylate)
SMS	Poly(styrene-b-methyl methacrylate-b-styrene)
BAMS	Bar-assisted meniscus shearing
HDMS	hexamethyldisilazane

Abstract

The ultimate goal of electrical circuits is miniaturization by using single molecules or collections of single molecules as electronic building blocks. It is expected that the smaller size of the electronic components will decrease the power consumption while increasing the sensitivity and the performance of the device.

Research efforts are concentrated in two directions. The first one is focused in the study, at a fundamental level, of new molecules with specific properties or functionalities, which provides a deeper understanding of molecular structure, dynamics and reactivity. The second one is dedicated to develop new techniques for the implementation of these molecules in electronic devices.

Often, to construct a molecular device it is necessary to deposit molecules or material on a suitable substrate. Since the ordering and packing of the molecules are crucial aspects for the operation of the devices, it is important to have a good control of how solvent, substrate or molecular functionalization influences on the resulting molecular assemblies and the intermolecular interactions.

The present Doctoral Thesis is focused on the development of new molecular electronic devices based on electroactive self-assembled monolayers (SAMs), and on the electrochemical study of the electron transfer phenomena associated to them. In the first part of the Thesis, it is described the use of different redox molecules immobilized on gold substrates as molecular switches. The state of the electroactive compounds can be tuned when a specific potential is applied to the substrate, and the capacitance response has been successfully implemented as the read-out of the switch. It is important to highlight that these electrical molecular switches have been also obtained using ion gels as solid electrolytes, demonstrating the feasibility to integrate these systems in future electronic and/or flexible devices.

In the second part of the Thesis, it is reported the electron transfer (ET) mechanism study, by electrochemical means, in a family of polychlorothriphenylmethyl radical (PTM) derivative compounds attached to gold substrates. The family of PTM molecules contains a thiol terminal group connected to the PTM through an alkyl chain with different lengths. It has been studied the ET process through PTM-SAMs in different organic electrolytic media and as a function of the surface coverage of the modified gold substrate. Hence, it was demonstrated that the interaction with the solvent plays an important role in the adiabaticity character of the redox process. Further, with neighbouring molecules, the intermolecular electronic coupling between PTM centers promotes a reduction of the ET constant rate.

Finally, in the last part of the Thesis, it has been fabricated a functioning OFET using an ion gel as gate dielectric, and its properties has been examined. The OFET was prepared with side-gate geometry, where the ion gel was placed on top the gate electrode and the substrate with the semiconductor channel. The ion gel gated OFET properties were compared with a reference OFET structure, which had a conventional SiO_2 gate dielectric, demonstrating that the ion gels are highly attractive to be applied in low cost and flexible organic transistors.

Contents

List of Figures

List of Tables

Chapter 1

Introduction and Objectives

CHAPTER 1. Introduction and Objectives

1.1 General Introduction

The term Electronics was originally considered as the study of electron behaviour and movement, particularly as observed in the first electron tubes. Today "Electronics" involves the branch of science, inside Physics and Electrical engineering, which deals with the emission, behaviour, and effects of electrons, and, with electronic devices. Many scientific and technical disciplines deal with different aspects of electronics.[1] The ability of electronic devices to act as switches makes digital information processing possible.

Since the discovery of the electron in 1897 by J. J. Thomson,[2] most of the first half of the 20th century was dedicated to controlling electrons in a vacuum with electric and magnetic fields to make amplifiers, oscillators, and switches. These brought new developments in communications and information technologies such as the appearance of radio, television, radar, and the first computers.

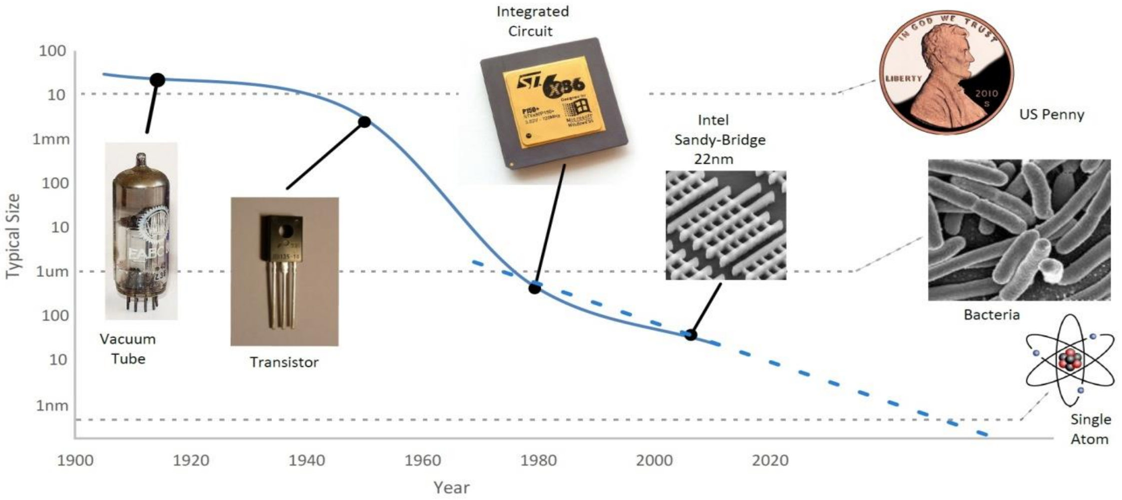

Figure 1.1 Advances in Electronics from the beginning of the 20th century.[3]

After the invention of the first transistor in 1947,[4] the last half of the century saw the introduction of electronics at the micro-levels and the rise of solid-state electronics by the invention of integrated circuits (ICs) and later on the Junction Field – Effect Transistors (JFETs) and the Metal–Oxide–Semiconductor Field–Effect Transistors (MOSFETs) by improving the device design process and by making more reliable and powerful transistors.[5] The integration of complete circuits on silicon, by top-down approaches and microfabrication methods, was the stimulus for the increase of computational power (Figure 1.1).[3] The electronic information technologies started to emerge, and transistor based information processing, semiconductor laser-based information transmission and magnetic based information storage have become dominant and completely changed human life into an "information society" (Table 1.1). [6]

CENTURY	BC – 19th	20th	21st
Information Processing	STONE PAPER	Semiconductor	MOLECULE
Information Transfer		Laser / semiconductor	
Information Storage		Magnetic Disk	
	Inorganic Bulk / Organic Bulk	Inorganic (Functional)	Organic (Functional)

Table 1.1 History of information processing devices.[6]

Since the size of components in integrated circuits is becoming smaller, in accordance with Moore's law, it is a simple matter to suggest that the ultimate integrated circuits will be constructed at the molecular or atomic level. Such state was suggested in a 1959 lecture by the distinguished physicist and futurist, Richard Feynman.[7] Years later, in the 1970s with the work of Aviram and Ratner,[8] the first attempt to predict and characterize a molecular – scale electronic phenomenon appeared by theoretical calculations of a rectifier formed by a donor – acceptor diad (Figure 1.2). These events pave the way to Molecular Electronics, discipline that involves the use of single or a small group of molecules in device-based structures that can be used as the fundamental units for electronic components such as wires, switches, memories and gain elements.[5]

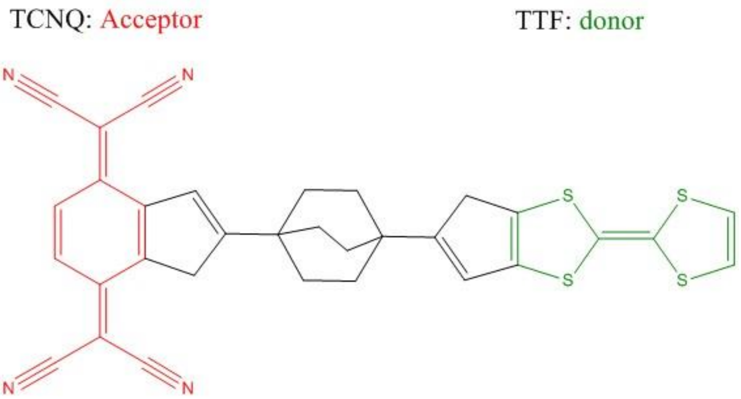

Figure 1.2 Schematic representation of Aviram and Ratner's theoretical rectifier.[8]

1.1.1 Molecular Electronics

Following the bottom-up approach, the goal in Molecular Electronics is to use molecules designed with specific properties and behaviours, as an alternative to the present solid-state electronic devices that are constructed using lithographic technologies from the top-down route.[5] Moreover, bottom-up implies the construction of functionality into small features such as molecules, with the opportunity to have the molecules further self-assembled into higher ordered structural units or rely on positional assembly. In principle, it can be suggested that any device exploiting molecular properties is a molecular electronic device. However, in order for a molecular system to be considered a device, there are several requirements that it must meet depending on the final application (switches, wires, diodes, memories, etc.).

A particularly attractive type of molecular functionality is that of a switch, and represents the simplest device easily conceived.[9] These types of systems are based on molecules that can be reversible shifted between two or more stable states, in response to an external stimuli (such as changes in light, temperature, electric current, etc.).[10] Their defining characteristic is the bistability between "ON" and "OFF" positions. In its "ON" position, the switch must either perform some function or allow another device to perform its function. In the "OFF" position, it must totally impede the function. The development of a molecular switch is perhaps the single most important element in developing molecular replacements for conventional integrated circuits.

For the progress of electronic molecular devices is important to attach the molecules to solid conducting substrates. A variety of techniques have been developed to construct metal–molecule junctions, however, the bottom-up assembly of molecules on metallic electrodes by using solution based methods[11,12] is a very promising route towards mass production of single-molecule devices.

1.1.2 Self-Assembled Monolayers

Self-assembly is a thermodynamically favourable process where the molecules interact and form some organized aggregate structures. Bottom-up construction is bio-inspired, a natural method of manufacture, and a methodology which is certain to influence much of the use of nanotechnology, and specially Molecular Electronics.[5] The use of self-assembly processes could lead to enormous advances in future manufacturing for Electronics once scientists learn to further control specific molecular level interactions.

Self-assembled monolayers (SAMs) chemically bonded to a substrate provide a convenient, flexible, and simple system to modify the interfacial properties of metals, metal oxides, and semiconductors.[13] SAMs are organic assemblies formed by the adsorption of molecular constituents from solution or the gas phase onto the surfaces; the adsorbates organize spontaneously (and sometimes epitaxially) into crystalline (or semicrystalline) structures. SAMs are well-suited for studies in nanoscience and technology because they are easy to prepare, the versatility of the components and the possibility to modify their macroscopic properties by changing the structure at molecular level.

The molecules or ligands that form SAMs have a chemical functionality, or "headgroup", and an anchoring group with a specific affinity for a substrate, separated by a spacer (Figure 1.3). The overall performance of a molecular electronic device is determined by the electrode/molecule interface (anchor) and the internal electronic structure of the terminal group. Thus, chemical design and synthesis are of paramount importance for molecular electronic devices.

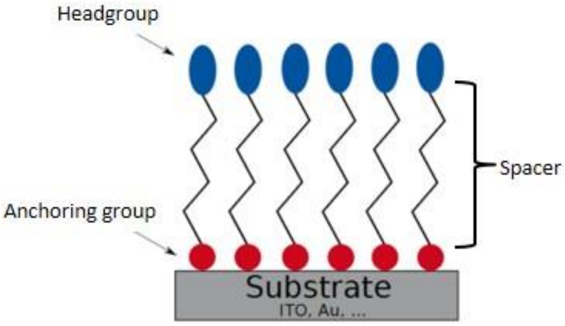

Figure 1.3 Schematic representation of a self-assembled monolayer (SAM) covalently bonded to a substrate.[14]

Anchoring groups

The anchoring group, responsible for the direct contact between metal and the molecular core, needs to be considered in terms of its mechanical stability and also regarding its electronic transparency (weak or strong coupling). There are a number of anchoring groups that bind to specific material substrates. The formation of efficient and reproducible molecule–metal electrode coupling is one key factor for the integration of molecules into circuits in the future.[15] The choice of electrode material is important to the measurement of electron transfer constant rates (k_{ET}), due to the implication of the density of electronic states in Marcus theory. The most studied class of SAMs is derived from the adsorption of alkanethiols on gold.[16–24] The high affinity of thiols for the surfaces of noble metals makes it possible to generate well-defined organic surfaces with useful and highly alterable chemical functionalities displayed at the exposed interface.[20,25]

Spacer groups

The bridge is a key component of SAMs, controlling the distance between the electrode and the functional center, and thereby controlling the electronic coupling between an electron donor and acceptor (H_{AB}) and the electron transfer constant rate (k_{ET}) (Figure 1.3). Long length bridges are typically used in order to slow the electron transfer rate to a measurable value. The structure of the bridge is key to controlling the electronic coupling. Saturated and conjugated bridges have been investigated as well as functional bridges such as peptides.[26–29]

Terminal groups

This is the part of the molecular system, which largely defines the electronic functionality of the monolayer device. That is, for a given electronic structure of the molecular core, the device function might turn out to be a resistor, a diode, a transistor, etc.

SAMs can be prepared from spontaneously adsorption of molecules in solution or in vapour phase. The most general protocol to prepare SAMs from solution is the immersion method (Figure 1.4). This consists in the immersion of a clean substrate in a solution of the desired compound for several hours at controlled temperature under inert atmosphere. In the case of the most studied systems, the alkanethiols, it is known that the reaction between the molecules and the surface is very fast, getting highly packed surfaces in a short time. Nonetheless, the reorganization process is slower, and for that, it is necessary to apply immersion times of several hours in order to maximize the molecular density and minimize the SAM defects.

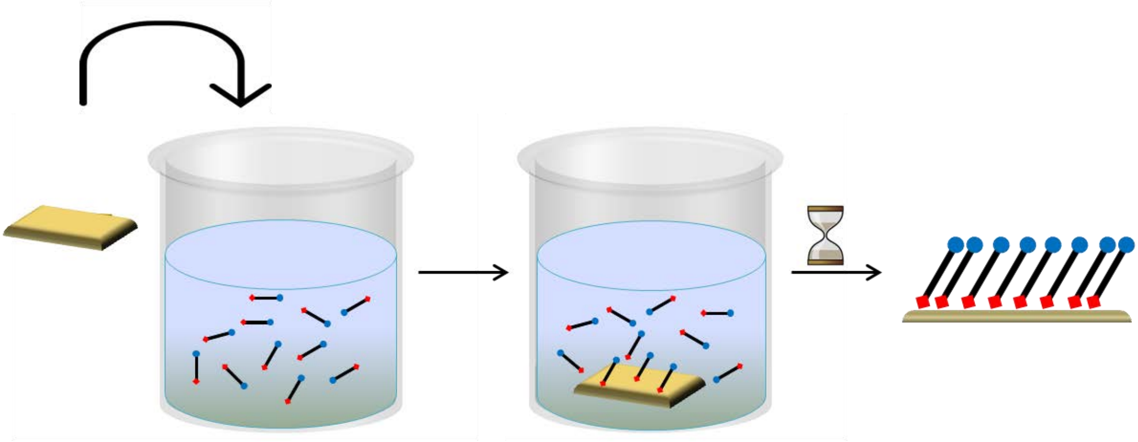

Figure 1.4 SAM preparation through the solution immersion methodology.

There are many parameters that can affect the final structure of the monolayer and should be taken into account such as:

- *Solvent*. The solvent affects to thermodynamics and kinetics of the assembly process due to the solvent-substrate and solvent-molecule interactions.

- *Temperature*. The temperature is directly related with the kinetics of the SAM formation and the number of the SAM defects. Some studies suggest that the effect of the temperature is crucial during the first minutes of the SAM formation.[30]

- *Molecular concentration and immersion time*. These two parameters are inversely related, because at low concentrations it is necessary high immersions times.[31,32] An optimal compromise between these parameters will give modified surfaces with high molecular coverage.

- *Purity of the adsorbate*. In general high purity degree of the employed molecules is necessary, although some experiments suggest that impurity traces less than 5% do not affect to the formation and structure of the SAM.[31,33]

- *Oxygen in solution*. Some works report that degasification of the solvent with an inert gas improves the reproducibility of the SAM properties.[23,33]

- *Substrate activation*. One of the most important steps in the preparation of a SAM is the substrate pre-treatment that concerns both specific cleaning and activation procedures for the appropriate anchoring of the molecules. Different cleaning procedures are commonly used depending on the surface, and can involve dry (oxygen plasma, UV/ozone plasma) or wet (piranha bath, hydrofluoric acid, and aqua-regia) chemistry.

Considering all these parameters, for each specific system the experimental conditions have to be optimised in order to achieve reproducible and well organized SAMs.

1.1.3 Electroactive SAMs

The realization of molecule-based devices with reduced dimensions is encouraging a transition from the solution to the solid state. The combination of self-assembly processes[34] with the nanofabrication of insulating, metallic, and semiconducting supports has already allowed the realization of molecule-based devices.[35–37]

SAMs of alkanethiols on gold provide an important and versatile class of spontaneously organized and structurally well-defined model interfaces. In particular SAMs of electroactive thiolated molecules constitute important model systems for the formation of electronic devices,[26] and they have been intensely investigated as model systems for interfacial electron transfer events.[13,26,38] By the use of SAMs containing electroactive groups, it is also possible to introduce dynamic substrates wherein the activities of the immobilized molecules can be switched "ON" and "OFF" in response to applied potentials.[26,39,40]

Principally in this thesis it has been studied SAMs of four different families of electroactive compounds: ferrocenes (Fc), anthraquinones (AQs), tetrathiafulvalenes (TTFs) and polychlorotriphenylmethyl radicals (PTMs).

Ferrocene (Fc)

Ferrocene is a type of organometallic chemical compound consisting of two cyclopentadienyl rings bound on opposite sides of a central metal atom. Such organometallic compounds are also known as "sandwich" compounds.[41–43]

Ferrocene was discovered in 1951 by Kealy and Pauson who were attempting to synthesize fulvalene.[44] This "sandwich" structure has been duplicated using a variety of transition metals including ruthenium,[45] cobalt[46] and nickel,[47] but these complexes have not been used for performing electrochemical SAM studies.

Ferrocene derivatives have attracted much attention due to their excellent properties like electrochemical activity, thermal and photochemical stability and liquid crystallinity. Ferrocene derivatives show unique and stable electrochemical properties due to the redox changes between Fe(II) and Fe(III) (Figure 1.5), which can be detected by cyclic voltammetry (CV).[48] Due to that, ferrocene is often used as an internal standard for calibrating redox potentials in non-aqueous electrochemistry.[49,50]

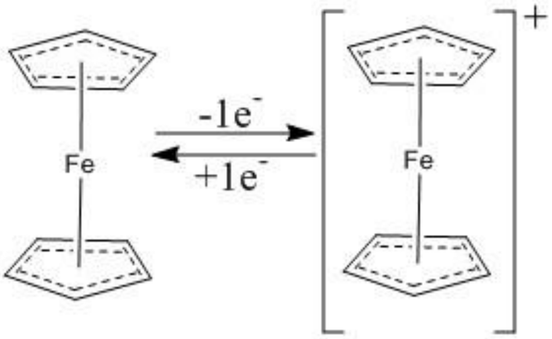

Figure 1.5 Ferrocene structure and redox process.

Ferrocene compounds show different properties like polarity, intermolecular force, solubility etc. in the different oxidation states (+2 and +3) of the iron atom. Taking advantage of these property changes, researchers have applied ferrocene derivatives in information storage devices,[51] molecular switches[52] and chemical detection.[53]

Ferrocene and its numerous derivatives have no large-scale applications, but have many nice uses that exploit the unusual structure (ligand scaffolds, pharmaceutical candidates)[54] and robustness (anti-knock formulations,[55] precursors to materials).

Since the pioneering work of Chidsey and co-workers[38] in 1990, CV studies of ferrocene terminated SAMs have been extensively reported in the literature. The influence of bridge architecture,[26,27,56,57] coadsorbed diluent molecules,[56,58] and supporting electrolytes[59] on the redox potential and shape of the voltammetric waves recorded for these SAMs has been well established. Further, the electrochemical properties of ferrocene and its immobilization on different substrates have permitted the study of different charge transport mechanisms[27,60] and also led to many interesting applications, such as (bio) sensors,[61–64] and molecular switches.[65–67]

Anthraquinone (AQ)

Quinones are a series of widespread compounds found in the living organisms performing a variety of biochemical and physiological functions.[68] A relatively small number of *p*-quinones have been recognized as biological electron carriers. The main activity of these compounds arises from their reversible electron transfer behaviour.[69] The term anthraquinone generally refers to one specific isomer, 9,10–anthraquinone, wherein the keto groups are located on the central ring (Figure 1.6). 9,10-anthraquinones are interesting compounds for investigations in electroanalytical chemistry due to the fact that they contain the reducible *p*-quinone system and also form conductive, electroactive films and monolayers,[70] so they can be used as surface modifier and redox mediator.[71-75]

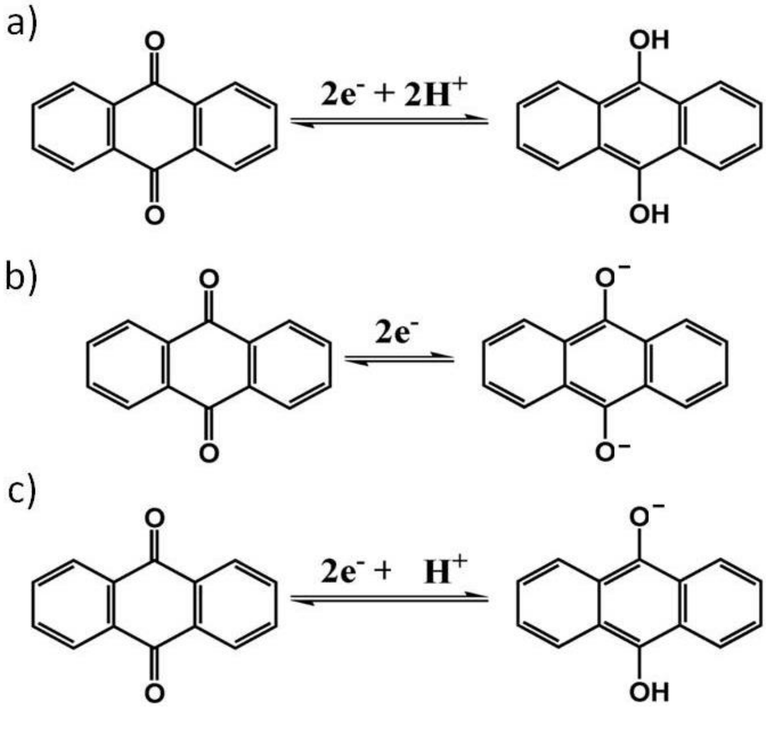

Figure 1.6. 9,10-anthraquinone structure and redox processes in: a) acidic, b) alkaline, and c) neutral aqueous buffer media.

The electrochemical reduction of quinones is a complicated process which has been extensively studied.[76] Quinones undergo a two-electron reduction which, depending on the availability of protons in the reaction media, might be accompanied by the uptake of two protons. Quinones undergo one-step two-electron reduction in aqueous buffer at acidic, neutral, and alkaline pH generating one reversible reduction wave. However, at acidic pH the reduction involves two protons (Figure 1.6.a) while at alkaline pH the reduction does not involve any proton (Figure 1.6.b). In neutral pH, the reduction may or may not involve protons depending upon the pK value of the phenolic –OH group of the hydroquinone (Figure 1.6.c).[77,78]

In aprotic and nonaqueous media, the quinones (Q) undergo two successive one-electron reduction steps to produce semiquinone ($Q^{\bullet-}$) and quinone dianion (Q^{2-}) generating two separate cathodic waves, in which the first step is completely reversible and the second step is quasi-reversible at customary scan rates (Figure 1.7).[79,80]

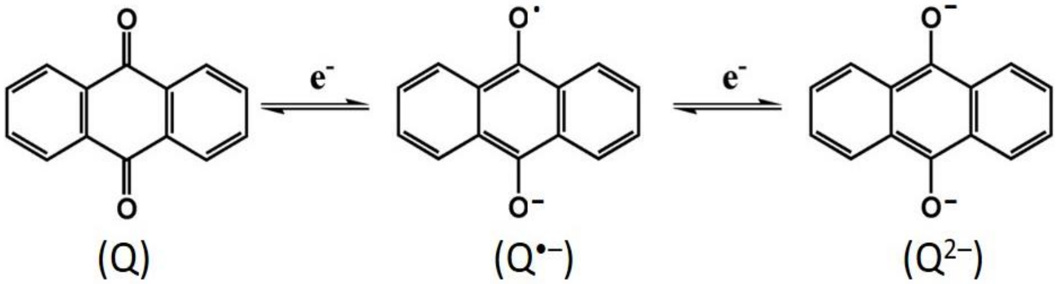

Figure 1.7 Two successive one-electron reduction steps of anthraquinone in aprotic media.

Recently, electrochemical reactions of SAMs having quinone redox centers have been studied.[81–84] Kaifer et al. synthesized three types of thiol-functionalized anthraquinone derivatives and observed that their voltammetric reversibility in alkaline solutions increased in mixed monolayers prepared by the self-assembly of the anthraquinone derivatives and 1-alkanethiols (C_{10}-C_{18}).[81] Taniguchi et al. studied structural differences in SAMs consisted of two anthraquinone derivatives with different substituted positions on silver and gold electrodes through CV and in situ surface-enhanced Raman spectroscopy (SERS) techniques.[85]

Although electrochemical reactions of quinone derivatives are complicated by multi-electron and multi-proton processes, they have recently been important redox chemicals in molecular devices.[86–89] Hummelen et al. prepared an anthraquinone based molecular wire (Figure 1.8) that can be reversibly switched electrochemically between cross-conjugated (a low conductance 'off' state) and linear-conjugated (a high conductance 'on' state) via two-electron reduction/oxidation reactions.

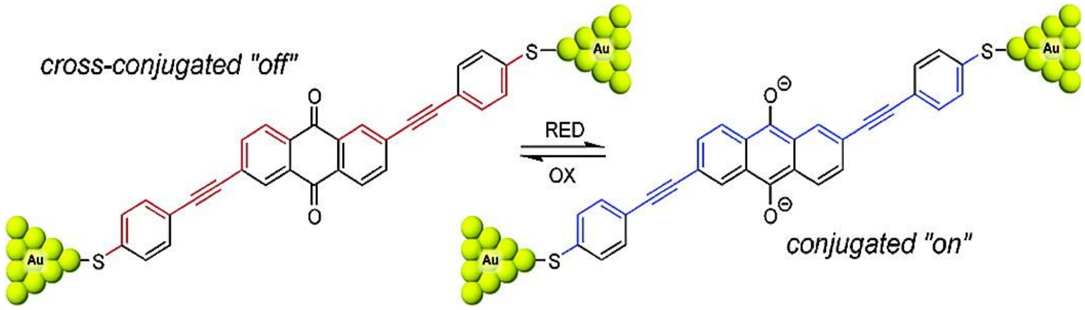

Figure 1.8 Anthraquinone molecular wire electrochemically reversible switched.[86]

Tetrathiafulvalene (TTF)

Tetrathiafulvalene is an organosulfur compound related to the hydrocarbon fulvalene, by replacement of four CH groups with sulphur atoms. Studies on this heterocyclic compound contributed to the development of molecular electronics.[90] TTF is a non-aromatic 14 π-electron molecule and can be easily and reversibly oxidized to TTF^+ and TTF^{2+} (Figure 1.9). Their redox activity is characterised by (i) two successive one-electron oxidation steps that can be carried out either chemically or electrochemically, and with full control over the oxidized species that are generated; (ii) both oxidation steps are reversible, which accounts for the good stability of both charged species $TTF^{\bullet+}$ and TTF^{2+}; (iii) the oxidised species are thermodynamically stable due to the gain of aromaticity that takes place.

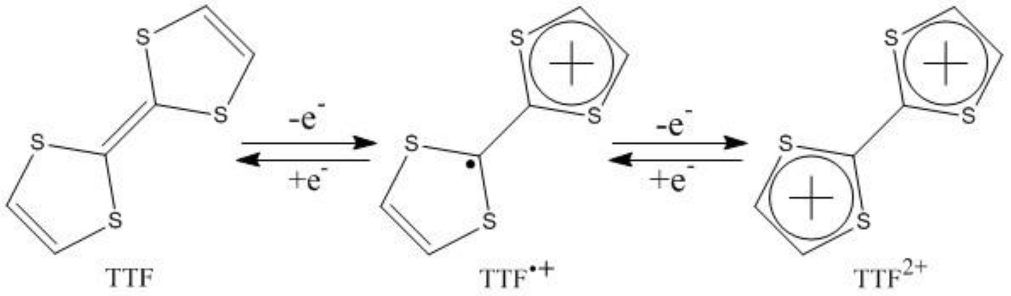

Figure 1.9 Redox processes of TTF.[91]

In 1970 Wudl et al. found that TTF forms a stable radical cation,[92] and in 1972 was reported to be a semiconductor.[93] Subsequently, the charge-transfer salt TTF-TCNQ was shown to be a narrow band gap semiconductor.[94] X-ray diffraction studies of TTF-TCNQ revealed stacks of partially oxidized TTF molecules adjacent to anionic stacks of TCNQ molecules. This unexpected type of stacking is responsible for the distinctive electrical properties, i.e. high and anisotropic electrical conductivity. Since these early discoveries, numerous analogues of TTF have been prepared. Well studied analogues include tetramethyltetrathiafulvalene (Me_4TTF), tetramethylselenafulvalenes (TMTSFs), and bis(ethylenedithio)tetrathiafulvalene (BEDT-TTF).[95] More recently, TTFs have also been successfully applied as active components in organic field effect transistors.[96]

TTF and its derivatives tend to self-assemble into nanostructures through π–π and S-S interactions.[97] Many authors have reported the electrochemical properties of TTF derivative SAMs. Yip et al.[98] first reported SAMs on gold electrodes of n-mercaptoalkyl tetrathiafulvalene carboxylate terminated in a thiol group, even though the SAMs were relatively unstable. Subsequently, a TTF incorporating four thiol groups, which form very robust SAMs on gold, was described.[99] Moore et al.[100] were the first ones to incorporate crown-ether groups into TTF-SAMs (Figure 1.10). This work exploited the direct electrochemical response of the surface-confined crown-TTF groups to measure the effect of ion complexation.

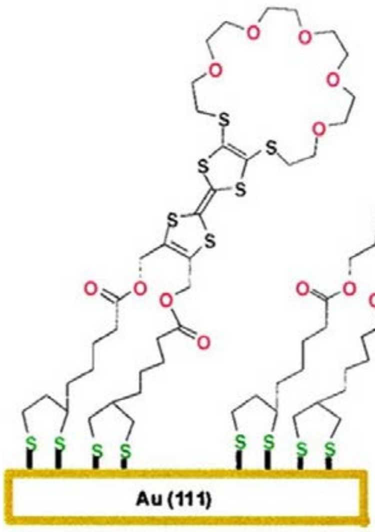

Figure 1.10 TTF-crown derivative immobilized on a metal surface.[100]

Polychlorotriphenylmethyl radical (PTM)

Molecules combining diverse magnetic, optical, and electric properties in the same structural unit have an increased value as components in the denominated multifunctional materials. An example of such compounds is the family of polychlorotriphenylmethyl (PTM) radicals that have been studied for several decades. Their multi-functionality and versatility as organic materials makes them promising candidates to be implemented in molecular electronics and spintronics.[101–103]

The PTM radicals are composed by three partially or totally chlorinated benzene rings connected to a central carbon with sp2 hybridization, known as α carbon, and are characterized by their great chemical and thermal stability (Figure 1.11).[104–106] Such stability arises from the six bulky chlorine atoms in *ortho* positions that provide steric shielding to the α carbon, where the spin density is mostly localized. Chlorine atoms in *para* positions have also a hindering effect towards aromatic substitution in such positions.

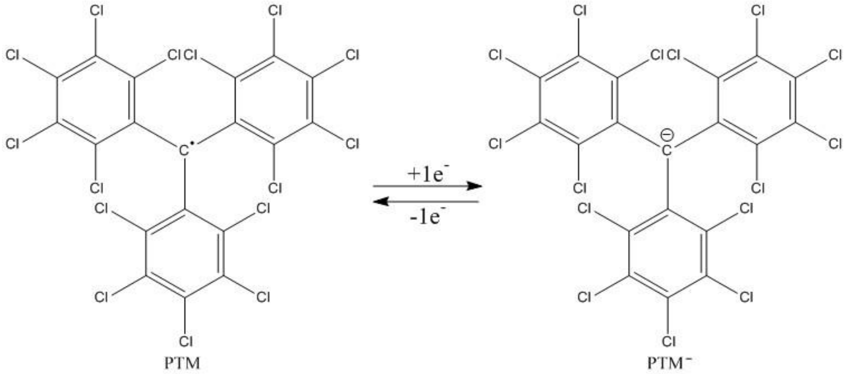

Figure 1.11 Redox processes of PTM radical group.

In solution, these compounds are stable to oxygen and to solvents and acids and are unstable only under white light. When radicals are irradiated in solution, the loss of the *ortho* chlorine atoms occurs, degenerating in ring closure and formation of fluorenil radical species.[107]

The high stability of the PTM radicals allows purifying them by standard techniques without significant decomposition. Additionally, in solid state these radicals show higher stability, being completely stable to moisture, oxygen and light, and decomposing without melting around 300ºC. PTMs are bistable in terms of their electroactive character, as they can be easily and reversibly reduced to the carboanion form (Figure 1.11). Because this redox process occurs at very low potentials, these molecules are promising for applications in charge storage memory devices. The redox pair also demonstrates unequivocally different magnetic and optical properties: the PTM radical is a paramagnetic species with maximum absorbance centred at 385 nm and fluorescence emission at 688 nm, but the anion is diamagnetic, with a maximum absorbance at ~ 510 nm, and does not emit fluorescence. Thus, SAMs of PTM on silicon oxide,[108] indium tin oxide (ITO),[109] and gold[110] have been successfully applied as molecular switches where an electrical input was translated into an optical and magnetic outputs.

The transport characteristics through PTM SAMs on gold has also been previously investigated by conductive probe atomic force microscopy (CP-AFM),[111] liquid metal junctions (alloy of eutectic gallium-indium (Ga_2O_3/EGaIn)),[112] and by electrochemical junctions.[113] It was observed that the PTM radicals exhibited a conductivity of two orders of magnitude higher compared to its analogue close shell form αH-PTM.[111] This is attributed to a SUMO (single unoccupied molecular orbital) assisted tunnelling transport mechanism.

Taking into account the described properties of the four different families of compounds, it can be concluded that these materials are suitable to be used as building blocks in Molecular Electronics.

1.1.4 Electrical characterization of Self-Assembled Monolayers

Molecular electronics aims to construct molecular devices with the functions of common electronic units (such as rectifiers, switches, or transistors) at the molecular scale.[114] Moreover, switching is a main basic function in logic and memory devices. Thus, it is highly attractive to design molecular junctions revealing a switching behaviour between "ON" and "OFF" states.

One of the major challenges in this field is to access the charge transport properties through molecules. A number of techniques have been developed for this purpose and can be mainly classified into two classes: techniques for measuring molecule groups which contain tens to thousands of individual molecules (evaporation of metals as top contact electrodes,[115] liquid metal junctions,[116] electrochemical methods,[117-119]...), and single-molecule break junction techniques (including scanning tunnelling microscope break junction (STM- BJ),[120] mechanically controllable break junction (MCBJ),[121] etc.). Figure 1.12 depicts some of the most common techniques employed to measure the transport properties of molecules ordered as a function of the number of connected molecules.[122]

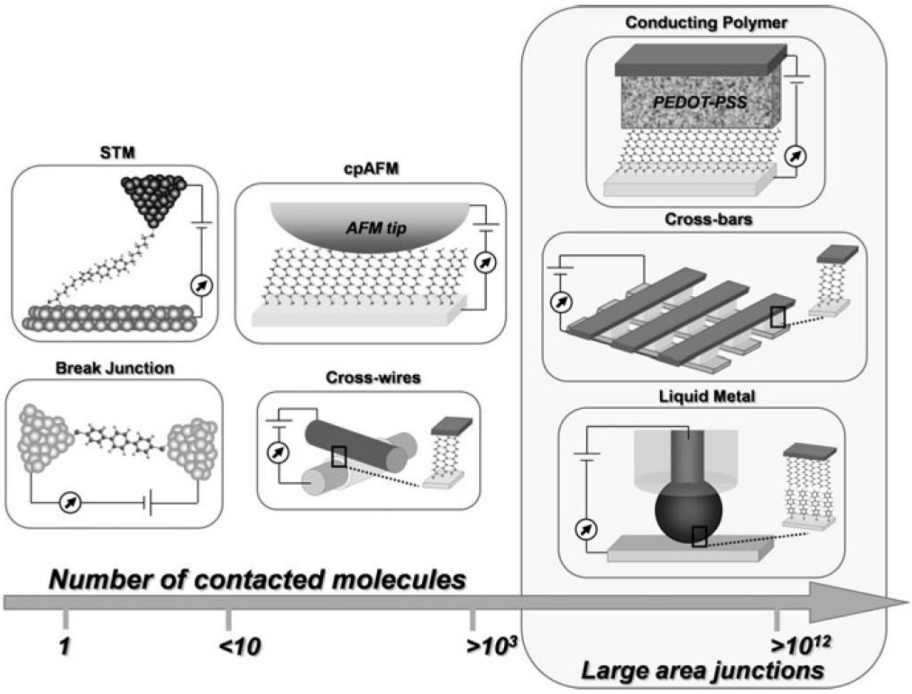

Figure 1.12 Schematic representation of the most commonly used molecular electronic junctions ordered as a function of the number of contacted molecules.[122]

The break junction approach can also be realized under electrochemical conditions by the introduction of ''electrochemical gating'' for single-molecule junctions[123] and have been used to determine the transport mechanism at room temperature.[124] This approach provides an interesting opportunity to tune the energy level of the molecule junctions and change the molecular redox states (Figure 1.13) under well-controlled conditions and performing the measurements in an electrolyte. However, these devices are technologically very demanding and currently show poor fabrication yields and device reproducibility.

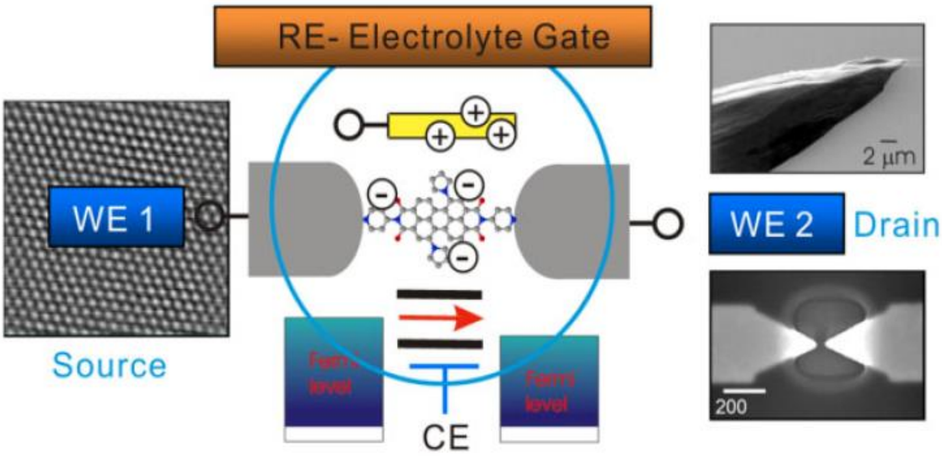

Figure 1.13 Working principle of ''electrochemical gating'' based on the BJ technique. WE1 and WE2 – working electrodes; RE – reference electrode; and CE – counter electrode.[125]

Among these different methodologies, electrochemical techniques represent inexpensive and simple procedures for the evaluation and characterization of nanostructured materials immobilized on metal substrates. Monolayers have been extensively analysed by cyclic voltammetry (CV),[126] potential step-chronoamperometry (CA),[26] electrochemical impedance spectroscopy (EIS),[127] and laser induced temperature jump methods (ILIT).[128]

CV and CA are the most common techniques, and allow the measurement of electron transfer parameters, λ, ΔG, H_{AB}, and k_{ET}. In CA measurements, the faradaic current is temporally separated from the charging current, and Tafel plots are fit using Marcus theory. EIS is used to determine k_{ET} as well as the solution resistance (R_{SOL}) and double-layer capacitance (C_{DL}) by the use of electrical equivalent circuits. However, λ, ΔG, and H_{AB} cannot be determined. Experiments are fairly simple to perform but because the phase must be considered, data analysis is complicated and can be difficult to interpret. Finally, ILIT technique was developed to measure rates for short bridge lengths, which electron transfer rates are around $k_{ET} < 10^4$ s^{-1}, and CV and CA techniques are generally considered to be limited for k_{ET} in that range.

In this Thesis, cyclic voltammetry and electrochemical impedance spectroscopy have been used as tools for the characterisation of molecular switches based on electroactive SAMs as well as for the study of their transport properties. In chapter 3, a more detailed description of the CV and EIS techniques is given.

1.2 Objectives

The present Doctoral Thesis is framed inside the field of Molecular Electronics, and it is focused on the use of electroactive organic and organometallic molecules for the fabrication of electronic devices. In these devices, the molecules can act as a channel of the electric current or switch properties.[129,130]

Thus, the main objective is focused in the preparation and characterization of different electroactive Self-Assembled Monolayers (SAMs) for the future implementation as switches in memory devices. Particular interest is placed on the understanding of the electron transfer phenomena associated to them and the use of solid electrolytes for the implementation of these systems in future real devices. The general objectives proposed in this work are:

1) Exploit the use of electrochemical impedance spectroscopy (EIS) to measure the capacitance of electroactive SAMs, and, therefore, favour the integration of molecular-based electrochemical switches in electronic devices by using electrical input and output signals.

2) Realization of molecular switches with multiple accessible redox states by the preparation of mono- and bi-component SAMs. In the case of mono-component SAMs, the approach is based in the use of molecules that exhibit more than 2 different redox states at accessible voltages, such as TTF molecules. The second strategy consists in the fabrication of binary SAMs, which are composed by two or more electroactive molecules (in this case, ferrocene and anthraquinone derivatives) in the same substrate. Both multi-state devices allow the increase of accessible states in the device, and therefore, the density of memory states increases inside the same electronic unit.

3) Fabrication and use of ion gels (based in the encapsulation of ionic liquids in a polymeric matrix) as solid-state electrolytes in electrochemical switches based on electroactive SAMs. The feasibility of this methodology would be encouraging for the integration of these molecular systems to future solid state electronic devices.

4) Study the electron transfer constant rate (k_{ET}) on a family of SAMs of PTM molecules that differ in the length of the spacer by EIS, paying attention to the influence of the solvent polarity on k_{ET}.

5) Taking advantage of the high capacitance values and easy processability of the previously synthesized ion gels, we propose to apply them as gate dielectric layers in Organic Field Effect Transistors (OFETs). In this way, it is aimed the development of low-voltage operating devices compatible with low-cost solution processing methods.

1.3 References

1 R. I. Scace, *Encyclopaedia Britannica*, 2016. Available from: https://global.britannica.com/topic/molecular-electronics

2 J. J. Thomson, *Philos. Mag. Ser. 5*, 1897, **44**, 293–316.

3 J. A. Muniz and S. P. Yu, *The Global Scientist*, 2014. Available from: https://theglobalscientist.com/2014/04/07/the-next-big-step-in-computers-what-can-physics-offer-us/

4 W. H. Brattain, *Laboratory Notebook, Case 38139-7*, 1947.

5 J. Tour, *Molecular Electronics: Commercial Insights, Chemistry, devices, Architecture and programming*, World Scientific Publishing Co. Pte. Ltd., 2003.

6 Y. Wada, *Curr. Appl. Phys.*, 2001, **1**, 28–38.

7 Feynman, *Eng. Sci.*, 2002, **23**, 1–8.

8 A. Aviram and M. A. Ratner, *Chem. Phys. Lett.*, 1974, **29**, 277–283.

9 L. Sun, Y. A. Diaz-Fernandez, T. A. Gschneidtner, F. Westerlund, S. Lara-Avila and K. Moth-Poulsen, *Chem. Soc. Rev. Chem. Soc. Rev*, 2014, **43**, 7378–7411.

10 J. P. Sauvage, V. Amendola, R. Ballardini, V. Balzani, A. Credi, L. Fabbrizzi, M. T. Gandolfi, J. K. Gimzewski, M. Gómez-Kaifer, C. Joachim, A. E. Kaifer, E. Katz, T. R. Kelly, J. Liu, C. Mangano, P. Pallavicini, A. R. Pease, L. Raehm, M. Sano, J. P. Sauvage, J. P. Sestelo, A. N. Shipway, J.-F. Stoddart, M. Venturi and I. Willner, Eds., *Molecular Machines and Motors*, Springer Berlin Heidelberg, Berlin, Heidelberg, 2001, vol. 99.

11 A. Hatzor and P. Weiss, *Science*, 2001, **291**, 1019–1020.

12 T. Dadosh, Y. Gordin, R. Krahne, I. Khivrich, D. Mahalu, V. Frydman, J. Sperling, A. Yacoby and I. Bar-Joseph, *Nature*, 2005, **436**, 677–80.

13 J. C. Love, L. A. Estroff, J. K. Kriebel, R. G. Nuzzo and G. M. Whitesides, *Chem. Rev*, 2005, **105**, 1103-1169.

14 RWTH Aachen University, I. Institute of Physics, 2015. Available from: *http://www.institut-1a.physik.rwth-aachen.de/cms/INSTITUT-1A/Forschung/Organische-Schichten/~ijov/Oberflaechenmodifikationen/?lidx=1*, 2015.

15 E. Lörtscher, *Nat. Nanotechnol.*, 2013, **8**, 381–384.

16 G. E. Poirier and E. D. Pylant, *Science*, 1996, **272**, 1145–1148.

17 R. G. Nuzzo and D. L. Allara, *J. Am. Chem. Soc.*, 1983, **105**, 4481–4483.

18 M. D. Porter, T. B. Bright, D. L. Allara and C. E. D. Chidsey, *J. Am. Chem. Soc.*, 1987, **109**, 3559–3568.

19 L. H. Dubois and R. G. Nuzzo, *Annu. Rev. Phys. Chem.*, 1992, **43**, 437–63.

20 C. D. Bain and G. M. Whitesides, *J. Am. Chem. Soc.*, 1989, **111**, 7155–7164.

21 C. D. Bain and G. M. Whitesides, *Science*, 1988, **240**, 62–3.

22 H. Biebuyck, C. Bain and G. Whitesides, *Langmuir*, 1994, **10**, 1825–1831.

23 P. Laibinis and G. Whitesides, *J. Am. Chem. Soc.*, 1991, **113**, 7152–7167.

24 L. Dubois, B. Zegarski and R. G. Nuzzo, *J. Chem. Phys.*, 1993, **1**, 678–688.

25 P. E. Laibinis and G. M. Whitesides, *J. Am. Chem. Soc.*, 1992, **114**, 1990–1995.

26 C. E. D. Chidsey, *Science*, 1991, **251**, 919–922.

27 S. Creager, C. J. Yu, C. Bamdad, S. O'Connor, T. MacLean, E. Lam, Y. Chong, G. T. Olsen, J. Luo, M. Gozin and J. F. Kayyem, *J. Am. Chem. Soc.*, 1999, **121**, 1059–1064.

28 Y. Arikuma, K. Takeda, T. Morita, M. Ohmae and S. Kimura, *J. Phys. Chem. B*, 2009, **113**, 6256–6266.

29 I. Bediako-Amoa, T. C. Sutherland, C.-Z. Li, R. Silerova and H.-B. Kraatz, *J. Phys. Chem. B*, 2004, **108**, 704–714.

30 M. Kawasaki, T. Sato, T. Tanaka and K. Takao, *Langmuir*, 2000, **16**, 1719–1728.

31 C. D. Bain, E. B. Troughton, Y. T. Tao, J. Evall, G. M. Whitesides and R. G. Nuzzo, *J. Am. Chem. Soc.*, 1989, **111**, 321–335.

32 F. Bensebaa, R. Voicu, L. Huron, T. Ellis and E. Kruus, *Langmuir*, 1997, **13**, 5335–5340.

33 J. C. Love, D. B. Wolfe, R. Haasch, M. L, K. E. Paul, G. M. Whitesides, R. G. Nuzzo and M. L. Chabinyc, *J. Am. Chem. Soc.*, 2003, **125**, 2597–2609.

34 A. Ulman, in *An Introduction to Ultrathin Organic Films*, Elsevier, 1991, pp. 237–304.

35 R. M. Metzger, *Acc. Chem. Res.*, 1999, **32**, 950–957.

36 A. R. Pease, J. O. Jeppesen, J. F. Stoddart, Y. Luo, C. P. Collier and J. R. Heath, *Acc. Chem. Res.*, 2001, **34**, 433–444.

37 A. N. Shipway, M. Lahav and I. Willner, *Adv. Mater.*, 2000, **12**, 993–998.

38 C. E. D. Chidsey, C. R. Bertozzi, T. M. Putvinski and a M. Mujsce, *J. Am. Chem. Soc.*, 1990, **112**, 4301–4306.

39 C. D. Hodneland and M. Mrksich, *J. Am. Chem. Soc.*, 2000, **122**, 4235–4236.

40 W.-S. Yeo and M. Mrksich, *Langmuir*, 2006, **22**, 10816–10820.

41 D. Lide, in *CRC Handbook of Chemistry and Physics*, ed. D. R. Lide, Taylor & Francis Group, Boca Raton, 85th ed., 2009, vol. 90, pp. 1–523.

42 V. A. Federman Neto, Alberto; Pelegrino, Alessandra Caramori; Darin, *ChemInform*, 2004, **4**, 147–169.

43 P. L. Pauson, *J. Organomet. Chem.*, 2001, **637–639**, 3–6.

44 T. J. Kealy and P. L. Pauson, *Nature*, 1951, **168**, 1039–1040.

45 G. Wilkinson, *J. Am. Chem. Soc.*, 1952, **74**, 6146–6147.

46 M. Y. Antipin, R. Boese, N. Augart and G. Schmid, *Struct. Chem.*, 1993, **4**, 91–101.

47 G. Wilkinson, P. L. Pauson and F. a. Cotton, *J. Am. Chem. Soc.*, 1954, **76**, 1970–1974.

48 M. Abe, H. Yamada, T. Okawara, M. Fujitsuka, T. Majima and Y. Hisaeda, *Inorg. Chem.*, 2016, **55**, 7–9.

49 M. Sharp, M. Petersson and K. Edström, *J. Electroanal. Chem. Interfacial Electrochem.*, 1980, **109**, 271–288.

50 M. I. Montenegro and D. Pletcher, *J. Electroanal. Chem.*, 1986, **200**, 371–374.

51 D. T. Gryko, F. Zhao, A. A. Yasseri, K. M. Roth, D. F. Bocian, W. G. Kuhr and J. S. Lindsey, *J. Org. Chem.*, 2000, **65**, 7356–7362.

52 M. Li, Z. Guo, W. Zhu, F. Marken and T. D. James, *Chem. Commun.*, 2015, **51**, 1293–1296.

53 J. Y. C. Lim, M. J. Cunningham, J. J. Davis, D. Paul, M. Road and S. References, *Chem. Commun.*, 2015, **51**, 1–26.

54 D. E. Herbert, U. F. J. Mayer and I. Manners, *Angew. Chemie Int. Ed.*, 2007, **46**, 5060–5081.

55 M. J. S. Monte, L. M. N. B. F. Santos, M. Fulem, J. M. S. Fonseca and C. A. D. Sousa, *J. Chem. Eng. Data*, 2006, **51**, 757–766.

56 L. Y. S. Lee, T. C. Sutherland, S. Rucareanu and R. B. Lennox, *Langmuir*, 2006, **22**, 4438–4444.

57 J. J. Sumner, K. S. Weber, L. A. Hockett and S. E. Creager, *J. Phys. Chem. B*, 2000, **104**, 7449–7454.

58 J. J. Sumner and S. E. Creager, *J. Phys. Chem. B*, 2001, **105**, 8739–8745.

59 G. K. Rowe and S. E. Creager, *Langmuir*, 1991, **7**, 2307–2312.

60 C. A. Nijhuis, W. F. Reus and G. M. Whitesides, *J. Am. Chem. Soc.*, 2009, **131**, 17814–17827.

61 L. Zhang, L. A. Godínez, T. Lu, G. W. Gokel and A. E. Kaifer, *Angew. Chemie Int. Ed.*, 1995, **34**, 235–237.

62 E. R. Dionne, T. Sultana, L. L. Norman, V. Toader and A. Badia, *J. Am. Chem. Soc.*, 2013, **135**, 17457–17468.

63 M. Y. Ho, P. Li, P. Estrela, S. Goodchild and P. Migliorato, *J. Phys. Chem. B*, 2010, **114**, 10661–10665.

64 A. Labande, J. Ruiz and D. Astruc, *J. Am. Chem. Soc.*, 2002, **124**, 1782–1789.

65 M. Kažem≐kait≐, A. Bulovas, V. Smirnovas, G. Niaura, E. Butkus and V. Razumas, *Tetrahedron Lett.*, 2001, **42**, 7691–7694.

66 K. Namiki, A. Sakamoto, M. Murata, S. Kume and H. Nishihara, *Chem. Commun.*, 2007, 4650–4652.

67 J. Lehr, M. Tropiano, P. D. Beer, S. Faulkner and J. J. Davis, *Chem. Commun.*, 2015, **51**, 6515–6517.

68 R. Ojani, J. Raouf and M. Ebrahimi, *Iran. J. Chem. Chem. Eng.*, 2001, **20**, 75–81.

69 S. A. Petrova, M. V. Kolodyazhny and O. S. Ksenzhek, *J. Electroanal. Chem.*, 1990, **277**, 189–196.

70 A. Zon, M. Palys, Z. Stojek, H. Sulowska and T. Ossowski, *Electroanalysis*, 2003, **15**, 579–585.

71 S. Hu, C. Xu, G. Wang and D. Cui, *Talanta*, 2001, **54**, 115–123.

72 M. P. Soriaga and A. T. Hubbard, *J. Am. Chem. Soc.*, 1982, **104**, 2735–2742.

73 P. He, R. M. Crooks and L. R. Faulkner, *J. Phys. Chem.*, 1990, **94**, 1135–1141.

74 J. Zhang and F. C. Anson, *J. Electroanal. Chem.*, 1992, **331**, 945–957.

75 M. T. McDermott, K. Kneten and R. L. McCreery, *J. Phys. Chem.*, 1992, **96**, 3124–3130.

76 E. Laviron, *J. Electroanal. Chem. Interfacial Electrochem.*, 1983, **146**, 15–36.

77 P. S. Guin, S. Das and P. C. Mandal, *Int. J. Electrochem. Sci.*, 2008, **3**, 1016–1028.

78 P. S. Guin, S. Das and P. C. Mandal, *J. Phys. Org. Chem.*, 2010, **23**, 477–482.

79 N. Gupta and H. Linschitz, *J. Am. Chem. Soc.*, 1997, **119**, 6384–6391.

80 D. H. Evans, in *Encyclopedia of electrochemistry of the elements*, eds. A. J. Bard and H. Lund, Marcel Dekker, Inc, New York, NY, 1978.

81 L. Zhang, T. Lu, G. W. Gokel and A. E. Kaifer, *Langmuir*, 1993, **9**, 786–791.

82 Y. Sato, M. Fujita, F. Mizutani and K. Uosaki, *J. Electroanal. Chem.*, 1996, **409**, 145–154.

83 T. Kondo, M. Yanagida, S. Nomura, T. Ito and K. Uosaki, *J. Electroanal. Chem.*, 1997, **438**, 121–126.

84 F. Mukae, H. Takemura and K. Takehara, *Bull. Chem. Soc. Jpn.*, 1996, **69**, 2461–2464.

85 K. Nishiyama, S. Tahara, Y. Uchida, S. Tanoue and I. Taniguchi, *J. Electroanal. Chem.*, 1999, **478**, 83–91.

86 E. H. van Dijk, D. J. T. Myles, M. H. van der Veen and J. C. Hummelen, *Org. Lett.*, 2006, **8**, 2333–2336.

87 S. Tsoi, I. Griva, S. A. Trammell, A. S. Blum, J. M. Schnur and N. Lebedev, *ACS Nano*, 2008, **2**, 1289–1295.

88 T. Markussen, R. Stadler and K. S. Thygesen, *Nano Lett.*, 2010, **10**, 4260–4265.

89 D. Fracasso, H. Valkenier, J. C. Hummelen, G. C. Solomon and R. C. Chiechi, *J. Am. Chem. Soc.*, 2011, **133**, 9556–9563.

90 M. Bendikov, F. Wudl and D. F. Perepichka, *Chem. Rev.*, 2004, **104**, 4891–4945.

91 E. Ertas, İ. Demirtas and T. Ozturk, *Beilstein J. Org. Chem.*, 2015, **11**, 403–415.

92 F. Wudl, G. M. Smith and E. J. Hufnagel, *J. Chem. Soc. D*, 1970, 1453–1454.

93 F. Wudl, D. Wobschall and E. J. Hufnagel, *J. Am. Chem. Soc.*, 1972, **94**, 670–672.

94 J. Ferraris, D. O. DO Cowan, V. Walatka and J. H. Perlstein, *J. Am. Chem. Soc.*, 1973, **95**, 948–949.

95 J. Larsen and C. Lenoir, *Org. Synth.*, 1995, **72**, 265.

96 M. Mas-Torrent and C. Rovira, *Chem. Soc. Rev.*, 2008, **37**, 827–838.

97 C. Rovira, *Chem. Rev.*, 2004, **104**, 5289–5317.

98 C. M. Yip and M. D. Ward, *Langmuir*, 1994, **10**, 549–556.

99 H. Fujihara, H. Nakai, M. Yoshihara and T. Maeshima, *Chem. Commun.*, 1999, 737–738.

100 A. J. Moore, L. M. Goldenberg, M. R. Bryce, M. C. Petty, A. P. Monkman, C. Marenco, J. Yarwood, M. J. Joyce and S. N. Port, *Adv. Mater.*, 1998, **10**, 395–398.

101 M. Mas-Torrent, N. Crivillers, V. Mugnaini, I. Ratera, C. Rovira and J. Veciana, *J. Mater. Chem.*, 2009, **19**, 1691–1695.

102 M. Mas-Torrent, N. Crivillers, C. Rovira and J. Veciana, *Chem. Rev.*, 2012, **112**, 2506–2527.

103 R. Frisenda, R. Gaudenzi, C. Franco, M. Mas-Torrent, C. Rovira, J. Veciana, I. Alcon, S. T. Bromley, E. Burzurí and H. S. J. van der Zant, *Nano Lett.*, 2015, **15**, 3109–3114.

104 M. Ballester, J. Riera-Figueras, J. Castaner, C. Badfa and J. M. Monso, *J. Am. Chem. Soc.*, 1971, **93**, 2215–2225.

105 M. Ballester, *Acc. Chem. Res.*, 1985, **18**, 380–387.

106 O. Armet, J. Veciana, C. Rovira, J. Riera, J. Castaner, E. Molins, J. Rius, C. Miravitlles, S. Olivella and J. Brichfeus, *J. Phys. Chem.*, 1987, **91**, 5608–5616.

107 M. A. Fox, E. Gaillard and C. C. Chen, *J. Am. Chem. Soc.*, 1987, **109**, 7088–7094.

108 N. Crivillers, M. Mas-Torrent, S. Perruchas, N. Roques, J. Vidal-Gancedo, J. Veciana, C. Rovira, L. Basabe-Desmonts, B. J. Ravoo, M. Crego-Calama and D. N. Reinhoudt, *Angew. Chemie Int. Ed.*, 2007, **46**, 2215–2219.

109 C. Simão, M. Mas-Torrent, N. Crivillers, V. Lloveras, J. M. Artés, P. Gorostiza, J. Veciana and C. Rovira, *Nat. Chem.*, 2011, **3**, 359–364.

110 N. Crivillers, M. Mas-Torrent, J. Vidal-Gancedo, J. Veciana and C. Rovira, *J. Am. Chem. Soc.*, 2008, **130**, 5499–5506.

111 N. Crivillers, C. Munuera, M. Mas-Torrent, C. Simão, S. T. Bromley, C. Ocal, C. Rovira and J. Veciana, *Adv. Mater.*, 2009, **21**, 1177–1181.

112 L. Yuan, C. Franco, N. Crivillers, M. Mas-Torrent, L. Cao, C. S. S. Sangeeth, C. Rovira, J. Veciana and C. A. Nijhuis, *Nat. Commun.*, 2016, **7**, 12066–12075.

113 A. V. Rudnev, C. Franco, N. Crivillers, G. Seber, A. Droghetti, I. Rungger, I. V. Pobelov, J. Veciana, M. Mas-Torrent and C. Rovira, *Phys. Chem. Chem. Phys.*, 2016, **18**, 27733–27737.

114 J. C. Cuevas and E. Scheer, *Molecular Electronics. An Introduction to Theory and Experiment*, World Scientific, Singapore, 2010.

115 J. Chen, T. Lee, J. Su, W. Wang, M. A. Reed, A. M. Rawlett, M. Kozaki, Y. Yao, R. C. Jagessar, S. M. Dirk, D. W. Price, J. M. Tour, D. S. Grubisha and D. W. Bennett, in *Molecular Nanoelectronics*, eds. M. A. Reed and T. Lee, American Scientific Publishers, Valencia, 2003, p. p1.

116 R. C. Chiechi, E. A. Weiss, M. D. Dickey and G. M. Whitesides, *Angew. Chemie Int. Ed.*, 2008, **47**, 142–144.

117 J. F. Smalley, S. W. Feldberg, C. E. D. Chidsey, M. R. Linford, M. D. Newton and Y.-P. Liu, *J. Phys.*

Chem., 1995, **99**, 13141–13149.

118 K. Weber, L. Hockett and S. Creager, *J. Phys. Chem. B*, 1997, **101**, 8286–8291.

119 K. Slowinski, R. V. Chamberlain, C. J. Miller and M. Majda, *J. Am. Chem. Soc.*, 1997, **119**, 11910–11919.

120 B. Xu, *Science*, 2003, **301**, 1221–1223.

121 C. J. Muller, J. M. van Ruitenbeek and L. J. de Jongh, *Phys. Rev. Lett.*, 1992, **69**, 140–143.

122 B. Branchi, C. Herrmann, K. W. Hipps, M. Hliwa, C. Joachim, C. Li, D. L. Mattern, R. M. Metzger, A. Mishchenko, M. A. Rampi, M. A. Ratner, N. Renaud, F. C. Simeone, G. C. Solomon and T. Wandlowski, *Unimolecular and Supramolecular Electronics II*, Springer Berlin Heidelberg, Berlin, Heidelberg, 2012, vol. 313.

123 A. R. Champagne, A. N. Pasupathy and D. C. Ralph, *Nano Lett.*, 2005, **5**, 305–308.

124 Xu, Xiao, X. Yang, L. Zang and Tao, *J. Am. Chem. Soc.*, 2005, **127**, 2386–2387.

125 C. Li, V. Stepanenko, M.-J. Lin, W. Hong, F. Würthner and T. Wandlowski, *Phys. status solidi*, 2013, **250**, 2458–2467.

126 E. Laviron, *J. Electroanal. Chem. Interfacial Electrochem.*, 1979, **101**, 19–28.

127 T. M. Nahir and E. F. Bowden, *J. Electroanal. Chem.*, 1996, **410**, 9–13.

128 J. F. Smalley, L. Geng, A. Chen, S. W. Feldberg, N. S. Lewis and G. Cali, *J. Electroanal. Chem.*, 2003, **549**, 13–24.

129 A. Ribayrol, *Microelectron. Eng.*, 2002, **39**, 1–16.

130 J. R. Heath, J. F. Stoddart and R. S. Williams, *Science*, 2004, **303**, 1136a–1136.

Chapter 2

Setup cell design and optimization for the characterization of electroactive self-assembled monolayers in different electrolytes

CHAPTER 2. Setup cell design and optimization for the characterization of electroactive self-assembled monolayers in different electrolytes

2.1 Introduction

Electrochemical experiments vary from potentiostatic and potentiodynamic techniques (as chronoamperometry or cyclic voltammetry), to complex AC techniques such as impedance spectroscopy. Furthermore, each individual technique may have multiple possible experimental setups. In this chapter, it is going to be discussed the optimal design of the electrochemical cell that has been carried out for the characterization of electroactive compounds immobilised on a conductive support.

An electrolytic cell is a device that facilitates electrochemical reactions through the application of external electrical energy.[1] For the design or selection of a specific cell, the cell design will influence on the electrochemical process, and thus, parameters such as potential and current density, materials and geometry of the electrodes or electrolyte composition and concentration have to be optimised for each particular system.

Apart from this, it should be taken into account another factors, such as cost, viability, suitability, versatility and simplicity.[2] Therefore, the objective is to find a proper design for the required working conditions obtaining good electrochemical results and reduce the uncertainty of the interpretation.[2]

The main variables that play an important role in the electrochemical cell configuration are:

- *Electrodes*: number of electrodes, materials, geometry and chemically modification of the surface.
- *Application*: redox characterization, electrolysis, flow-through, batteries and sensors.
- *Other factors*: temperature, vacuum, inert atmosphere and electrolytes.

For the characterization of chemically modified electrodes in electronic applications, the most common electrochemistry system used is the three-electrode configuration. It consists on a working electrode (WE), which is typically the modified electrode, a reference electrode (RE) and a counter electrode (CE) in contact through the electrolyte media.[3]

Many electrochemical studies should be done under an inert atmosphere (nitrogen or argon). The presence of trace amounts of oxygen in all solutions, and/or water in non-aqueous solutions, may lead to new oxidation/reduction peaks in the cyclic voltammetry (CV). In this way, the inert atmosphere will prevent the interference of oxygen reactions at the electrode surface.[4] Despite the fact that nitrogen is less expensive, the higher density of argon than air provides a better protection layer for the electrochemical experiment. This fact is really important when using volatile organic media.[4] Generally, before the electrochemical experiments, the solution is degassed with the inert gas for at least 15 min. Then it is recommended to withdrawn the tubing from the solution, only a few mm above the solution surface. In this way, an inert atmosphere is maintained inside the cell.

2.1.1 Electrodes

The common electrochemical processes consist on the immersion of the WE in the electrolyte, so then, the electrochemical reaction is taking place in its surface. When the voltage is applied to the WE, the transfer of electrons between electrode and electrolyte happens. The current produced at the electrode will pass through the CE, maintaining the equilibrium and closing the system. The RE only acts as a reference for measuring the potential at the WE.[5]

The **working electrode** is the electrode on which the reaction of interest happens. The most commonly used materials as WE are Au, Ag, Pt, glassy carbon (GC) and Hg. The size and shape is chosen depending on the application. Au electrodes have been largely used for the preparation of chemically bonded self-assembled monolayers (SAMs).[6] Despite the similar behaviour to platinum, gold electrodes have limited efficacy in the positive potential range due to the oxidation of its surface.[7]

The main role of the **reference electrode** in the electrochemical experiments is to be a point of reference for the control of the voltage and measurement. Primarily this electrode should have a stable and well-known potential, besides high stability. The saturated calomel electrode (SCE) is a reference electrode based on the reaction between elemental mercury and mercury chloride. It has been widely replaced by the silver chloride electrode, however the calomel electrode has a reputation of being more robust.[8] Silver–silver chloride is commonly selected in the three-electrode system, avoiding the contamination of the solution by insulating it with an intermediate bridge.[9] In the case of ionic liquids or non-aqueous electrolytes, silver wires are frequently used as pseudo-reference because of their simplicity and the possibility to be directly immersed into the electrolyte. This also reduces the effect of the ohmic resistance and the contamination of the electrolyte solution.[10]

The **counter electrode** is made of an inert material, and the principal task consists in closing the current circuit in the electrochemical cell. Normally it does not participate in the electrochemical process. The surface area of the CE is recommended to be higher than the area of the WE so that it will not be a limiting factor in the kinetics of the electrochemical process.[11]

The electrode geometry regulates the mass transport, that is, where material moves to and from the electrode surface. There are three modes of mass transport:[12]

- *Diffusion*: material moves to equalise concentration gradients in the solution.
- *Migration*: charged particles move to equalise potential gradients in the solution.
- *Convection*: material is moved by an external force such as flow, or rotation of the electrode.

For the control of charge movement, there are different methodologies to apply. For example, the use of an excess of the supporting electrolyte is used to eliminate migration effects from the experiment. In this way, the supporting electrolyte ions move to level the potential gradients, and not the electroactive species under study.[13] In these situations, only convective-diffusion processes are considered to describe the mass-transport. Alternatively, to avoid the convection mechanisms, it is necessary to remove stirring or agitation of the electrolyte solution and/or electrodes.[14] In this Thesis, there is a special attention to the study of electroactive SAMs, where the species of interest are adsorbed onto the electrode surface and will give rise to different voltammetry response. For an ideal case, the following theoretical assumptions are made:[15]

- The redox couple is not present in the bulk phase or is present in such low concentrations that the contribution to the current from electron transfer reactions of molecules diffusing to the electrode is negligible.
- All the adsorption sites are equivalent (homogeneous surface).
- The area occupied by the oxidized and reduced adsorbates is equivalent.
- Adsorption and desorption processes do not control the kinetics of the reaction as the species are currently chemically bonded to the surface of the electrode
- Faradaic and capacitive currents can be separated.

Adsorption is considered to be so strong that in the timescale of the experiment desorption is negligible. The diffusion can then be ignored and it follows that the total adsorbate concentration is constant. Consequently, electroactive SAMs eliminate problems associated with diffusive mass transport and allow double-layer effects to be controlled.

In electrochemical systems with flat electrodes, the flow in all the regions of the diffusion layers is always linear (one-dimensional). When the conducting material is a rectangle or disc of a few millimetres, it is considered as a planar electrode. If one or more electrode dimensions are reduced to a few microns, then is known as a microelectrode.[16]

The geometry of the cell should be optimized to reduce the ohmic drop, and its value depends on the following factors:[17]

- *The current and potential distribution in the electrolyte*. The current and potential distribution in turn depends on the geometry of the experimental cell (e.g. changing the size or shape of the working electrode will change the shape of the equipotential lines).
- *The position of the RE with respect to the WE*. If the reference is placed exactly at the electrode surface then the ohmic drop is zero. As the RE is moved away from the WE, the ohmic resistance and hence the ohmic drop increases.
- *The conductivity of the electrolyte solution*. Lower the conductivity of the electrolyte, higher the ohmic resistance and consequently higher the ohmic drop.

For fast experiments, the time constant cell (the product of the circuit resistance and the double layer capacitance, $\tau = R_{\Omega} \cdot C_{dl}$) has a significant influence on the errors in the real potential at the WE surface.[18] For slow experiments, high ohmic resistance can lead to incorrect results, which can be minimized by:

- Increasing the conductivity of the solution by using a supporting electrolyte.
- Decreasing the size of the WE to decrease C_{dl} proportionally.
- Moving the RE as close to the WE as possible to reduce the ohmic drop.

There are a variety of materials that can be used to make electrochemical cells. The most common ones are glass (Pyrex and quartz), Teflon, Kel-F, and Nylon.[4] A practical consideration in selecting these materials is their processability, cost-effective, and that they should be inert to the electrochemical processes and compounds. In the majority of the cases, Pyrex glass cells are used because their ease to fabricate and their low cost. However, when the reaction involves corrosive media to glass, then Teflon, Kel-F, Nylon or other polymeric materials should be used instead. On the other hand, plastic materials can decompose in the presence of some organic solvents, leading to contamination in the measurements.

Ionic liquids (ILs) represent a particular class of electrolyte media. These materials may be corrosive, sensitive to moisture/oxygen, and/or with a high melting temperature.[4] All these factors must be taken into account in the design of electrochemical cells for ILs research.

2.1.2 Experimental Techniques and conditions

The exact design of an electrochemical cell depends on the particular needs of the experiment. Usually, for laboratory scale, the amount of electrolyte is around 25 – 50 mL (or even larger). When the volume sample is limited, a solution of a few mL is enough. For smaller volumes (around μL), electrodes of ultra-small dimensions have to be used and aligned properly.

The experimental technique controls how the mass transport and rate law are combined to form the overall material balance equation. Each experimental technique has an associated variable/scan parameter. This controls how the system is perturbed by the experiment. Each of the common electrochemical four branches is described below:[19]

- *Equilibrium experiments*: those carried out without current flow, and only provide thermodynamic information.
- *Steady-state experiments*: those that generate an interrelation between current and potential, independently of time or frequency. For a steady state to be established, it is necessary that the relevant parameters, at any point in space, do not vary with time.
- *Periodic experiments*: those in which the current and potential vary periodically with time, at a specific frequency. The most widely used example is electrochemical impedance spectroscopy.
- *Transient experiments*: those in which current and potential vary with time in a non-repetitive fashion. Usually one of the two electrical parameters is forced to undergo a prescribed variation with time, and the dependence of the other is monitored.

The steady-state, periodic and transient techniques offer the possibility of measuring transport and kinetic parameters. Generally, electrochemical methods fall into one of these two categories: those in which a potential is imposed on the cell, and the current is monitored; and those in which the current is applied, and the potential monitored.[20]

2.2 Design and fabrication of electrochemical cells for the study of planar surface-modified electrodes

Electrochemical cells are designed to hold a working, a reference, and a counter electrode in an appropriate geometry, but beyond that there are a big variety of arrangements. Herein a detailed description of three different electrochemical cells designed and fabricated in this Thesis (Figure 2.1, Figure 2.2 and Figure 2.3) for the characterization of planar surface-modified electrodes are described. To understand the effect of the setup cell geometry, CVs of electroactive SAMs were performed in such three homemade electrochemical cells.

1st setup (Figure 2.1): This electrochemical cell has been adapted from a conventional one for electrochemical processes in solution. The cell design consists of a glass body vessel with a Teflon top with four holes of different size for placing the WE, RE and CE wires, and another one with a purging tube for bubbleling an inert gas. At the bottom of the glass there is another Teflon piece with a narrow slit and holes designed to fix the electrodes in the correct position inside the cell. This avoids the movement of the electrodes and allows the control of the position and distance between electrodes.

The easy of assembly / disassembly the different parts of the cell, together with the fixed position of the electrodes, are the main advantages of this 1st setup. However, the minimum volume of electrolyte required for the experiments should be higher than 5 – 10 mL, and is difficult to control the area of the WE immersed in the solution, so the determination of some electrochemical parameters, such as surface coverage (Γ), is not accurate.

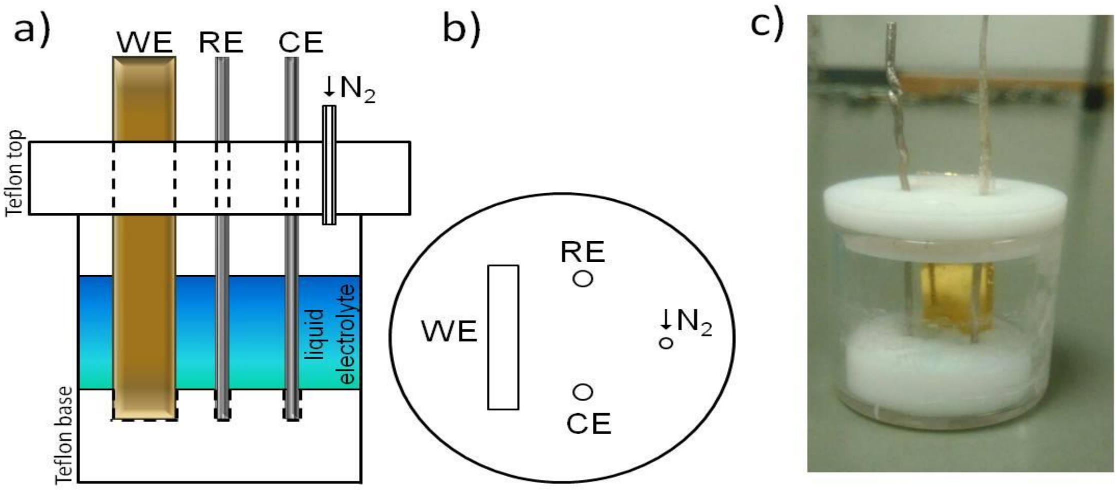

Figure 2.1 Schematic representation of the 1st setup designed for the characterization of a planar modified WE in liquid electrolytes. a) and b) correspond to schematic side and top views of the cell with the position of the electrodes indicated. c) Picture of the cell setup.

<u>2nd setup</u> (Figure 2.2): This cell is based on a Teflon body cell divided in three parts. One planar Teflon base, in which the WE is placed on it with the modified surface facing upright. A second piece perforated in the middle for inserting the electrolyte, and with two 1 mm-diameter lateral holes to introduce the CE and RE wire electrodes parallel to the WE. Finally, a third Teflon piece is placed on the top to close the cell. The cell is ensured with screws and o-rings between the Teflon pieces to avoid leakage of the liquid electrolyte and to delimit the area of the WE in contact with the electrolyte.

The most characteristic feature of this 2nd electrochemical cell design is related to the small volume of electrolyte (0.5 – 1 mL) required for the experiments, being suitable for the characterization of rare or expensive materials. Another important advantage of this configuration is the control of the WE area, delimited by o-rings, so in this way it is possible to obtain a good electrode performance study. All the body pieces of the cell are made of Teflon, which makes it resistant to a large variety of organic solvents and alkaline solutions.

However, to isolate the system from the atmospheric environment is necessary to assemble the electrochemical cell inside a glovebox. Furthermore, if the o-rings are not well positioned, some troubles of liquid leakage can appear.

Due to the specific design, the RE is limited to the use of wires of 1mm of diameter to act as pseudo-reference electrodes, being not possible to use other well-known stable reference electrodes, such as Ag/AgCl or SCE electrodes. Moreover, the small area of the counter electrode (CE), in comparison to the WE, can produce an excess of the density current in the CE surface promoting the increase of resistance elements and/or the possibility of parallel electrochemical reactions in the counter electrode surface, contaminating the system.

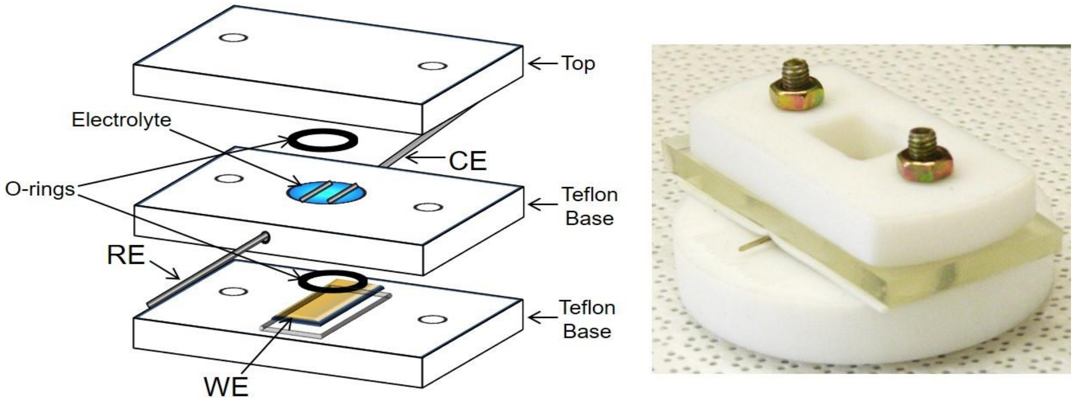

Figure 2.2 Schematic representation of the 2nd setup employed for the characterization of a planar modified WE.

3rd setup (Figure 2.3): The initial prototype was drawn with AutoCAD software, and later the final design was improved and fabricated with the collaboration of Miguel García (technician from the Electronic Engineering Department at the Universitat Politècnica de Catalunya). This final configuration is quite similar to the 2nd one, and consists of three Teflon pieces that permit to hold the modified WE exposing an specific active area to the electrolyte solution (0.5 cm^2), as well as to seal the cell and to incorporate the CE and the RE through the upper part of the cell, in this case in a perpendicular orientation with respect to the WE.

The cell was designed with three different electrolyte containers size, to use one or the other depending on the volume of electrolyte required in each individual experiment. The hole for the reference electrode is 5 mm in diameter which allows to use an Ag/AgCl electrode but also has an adapter that reduces the hole to 1 mm for the finest metal wires to act as pseudo-reference. The use of screws and o-rings allows the system to be completely isolated from the ambient conditions. Inherently, the o-ring in contact with the WE is delimiting its area and the WE is contacted through a Au-covered needle.

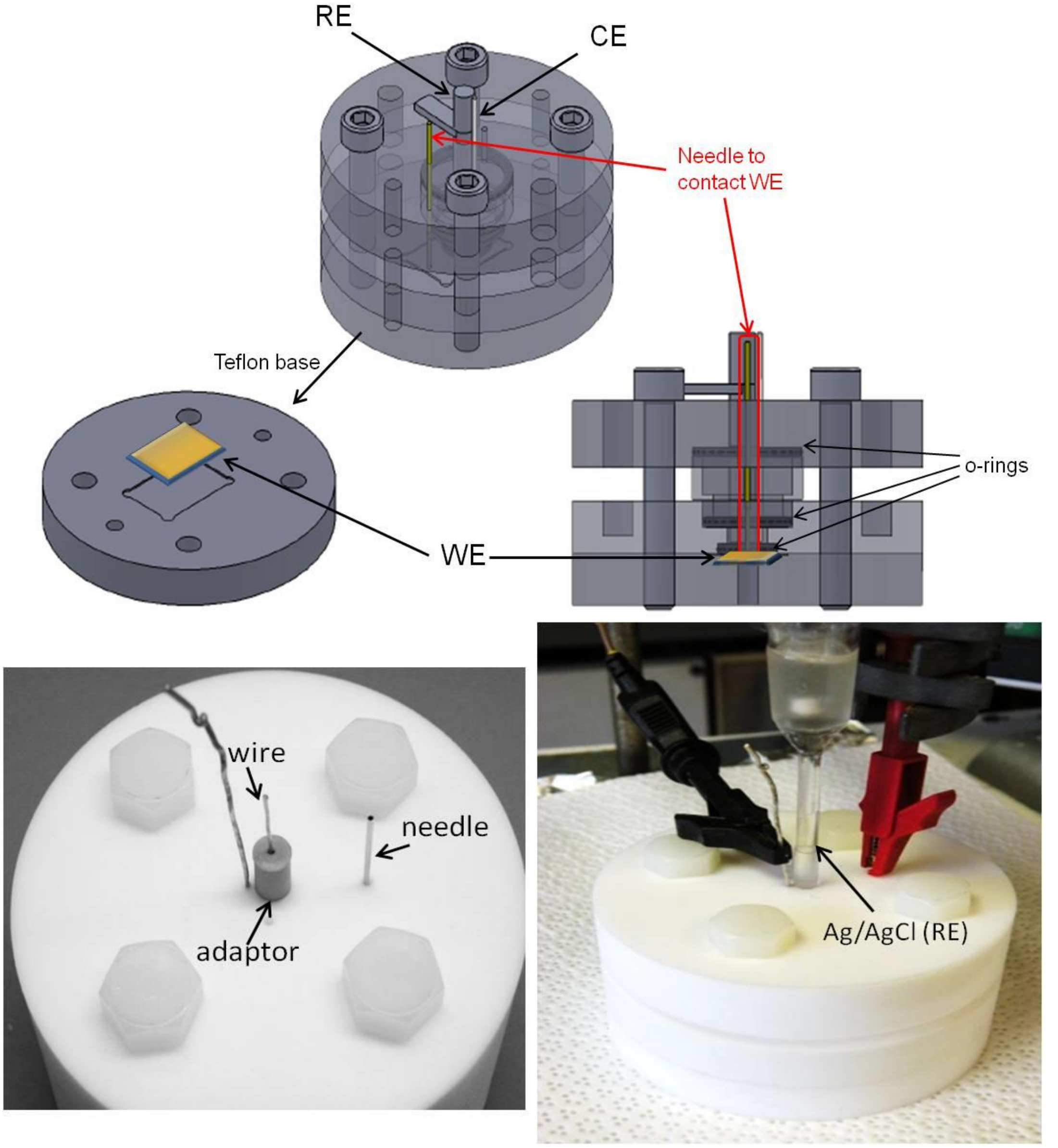

Figure 2.3 Isometric and lateral view of the 3rd setup designed for the characterization of a planar modified WE. It is indicated the parts of the body cell and the holes to introduce the different electrodes.

The perpendicular layout of the CE and RE facilitates their position as close as possible to the WE surface. And also, the cavity of the electrolyte container allows the use of a spiral Pt wire or a mesh as CE to increase the area of the CE respect to the WE (to avoid excess of density current and/or secondary processes on the surface of the counter electrode).

In order to evaluate the response obtained with each electrochemical setup, electroactive SAMs based in ferrocene compounds have been prepared and measured. The results and comparisons are presented below.

2.2.1 Comparison of the CV response of a Ferrocene SAM in the different electrochemical cells

Prior to the preparation of the chemically modified SAMs, the Au substrates were cleaned using different solvents and dried with a nitrogen stream. After that, Au substrates were immersed in 1 mM solution of 11-(ferrocenyl) undecanethiol ($FcC_{11}SH$) in ethanol under inert atmosphere and room temperature (25 ± 3°C). The Au substrates were immersed inside the solution for 18 hours, and after that, they were removed from the solution and cleaned exhaustively with ethanol, and finally dried under nitrogen stream (for more details of the SAM preparation, see Chapter 6, section 6.4.1 and 6.4.2).

All the samples were prepared in the same batch, trying to keep a high reproducibility between the samples studied. The electrochemical behaviour of the SAMs was investigated by CV in aqueous solution, using $HClO_4$ 0.1 M in milliQ water.

The CV experiments were recorded at different scan rates, varying between 50 and 1000 mV/s. Figure 2.4 shows the measured CV curves under the potential window ranging from -0.2 to $+0.5V_{vs\ Ag(s)}$ at the different setups.

It can be clearly seen that the three samples are quite similar in nature but they differ slightly in the shape and evolution of the redox peak. For a deeply analysis, specific electrochemical parameters, such as $E^{1/2}$, ΔE, E_{FWHM}, and I_p should be considered.

The formal redox potential, $E^{1/2}$, is determined from the average of the anodic and cathodic peak potentials, $E_{p,a}$ and $E_{p,c}$, and the peak separation, ΔE, is calculated by $E_{p,a} - E_{p,c}$.

As the scan rate increases, peak separation increases. The Δ*E* values are usually small in surface confined species but not zero volts as expected for the Nernstian reaction of an ideal adsorbed monolayer. The peak shape is an indicator of the homogeneity of the monolayer and can be evaluated by the full width at half of the peak maximum height (ΔE_{FWHM}).[21] The values obtained for the formal redox potential ($E^{1/2}$), ΔE and ΔE_{FWHM} for the three different setups are presented in Table 2.1.

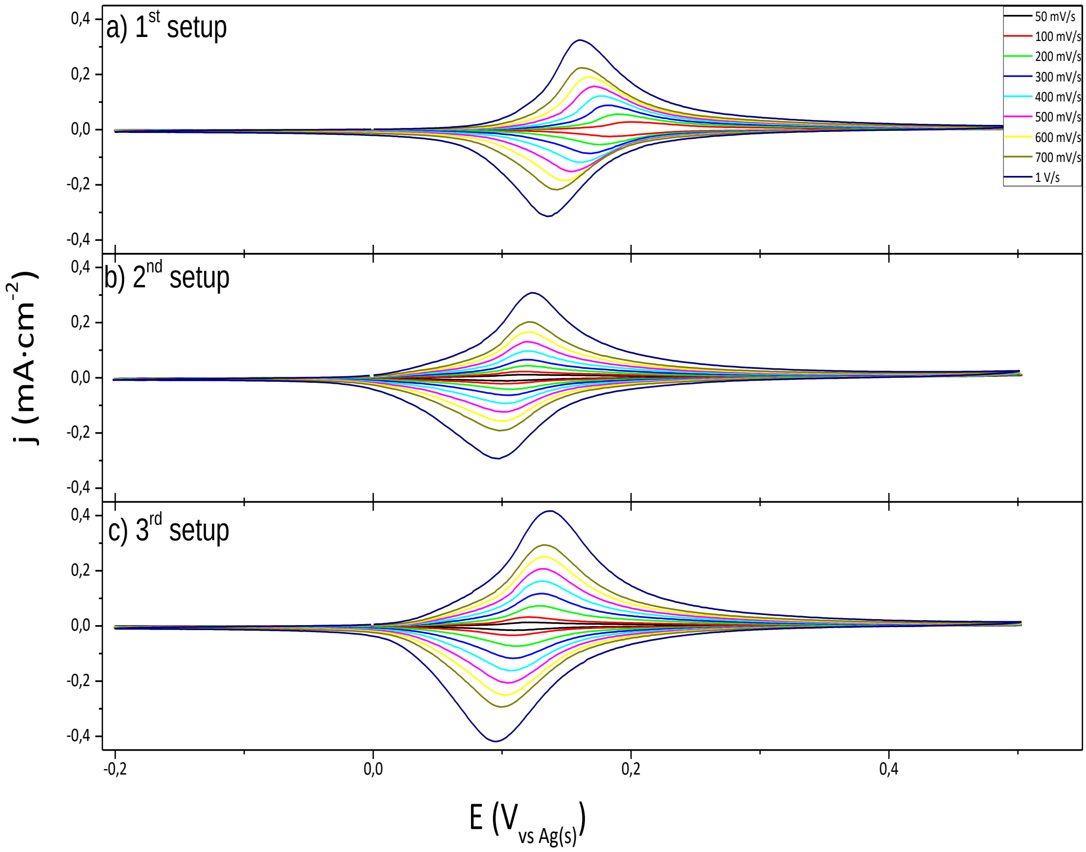

Figure 2.4 CVs of $FcC_{11}SH$-SAMs in $HClO_4$ 0.1 M at different scan rates for: a) 1st setup, b) 2nd setup, and c) 3rd setup.

Electrochemical cell	**$E^{1/2}$ ($V_{vs\ Ag(s)}$)** *ν=100mV/s*	**ΔE (mV)** *ν=100mV/s*	**ΔE_{FWHM} (mV)** *ν=100mV/s*
1st setup	0.16	27.8	63.0
2nd setup	0.11	16.7	73.8
3rd setup	0.12	24.2	70.6

Table 2.1 Values for $E^{1/2}$, ΔE and ΔE_{FWHM} for the Fc-SAMs in the different setups.

The values obtained for $E^{1/2}$ are practically the same in the three different setups, indicating a good reproducibility of the samples prepared. It is possible to observe that ΔE is always greater than the value expected for an ideal reversible confined system. Therefore, the redox couple in the modified electrode shows a quasi-reversible behaviour in an aqueous medium[5]. On the other hand, the values of ΔE_{FWHM} are slightly lower than the theoretically expected (ΔE_{FWHM} < 90.6 mV, for Fc/Fc^+ redox process). This variation is attributed to electrostatic attracting interactions incurred by neighbouring charged species, and depends basically on the packing of the surface monolayer, not on the geometry of the electrochemical cell.

From the CV data shown in Figure 2.4, the magnitudes of the peak potentials ($E_{p,a}$ and $E_{p,c}$) and the formal redox potential ($E^{1/2}$) have been plotted as a function of the potential scan rate, in logarithmic scale (E_p vs log ν, see Figure 2.5).

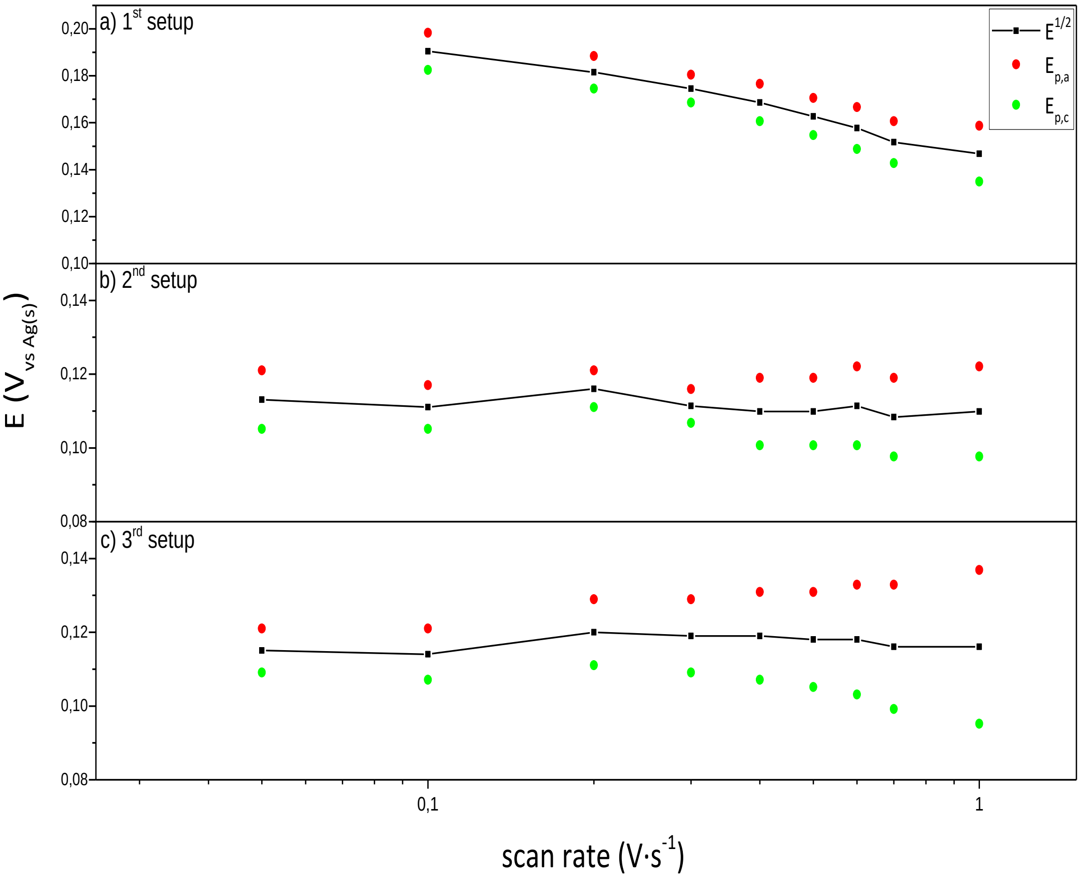

Figure 2.5 Formal redox potential ($E^{1/2}$, black squares) and anodic and cathodic peak potential ($E_{p,a}$ –red points; $E_{p,c}$ –green points) vs. scan rate (ν) for: a) 1st setup, b) 2nd setup, and c) 3rd setup.

For the 1st setup, it is possible to observe that the potential of the anodic and cathodic peak is shifted to lower potentials as the scan rate increases. This result is also reflected in the variation of the redox formal potential ($E^{1/2}$). One possibility that can explain this potential decrease can be associated to the combination of the use of a Ag wire as pseudo-reference, together with a slightly penetration of atmospheric moisture or oxygen to the system during the performance of the experiments, as the bubbleling tube was removed during the measurements.

In the case of the 2nd configuration, the variation of the peak potentials is not following a linear tendency with the scan rate. However, the $E^{1/2}$ is kept almost constant, that is in concordance with the fact that the system is isolated from the atmospheric environment, in contrast to the 1st electrochemical cell. Finally, it is found that, for the 3rd setup, the E_p values vary proportionally to log (ν) for values higher than 100 mV s^{-1},[22] being $E^{1/2}$ practically stable in the range of scan rates analysed. This happens because the kinetics of the reaction is slow in comparison to the voltage scan rate and thus, the equilibrium is not established rapidly. Consequently, the current takes more time to respond to the applied voltage than the ideal reversible case.

The irregularities found at low scan rates, in the 2nd and 3rd configurations, can be related to the contribution of an electrical resistance, due to geometric factors, that affect the redox process and become more dominant at low scan rates; although at rapid scans, that resistance become negligible in comparison to the charge transfer resistance of the redox process.

Continuing with the electrochemical analysis, but now in terms of current, in Figure 2.6 the variation of the oxidation and reduction current peak ($I_{p,a}$ and $I_{p,c}$, respectively) with the scan rate is represented. Anodic and cathodic peak currents values are linearly dependent on the scan rate for the range 50 to 1000 mV·s^{-1}, in agreement with a surface-confined controlled redox process at the modified electrode.

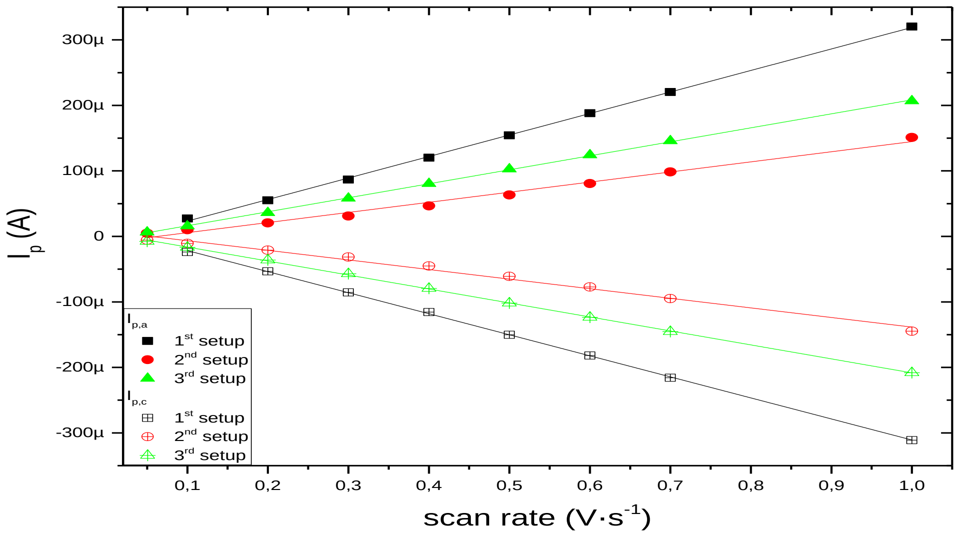

Figure 2.6 I_p vs v for the different geometries: 1st setup (black diamonds), 2nd setup (red squares) and 3rd setup (green triangles).

Finally, to achieve an optimal cell configuration, it is important to take into account different non-electrochemical factors, such as the control of the working area electrode (A_{we}), to avoid the liquid electrolyte leakage, and the control of the electrolyte volume for the measurements.[4]

The control of the working electrode area (A_{we}) is absolutely important to obtain certain parameters, such as surface coverage (Γ), diffusion coefficients (in case of liquid electroactive sample analysis), and the evaluation of kinetic parameters (*i.e.* electron transfer rates (k_{ET})). In the 1st configuration, it is quite difficult to control the area of the working electrode immersed in the solution. For the 2nd and 3rd electrochemical cells fabricated, the A_{we} is always delimited by a Teflon o-ring, keeping always the same A_{WE} covered by the electrolyte. This is very important when comparing different experiment reproducibility.

To avoid the presence of atmospheric oxygen or moisture and the liquid leakage, it is necessary to properly seal the cell inside a glovebox and to use o-rings made by resistant materials (such as Teflon or EPDM, ethylene propylene diene monomer). That is the case of the 2nd and 3rd configurations, where the system is completely sealed.

Finally, when using ionic liquids as electrolytes, due to their cost the use of small amounts of electrolyte volume is an important factor (around 0.5 or 1 mL). For these experiments, the 1st electrochemical cell geometry is not recommended, being the 2nd and 3rd cells more suitable.

2.3 Summary

In this chapter, the design, optimization and fabrication process of three different electrochemical cells have been described for the application of electrochemical techniques to characterize electroactive compounds anchored to planar conducting substrates.

Considering the results obtained in the three different cell setups, it can be concluded that the geometry and configuration of the electrochemical cell slightly affects the performance of the measurements, and the non-ideal behavior is mainly attributed to different factors related to the monolayer itself, for example the influence of lateral interactions between electroactive centers, double layer effects, ion pairing, etc.

Despite the comparable results obtained from CV in all the setups studied, the most relevant differences between geometries are the possibility to extract specific electrochemical parameters, thanks to the control of the area of the working electrode, the fixed position and distances between electrodes, the isolation of the system from the external contamination (moisture and oxygen), the dissipation of liquid leakage and the control of electrolyte volume. It has been observed that the setups that meet these requirements show more ideal electrochemical results.

Finally, it is important to highlight that the electrochemical experiments have been successfully performed with all the setups, and depending on the type of samples to analyse and the information sought, the configuration of the electrochemical cell can be adapted, taking into account all the parameters that play an important role during the measurements.

2.4 References

1 G. F. McGuffie, *Chemistry for changing times*, Prentice Hall, 9th ed., 1982, vol. 59.

2 F. C. Walsh, *A First Course in Electrochemical Engineering*, The Electrochemical Consultancy, 1993.

3 P. Daum and R. W. Murray, *Chemically modified electrodes*, Wiley-VCH Verlag GmbH & Co. KGaA, Weinheim, Germany, 2009, vol. 103.

4 C. G. Zoski, *Handbook of Electrochemistry*, Elsevier, 2007.

5 A. J. Bard and L. R. Faulkner, *Electrochemical Methods: Fundamentals and Applications*, John Wiley & Sons, Inc., New York, NY, 2nd ed., 2001.

6 M. D. Porter, T. B. Bright, D. L. Allara and C. E. D. Chidsey, *J. Am. Chem. Soc.*, 1987, **109**, 3559–3568.

7 U. Oesch and J. Janata, *Electrochim. Acta*, 1983, **28**, 1237–1246.

8 M. G. Banus, *Science*, 1941, **93**, 601–602.

9 G. Li and P. Miao, in *Electrochemical Analysis of Protein and Cells*, Springer Berlin Heidelberg, Berlin, Heidelberg, 2013, pp. 1–18.

10 G. Gritzner, *Handbook of Reference Electrodes*, Springer Berlin Heidelberg, Berlin, Heidelberg, 2013.

11 P. T. T. Kissinger and W. R. Heienman, *Laboratory techniques in electroanalytical chemistry*, Marcel Dekker, Inc, New York, NY, 2nd ed., 1996, vol. 15.

12 A. J. Fry, *Synthetic Organic Electrochemistry*, John Wiley & Sons, Inc., 2nd ed., 1989.

13 J. J. Wolff and R. Wortmann, *Organic Materials for Second-Order Non-Linear Optics*, 1999, vol. 32.

14 M. Amblard, J.-A. Fehrentz, J. Martinez and G. Subra, *Fundamentals of modern peptide synthesis.*, John Wiley & Sons, Inc., Hoboken, NJ, USA, 2nd ed., 2005, vol. 298.

15 M. J. Honeychurch and G. A. Rechnitz, *Electroanalysis*, 1998, **10**, 285–293.

16 M. Mastrangeli, S. Abbasi, C. Varel, C. Van Hoof, J.-P. Celis and K. F. Böhringer, *J. Micromechanics Microengineering*, 2009, **19**, 83001-83038.

17 M. Gratzl, D. F. Hsu, A. M. Riley and J. Janata, *J. Phys. Chem.*, 1990, **94**, 5973–5981.

18 M. E. Orazem and B. Tribollet, in *Electrochemical Impedance Spectroscopy*, John Wiley & Sons, Inc., 2008, pp. 108–128.

19 A. M. Bond, K. B. Oldham and C. G. Zoski, *Anal. Chim. Acta*, 1989, **216**, 177–230.

20 C. M. A. Brett and A. M. C. F. Oliveira Brett, *Compr. Chem. Kinet.*, 1986, **26**, 355–441.

21 A. L. Eckermann, D. J. Feld, J. A. Shaw and T. J. Meade, *Coord. Chem. Rev.*, 2010, **254**, 1769–1802.

22 E. Laviron, *J. Electroanal. Chem. Interfacial Electrochem.*, 1979, **101**, 19–28.

Chapter 3

Development of electrochemical switches operated by electrical input and output signals

CHAPTER 3. Development of electrochemical switches operated by electrical input and output signals

3.1 Introduction

One of the ultimate goals of Molecular Electronics is the development of computer components based on bistable molecules and supramolecular structures. Bistability means the possibility that exists, in a single system, two or more thermodynamically stable states corresponding to local minimums in potential surface energy. In the field of computer systems, these structures are related to the concept of logical zeros (0) and ones (1), corresponding to the rearrangements of bistable structures associated with information transitions between states.

For that purpose, molecular switches represent one of the most studied systems in Molecular Electronics, and are based on molecules with two or more stable states with different properties that can be reversibly interchanged by applying an external stimulus (Figure 3.1). The molecules may be shifted between the states in response to environmental stimuli, such as changes in pH, light, temperature, an electric current or in the presence of a ligand. The change between these states is interrelated with changes in physical or chemical properties and even in the appearance of new intrinsic properties in a particular state. These discernible properties can be thus exploited for reading the system, that is, as an output signal.

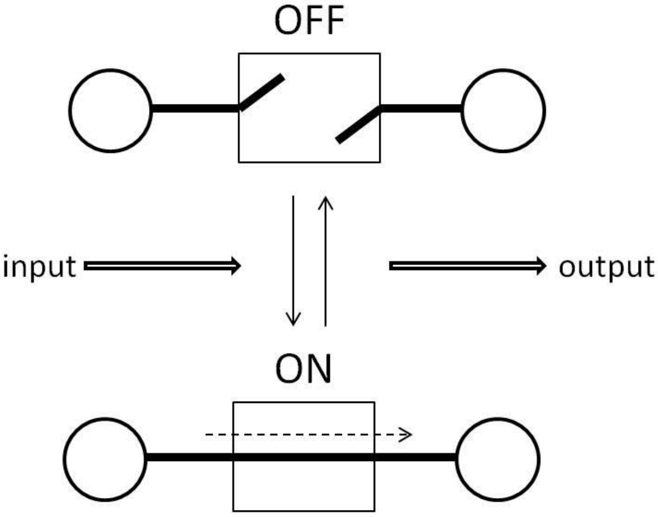

Figure 3.1 Schematic description of a switch.[1]

The switching process must satisfy some basic requirements to be useful: i) to have high differences in the magnitude of the initial and final value of the properties, ii) to be stable enough to read information of the states without disrupting them, and iii) the interconversion barrier between the states has to be higher than the thermal energy at the working temperature.

Molecular switches represent the maximum limit of miniaturization to create functional molecular devices[2,3] and they cover a wide range of frontiers in science: from molecular computing to sensors,[4,5] displays and smart materials[6] and from drug delivery to control of biomolecular processes.[7] In the ongoing quest for nanodevices and molecular machines, the design of molecular switching elements integrated with a variety of functions is a challenge. Research on molecular switches has been greatly stimulated by prospects of memory elements as small as the single molecule and their potential for information technology.

Molecular switches have been intensively studied in solution,[1] however, when these switches are assembled on solid surfaces, it makes possible the placement, addressability, and cooperative operations for the development of devices.[8]

One way to immobilize the molecular switches in solid substrates consists in the preparation of self-assembled monolayers (SAMs), which have been extensively characterized as well-organized arrays of organic molecules on solid surfaces.[9-13] Electrochemically active SAMs prepared on metal surfaces bear not only scientific interest, but they have also attracted much interest in recent years for their application in sensors and molecular electronic devices. SAMs of electroactive molecules have recently been exploited as electrochemical switches. Typically, the state of these switches can be read out through their optical and/or magnetic response,[14-16] although these output responses are difficult to integrate into devices. Herein, this bottleneck is overcome by the fabrication of switches using electrical signals as input and output at the same time, encouraging in this way the implementation of these switches in future electronic applications.

3.1.1 Electrochemical techniques

A wide variety of electroactive SAMs have been extensively studied by a number of electrochemical methods, including cyclic voltammetry, pulse voltammetry, ohmic drop analysis, chronoamperometry, and electrochemical impedance spectroscopy. Below the most significant techniques applied in this thesis will be described: cyclic voltammetry and electrochemical impedance spectroscopy.

Cyclic Voltammetry (CV)

Cyclic voltammetry is the most extensively used technique for acquiring qualitative information about electrochemical reactions. It tenders the rapid identification of redox potentials distinctive to the electroactive species under investigation, providing considerable information about the thermodynamics of a redox process, kinetics of heterogeneous electron-transfer reactions and analysis of coupled electrochemical reactions or adsorption processes. This technique is a potential sweep method where the current is recorded while the electrode potential is changed linearly with time between two values chosen as for potential step methods.[17,18]

The initial potential, E_1, is normally the one where there is no electrochemical activity and the final potential, E_2, is the one where the reaction is mass transport controlled. In linear sweep voltammetry, the scan stops at E_2, whereas in cyclic voltammetry, the sweep direction is reversed when the potential reaches E_2 and the potential returns to E_1. The rate at which this is achieved is the scan rate. Depending on the information required, either single or multiple cycles can be performed. The plot of current (I) vs. voltage (E) is called "cyclic voltammogram".

Figure 3.2 shows a typical CV curve for the case of an electrochemical process of an electroactive compound in solution, where the current response is monitored under the application of a linear variable potential. Characteristics of the voltammetry which are routinely monitored and reported are the peak height (I_p) and the potential at which the peak occurs (E_p). The formal redox potential can be found as the mid-way between the two redox peaks comprising the voltammetry:

$$E^{1/2} = \left(E_p^{ox} + E_p^{red}\right)/2 \qquad \text{(Eq. 3.1)}$$

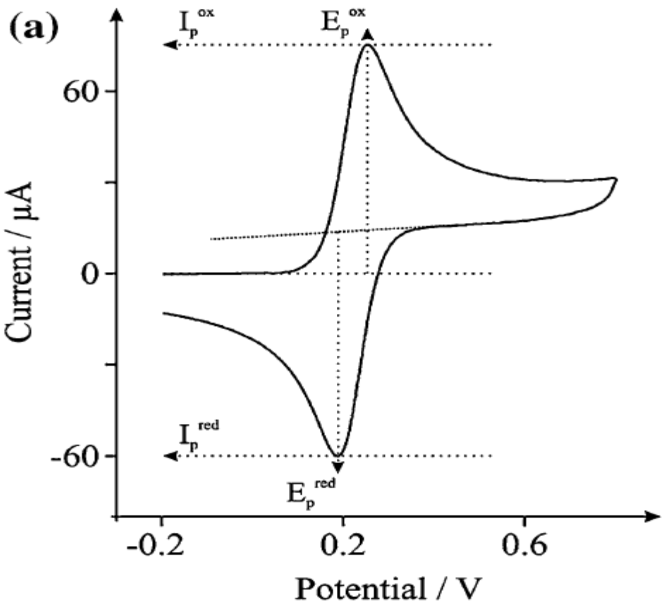

Figure 3.2 Theoretical CV for an electroactive molecule in solution, depicting the peak position E_p and peak height I_p.[18]

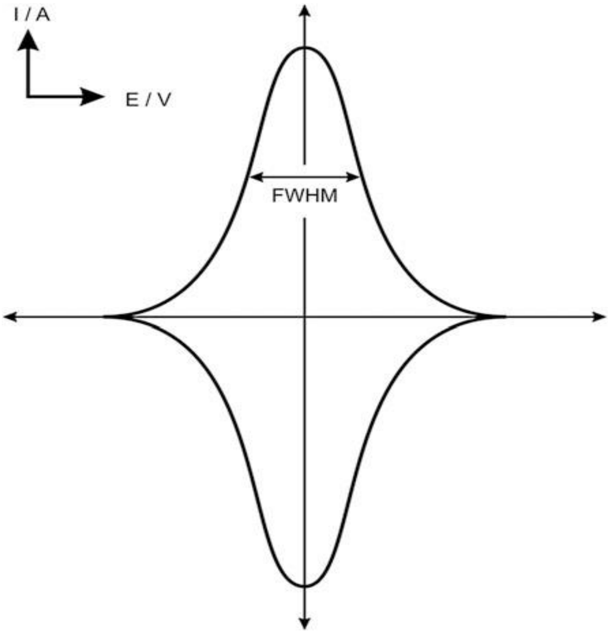

Figure 3.3. Theoretical CV for the reversible reaction of surface-confined species.[18]

In the case of electroactive SAMs, the species of interest are adsorbed onto the electrode surface and will give rise to different voltammetry response. Figure 3.3 shows the typical shape for an ideal Nernstian electron transfer. It consists of two symmetrical peaks, where the charges (the areas under the peaks) for oxidation and reduction are equal as all the adsorbed species undergo reduction/oxidation. The current symmetrically peaks and decays to zero because there is a fixed amount of reactant present (i.e., no diffusion). The charge passed must remain constant.

The peak height current (I_p) can be related directly to the surface coverage (Γ) and potential scan rate (v) for a reversible process:

$$I_p = \frac{n^2F^2\Gamma Av}{4RT} \quad \text{(Eq. 3.2)}$$

where n is the number of electrons transferred in the reaction, A is the area of the working electrode, R is the universal gas constant, T is the temperature (in Kelvin), and F is the Faraday constant. In surfaces with adsorbed electroactive species the effect of scan rate on the current intensity peak (I_p) should yield a linear response. From the integration of the area under the peaks shown in Figure 3.3, the charge (Q) can be deduced, which is related to the surface coverage (Γ) by the following expression:

$$Q = nFAv\Gamma \quad \text{(Eq. 3.3)}$$

The full width at half of the peak maximum height (ΔE_{FWHM}, Figure 3.3) is given by:

$$\Delta E_{FWHM} = 3.53RT/nF \quad \text{(Eq. 3.4)}$$

The characteristic features of a cyclic voltammetry involving an ideal Nernstian adsorption are the following:

$$\Delta \mathrm{E} = 0 \quad \text{(Eq. 3.5)}$$

$$I_{pa} = -I_{pc} \quad \text{(Eq. 3.6)}$$

$$Q_a = -Q_c \quad \text{(Eq. 3.7)}$$

$$\Delta E_{FWHM} = \frac{3.53RT}{nF} = \frac{90.6}{n} mV\ at\ 298K \quad \text{(Eq. 3.8)}$$

The shape of the peaks is indicative of the nature of the interactions between the surface-confined species, and the position of the peaks along the potential axis is indicative of the reversibility of the electron transfer process. The larger the ΔE, the more irreversible is the electron transfer.

Conventional electrochemical techniques such as CV or potential and current pulses allow characterization of rates and reaction mechanisms, double layer capacitances, diffusion properties, morphology and/or interface structure of the electrodes. However, these techniques generally move the system away from equilibrium, so that the reaction rates of the interfacial parameters can be altered by the methodology itself.

Electrochemical Impedance Spectroscopy (EIS)

Electrochemical impedance is an AC technique that is usually applied to investigate the interface between an electrode material and a solution. This type of measurements provide complementary information to that obtained from DC electrochemical techniques such as cyclic voltammetry, pulse voltammetry, ohmic drop analysis, and chronoamperometry.

This technique involves applying a low amplitude pure sinusoidal current or voltage waveform to the cell at a particular frequency and then calculating the impedance of the cell at that frequency from the measured AC voltage across the cell or the AC current passing through the cell. This measurement process is repeated at a number of frequencies in order to fully characterize the cell impedance across the frequency range of interest.

Electrochemical impedance experiments comprise the following steps: (1) the electrochemical cell is subjected to a small amplitude periodic electrical perturbation (Figure 3.4); (2) its electrical response is acquired over a range of perturbation frequencies; (3) an equivalent electrical circuit is worked out; (4) components of the equivalent circuit are related to key physical or chemical characteristics of the electrochemical system.[17]

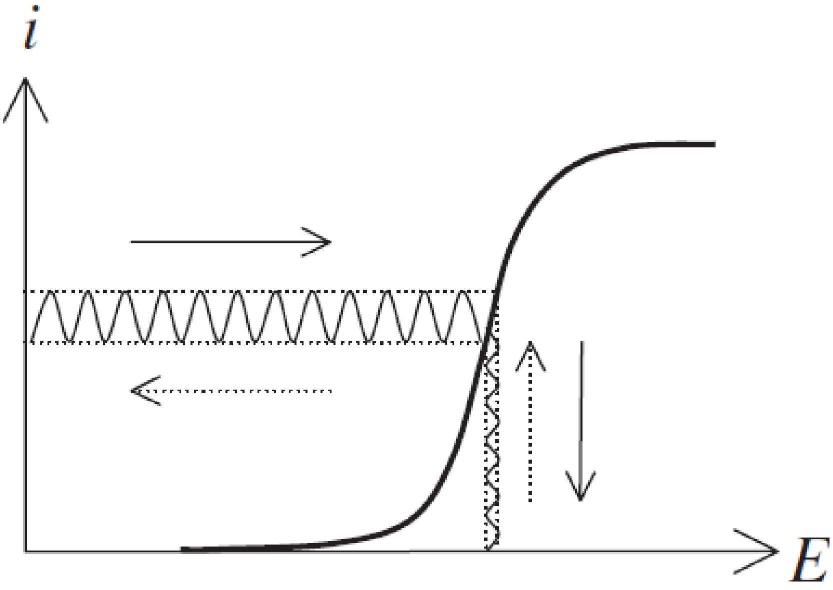

Figure 3.4 Solid arrows: an AC current is applied to the electrode and an AC potential response is obtained. Dashed arrows: an AC potential is applied to the electrode and an AC current is obtained. The i–E relationship is recorded over a range of frequencies.[17]

A low amplitude sinusoidal stimulus (usually around 5 – 10 mV) is used in order to operate within a linear region of the cell. This is very important since the non-linear nature of electrochemical cells can lead to impedance measurement inaccuracies when using higher amplitude signals.

For a complete impedance characterization, the frequency of the stimulus sine wave is swept across the frequency range of interest and measurements are taken at each frequency point. Frequency response analysers give very accurate measurements but are limited in their measurement speed due to having to sweep the measurement frequency. This has limited their use for measurements on fast changing systems.

Impedance $Z^*(f)$ can be represented using Bode or Nyquist plots.[17,19,20] In Bode plots, the log of the magnitude of the impedance ($|Z|$), and the phase (φ) are plotted separately versus the logarithmic frequency. In a Nyquist representation, the ordinate is the imaginary component of the impedance (Z_{im}) and the abscissa the real component (Z_{re}). The advantage of using an EIS approach is that several parameters, such as electrolyte resistance (R_{sol}), double-layer capacitance (C_{dl}), charge transfer resistance (R_{ct}), electrode surface area (A), and surface coverage (Γ), can be measured in one experiment.

The key step in electrochemical impedance experiments is the construction of an equivalent circuit that simulates the electrical behaviour of the electrochemical system.[21,22] For this, it is necessary to consider the different ways in which the ionic charges are involved in the passage of current (i.e., ion pairing). The Randles circuit is one of the simplest models for electron transfer phenomena in redox species attached as monolayers on a conductive substrate which is described as follows:[23] between the electrodes, the solution behaves as an ionic conductor with a resistance (R_{sol}), known as the ohmic solution resistance. At the electrode–solution interface, some of the ions are used to adjust the ionic environment until the charge is balanced between the electrode surface and the solution. Electrically, this is equivalent to the charge or discharge of a capacitor with capacitance (C_{dl}), known as the double layer capacitance. Simultaneously, redox attached species undergo an electron transfer with the electrode; this yields the faradaic current whose magnitude reflects the rate of the electron transfer process. Electrically, this is equivalent to a resistor in series to a capacitor: one for the kinetics of the electron transfer process (R_{ct}), known as the charge transfer resistance, and one for the charge or discharge of the adsorbed electrochemical monolayer (C_{ad}). Pulling all this together, the simplest electrical equivalent circuit consists of four components connected as shown in Figure 3.5, the Randles circuit.

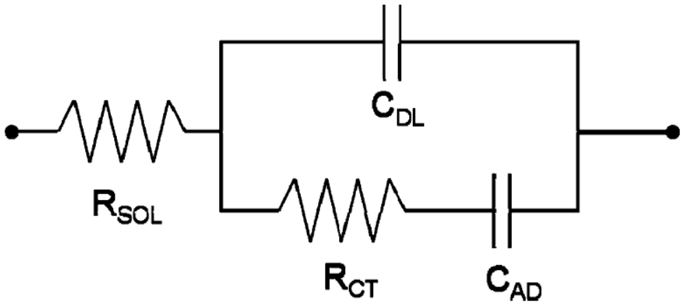

Figure 3.5 Randles circuit for redox species grafted to a conductive substrate.[24]

The solution resistance is determined by the solution conductivity and the geometry of the cell. The double layer capacitance reflects the electrostatic interplay between the electrode and the electrolyte and depends on the nature and area of the electrode, and on the electrolyte ionic strength and permittivity. R_{ct} reflects the charge transfer kinetics and can be thought of as the ratio of overpotential to current in absence of mass transfer limitation.

Problems may, however, appear due to the non-ideal behaviour of resistances (charge transfer) and capacitances (double layer) of the system under study or by the limitations imposed through the use of an inappropriate circuit, that can distort the derived parameter values and consequently in the modelling.[23]

Electroactive Monolayer Capacitive Spectroscopy (EMCS)

With the objective of using a versatile and self-consistent approach to establish the redox characteristics of electroactive molecular films, a capacitive frequency-resolved methodology has been employed. This approach avoids the need to fit acquired data to a specific equivalent circuit.[23] The information is acquired from measurements at specific electrode potentials (one at the redox potential and one aside the redox peak). In this way it can be achieved a better understanding of the different contributions in the current response, but also the establishment of a more robust means of segregating faradaic contributions of the response from the capacitive background.[25]

The Electroactive Monolayer Capacitive Spectroscopy procedure consists in the conversion of the complex impedance function (Z*(*f*)) into complex capacitance function (C*(*f*)) by the following expressions:

$$Z^{*}(f) = Z_{re} - j \cdot Z_{im} \leftrightarrow C^{*}(f) = C_{re} + j \cdot C_{im} \qquad \text{(Eq. 3.9)}$$

$$C^{*}(f) = \frac{1}{j(2\pi f)Z^{*}(f)} \rightarrow \begin{cases} C_{re} = \frac{1}{2\pi f} \cdot \frac{Z_{im}}{\left(Z_{re}^{2}+Z_{im}^{2}\right)} \cdot \frac{1}{A} \\ C_{im} = \frac{1}{2\pi f} \cdot \frac{Z_{re}}{\left(Z_{re}^{2}+Z_{im}^{2}\right)} \cdot \frac{1}{A} \end{cases} \qquad \text{(Eq. 3.10)}$$

Practically, this involves taking the data resolved in a standard impedance analysis (Z*(*f*)), sampled across a range of frequencies at any steady-state potential, and converting it phasorially into complex capacitance (C*(*f*)) with its real and imaginary components.[26] If one carries out this analysis inside of the surface potential window where redox activity is observed and then outside the potential window, the difference (between the two impedance measurements) is obtained as the pure electrochemical response constituting of a resistance and a capacitance in series.[25,26]

Figure 3.6 depicts simulated EMCS spectra of a homogeneous SAM/interface taking the background capacitance (C_{dl}) as null.[27] In the theoretical predictions is evident that the Nyquist representation (Figure 3.6.a) looks like straight vertical lines parallel to the *y*-axis and provides little information, but the capacitance directly reports the SAM-layer capacitance (C_{ad}) (Figure 3.6.b). The onset of this semicircle directly reports C_{dl}, and the diameter of the semicircle equates to C_{ad}. Bode plot of the real part of the complex capacitance (Figure 3.6.c) provides a facile means of quantifying the C_{ad} contribution and thus the layer dielectric polarizability as a function of frequency (with the plateau at low frequency corresponding to the sum of C_{ad} and C_{dl}).

The use of EMCS, especially in the form of Cole−Cole diagrams, has shown to be a very powerful method to study molecular monolayers, allowing a clear segregation between the background signal from the faradaic activity.

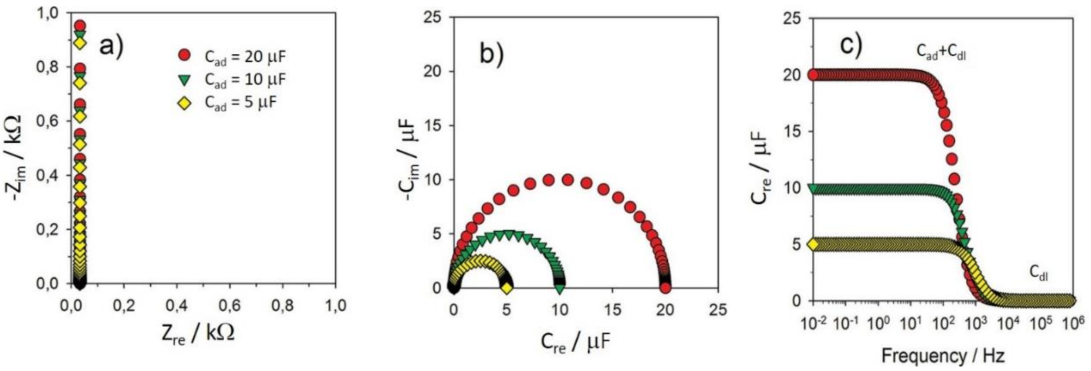

Figure 3.6(a) Theoretical Nyquist plot of a SAM-modified interface for different magnitudes of SAM-layer capacitance (C_{ad}) (b) The same theoretical interface presented as a capacitive diagram (c) Bode diagram of the real part of the complex capacitive function, $C^*(f)$. C_{ad} is directly visualized from the diameter of the semicircle in part b or the plateau value in part c (20, 10, or 5 μF).[27]

3.1.1 Liquid and solid electrolytes: Ionic liquids and ion gels

Aqueous electrolytes have several limitations as electrochemical media:[28] 1) there are too many chemical substances of potential electrochemical reactivity which are insoluble in water (mostly organic compounds); 2) water, as a protic solvent, is highly reactive with a variety of electrode materials and compounds of interest, such as active metals, organic salts which undergo fast hydrolysis, basic or acidic compounds, complexes, etc.; 3) the applicability of aqueous solutions is limited to temperatures in which these media are in the liquid state; and 4) the electrochemical window of water is too narrow. These limitations can restrict their application.

The use of non-aqueous systems increases the range of applicability of electrochemical techniques to many organic and inorganic compounds that are either unstable or insoluble in water, besides the wider electrochemical window of many non-aqueous systems.[29]

Electrochemistry in non-aqueous solutions has played an important role in exploring new chemical possibilities as well as in providing the methods to evaluate static solvent effects on various chemical processes. Furthermore, many new electrochemical technologies have been developed using non-aqueous solvents. However, it is also true that some useful solvents have properties that are problematic to human health and the environment. Today, efforts are being placed on finding environmentally friendly media for chemical processes. For electrochemical purposes, replacing hazardous solvents by harmless solvents, where ionic liquids and supercritical fluids appear to be promising.

Ionic liquids (ILs) are melted salts at ambient temperature. Because ILs are composed of only ions, they show very high ionic conductivity, non-volatility, and non-flammability.[30] Non-flammable liquids with high ionic conductivity are practical materials for use in electrochemistry. From the point of view of thermal stability, they have the disadvantage that because of their higher viscosity, they rapidly lose their electrolytic conductivity as the temperature decreases. In Figure 3.7 are presented some examples of anions and cations used for the formation of ILs.

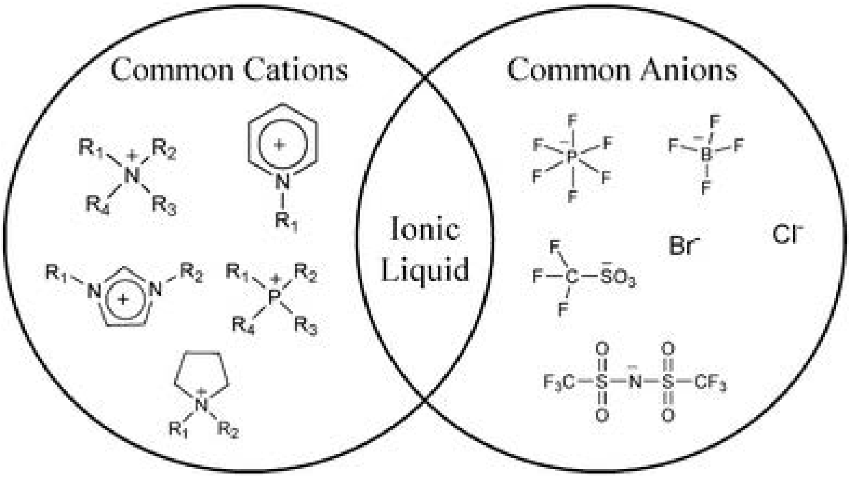

Figure 3.7 Some examples of anions and cations used in the formation of ionic liquids.[31]

A particular attention in this work has been focused on the use of ILs as electrolytes, which are currently catching the attention as ''green" electrolytes for electrochemical science and engineering.[32–34] The physicochemical properties of ILs can be tuned by the choice of the anion-cation pair, which opens millions of possibilities.[35,36] Moreover, the combination of non-volatility and favourable solubilising characteristics of ILs has motivated the interest as a replacement for organic solvents in many industrial applications like catalysis[37,38] and extraction.[39]

Measurements of electrochemically active species in ILs have revealed their potentially application as electrolytes.[40] However, further studies are required to completely understand the role of anions and cations of the ILs as electrolytes.

The growing use of ILs in the materials field comes from their structural and physicochemical features. There is a challenging need for immobilizing ILs in solid matrixes, while keeping their exclusive properties. This purpose involves the formation of a three-dimensional network soaked by the IL and creating a solid-like final material, called ion gel (IG).[41] The peculiarity is the insignificant vapour pressure and the thermal stability of the liquid phase, which makes IGs stable materials over time and allows for using them up to temperatures much higher than ambient.

The gelation of ILs is a conventional method for making gel electrolytes; therefore it is expected to play a role in the field of solid electrolytes. Solid electrolytes, which are electrically conductive solids with ionic carriers, have received special attention because of their potential use in solid-state batteries, fuel cells, energy storage, and chemical sensors.[42–44]

Solid electrolytes are promising candidates to replace liquid electrolytes due to their inherent properties, such as low reactivity, ease handling and high flexibility in geometry properties for the various applications. They eliminate the problems of corrosive solvent leakage and harmful gas compared to liquid electrolytes.[45]

In this present work, poly (vinylidene fluoride–co–hexafluoropropylene) (PVdF–HFP), and 1–ethyl–3–methylimidazolium bis(trifluoromethylsulfonyl) imide (EMIM-TFSI) were used as host polymer and ionic liquid, respectively. PVdF–HFP is a talented candidate as matrix material for solid polymer electrolytes due to its high solubility in various organic solvents, low crystallinity, low glass transition and melting temperatures, and high anodic stability due to strong electron withdrawing functional group. In addition, it is an ideal material due to its high chemically resistance, relatively high dielectric constant (ε_r=9.4–10.6) and superior mechanical integrity as well as good electrochemical stability.[46–50]

3.1.2 Objectives

In this chapter different electroactive SAMs on gold have been exploited as electrochemical switches. The main objective was to operate these molecular switches not only by the application of an electrical input to interconvert the states, but also to use electrical output signals to read the switch. To achieve this, here it is proposed to implement the capacitance response of the SAMs to monitor the switches. As a reference system, this methodology has been explored in ferrocene derivative SAMs using different liquid environments (see section 3.2).

A second objective of this part of the Thesis was to prepare for the first time solid state switchable devices based on electroactive SAMs by using ion gels. This would lead to more applicable devices due to the fact that liquid electrolytes would be omitted.

Finally, to increase the density of information storage by electrochemical means, it has been planned to fabricate multi-state devices following two different approaches:

a) by the use of binary SAMs composed with two different functional electroactive molecules. Ferrocene and anthraquinone derivative molecules as electron donor (D) and electron acceptor (A) groups, respectively, were selected for this purpose (see section 3.4.1).

b) by the use of mono-component SAMs based on electroactive molecules with more than one redox process, in this case a TTF derivative (see section 3.4.2).

In all the cases, the methodology to electrochemically characterise the SAMs consist in the initial study of the SAMs by cyclic voltammetry (CV) followed by the use of electrochemical impedance spectroscopy (EIS) for the evaluation and exploitation of capacitance switches. Complementary information for the characterization of the different modified surfaces has been obtained by means of atomic force microscopy (AFM), X-ray photoelectron spectroscopy (XPS), time-of-flight secondary ion mass spectroscopy (ToF-SIMS) and contact angle techniques.

3.2 Bi-state Switches: Ferrocene derivative SAMs (Fc-SAMs) in liquid electrolytes

Herein, ferrocene derivative self-assembled monolayers (Fc-SAMs) have been investigated as electrochemical switch by applying different DC bias voltages and using the electrochemical impedance spectroscopy (EIS) to measure the capacitance response (Figure 3.8). Different electrolytes have been explored in this work: 1) perchloric acid ($HClO_4$) in an aqueous solution (as reference system) and 2) three different ionic liquids, namely 1-Ethyl-3-methylimidazolium bis (trifluoromethylsulfonyl) imide (EMIM-TFSI), 1-Ethyl-3-methylimidazolium tetrafluoroborate (EMIM-BF_4), and 1-Ethyl-3-methylimidazolium ethyl sulphate (EMIM-$EtSO_4$). These ILs only differ in the anionic part. This work is focused on the influence of the electrolyte on the Fc monolayer electrochemical performance for its application as capacitive molecular switch.

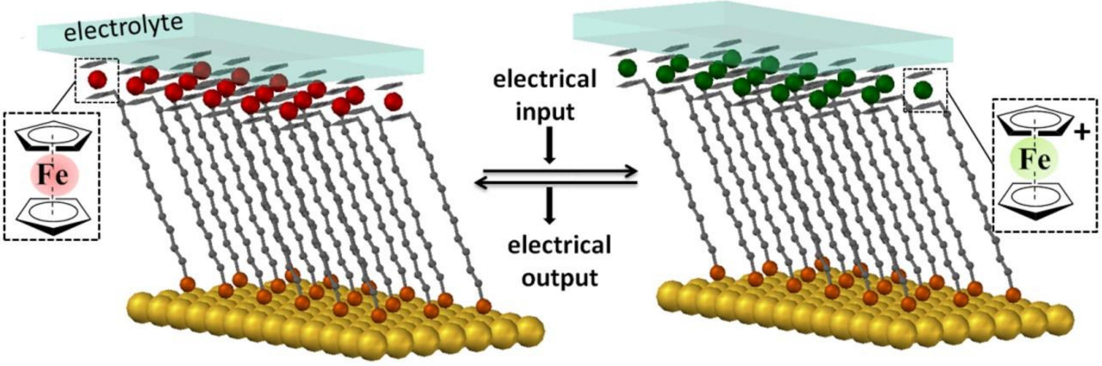

Figure 3.8 Scheme of the electrical molecular switch based on a ferrocene SAM on gold.[51]

3.2.1 Ferrocene derivative SAMs (Fc-SAMs) on Au

Two types of Au substrates were initially used: Au supported on mica (commercially available from Georg Albert PVD-Beschichtungen), and Au thermally evaporated on glass, using 15 nm of chromium as adhesion layer. The general procedure for the preparation of SAMs on Au started with the cleaning of the Au substrates. Firstly, the substrates were degreased by using different solvents series with increased polarity (i.e., dichloromethane, acetone and ethanol) and dried under a nitrogen stream. Just before use, the substrates were treated in a UV ozone chamber for 20 minutes and the resulting oxide layer was removed by leaving the substrates for at least 30 minutes in ethanol, then rinsed with isopropanol and dried under nitrogen stream.

Once the substrates were cleaned, they were immediately immersed in a 1 mM solution of 11-(ferrocenyl) undecanethiol ($FcC_{11}SH$) in ethanol under inert atmosphere and at room temperature (25 ± 3°C). The Au substrates were immersed in the solution for 18 hours, and after that, they were removed from the solution and cleaned exhaustively with ethanol, to eliminate the physisorbed molecules on the surface, and finally dried under a nitrogen stream.

The Fc-SAMs have been characterized by contact angle, atomic force microscopy (AFM), X-ray photoelectron spectroscopy (XPS), and Time-of-Flight secondary ion mass spectroscopy (ToF-SIMS).

Contact angle measurements were performed to examine the surface wetting properties of the Fc-SAMs with water and ionic liquid electrolytes. The measurements were performed with 3 μL drops positioned on the SAMs in air at room temperature using the sessile drop method. The average values obtained for three different measurements were 78.0 ± 3.4°, 66.5 ± 0.4°, 56.3 ± 0.7°, and 38.6 ± 1.2°, using milliQ water, EMIM-BF_4, EMIM-$EtSO_4$ and EMIM-TFSI, respectively (Figure 3.9). These results demonstrate a higher tendency of EMIM-TFSI to wet the modified surface and thus, this IL might lead to a higher ionic inclusion within the Fc-SAM during the electrochemical experiments.

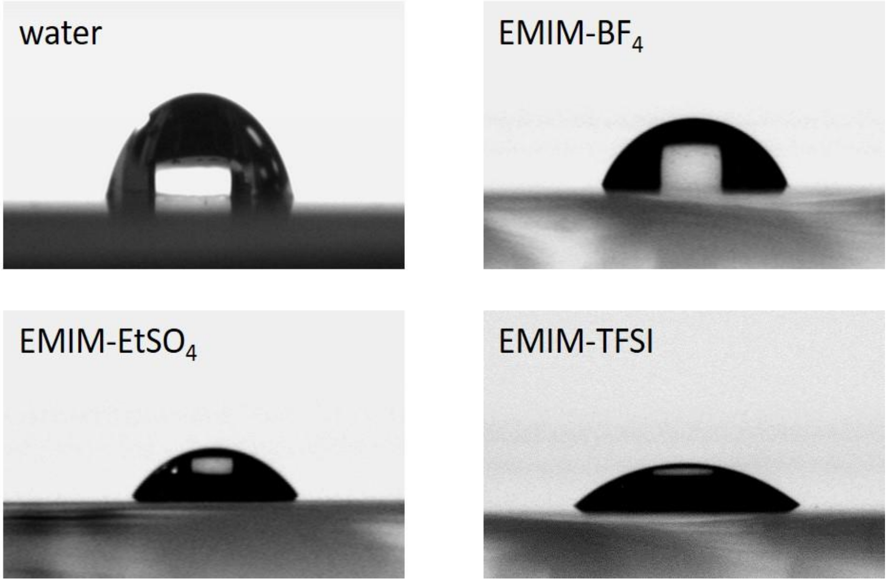

Figure 3.9 Contact angle images of Fc-SAMs with: water, EMIM-BF_4, EMIM- $EtSO_4$, and EMIM-TFSI.

The topography and roughness of the Fc-SAMs have been studied by AFM using the two different Au substrates. In Figure 3.10 the images corresponding to the Au-mica substrates before and after modification with $FcC_{11}SH$ molecules are shown. From the images it can be obtained the R_{RMS} factor (Root Mean Square), to numerically estimate the roughness of the layer. In this case, R_{RMS} increases significantly from 0.1 to 0.5 nm, due to the surface modification with the ferrocene group.

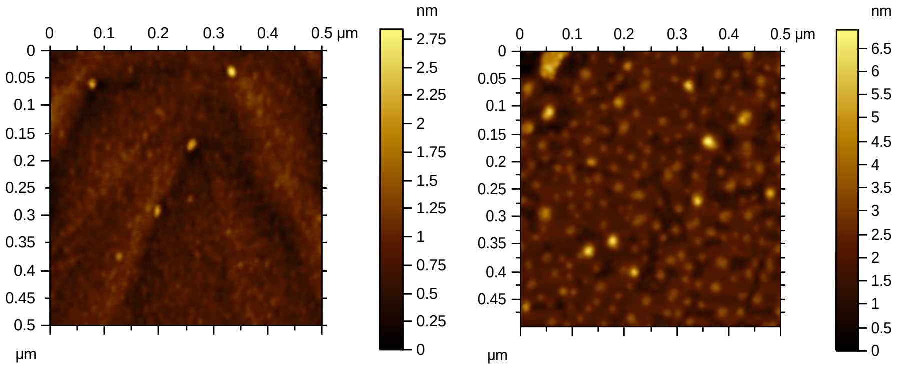

Figure 3.10 Topographic AFM images of bare Au (left) and Fc-SAM (right) on Au-mica.

In comparison, Figure 3.11 displays the images corresponding to the Au substrates evaporated on glass before and after modification with $FcC_{11}SH$ molecules. Due to the roughness of the Au-glass substrates (R_{RMS} = 2.3 nm), it is not possible to observe significant differences when the Au is modified with ferrocene (R_{RMS} = 2.1 nm). Despite the Au surface roughness is an important factor in the quality of the SAM, the advantage of Au-glass substrates relies on the possibility to fabricate specific electrode designs by using a mask during the thermal evaporation process. Further, the surface roughness degree has not considerably affected the following characterization and electrochemical study. This is the Au employed in the studies described below.

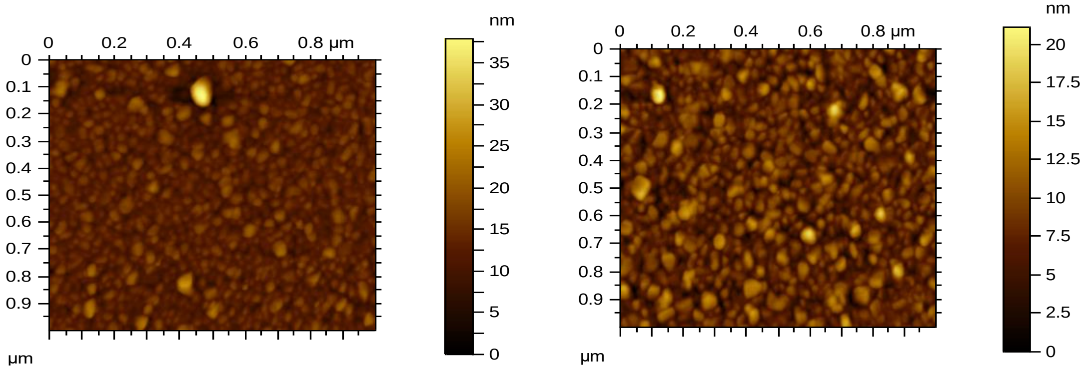

Figure 3.11. Topographic AFM images of bare Au (left) and Fc-SAM (right) on Au evaporated on glass (Cr 5nm, Au 75nm).

For the elemental analysis of the Fc-SAMs, and to confirm the binding of the ferrocene derivative to the gold via the Au–S bond, the X-ray photoelectron spectroscopy (XPS) and Time-of-Flight secondary ion mass spectroscopy (ToF-SIMS) techniques were used. As it can be seen in Figure 3.12.a, the XPS data showed the presence of sulphur. The deconvoluted S 2p spectrum gave rise to two S_{2p} doublets with binding energy values of 161.5 and 162.9 eV, with a relative area of 2:1 and peak separation of 1.4 eV, indicating that $FcC_{11}SH$ were chemisorbed on gold via the formation of a Au−S bond.[52] XPS spectrum also showed the peaks for Fe $2p_{3/2}$ and Fe $2p_{1/2}$ with binding energies of 707.6 and 720.3 eV, respectively, which are characteristic for Fe (II) in the ferrocene label (Figure 3.12.b). The broad structure to higher binding energy (~710 eV) of the main Fe $2p_{3/2}$ peak is due to Fe^{3+} states from oxidation of the surface.

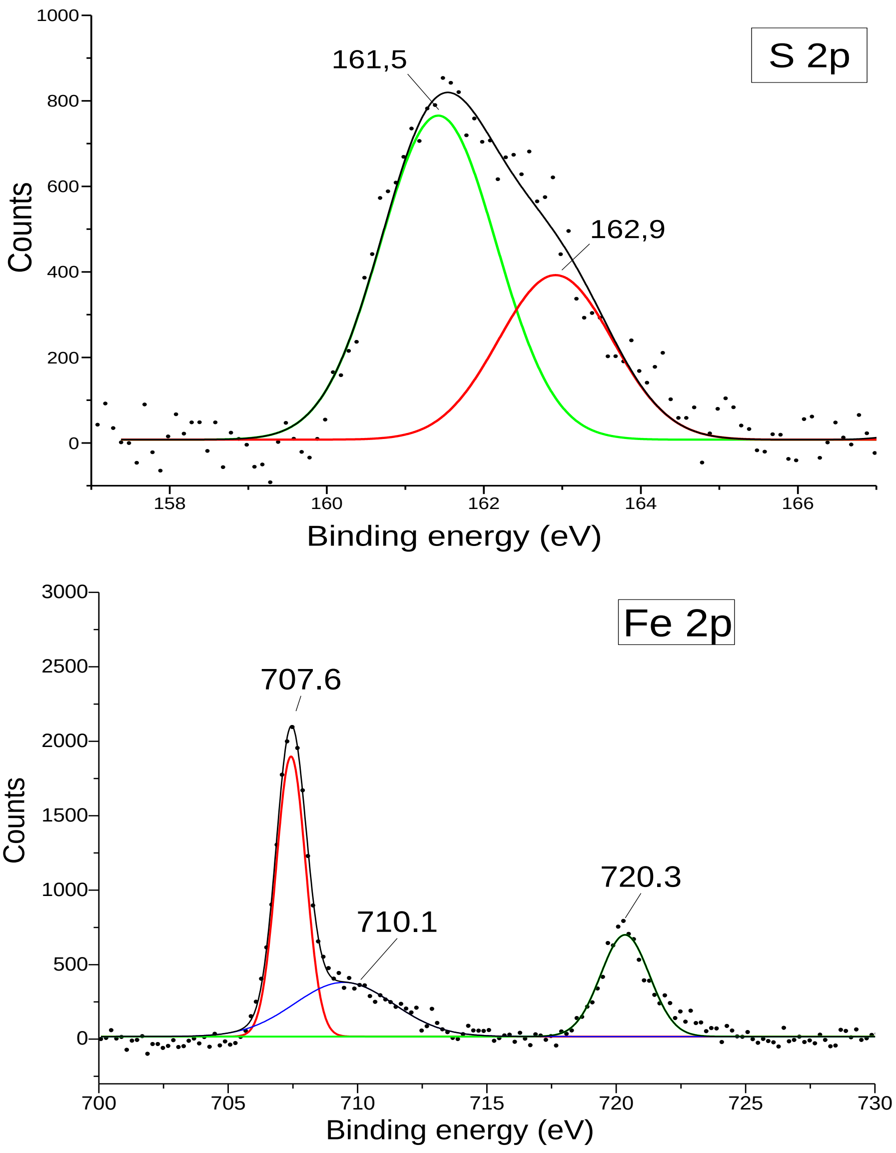

Figure 3.12 XPS spectra of Fc-SAMs on gold for a) S 2p, b) Fe 2p.

Additional confirmation of the successful formation of the Fc-SAM on the gold surface was provided by the ToF-SIMS results (Figure 3.13). This technique is highly useful for the identification of different chemical groups present on the surface.[53] Effectively, the ToF-SIMS spectra showed the Fc fragment ion intensity at m/z = 186.

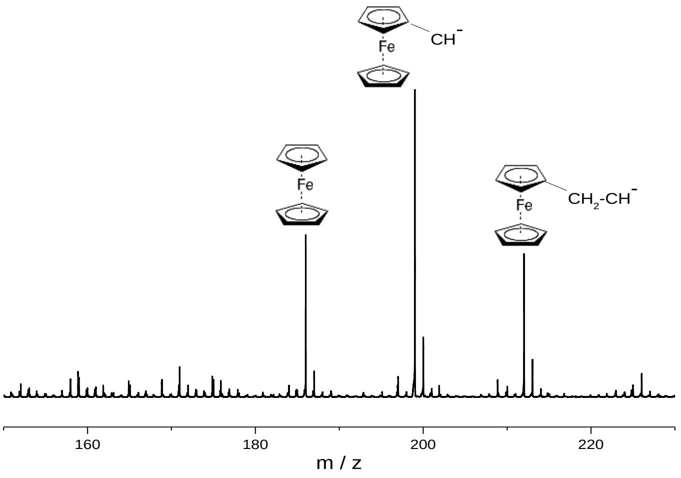

Figure 3.13 ToF-SIMS spectrum for Fc-SAM where it can be observed the peak for Fc fragment at m/z = 185.

3.2.2 Electrochemical characterization of Fc-SAMs on Au

The electrochemical properties of the Fc-SAMs were studied by cyclic voltammetry (CV) and electrochemical impedance spectroscopy (EIS) in four different electrolytes: in aqueous $HClO_4$ 0.1 M solution (as standard electrolyte), and three different ionic liquids, EMIM-TFSI, EMIM-BF_4, and EMIM-$EtSO_4$. The selected ionic liquids have the same cationic part, $EMIM^+$, and they differ in the anionic one (Figure 3.14). As previously reported by Sun et al.[54], it is expected that the redox shape of the CV peak of the Fc-SAMs will be affected by the interaction of the ferrocenyl headgroups (Fc) with the ionic liquids, especially their anions counter parts with the redox group in the oxidized ferrocenium state (Fc^+).

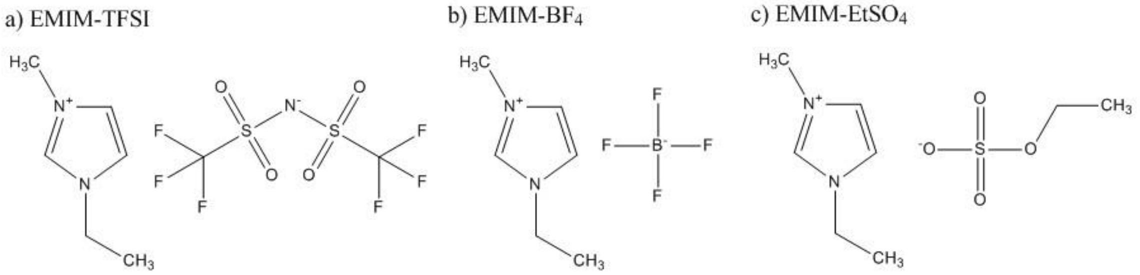

Figure 3.14 Structure of the ionic liquids employed: a) EMIM-TFSI, b) EMIM-BF_4, and c) EMIM-$EtSO_4$.

For this study, it was employed the homemade electrochemical cell that was previously described (see chapter 2, section 2.2, figure 2.2) namely 2nd setup. To obtain the redox response of the modified SAMs, the functionalized Au substrates were used as working electrodes (WE). The rest of the electrodes that complemented the setup were a Ag wire and a Pt wire as pseudo-reference (RE) and counter electrodes (CE), respectively.

The different CVs obtained for the Fc-SAMs are shown in Figure 3.15. In these conditions, it is possible to observe one reversible redox process with the formal redox potential values ($E^{1/2}$) of 0.03, 0.51, 0.49 and 0.54 $V_{vs\ Ag(s)}$ for $HClO_4$ (aq), EMIM-TFSI, EMIM-BF_4 and EMIM-$EtSO_4$, respectively. In Table 3.1 the main electrochemical parameters extracted from the CV measurements (calculated at the scan rate of 100 mV/s) are summarized.

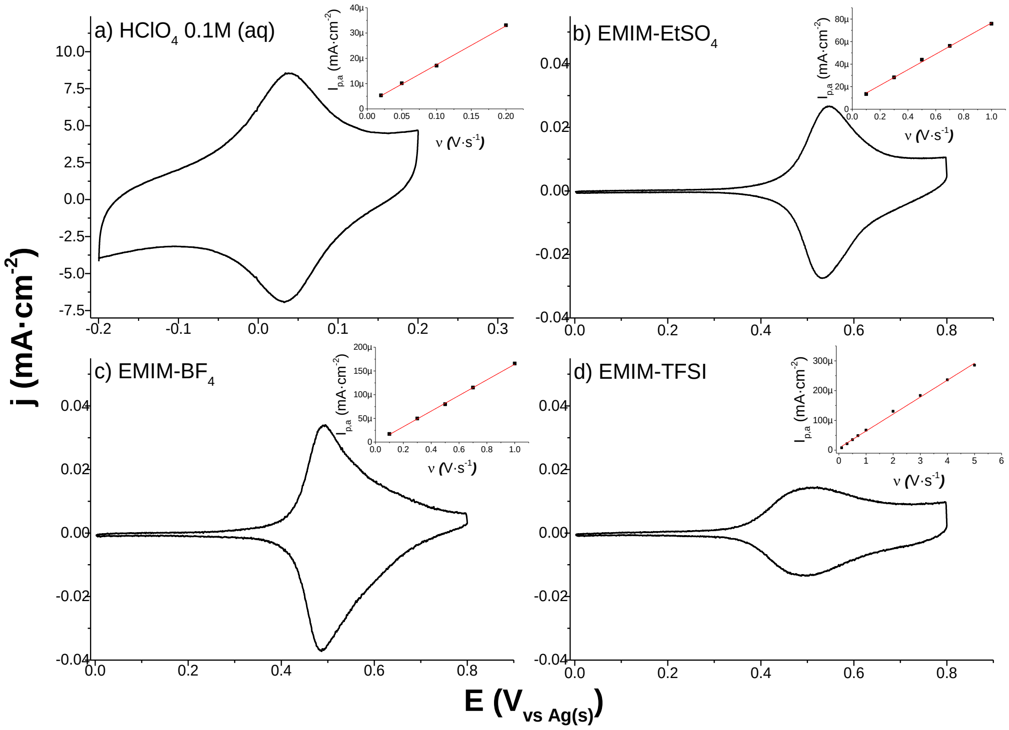

Figure 3.15 CVs of Fc-SAMs on Au scanned at 100 mV/s in four different electrolytes: a) $HClO_4$ 0.1M in water, b) EMIM-$EtSO_4$, c) EMIM-BF_4 and d) EMIM-TFSI.

The small difference observed between the cathodic and the anodic peak (ΔE), together with the linear dependence of the current redox peak with the scan rate (inset plots in Figure 3.15) are characteristic features of electroactive surface confined species.

ELECTROLYTE	**$E^{1/2}$ ($V_{vs\ Ag(s)}$)**	**ΔE (mV)**	**ΔE_{FWHM} (mV)**	**Γ_{ox} (mol·cm^{-2})**	I_{pa}/I_{pc}	**$C_{dl,0}$(*) (μF·cm^{-2})**	**$C_{dl,1}$(*) (μF·cm^{-2})**	$C_{dl,1}/C_{dl,0}$
$HClO_4$ 0.1 M	0.03	1.4	93.1	$4.4 \cdot 10^{-10}$	1.2	103.8 (-0.1V)	118.7 (0.15V)	1.1
EMIM-TFSI	0.51	17.0	181.3	$3.7 \cdot 10^{-10}$	1.1	3.1 (0.01V)	60.8 (0.75V)	19.4
EMIM-BF_4	0.49	6.0	114.7	$4.2 \cdot 10^{-10}$	0.9	5.2 (0.01V)	14.1 (0.75V)	2.7
EMIM-$EtSO_4$	0.54	13.0	113.8	$3.0 \cdot 10^{-10}$	1.0	3.2 (0.01V)	25.7 (0.75V)	8.1

Table 3.1 Electrochemical information of Fc-SAMs extracted by CV. (*) In brackets the potential at which C_{dl} has been estimated is indicated.

One of the parameters used for the study of redox centres interactions is the full width at half maximum potential (ΔE_{FWHM}). In an ideal situation, where there is no interaction between redox centres, ΔE_{FWHM} = 3.53 RT/nF (90.6/n mV at 25° C), where n is the number of electrons involved in the redox process.[55] The deviations from this value are attributed to interactions between redox centres. In the cases studied in this work, the values obtained in Fc-SAMs in ILs are slightly higher than the theoretically expected value (90.6 mV), indicating the existence of repulsion between electroactive centers.

The estimation of the surface coverage has been extracted from the CVs, using the area under the peak curve to calculate de charge (Q), and subsequently the surface coverage (Γ). The results for each electrolyte system are presented in Table 3.1. The maximum theoretical value ($\Gamma_{max,t} = 4.5 \cdot 10^{-10}$ mol/cm^2),[56] has been obtained for the SAMs characterized in $HClO_4$ (aq). Taking into account that all the Fc-SAMs have been prepared in the same experimental conditions, the different surface coverages obtained by CV with the ILs can be attributed to the variation of the anion size of the electrolyte, which determines the ion pairing formation with the oxidized ferrocinium species. Therefore, large anions like $TFSI^-$ or $EtSO_4^-$ could not fully compensate the positive charges of a fully oxidised Fc^+ monolayer leading to a smaller measured surface coverage of active sites (Figure 3.16). Another factor that can slightly influence in this results is the roughness of the gold surface, which can induce some structural disorder of the organic layer.

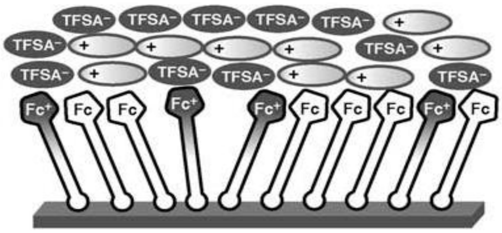

Figure 3.16 Schematic illustration of the change in the alignment of TFSI⁻ anions at the surface of a Fc-SAM during the redox process (Fc – 1e⁻ → Fc⁺).[54]

Complementary, the values of current peak ratios ($I_{p,a}/I_{p,c}$) close to 1 in all the cases (see Table 3.1) indicate a high symmetry and reversibility of the redox process and the adsorption of the electroactive species to the surface electrode.

For the future consideration of this system as switchable molecular device, it is indispensable to study the stability of the Fc-SAMs during time in the electrolytic media. For that, several CVs were acquired during several consecutive days without disassembling the electrochemical cell. The surface coverage (Γ) value was used as parameter to evaluate the variation of the electrochemical response, and the results are shown in Figure 3.17. The evolution of Γ vs. time demonstrates that EMIM-TFSI gives the most stable electrolyte/Fc-SAM/Au interface, maybe due to the higher hydrophobic character of EMIM-TFSI with respect to the others ionic liquids used in this study, but also can be influenced by a higher interaction of the IL anions with the ferrocene moieties, corresponding to a larger wettability (as EMIM-TFSI presents the lowest contact angle value, previously shown in Figure 3.9).

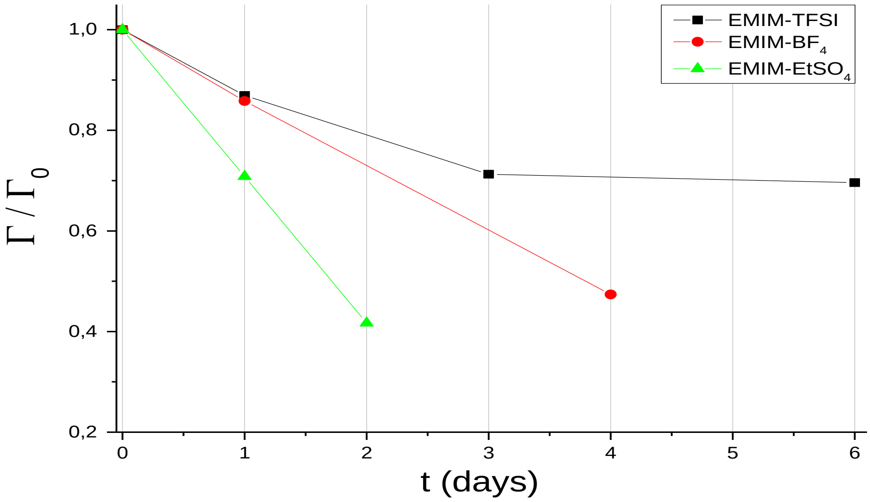

Figure 3.17 Relative surface coverage (Γ/Γ_0) evolution of Fc-SAMs in the different ionic liquids studied: EMIM-TFSI, EMIM-BF$_4$, and EMIM-EtSO$_4$. Γ_0 is the initial surface coverage of each Fc-SAM studied.

Finally, for the evaluation of the electrical response as output signals, it has been initially estimated the double layer capacitance (C_{dl}) of the Fc-SAMs at two different potentials selected before and after the redox peak process. The non-faradaic process is associated with the movement of electrolyte ions, reorientation of solvent dipoles, adsorption/desorption, etc. at the electrode-electrolyte interface. This corresponds to the background current in voltammetric measurements.

Hence, going back to the CV experiments shown in Figure 3.15, C_{dl} has been estimated in the non-faradaic regimes (E_0 and E_1, before and after the redox process, respectively, and specified in brackets in Table 3.1) using the expression: $I_{ch} = C_{dl} \cdot A \cdot \nu$, where I_{ch} is the charging current, ν is the scan rate, and *A* is the area of the working electrode. In Table 3.1 are collected the C_{dl} values for the two potentials selected at the four different electrolytes, and their corresponding ratio between the two states ($C_{dl,1}/C_{dl,0}$). Despite the high values of capacitance for the $HClO_4$ (103.8 and 118.7 $\mu F \cdot cm^{-2}$ at E_0 and E_1, respectively), in comparison with the ILs, the difference between states is relatively low. In contrast to that, for EMIM-EtSO$_4$ and EMIM-TFSI, the ratio is quite significant, especially for the last one. In view of the stability and the capacitance estimation values, the use of Fc-SAMs in EMIM-TFSI electrolyte was considered as the most promising system for the development of purely electrical molecular switches.

3.2.3 Impedance characterization of Fc-SAMs on Au

The impedance measurements of the Fc-SAMs were obtained over a frequency range of 100 kHz to 1 Hz at two different DC potentials that do not overlap with the faradaic process, E_0 and E_1, the same values selected previously for the estimation of C_{dl} (see Table 3.1).

The EIS results are presented in the form of the real part of the interfacial complex capacitance as a function of frequency. The real part of the capacitance per unit area (C_{re}) was calculated by the following equation: [57–59]

$$C_{re} = \frac{1}{2\pi f} \cdot \frac{Z_{im}}{(Z_{re}^2 + Z_{im}^2)} \cdot \frac{1}{A} \qquad \text{(Eq. 3.10)}$$

where A is the area of the working electrode, Z_{re} and Z_{im} are the real and imaginary parts of the complex impedance, respectively, and *f* is the frequency.

The resulting capacitance data for the Fc-SAMs are represented in Figure 3.18, showing the dependence of C_{re} with the frequency at the DC bias voltages applied for the four different electrolytes studied. All the capacitance plots have in common the presence of two main different regions: at high frequencies (1 kHz < freq <100 kHz), the real part of the capacitance is dominated by the bulk response of the system; whereas at low frequencies the interfacial capacitance is reflected and a plateau is reached (with the exception of $HClO_{4\ (aq)}$ electrolyte). In general, the electroactive SAMs behave as ideal capacitors with the Au metal surface acting as one capacitor plate and the physisorbed ions at the SAM/electrolyte interface acting as the other capacitor plate.

Aqueous salt solutions, such as $HClO_4$ 0.1 M, are good electrolytes for electrochemical studies. However, because of the low variation in the capacitance response between the two DC-bias potentials applied (Figure 3.18.a), it has not been considered for the following study of the electrical switch based on Fc-SAMs.

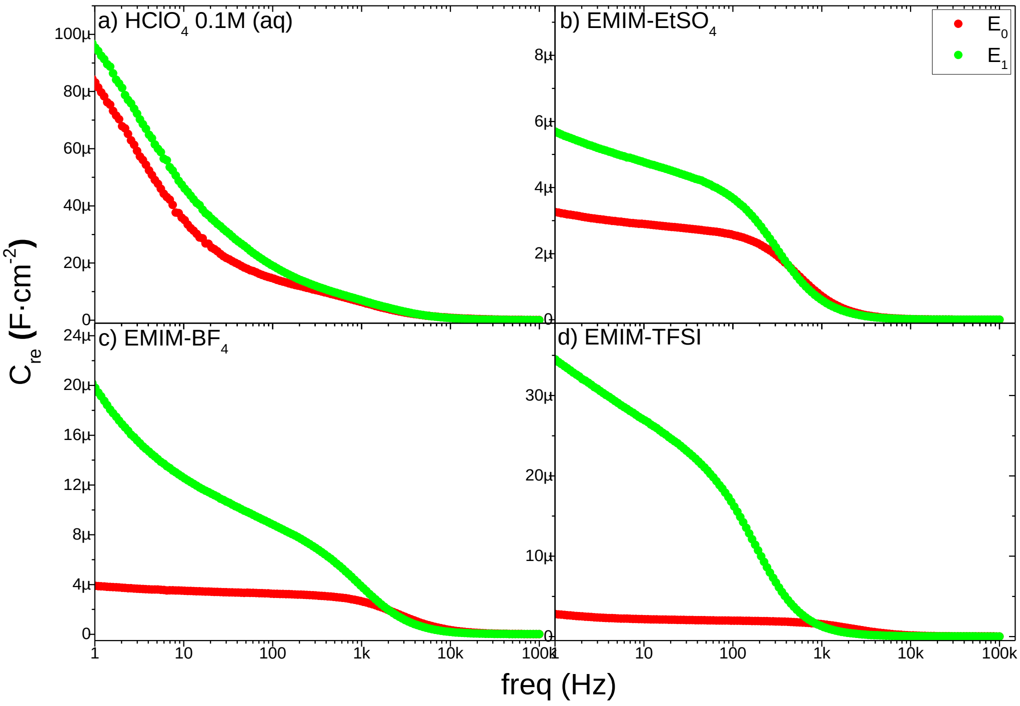

Figure 3.18 Impedance results represented by the real part of the capacitance (C_{re}) vs frequency, at two DC-bias potentials (E_0 and E_1) for Fc-SAMs on Au in different electrolytes: a) $HClO_4$ 0.1 M, b) EMIM-$EtSO_4$, c) EMIM-BF_4, and d) EMIM-TFSI.

In the case of ionic liquids, the different capacitance response at the applied DC bias in the low frequency region (Figure 3.18.b, c and d), makes all of them good candidates for their implementation in electrical switches. In particular, the large on/off ratio response obtained in

EMIM-TFSI (Figure 3.18.d) at 1Hz of frequency is highly relevant, and encouraging for using the capacitance response as parameter to read-out the system. This difference in capacitance can be attributed mainly to the charges accumulated at the electrode interface influenced by the redox state of the Fc molecules, although a certain contribution coming from structural changes in the SAM cannot be ruled out completely.

Taking into account the high stability of the Fc-SAMs and the high on/off ratio capacitance response when EMIM-TFSI is used as electrolyte media, as observed by CV and EIS, the following electrical switch methodology has been studied and developed employing this specific electrolyte.

3.2.4 Switching capacitance response of the Fc-SAMs on Au

Through the results obtained by EIS, especially with EMIM-TFSI (Figure 3.18.d), it can be observed that, at the low frequency region, the capacitance is clearly dependant on the redox state of the molecule and, thus, on the applied DC voltage. Therefore, this result motivated the study of the capacitance response of the electrochemically switchable Fc-SAMs in EMIM-TFSI at low frequency. For that, EIS measurements were performed at two different applied DC-bias voltages, before (E_0 = +10 mV) and after (E_1 = 700 mV) the redox peak, which define the state 0 (where the Fc is in the neutral state) and the state 1 (where the Fc molecules should exist as Fc^+ cation) of the switch. The AC impedance switching process was recorded in all the frequency range, and a low AC voltage of 5 mV was superimposed at the two different DC-bias potentials. These cycling experiments were performed by pre-biasing the sample at the corresponding DC voltage for each state during 5 seconds. In Figure 3.19 the C_{re} profile for states 0 and 1 in the 1st cycle is depicted, and, in the inset plot of the same figure, the values of C_{re} at 1 Hz in the two states when 18 cycles are applied are shown.

It can be noticed that there is a decrease in the initial capacitance value of 30 % in state 1, after the cycling test, which can be attributed to ion permeation, that is, the penetration of the ionic liquid molecules between the alkyl chains of the Fc-SAM, promoting the re-organization or even the desorption of Fc molecules from the SAM.[40]

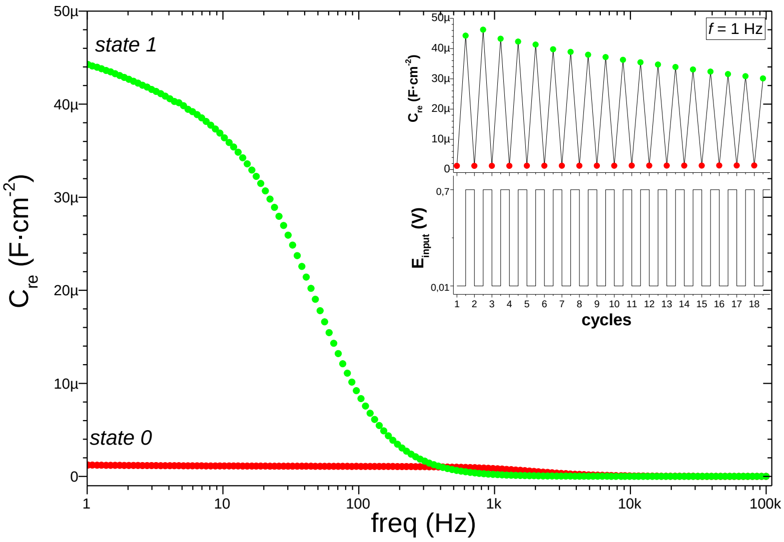

Figure 3.19 C_{re} vs frequency, for Fc-SAMs on Au using EMIM-TFSI as electrolyte. State 0 (red) and state 1 (green) correspond to DC applied biases of 10 mV and 700 mV, respectively. In inset figure is represented C_{re} (extracted at 1Hz) for each DC bias voltage, after the application of EIS in all the frequency range.

On the other hand, the use of Ag wire as pseudo-reference electrode can affect the results when the measurements take long periods of time for the acquisition of data, as it was in this case (the duration of each cycle in the measurement took 5 min since EIS was measured in all the frequency range, and during that period, the sample was submitted to the bias-voltage). Both effects are clearly observed by the reduction of the integration of the peak area and the potential shift of the CV curve when the voltammetry registered before and after the cycling process are compared, as it can be seen in Figure 3.20.

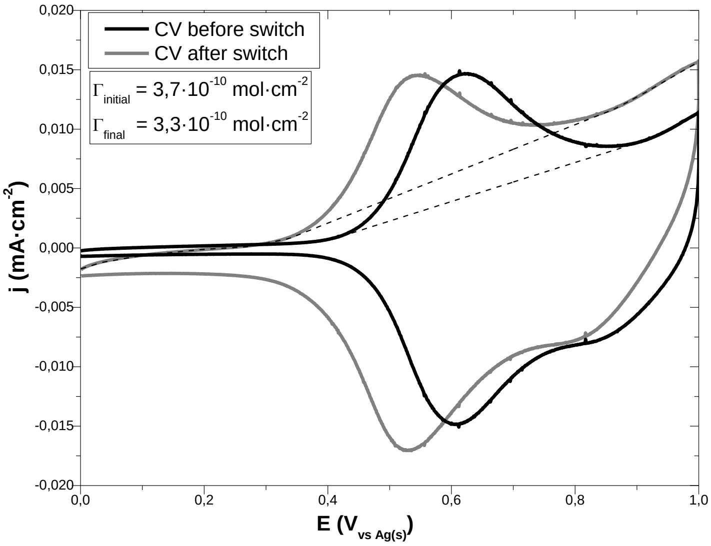

Figure 3.20 CV of a Fc-SAM in EMIM-TFSI at 100 mV/s before and after the impedance switching process.

For using ion gels as solid electrolytes (described later in section 3.3), it was necessary to modify the setup of the electrochemical cell by using a co-planar electrode geometry. This configuration permits the in situ preparation of the ion gel on top of the electrodes, ensuring the contact between the electrolyte with the three electrodes involved in the measurement. For this, and in order to compare the results, this new setup was also used first to study the SAM with the IL.

Mainly, the variations of the setup consisted in the fabrication of three co-planar Au electrodes (counter, reference and working electrodes) by thermal evaporation through a mask on a glass substrate (Figure 3.21.a). Then, only the Au-WE was modified with the Fc-SAM by its immersion in a 1 mM solution of FcC$_{11}$SH in ethanol for 18 hours. Further, a silicon mold or a Teflon ring was used to delimit a fixed area of the electrolyte in contact with the electrodes, as it is shown in Figure 3.21.b.

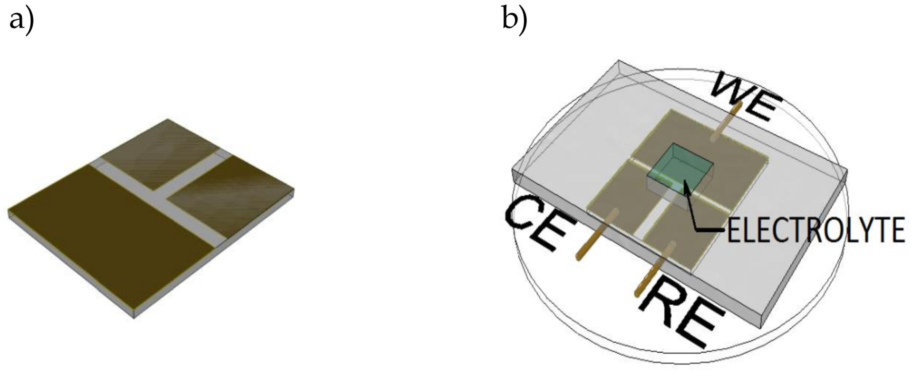

Figure 3.21 Representation of (a) three co-planar Au electrodes prepared by thermal evaporation on glass, and (b) home-made electrochemical cell with a silicon mold to contain the electrolyte.

The CV of the Fc-SAMs in EMIM-TFSI using this setup is shown in Figure 3.22. In Table 3.2 the comparison of CV parameters obtained for Fc-SAMs on gold in the standard and in the co-planar electrochemical cell configurations are collected. In general, FcC$_{11}$SH molecules are very well confined to the gold ($\Delta E \approx 0$) and the redox process is highly reversible ($I_{p,a}/I_{p,c} \approx 1$). In the two configurations studied, it is important to note the difference in the formal redox potential peak ($E^{1/2}$), due to the use of a different reference electrode in each setup (Ag wire in the standard cell, and Au in the co-planar system). It is important to note that, independently of the geometry variation, it has been obtained the same the surface coverage, indicating a very high reproducibility in the SAM preparation methodology and that both setups work in a very efficient manner.

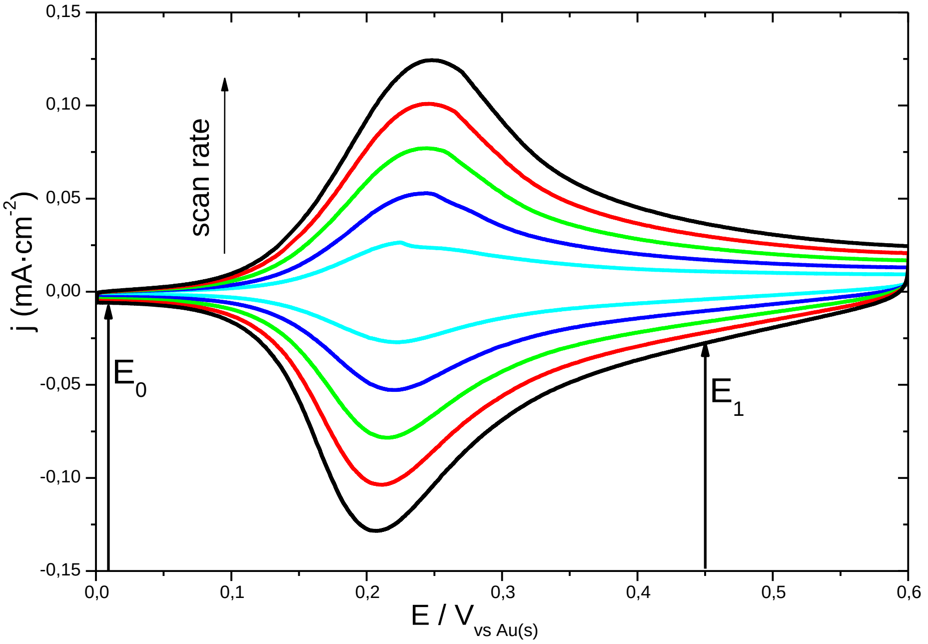

Figure 3.22 CVs of Fc-SAMs on Au in a co-planar configuration, using EMIM-TFSI as electrolyte. CVs scanned at: 100, 200, 300, 400 and 500 mV/s.

GEOMETRY	**$E^{1/2}$**	**ΔE (mV)**	**ΔE_{FWHM} (V)**	**$I_{p,a}/I_{p,c}$**	**Γ_{ox} (mol ·cm^{-2})**
Standard	0.49 $V_{vs\ Ag}$	12.0	0.195	1.1	$3.7 \cdot 10^{-10}$
Co-planar	0.23 $V_{vs\ Au}$	26.1	0.137	1.0	$3.7 \cdot 10^{-10}$

Table 3.2 CV parameters obtained at a scan rate of 100 mV/s for Fc-SAMs in EMIM-TFSI using two setups.

The impedance switching study of the system in the coplanar setup was performed. In this case, state 0 and state 1 were written using a DC voltage of 10 and 450 mV $_{vs\ Au(s)}$, respectively. The Bode magnitude plot (impedance modulus (|Z|) vs. freq) is shown in Figure 3.23 (left plot). At low frequencies, the graphs for the two states are two parallel straight lines with slopes of approximately −0.9. This behaviour is characteristic of capacitor-like systems and the deviation from a slope of −1 can be explained by capacitance dispersion owing to the adsorption of ions on the electrodes and the roughness of the electrode surface.[60]

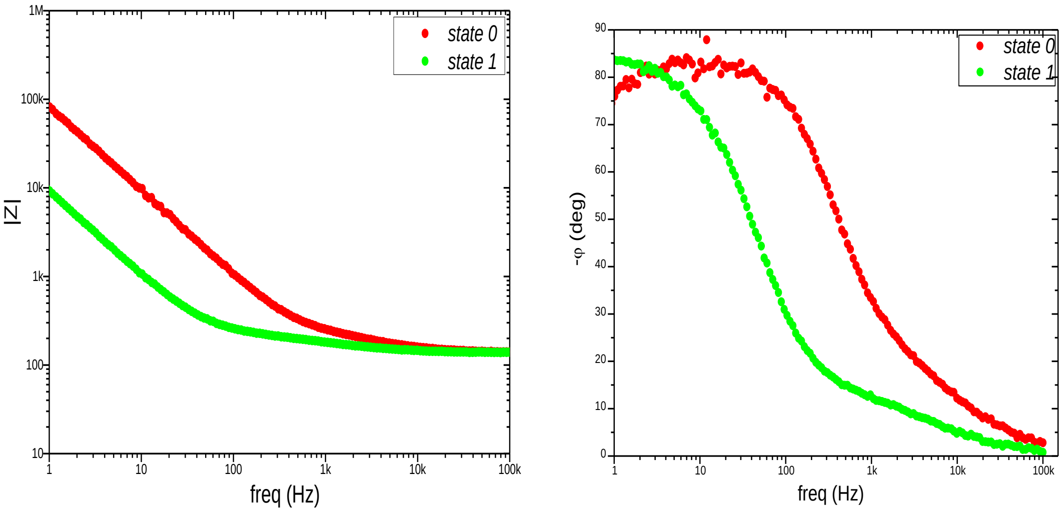

Figure 3.23 Bode plots (module – left plot - and phase –right plot - vs freq) for Fc-SAM on Au using EMIM-TFSI as electrolyte. All graphs are shown for state 0 and state 1.

Accordingly, in the Bode phase plot (-φ vs. freq), the phase angle slightly deviates from 90° at low frequency, which would be expected for an ideal ionic insulator (Figure 3.23.right).[61] As previously observed, a significant decrease in |Z| of one order of magnitude was observed between state 0 and state 1 at low frequencies, indicating that the changes observed in |Z| for the Fc-SAMs can be attributed to the redox state of the electroactive species.

At higher frequencies (freq > 10 kHz), the frequency-independent impedance and a phase angle close to zero (Figure 3.23) indicate that the system behaves as a resistor, that is, the total impedance is dominated by the solution resistance.[62] This is due to the fact that at high frequencies, the capacitor behaves as a short-circuit element as the charging time is too short, allowing the AC current to pass.

The dependence of the C_{re} value on the frequency for the Fc-SAMs at both applied DC bias voltages is shown in Figure 3.24, which are in concordance with the results obtained with the previous configuration used (Figure 3.19). The C_{re} value measured at 1 Hz is significantly different for state 0 (V = 10 mV) and state 1 (V = 450 mV), making it possible the use of this parameter to follow the switch.

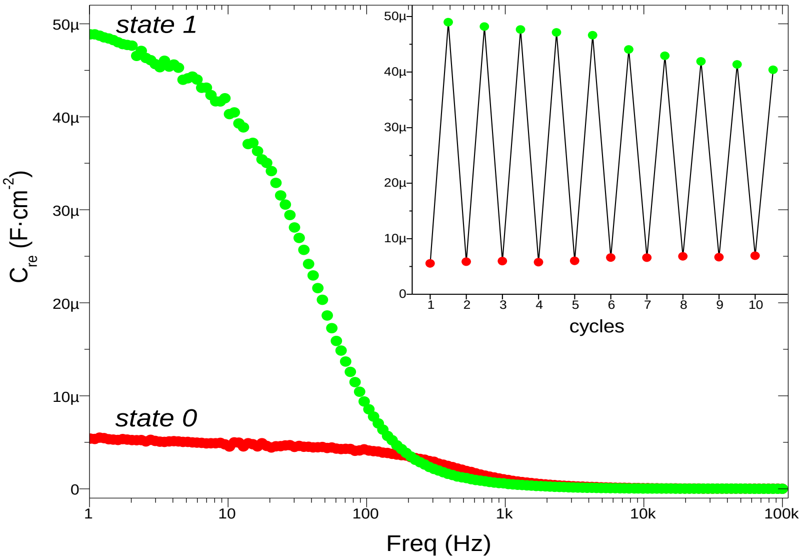

Figure 3.24 The real part of the complex capacitance vs frequency (C_{re} vs. freq) for the Fc-SAM on Au using EMIM-TFSI as the electrolyte. State 0 at +10 mV (red), and state 1 at +450 mV (green). In the inset figure is represented the value of C_{re} extracted at 1 Hz, for each DC bias voltage, after the application of EIS in all the frequency range.

In the inset plot of Figure 3.23 the evolution of C_{re} at 1Hz (value extracted after the application of the EIS measurement in all the frequency spectra) can be observed. It is important to remark the loss of capacitance response for both DC voltages applied. It is associated to a fatigue effect in the Fc-SAM, due to the bias voltages applied for a long period of times during the registration of the impedance measurements in all the frequency range selected, and consequently affecting the ferrocene monolayer.

To explore the stability of the switching process while improving the performance of the device to the fatigue effect described above, the Fc-SAM was subjected to 100 switching cycles, where the EIS was applied at the same two DC bias voltages, but in this case at only one specific frequency, 1Hz, and the C_{re} values measured were represented in Figure 3.25 as a function of the cycling number. In this plot, the capacitance is expressed in relative values, using the first value of the capacitance response of the system at the state 1 as the maximum capacitance ($C_{re,0}$). As it has been mentioned before, there is a small decrease of the on/off ratio response (attributed to ion permeation). Nevertheless, in comparison with the standard configuration, this difference is quite low (the initial capacitance value decreases only 10 % in the state 1 after 100 cycles), which entails an improvement of the stability and a better performance of the device.

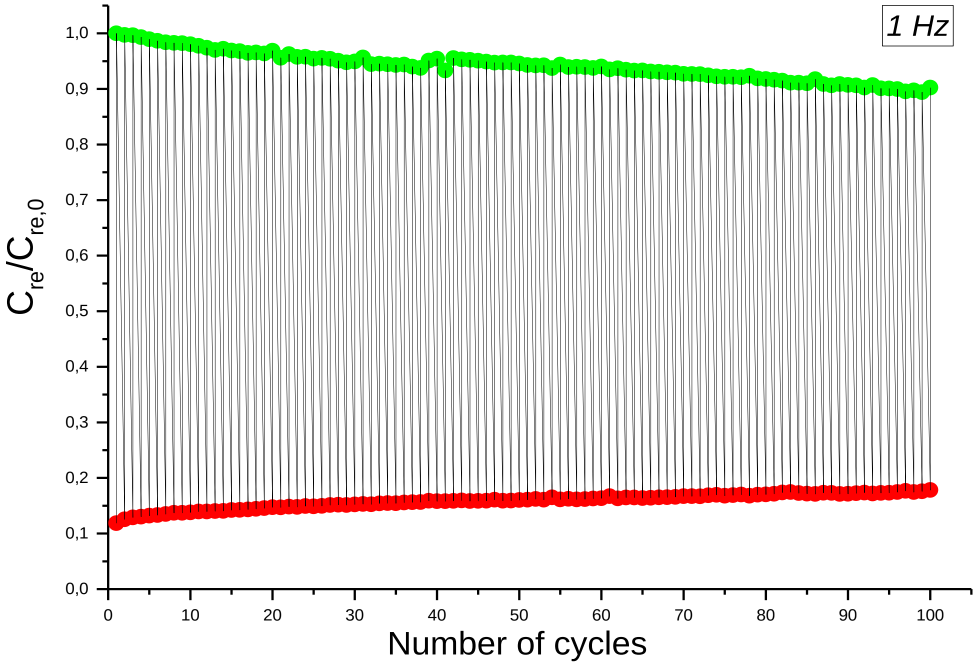

Figure 3.25 C_{re} /$C_{re,0}$ (at 1Hz) switching over 100 cycles by alternating the applied bias between state 0 (red) and state 1 (green), and using EMIM-TFSI as electrolyte.

Complementary, in order to estimate the time response of the switching device, i.e. the time that the device takes to react to a given input, it has been performed different switching measurements by applying the corresponding DC voltage at each state for different pre-biasing times: from 5 minutes down to 0 seconds. The capacitance results obtained (at 1 Hz of frequency) are presented in Figure 3.26.

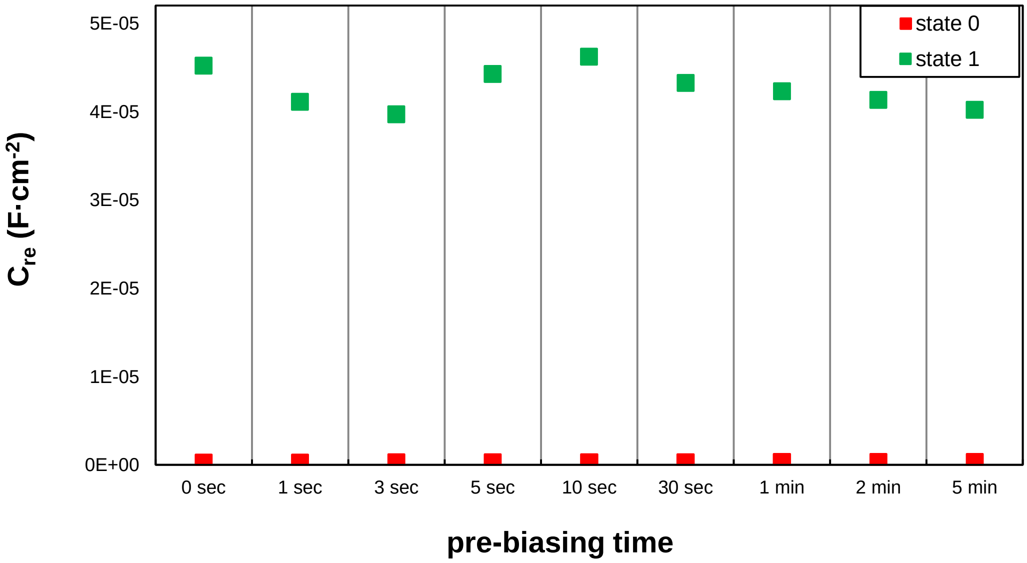

Figure 3.26 C_{re} switch for Fc-SAM using EMIM-TFSI at different pre-bias time.

It is important to note, that, independently of the pre-bias time applied, the capacitance is practically constant, around 1.2 and 42.6 μF·cm^{-2} for state 0 and state 1, respectively, even when there is no pre-bias voltage. Thus, we can conclude that the response of the switch is faster than the time required for taking a measurement in our equipment.

3.2.5 Summary

In this section, cyclic voltammetry and electrochemical impedance spectroscopy have been used as tools for the characterisation of a molecular switches based on an electroactive SAM, demonstrating that it is possible to write and read an electrochemical switch by using an electrical input to control the switch as well as an electrical output to monitor it, such as the monolayer capacitance. The devices were cycled 100 cycles demonstrating a remarkable stability. The method employed here is inexpensive and simple and can also be extended to other redox-active molecules, as it will be proved in the next sections.

3.3 Solid State Switches: Ferrocene derivative SAMs and Ion Gels (IGs)[1]

Currently, the electrochemical control of redox molecular devices requires the use of liquid electrolytes to switch between the different accessible redox states of the molecular systems, for stabilizing the charged states and ensuring ionic conductivity in the electrochemical cell. An important challenge in this field is the lack of solid-state devices with such electrochemically switchable SAMs.

To deal with this task, here it has been planned the preparation and application of an ionic gel (IG) as the electrolyte medium to switch the Fc-SAMs, giving a solid-state device based on a single molecular layer. These devices are more appealing for the integration of hybrid surfaces in future electronic applications.

3.3.1 Preparation and characterization of ion gels

The IG based on poly (vinylidene fluoride-co-hexafluoropropylene) (PVdF-HFP) (Figure 3.27) and EMIM-TFSI (1:4) was prepared by initially dissolving the PVdF-HFP pellets in acetone in a weight ratio 1:10 of polymer to solvent. The polymer solution was stirred continuously until a homogeneous mixture was achieved. Then the ionic liquid (EMIM-TFSI) was added to the solution in a mass ratio 1:4 of polymer to IL. The solution was prepared at room temperature and under argon atmosphere. The films were prepared by drop-casting and spin-coating techniques. A schematic representation of the formation of the ion gel film is shown in Figure 3.27.

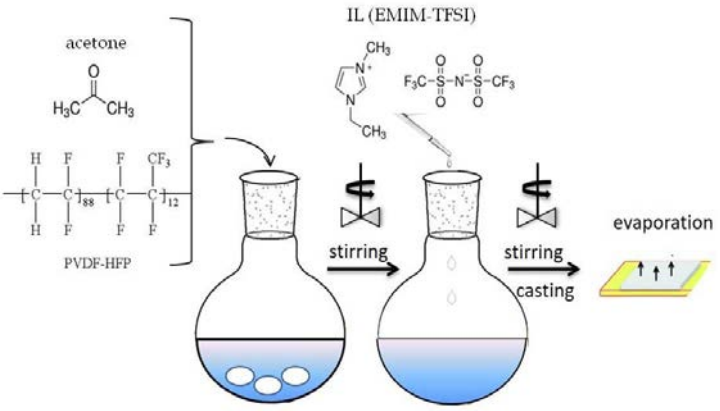

Figure 3.27 Schematic representation of the ion gel formation procedure.

---

[1] This work has been published in *Angew. Chem. Int. Ed.* 55 (**2016**) 368 –372.

Spin-coated ion gels were prepared at room conditions at a spin speed of 1500 rpm for 30 s. For the drop-casting method, to avoid the spread of the solution mixture, a silicon mask was used to delimit the area onto the planar homemade electrodes for the formation of the ion gel. The drop-casted films were prepared inside an argon atmosphere glovebox ($[O_2] < 1$ ppm; $[H_2O] < 1.5$ ppm), where the solvent was allowed to evaporate slowly. After solvent evaporation and solidification of the gel mixture, the sample was removed from the glovebox and analysed in air.

In Figure 3.28 a photograph of the solid state device based on the IG film prepared by drop-casting is shown. The resulting ion gels can be cut with a blade and peeled-off using tweezers because of the outstanding mechanical integrity of the ion gel (Young's modulus values reported by Lee et al.[63]).

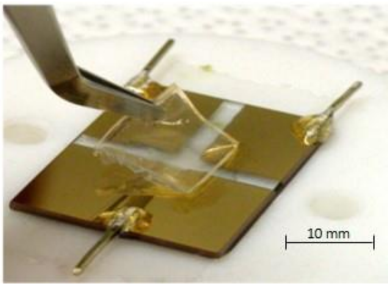

Figure 3.28 Co-planar electrode device with drop-casted IG.

The thicknesses of the films were measured by scanning electron microscopy (SEM), obtaining a thickness of 7 – 8 μm in spin-coated gels, and 240 – 250 μm in drop-casted gels (see Figure 3.29). Furthermore, the morphology of the ion gels prepared by the two methods looks qualitatively the same and no significant changes were observed in the resulting films.

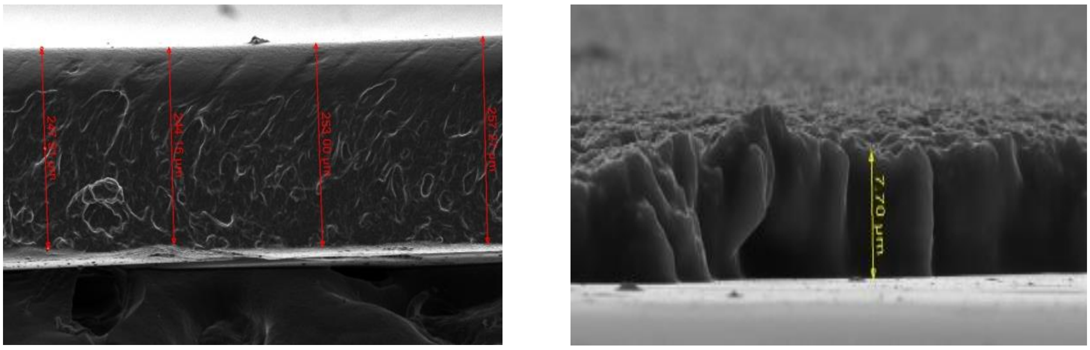

Figure 3.29 SEM picture of the ion gel film prepared by drop-casting (240 – 250 μm thick, left side) and by spin-coating (7 – 8 μm thick, right side).

FT-IR was employed to study the possible ion−polymer interaction and identify the conformational changes in the host polymer PVdF-HFP matrix due to the incorporation of the ionic liquid. In order to form a valid comparison, the spectra presented in Figure 3.30 correspond to EMIM-TFSI, the copolymer PVdF-HFP, and the ion gel in the final solid form.

The FT-IR bands at 3130 and 3173 cm^{-1} belong to the C-H stretching vibration of imidazolium cation ring.[64] The vibration bands of pure polymer PVdF-HFP observed at 614, 762, 796, 854 and 976 cm^{-1} are due to the crystalline phase (α-phase) of the polymer.[65] Upon incorporation of EMIM-TFSI in the polymer network, the peaks at 841 and 879 cm^{-1}, belonging to the amorphous β-phase, become prominent, indicating the amorphicity increase of the IG.[66]

The FT-IR results also confirm the completely evaporation of the acetone solvent from the ion gel as well as the absence of water. Importantly the films did not show variation of the characteristic bands with time under environmental conditions.

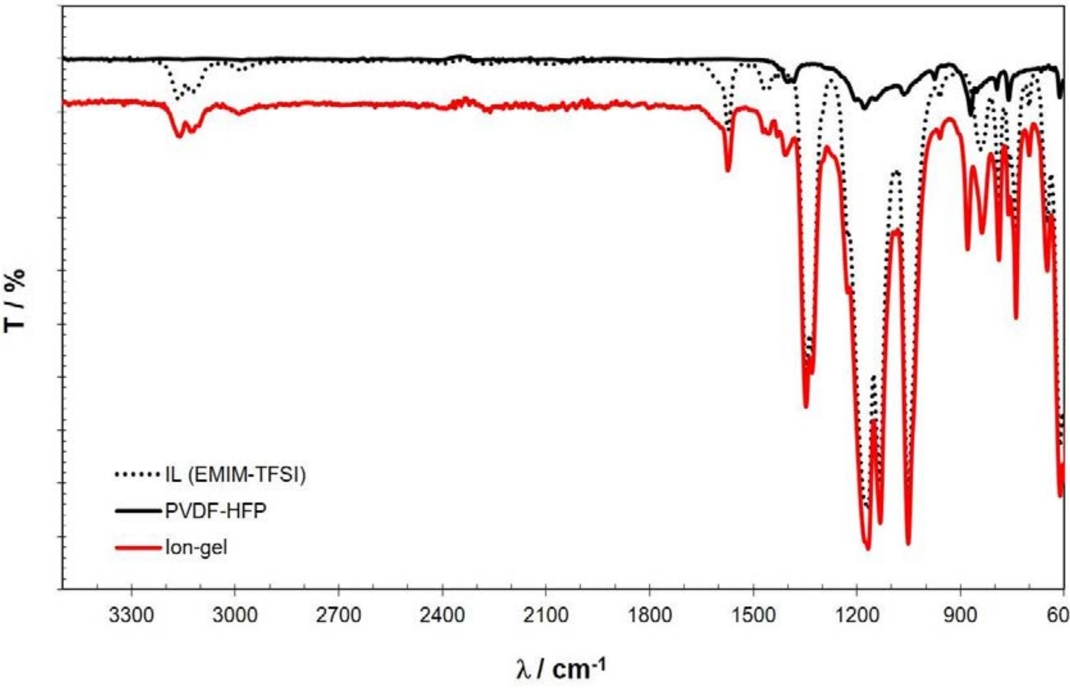

Figure 3.30 FT-IR spectrum of the ionic liquid EMIM-TFSI, the polymer PVdF-HFP and the ion gel.

The thermal stability of the ion gel and the host polymer was characterized via differential scanning calorimetry (DSC) under a nitrogen atmosphere with a heating rate of

10 °C/min (see Figure 3.31). The ion gel was determined to be thermally stable in the temperature range from -50 to 200 °C, inside the broadly accepted grades of operating temperatures for commercial and industrial electronic devices.

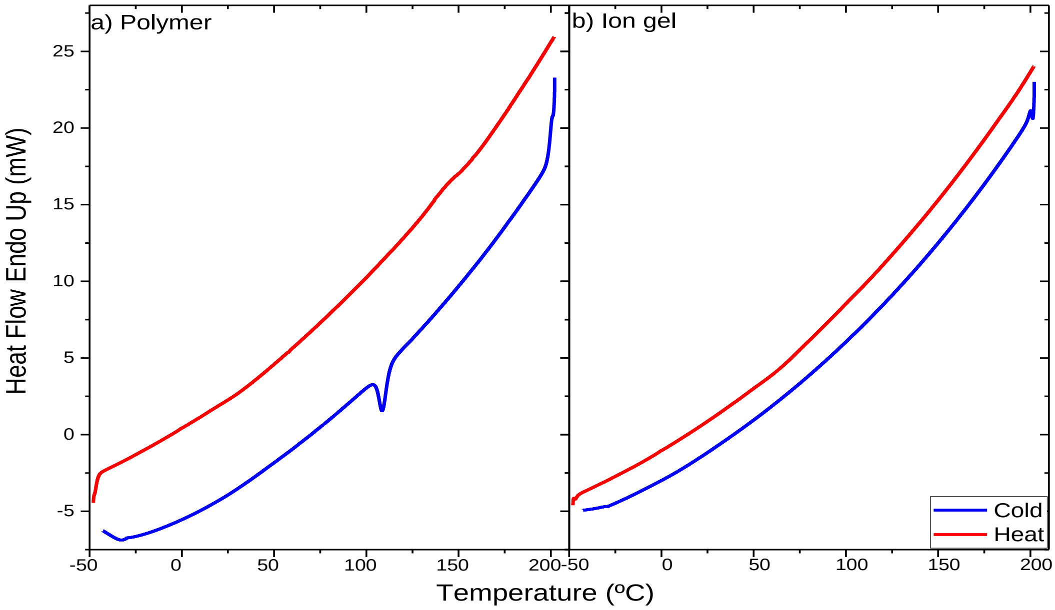

Figure 3.31 DSC measurements for a) PVdF-HFP, and b) ion gel, conducted from –50 °C to 200 °C at heating/cooling rates of 10 °C min^{-1}. Curves collected during the 2nd heating and cooling scans to remove any prior thermal history.

3.3.2 CV characterization of Fc-SAMs on Au in a co-planar setup using IGs

Figure 3.32 shows the CV of the Fc-SAMs acquired using both the IG prepared by drop-casting and by spin-coating. The most optimum CV response, considering the lower ΔE (difference between oxidation and reduction peaks), was achieved in films with thickness in the range of 250 - 300 µm (prepared by drop-casting). This result is also related to the variation of conductivity with the electrolyte thickness, as Lee and co-workers[67] previously investigated. They studied the electrical properties of spin-coated ion gels as a function of the film geometry, obtaining that their conductivity could in principle change with film thickness, because it is possible for the films to have different compositional ratios or gradients produced by the different preparation methodologies.[68] Therefore, in this case, the final method selected for the formation of the ion gel on top of the planar electrodes for the electrochemical switch fabrication has been the drop-casting technique.

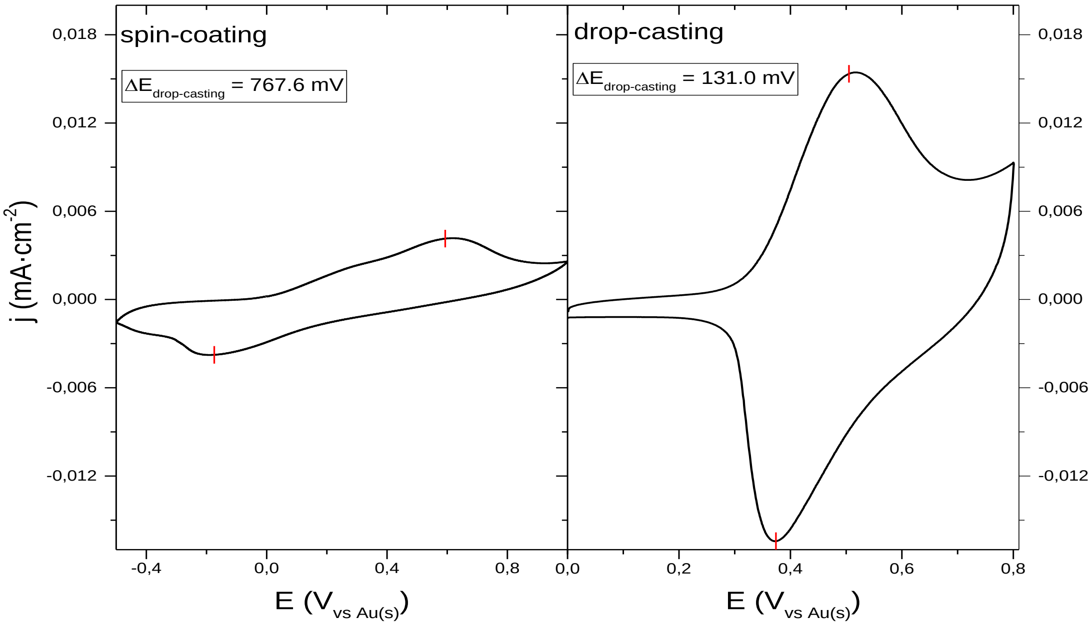

Figure 3.32 CVs of Fc-SAMs using the drop-casted (right plot) and spin-coated IGs (left plot) at 100 mV/s.

As shown in Figure 3.33, the CV electrochemical characteristics of the Fc-SAMs have been successfully determined by using co-planar Au electrodes coated with the transparent and flexible solid IG.

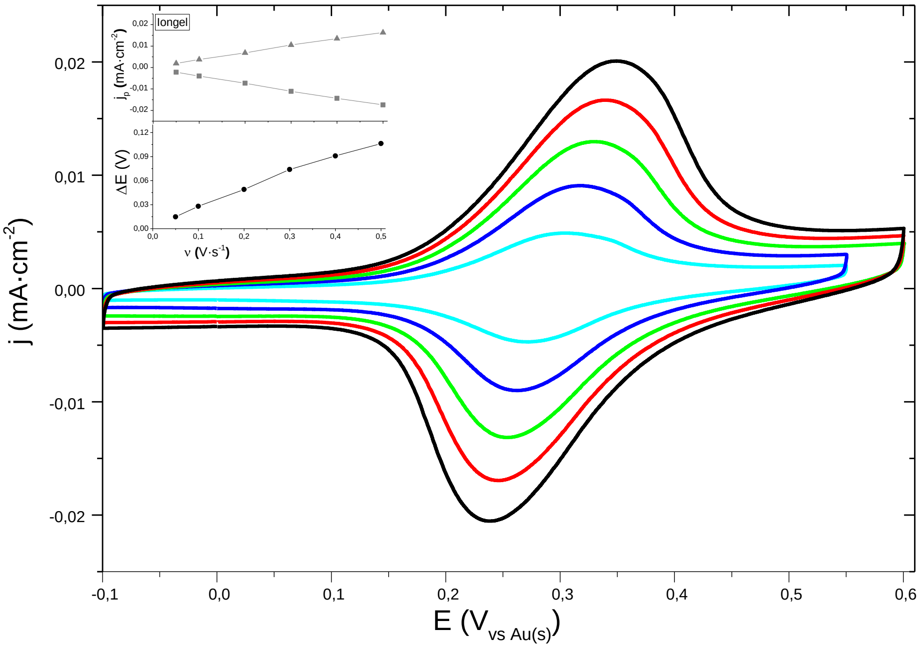

Figure 3.33 CVs of Fc-SAMs on Au in a co-planar configuration, using IG as electrolyte. CVs scanned at: 100, 200, 300, 400 and 500 mV/s. Inset figures of ΔE and I_p vs scan rate (ν).

When the CV obtained with the solid electrolyte is compared to the one obtained with the IL, there are a few differences in the electrochemical characteristics commonly used for evaluating the response of surface-grafted molecules. In the case of the IG, a larger peak-to-peak voltage difference (ΔE) was observed, which also depended more strongly on the scan rate. This is indicative of a slower electron-transfer process, which is expected to occur because of the lower ion mobility in the solid IG film. Furthermore, a lower current density was observed for the IG despite the fact that the density of the ferrocene molecules grafted onto the gold electrode should be very similar to that of the SAMs studied with the IL. In other words, the number of redox-active ferrocene species electrochemically visualized is considerably lower when the IG is used. This can be explained in terms of the less homogenous and intimate contact between the IG and the SAM as well as the less effective charge compensation of the ferrocinium molecules with the TFSI$^-$ ion, which is again probably due to the more limited ion diffusion at the solid state interface.

Remarkably, the CV could also be measured by employing a thin film of an IG that was prepared first on a glass slide and then transferred with tweezers and laminated on top of the three gold coplanar electrodes, with the WE modified with the ferrocene SAM. The cyclic voltammetry thus obtained (Figure 3.34) showed very similar features as the ones shown in Figure 3.33.

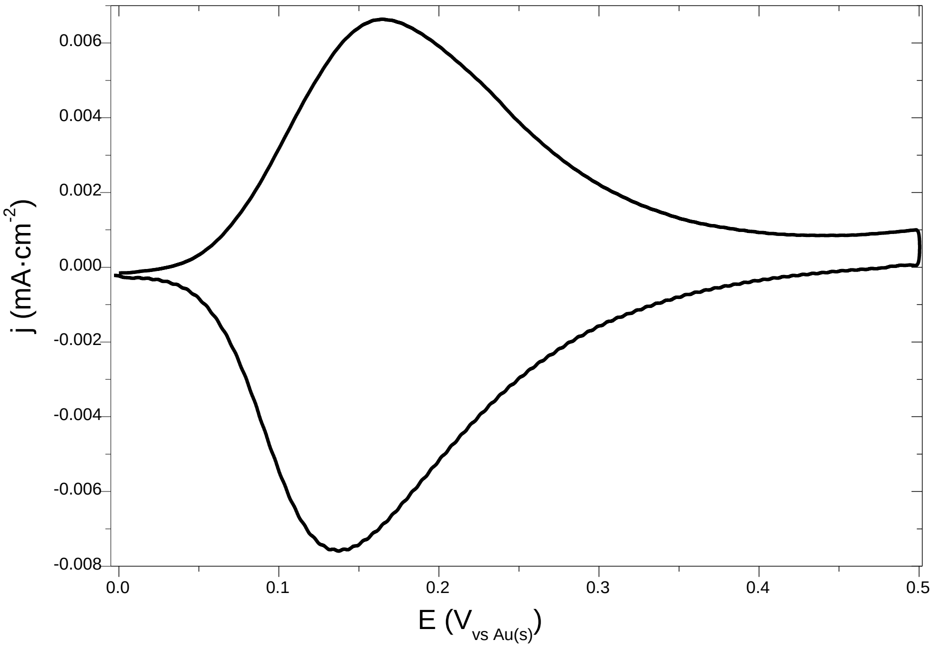

Figure 3.34 CV of the Fc-SAM with the IG prepared ex-situ and subsequently laminated on top of the modified gold electrode. The ion gel was prepared and transferred on top of the 3 co-planar gold electrodes under room conditions (25 ºC and approximately a humidity level of 55 %). Scan rate = 100 mV/s.

3.3.3 Impedance characterization of Fc-SAMs on Au in a co-planar setup using IGs

EIS measurements were also used to follow the switching process in this solid state device. In this case, state 0 and state 1 were written using a DC voltage of 10 mV and 600 mV $_{\text{vs. Au(s)}}$, respectively (bias voltages selected in accordance to the CV in Figure 3.33). The dependence of the impedance modulus, |Z|, on the frequency of the solid state device is depicted in Figure 3.35 (left). As before, there is a clear diminution of the impedance value on going from state 0 to state 1, although this time, the variation is smaller. Furthermore, a noticeable difference is that in the case of the IL based device, the on/off ratio of the |Z| values between the two states is maintained constant in the range 1–100 Hz, whereas in the IG device, the plots corresponding to the two states start to converge in the region of 10–100 Hz. This could again be caused by the lower mobility of the ions in the gel preventing the formation of a compensated double layer at lower frequencies.

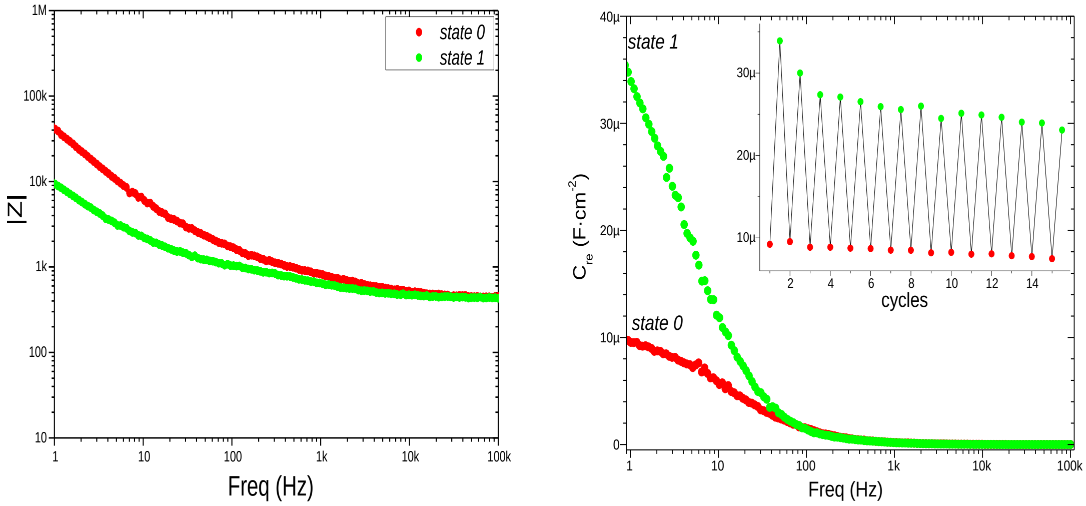

Figure 3.35 On the left, the Bode magnitude plot ((|Z|) vs. freq). On the right, the real part of the capacitance vs. Frequency. In both plots, it has been used the solid IG as the electrolyte.

The C_{re} value was calculated as previously explained for the IL-based switch (right plot in Figure 3.35). The C_{re} values at 1 Hz in state 0 for the IL and IG devices are very similar, namely 5.3 $\mu F \cdot cm^{-2}$ and 9.25 $\mu F \cdot cm^{-2}$, respectively. Although the on/off ratio is lower for the IG-based device than for the IL one, the ΔCre value is still outstanding, 25 $\mu F \cdot cm^{-2}$ at 1 Hz after the 3rd cycle.

As in the previous case, using EMIM-TFSI as electrolyte (see page 74), it has been repeated the stability study of the switch, subjecting the device to 100 switching cycles, and plotting the relative values of C_{re} measured at 1 Hz vs. the cycle number (Figure 3.36).

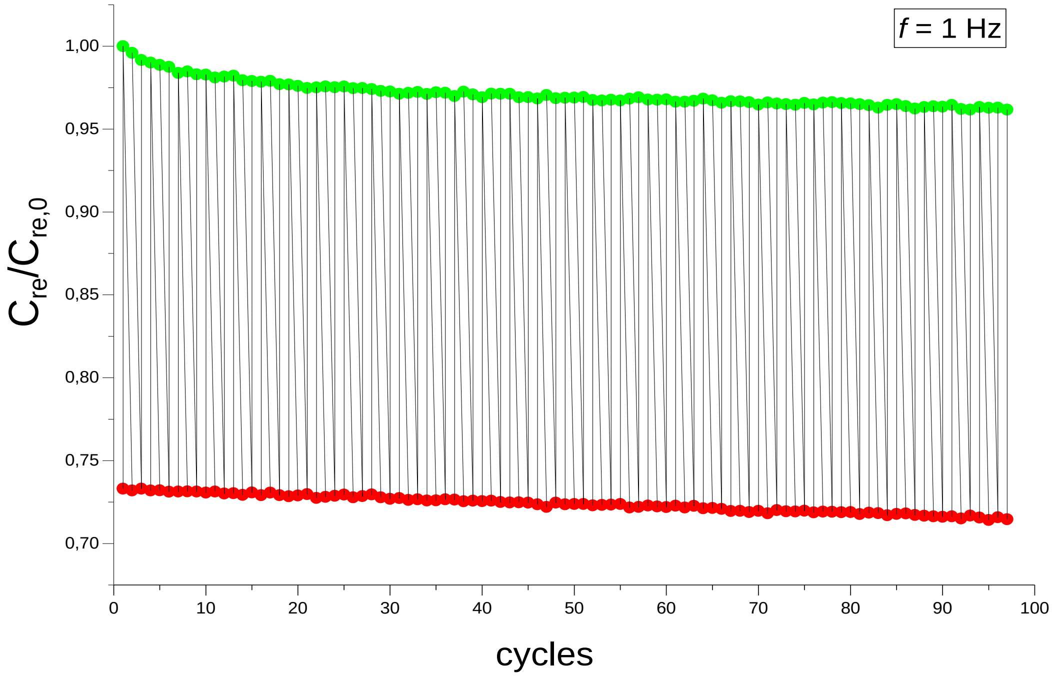

Figure 3.36 $C_{re}/C_{re,0}$ (at 1 Hz) switching over 100 cycles by alternating the DC applied bias with the IG as the electrolyte, for state 0 (red) and state 1 (green).

Remarkably, despite the lower on/off ratio, the stability of the switchable system, that is, the switching fatigue, was improved by the use of the solid electrolyte. This is probably due to the lower permeation of ions into the SAM that can damage it. This finding demonstrates the feasibility of using the C_{re} value as the output of the switch even when using a solid state electrochemical device.

For the estimation of the pre-biasing time in the solid state device, it has been applied the same procedure developed for the ionic liquid experiments. In this case, the system has been analysed in an accurately range of pre-bias time, between 5 to 15 seconds (Figure 3.37). The capacitance results obtained in this case are fluctuating for pre-bias time lower than 15 seconds, which corresponds with the minimum pre-bias time that is needed to apply in order to obtain a stable impedance response of the system. This lower time response is in accordance with the lower conductivity and limiting diffusion of ions in the solid electrolyte media.

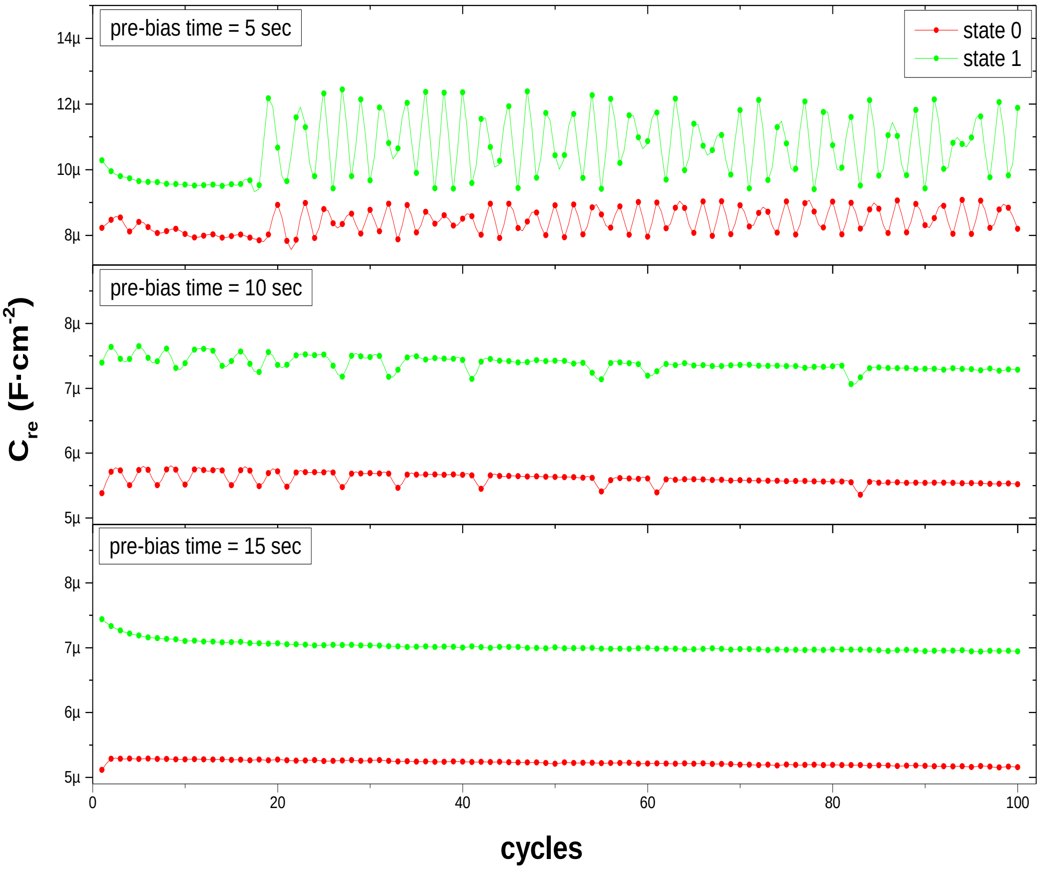

Figure 3.37 C_{re} (at 1 Hz) of the solid device measured at state 0 and state 1, for the sample pre-biased at the corresponding DC voltages during different periods of time (from 5 to 15 seconds) before the EIS measurement.

Finally, the moisture effect in the solid state electrochemical switch was investigated. Thus, the performance of the device in different ambient atmospheres was evaluated. To do that, the planar electrochemical cells were placed in a humidity controlled measurement chamber and CVs were recorded at 25°C and at two different values of relative humidity (RH): 20 and 80%. The CVs were registered at 100 mV/s after the drop-casting of the ion gel on top of the electrodes and the response was followed on time.

In Figure 3.38 the results obtained for the variation of ΔE, $E^{1/2}$ and I_p vs. the time after the IG is drop-casted on top of the co-planar electrodes are represented. It can be observed practically the same general tendency of these electrochemical parameters for each moisture conditions studied, slightly decreasing the intensity of the oxidation current peak (Figure 3.38.c) with time. This diminution can be related to a small desorption of the Fc molecules, also associated to the bias stress applied to the system during the time of data acquisition.

However, in all the cases, it has been obtained better electrochemical results ($E^{1/2}$, $I_{p,ox}$ and ΔE) for low humidity conditions. This effect can be related to the hygroscopic character of the ionic liquid and consequently, water absorption of the ion gel, which can negatively affect the stability of the electrolyte layer and lead to slightly lower ionic conductivity.

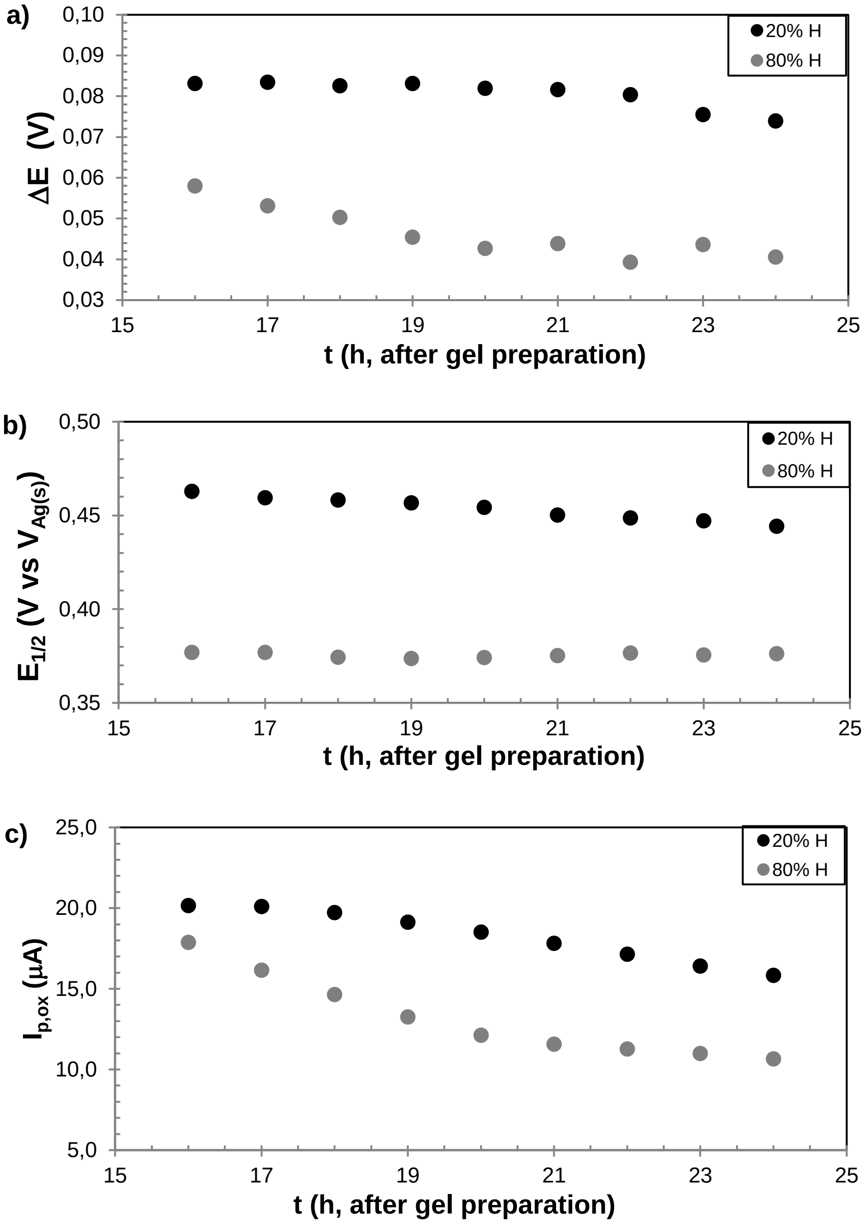

Figure 3.38 a) ΔE, b) $E^{1/2}$, and c) I_p, extracted from CVs using ion gel as solid electrolytes on Fc-SAMs using coplanar electrodes at room temperature for 20% of humidity (black points), and 80% of humidity (grey points)

Nevertheless, it can be conclude that the device works properly in different ambient conditions, and the presence of water during the formation of the electrolyte scarcely affects the electrochemical performance of the device.

3.3.4 Summary

In summary, here it has been proved that IGs can be a suitable electrolyte media to operate molecular switches based on electroactive SAMs achieving the preparation of solid state devices.

Further, the use of the surface interface capacitance as output of the switch has been also successfully exploited with the solid state devices. Noticeably, these devices are slower but much more stable. These results represent a proof-of-concept study of a feasible approach for the integration of molecular-monolayer-based electrochemical switches.

3.4 Multistate Switches

The development of molecules possessing different reversible redox stable states have attracted great interest for their potential as active units in charge-storage electronic devices.[69-71] The processing of higher memory densities in such devices could be achieved by increasing the number of memory states in each cell.[72] This can be realised by two different approaches: 1) employing molecules that exhibit multiple redox states,[73-75] and 2) preparing SAMs with molecules that contain two or more electroactive moieties.[76] However, in the former approach to read all the states it is commonly necessary to apply relatively high voltages which are in detrimental of the SAM stability. On the other hand, the synthesis of the molecules required in the later route can be quite complex. For this, the design of hybrid systems (organic molecule/metal electrode) that can operate in a narrow bias window is crucial.

In section 3.4.1, it is described an alternative route to enhance the number of accessible states based on the preparation of bi-component SAMs on gold composed of two redox-active species. In this way a ternary memory that operates in a quite narrow voltage window can be achieved. In particular, we employ ferrocene (Fc) as electron donor unit and, as electron acceptor, an anthraquinone (AQ).

On the other hand, in section 3.4.2, SAMs based on TTF molecules, with three redox states, have been prepared and successfully exploited as a 4-state electrochemical switch using the capacitance of the SAM as output signal by selecting appropriate DC voltages.

3.4.1 Systems based on bi-component Anthraquinone/Ferrocene binary SAMs[2]

Mixed molecular self-assembled monolayers on gold, based on two types of electroactive molecules, that is, an electron-donor (ferrocene) and an electron-acceptor (anthraquinone) molecules, are prepared as an approach to realise surfaces exhibiting multiple accessible redox states.

3.4.1.1 Preparation of Fc-SAMs and AQ-SAMs on Au

The molecules used in this section are 11-(ferrocenyl) undecanethiol **1** ($FcC_{11}SH$), which has a terminal thiol group for grafting to gold and can undergo one reversible oxidation process ($Fc \leftrightarrows Fc^+$), and the anthraquinone derivative **2** (AQ), which has a thioctic ester group bearing a disulfide that can react with gold. Generally, AQs exhibit two one-electron redox processes ($AQ \leftrightarrows AQ^{\bullet -} \leftrightarrows AQ^{2+}$) in a protic media and a single two-proton, two-electron reduction process ($AQ + 2H^+ + 2e^- \leftrightarrows AQH_2$) in protic environments (Figure 3.39).[77]

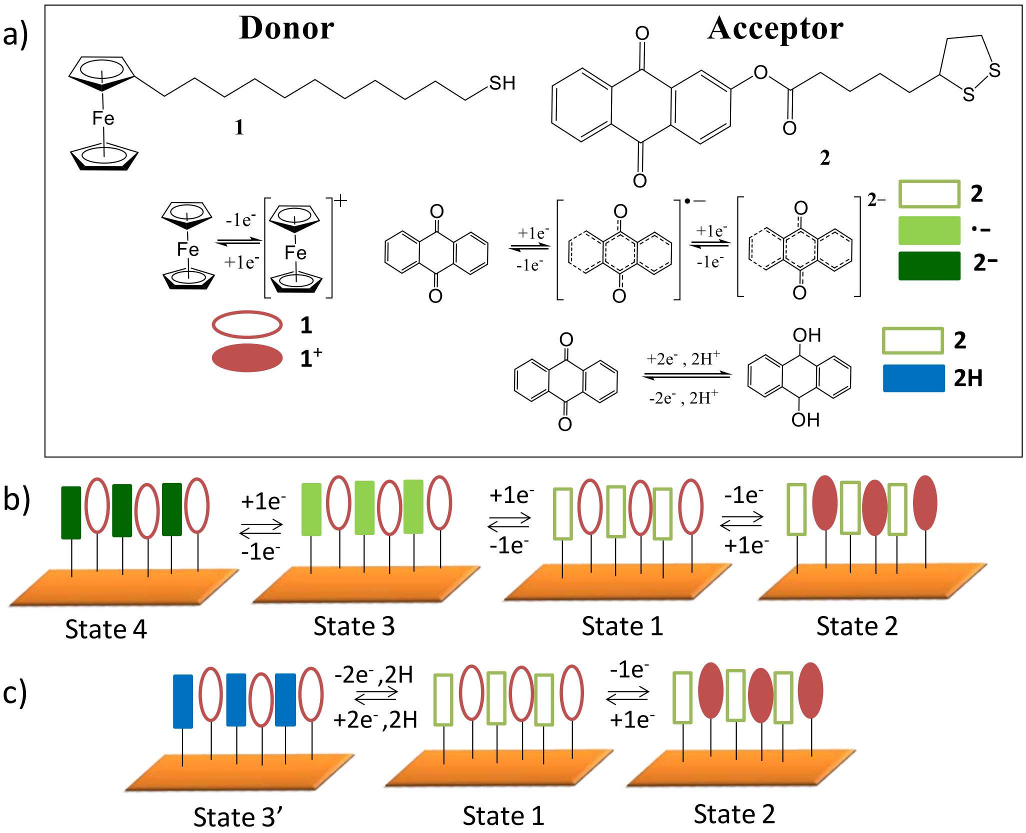

Figure 3.39 a) Molecular structure of the Fc donor **1** and the AQ acceptor **2** employed in this study. Scheme of the redox processes that could take place on a mixed AQ/Fc-SAM on Au employing as electrolyte b) an aprotic or c) a protic media.

---

[2] This work has been published in *ChemPhysChem* 17 (**2016**) 1810 – 1814.

As depicted in Figure 3.40, the AQ derivative compound (synthesized by Dr. J. Casado) was obtained by an esterification reaction between 2-hydroxyanthraquinone and α-lipoic acid, as reported by Casado et al.[78]

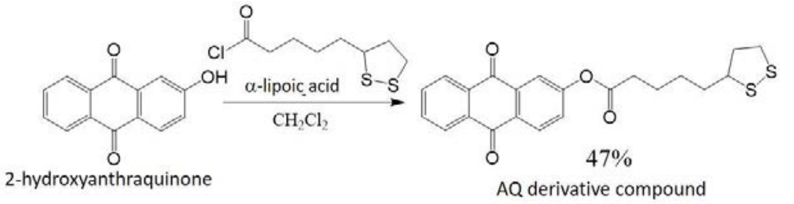

Figure 3.40 Synthesis of AQ derivative compound.[78]

Prior to formation of the binary AQ/Fc-SAMs, the mono-component monolayers were prepared and characterised. A commercial substrate consisting of a 50 nm polycrystalline gold film evaporated on glass was used for all the experiments described here. The characterization of Fc-SAMs have been fully described in this chapter, section 3.2.1 (see page 58). SAMs based on AQ were prepared by immersing the freshly cleaned Au substrates in a 0.5 mM solution of AQ in tetrahydrofuran (THF) for 40 h under inert atmosphere at room temperature with exclusion of light. The resulting modified substrates were characterised by XPS, ToF-SIMS, polarisation modulation IR reflection absorption spectroscopy (PM-IRRAS) and water contact angle.

In the XPS spectra of AQ-SAMs on Au (Figure 3.41), the S 2p peak has been analysed, observing two doublets with binding energies of 162.1 and 163.3 eV associated to S $2p_{3/2}$ and S $2p_{1/2}$, respectively. The doublet peak presents a relative area of 2:1 and peak separation of 1.2 eV, and is attributed to the S–Au bond.

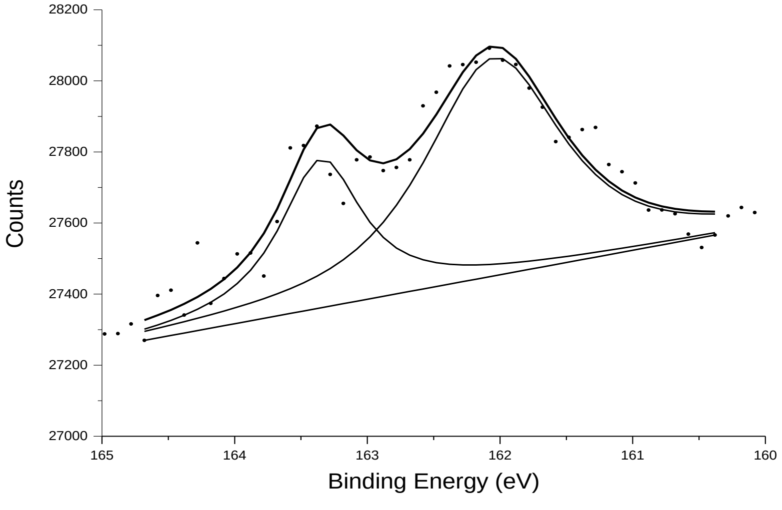

Figure 3.41 S 2p XPS spectra of AQ-SAMs on Au.

Additional information was provided by the ToF-SIMS results (Figure 3.42). The anthraquinone contents of the gold samples was investigated by the positive and negative secondary ion modes, respectively. The ToF-SIMS spectra showed the molecular ion peak at m/z = 412, and the main characteristic fragments of the substituted anthraquinone at m/z = 223 and 205.

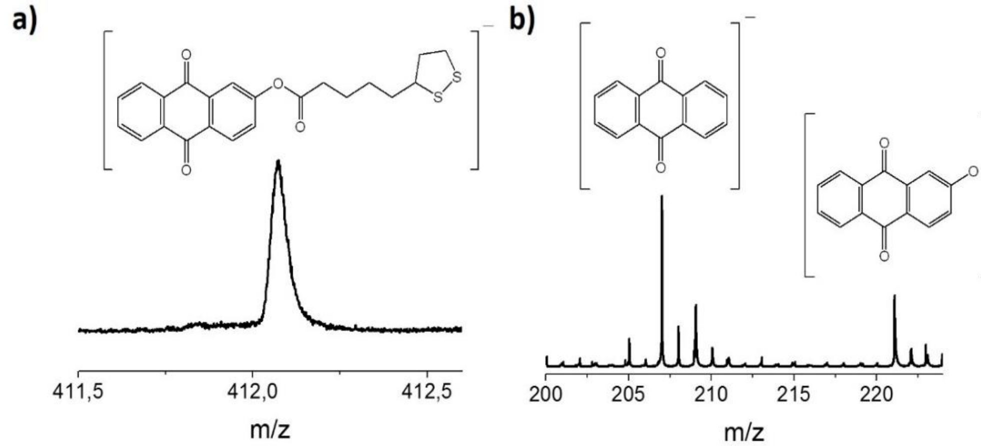

Figure 3.42 ToF-SIMS spectra for AQ-SAM in negative mode where it can be observed the peaks for a) molecular ion, and b) the most characteristic fragments.

The PM-IRRAS spectrum showed three stretching bands, two at 1676 and 1591 cm^{-1} corresponding to the carbonyl groups of the anthraquinone core and one at 1760 cm^{-1} corresponding to the ester group (Figure 3.43). The water CA of 83.1 ± 1.3° measured on the functionalised gold is close to those of other reported monolayers exhibiting an exposed phenyl group.[79] Both results indicate good formation of the AQ-SAM.

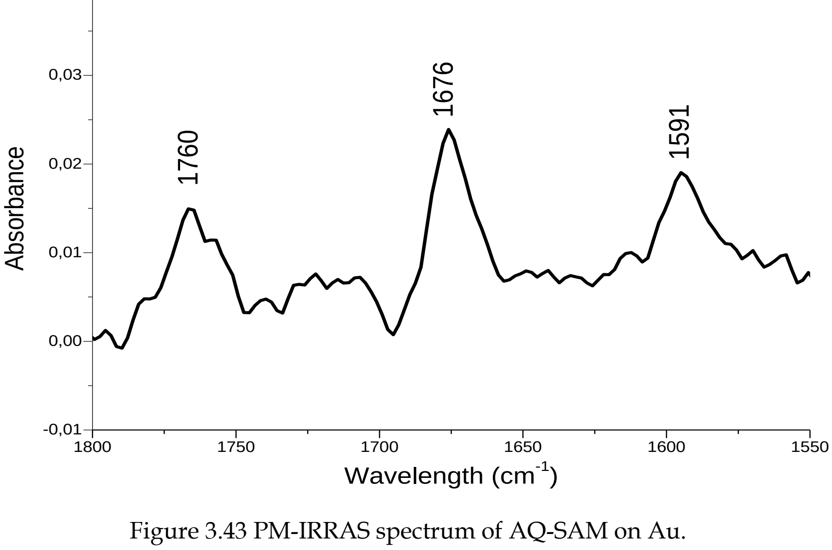

Figure 3.43 PM-IRRAS spectrum of AQ-SAM on Au.

In Table 3.3 the data characterization of both mono-component SAMs are collected.

Characterization Techniques	**AQ-SAM**	**Fc-SAM**
XPS (eV)	$S2p_{3/2}$ 162.1 $S2p_{1/2}$ 163.3	$S2p_{3/2}$ 161.5 $S2p_{1/2}$ 162.9 $Fe2p_{3/2}$ 707.6
ToF-SIMS (m/z)	$M^+ = 412$	185 (Fc^+)
Contact angle (deg)	83.1 ± 1.3	78.0 ± 3.4
PM-IRRAS (cm^{-1})	1676, 1590 and 1760	

Table 3.3 AQ-SAM and Fc-SAM characterization

These results confirmed the functionalization of the Au substrates with the electron donor (Fc) and acceptor (AQ) compounds, and the integrity of these molecules once confined on the surface.

3.4.1.2 Electrochemical characterization of Fc-SAMs and AQ-SAMs on Au

The electrochemical properties of the SAMs were investigated in different electrolyte media since the nature of these media strongly impact on the types of redox processes that take place and on the redox potentials. A clearly identified challenge here was hence to find electrolyte media suitable for switching and stabilising the different redox states of the prepared bi-component SAMs. For this purpose, three different electrolyte solutions were explored in this study: 1) an inorganic salt dissolved in an organic solvent (tetrabutylammonium hexafluorophosphate (NBu_4PF_6) in acetonitrile (ACN)), 2) an aqueous phosphate buffer solution, and 3) an ionic liquid (11-Butyl-3-methylimidazolium trifluoromethanesulfonate (BMIM-OTf)). Electrolytes (1) and (2) have been extensively employed for characterising electroactive SAMs. On the contrary, although ILs offer clear advantages for performing electrochemical studies as mentioned before (i.e. low vapour pressure, high thermal stability, high electrical conductivity and large electrochemical window), their use with SAMs has been less explored.

Cyclic voltammetry (CV) has been used as a tool to characterise the electrochemical properties of electroactive SAMs and the redox-accessible states shown in Figure 3.39. The type of solvent and the nature and size of the electrolyte ions have a strong influence on the CV response and hence on the performance of the electrochemical switch. Therefore, the optimum CV conditions can vary significantly depending on the electroactive system under examination.

For the electrochemical characterisation, it has been employed the 3rd setup cell (described in chapter 2, section 2.2, figure 2.3) with the modified gold substrate as the working electrode (with an area of 0.5 cm^2), a platinum wire as counter electrode and a silver wire as quasi-reference electrode. The first approach was to use the most common conventional conditions, that is, a salt dissolved in an organic solvent as the electrolyte solution.

For the AQ-SAM, different solvents (dichloromethane (DCM) with acetonitrile (ACN) in a ratio 9:1 (v/v), ACN, acetone and tetrahydrofuran (THF)) with different salts (tetrabutylammonium hexafluorophosphate (NBu_4PF_6), tetrabutylammonium perchlorate (NBu_4ClO_4) and lithium perchlorate ($LiClO_4$)) were combined as aprotic electrolytes. Under all tested conditions, the peak corresponding to the first reduction process (RP1; AQ $\leftrightarrows$ $AQ^{\bullet -}$) was observed between –0.8 and –1 $V_{vs\ Ag(s)}$, but the second reduction process (RP2; $AQ^{\bullet -}$ $\leftrightarrows$ AQ^{2-}) could not be measured due to the instability of the SAM when the voltage window was extended to more negative potentials. In Table 3.4 are shown $E_1^{1/2}$ and ΔE obtained for the different aprotic electrolytes studied for AQ-SAMs. CV registered in NBu_4PF_6 0.1 M in ACN (Figure 3.44) gave the lowest absolute $E^{1/2}$ (RP1) value ($E_1^{1/2}$=–0.8 $V_{vs\ Ag(s)}$), and the lowest peak-to-peak potential splitting (ΔE = 0.13 V at a scan rate (v) of 0.3 V·s^{-1}), which indicates that the reduced state is more accessible and the redox process is more reversible under these conditions.

Electrolyte salt	**solvent**	**$E_1^{1/2}$ (RP1)** ($V_{vs\ Ag(s)}$)	**ΔE (V)**
NBu_4PF_6	DCM:ACN 9:1 (v/v)	-0.91	0.20
NBu_4PF_6	ACN	-0.78	0.13
NBu_4PF_6	Acetone	-0.81	0.47
NBu_4PF_6	THF	-0.97	1.00
NBu_4ClO_4	ACN	-0.80	0.20
$LiClO_4$	ACN	-0.93	0.16

Table 3.4 $E_1^{1/2}$ and ΔE for the AQ-SAMs on Au in the different aprotic electrolytes. In all the cases, the electrolyte salt concentration is 0.1 M.

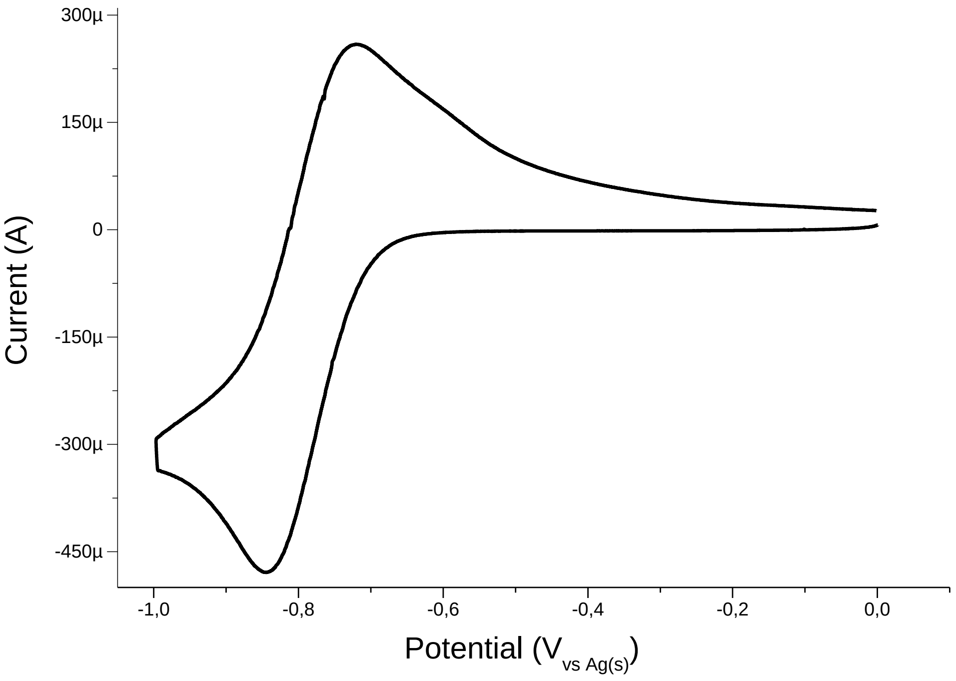

Figure 3.44 Cyclic voltammetry of the AQ-SAM on gold as working electrode vs Ag(s) and a Pt wire as the counter electrode in 0.1 M NBu_4PF_6 in acetonitrile at 300 mV/s.

In electrolyte solutions based on protic solvents, anthraquinones undergo a two-electron reduction process involving two protons that leads to the hydroanthraquinone form: $AQ+2H^+ +2e^- \leftrightarrows AQH_2$. This process typically takes place at voltages closer to 0 V than RP1 of AQ in an aprotic medium. Furthermore, it has been shown that the redox behaviour depends on the pH. Nagata et al. studied the electron transfer of a quinone SAM on gold and showed that, on increasing the pH of the solution, the peak potential shifts towards a more negative potential and the peak separation becomes smaller.[80] Taking this into account and in order to optimise the CV response of the herein-described monolayer, we characterised the AQ-SAM in a phosphate buffer solution at different pH values (5.0, 6.9 and 8.9). The measured $E^{1/2}$ values for increasing pH values were –0.31, –0.39 and –0.62 $V_{vs.\ Ag(s)}$, respectively, following the trend previously described in the literature. In addition, ΔE clearly depends on the pH. The ΔE value of 0.25 V at pH 5.0 and ν of 0.3 $V \cdot s^{-1}$ considerably diminishes to 0.07 and 0.06 V at pH 6.9 and 8.9, respectively. Hence, the buffer solution at neutral pH 6.9 was taken as optimal for the rest of the experiments, since under these conditions the redox process occurs at lower $|E^{1/2}|$ and shows greater reversibility (Table 3.5).

Electrolyte	$E^{1/2}$ ($V_{vs\ Ag(s)}$)	ΔE (V)
Buffer pH 5.0	-0.31	0.25
Buffer pH 6.9	-0.39	0.07
Buffer pH 8.9	-0.62	0.06

Table 3.5 $E_1^{1/2}$ and ΔE for the AQ-SAMs on Au in the different buffer pH electrolytes.

The electrochemistry of AQ derivatives has also been previously investigated in ionic liquids (ILs).[81,82] In this work, AQ-SAM were characterised by using 1-butyl-3-methylimidazolium trifluoromethanesulfonate (BMIM-OTf) as electrolyte. The IL was exhaustively dried prior to use, and the CVs were acquired under nitrogen in a glovebox to avoid moisture, which could lead to the formation of AQH_2. Interestingly, in the CV of the AQ-SAM in BMIM-OTf (Figure 3.45), the two reduction processes of AQ-SAM can be observed at $E_1^{1/2} = –0.31$ V (ΔE = 0.27 V, $\nu = 0.1\ V{\cdot}s^{-1}$) and $E_2^{1/2} = –0.61$ V (ΔE = 0.19 V, $\nu = 0.1\ V{\cdot}s^{-1}$).

For the Fc-SAM, exhaustive electrochemical characterisation was carried out in the optimised electrolytes found for the above-described AQ-SAM, that is, NBu_4PF_6 0.1 M in acetonitrile, BMIM-OTf and buffer solution (pH 6.9). The results showed stable and reproducible CVs with one oxidation wave in the three electrolytic media.

Table 3.6 summarises the $E^{1/2}$ values measured for the AQ-SAM and Fc-SAM on gold in the three electrolytes. They evidence that the chemical environment has a huge impact on the voltage at which the redox process is observed, and elucidate the importance of correctly choosing the conditions under which a redox-active monolayer is studied, since they can determine the number of states that can be accessed.

	[a] ACN/ NBu_4PF_6	[b] Phosphate buffer	BMIM-OTf
Fc-SAM	+0.41	+0.35	+0.41
AQ-SAM	-0.78	-0.39	-0.31 -0.61

Table 3.6 Values of $E^{1/2}$ ($V_{vs\ Ag(s)}$) obtained for the two mono-component SAMs in different electrolytes. [a] 0.1 M; [b] pH= 6.9.

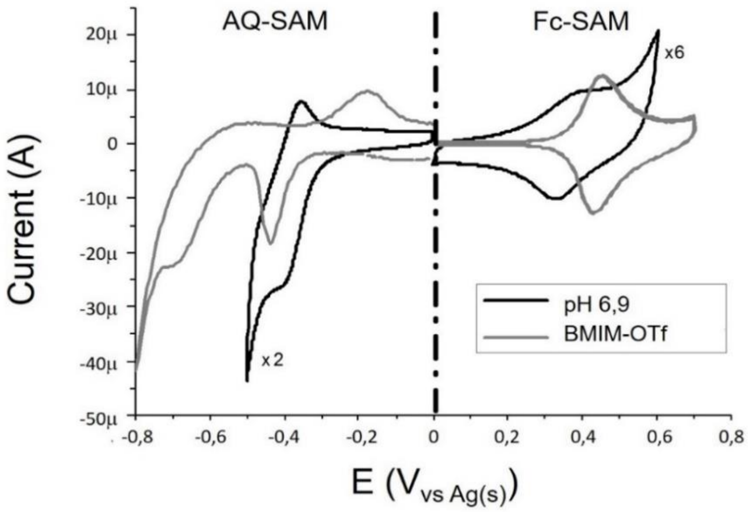

Figure 3.45 CVs of the mono-component Fc and AQ SAMs on gold in phosphate buffer solution at pH 6.9 (black) and in BMIM-OTf (grey). Scan rate: 100 mV·s^{-1}. The current intensity is scaled for a clearer comparison.

Importantly, it was found that the Fc–SAM is not stable below –0.8 V$_{vs\ Ag(s)}$ in the aprotic media, and therefore this electrolyte was not used for studying the bi-component monolayers. Notably, the AQ reduction peaks clearly shift to lower voltages in the IL compared to the ones observed in the electrolyte based on the organic solvent.

Figure 3.45 shows CVs of the two mono-component SAMs acquired in the electrolytes selected for studying the bi-component SAMs (i.e. buffer solution at pH 6.9 and BMIM-OTf). All the redox processes are observed below |0.8|V$_{vs\ Ag(s)}$, a voltage window in which the SAMs on gold should be stable.

3.4.1.3 Preparation and characterization of bi-component AQ/Fc-SAMs on Au

The bi-component SAMs were prepared by two approaches: 1) from a bi-component solution (one step) and 2) sequential immersion in solutions of each component (two steps). To determine the best methodology and to evaluate the reproducibility, the ratio Γ_{AQ}/Γ_{Fc} was used as indicator. Γ was extracted from the anodic peak of the Fc oxidation wave and from the cathodic peak of the $AQ \leftrightarrows AQ^{\bullet -}$ process in BMIM-OTf.

For the one-step procedure a freshly cleaned gold substrate was immersed in a mixed solution of the two compounds (in different molar ratios). This route always led to a very low percentage of AQ linked to the surface. This can be attributed to the strongly preferred adsorption of thiols over disulfides, as previously reported.[12] This is probably due to smaller steric hindrance of thiols on approaching the surface, a lower activation entropy of adsorption or possibly differences in the rates of conversion of the initially physisorbed species to the chemisorbed thiolate. For the two-step procedure, first the freshly cleaned substrate was immersed in a 0.5 mM solution of AQ (**2**) in THF for 40 h, and then, the modified substrate was rinsed and immersed in a 1 mM solution of the $FcC_{11}SH$ (**1**) in THF at room temperature for 1, 2 and 4 h under argon. In all cases good formation of the bi-component SAM was observed (see Figure 3.46).

The Γ_{AQ}/Γ_{Fc} ratio decreased from 10.0 to 5.0 on increasing the immersion time from 1 to 2 h, but no significant further decrease occurred when the immersion time was increased to 4 h. Hence, 2 h was established as the most suitable incubation time for the functionalization with Fc in the preparation of the bi-component SAM.

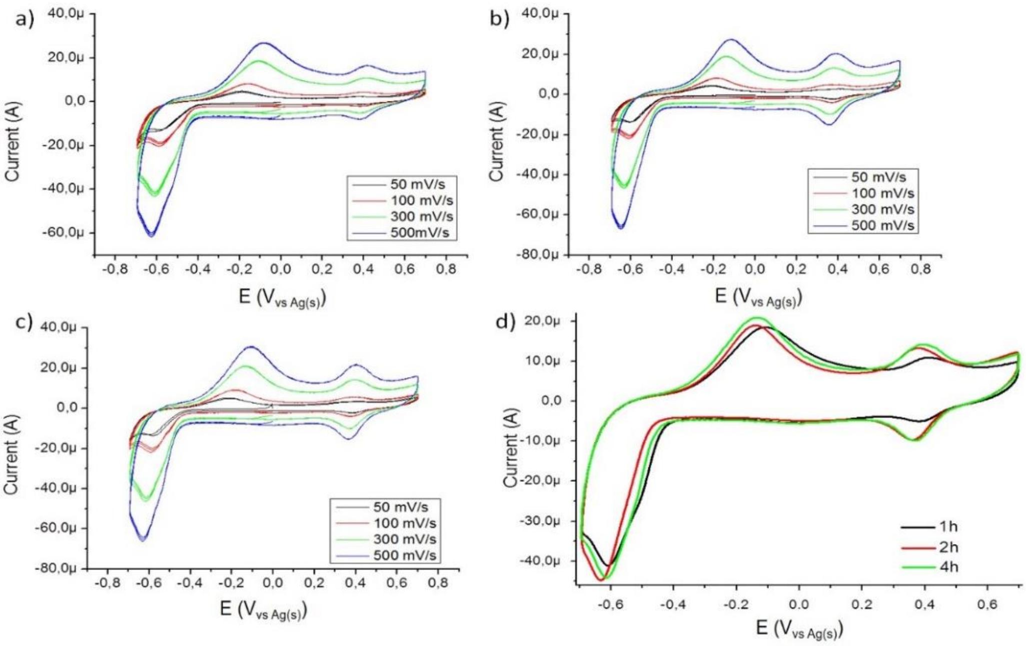

Figure 3.46 CVs of three different AQ/Fc-SAMs prepared following the two steps methodology. 1st preparation of the AQ-SAM on Au (40 h immersion) and 2nd immersion of the AQ-SAM on Au in the Fc solution for: 1 h (a), 2 h (b) and 4 h (c). CVs were acquired in BMIM-OTf at the different scan rates indicated in the legend. d) Overlap of the different CVs at the same scan rate (300 mV/s).

Immersion time	***Γ*(AQ)**	***Γ*(Fc)**	Γ_{AQ}/Γ_{Fc}
1 hour	$2.6 \cdot 10^{-10}$	$2.6 \cdot 10^{-11}$	10.0
2 hours	$2.4 \cdot 10^{-10}$	$4.9 \cdot 10^{-11}$	5.0
4 hours	$2.7 \cdot 10^{-10}$	$5.2 \cdot 10^{-11}$	5.2

Table 3.7 Surface coverages Γ (mol cm^{-2}) calculated for the three bi-component SAMs prepared with different immersion times of the AQ-SAM in the Fc solution.

The optimized bi-component SAMs were also characterised by contact angle, XPS and ToF-SIMS. Contact angle measurements were performed to examine the surface wetting properties of the bi-component SAMs with milliQ water. The average value obtained in this case was 75.5 ± 1.8°, slightly lower than the contact angle of the corresponding mono-component SAMs.

By XPS characterization the presence of S 2p, Fe 2p and O 1s was confirmed (see Figure 3.47). The S 2p peaks were fitted using doublet peaks with 2 p$_{1/2}$/ 2 p$_{3/2}$ ratio of 2:1 and separation of 1.2 eV, as previously reported. The doublet at 162.0 eV is attributed to the Au-thiolated species. A doublet located at 707.9 eV and 720.5 eV corresponding to the Fe 2p$_{3/2}$ and Fe 2p$_{1/2}$ demonstrates the presence of the Fc molecules in agreement with previous works.[83] The O 1s spectrum shows a peak with contribution of two peaks at 532.0 eV and 532.8 eV that could be attributed to the C-O of the ester and the C=O of the carbonyl groups present in the AQ core. These results support the presence of both species AQ and Fc on the gold surface as electrochemically observed.

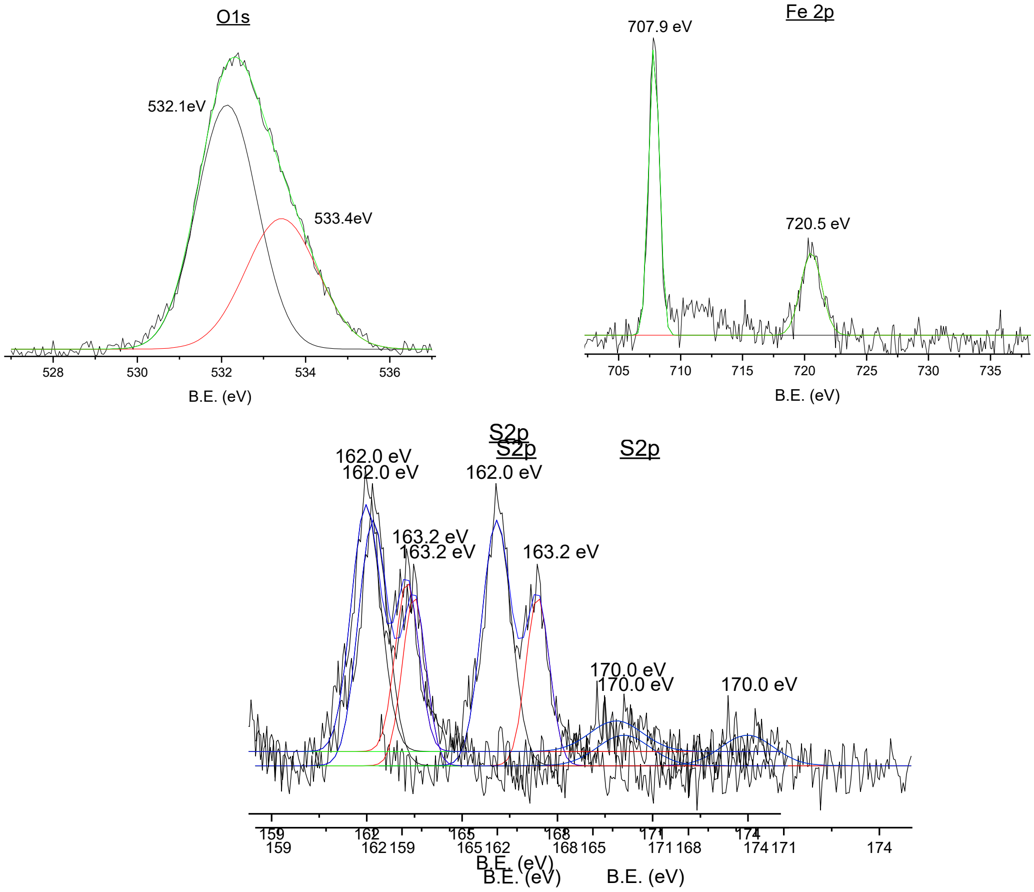

Figure 3.47 High-resolution XPS of S 2p, Fe 2p and O 1s spectra from the optimized bi-component SAM.

In the ToF-SIMS spectra (Figure 3.48), it is difficult to appreciate the peaks related to anthraquinone molecular ion. However, it can be observed an anthraquinone fragment peak at m/z = 223. The ferrocene molecular ion at m/z = 185, with different fragment peaks of $FcC_{11}SH$ are also observed.

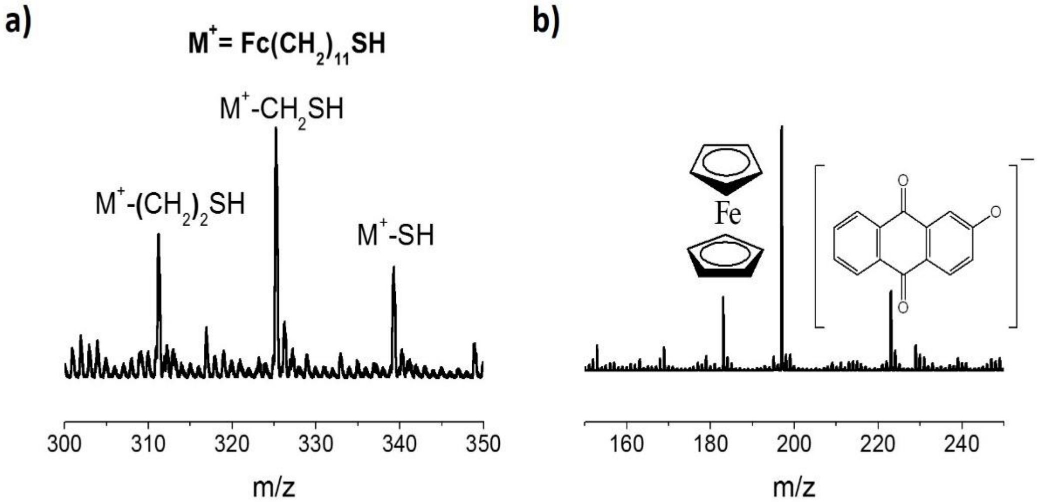

Figure 3.48 ToF-SIMS spectra for optimized AQ/Fc-SAMs in a) positive mode, b) negative mode.

CV allowed the different accessible redox states in the bi-component SAM to be identified. States 1, 2 and 3′ (see Figure 3.39.b and c) were electrochemically accessed by using the phosphate buffer at pH 6.9 (Figure 3.49.a), and states 1, 2 and 3 by employing BMIM-OTf (Figure 3.49.b). In both cases, we succeeded in realising a SAM-based molecular ternary switch in a voltage window in which SAMs are stable.

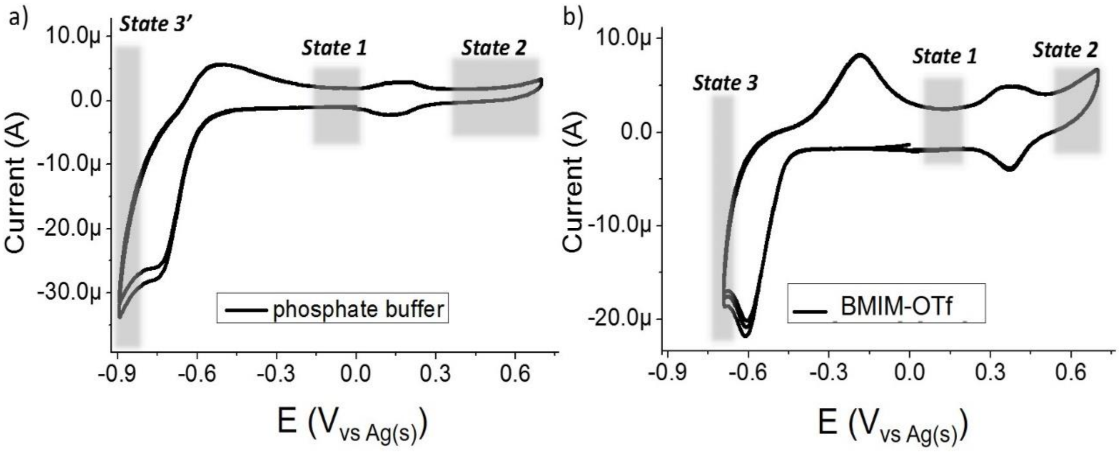

Figure 3.49 CV of the bi-component AQ/Fc-SAM on gold in a) phosphate buffer (pH 6.9) and b) BMIM-OTf. Scan rate: 100 mV·s^{-1}. The shaded areas indicate the different accessed states (see Figure 3.39).

Unfortunately, as shown in Figure 3.49, the AQ reduction potentials shifts towards more negative values in both electrolytes compared to the AQ mono-component monolayer, which could be attributed to the different chemical environments. For this reason, state 4 from Figure 3.39.b corresponding to coexistence of the dianionic form of AQ with the neutral ferrocene species (AQ^{2-}/Fc) was not possible to achieve due to desorption of the grafted Fc molecules at the voltage required for the reduction of $AQ^{\bullet -}$ to AQ^{2-} (see Figure 3.50).

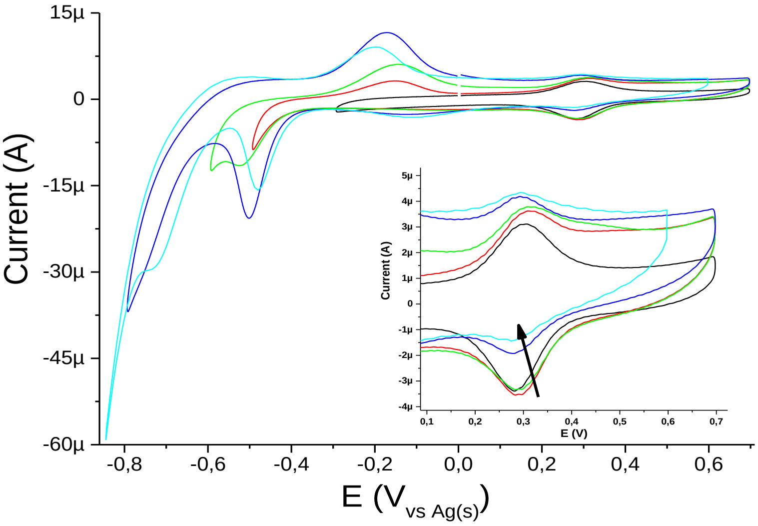

Figure 3.50 Cyclic voltammetry of the AQ/Fc-SAM prepared by the optimized conditions. In the inset figure is shown that the current intensity corresponding to the Fc redox peak decreases when the negative voltage limit is brought below -0.6 V (blue and cyan curves). That means that the Fc molecules are being desorbed from the surface.

Several consecutive voltage-sweeping cycles were acquired in both electrolytes without showing a significant decrease of the current intensity in the CVs, which revealed that the SAMs are stable (see Figure 3.51). In the phosphate buffer solution, there is only a slight variation of the intensity of the AQ redox peak which is stabilized after several cycles.

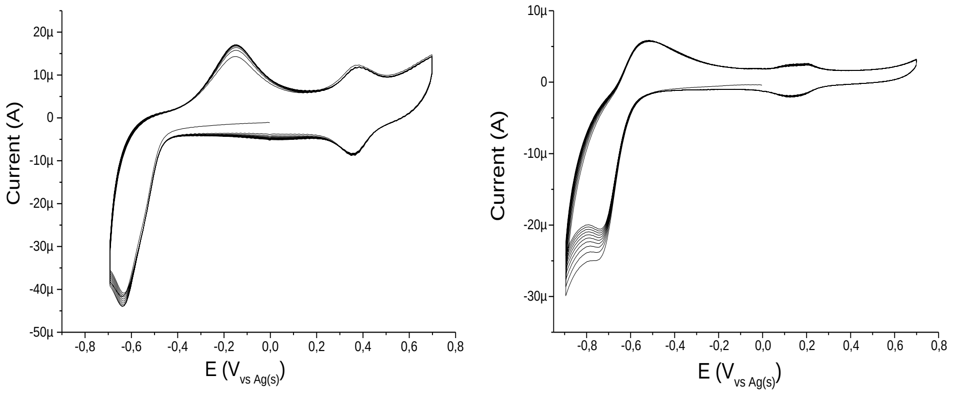

Figure 3.51 CVs of the bi-component SAMs in a) BMIM-OTf, and b) phosphate buffer solution (pH=6.9). In both cases 10 consecutives voltage sweeping cycles were acquired to corroborate the stability of the SAM.

3.4.1.4 Summary

In summary, a mixed SAM of an electron donor and an electron acceptor was successfully prepared to achieve a three-state redox molecular switch in a relatively narrow voltage window in which SAMs are stable. It was demonstrated in detail that the choice of electrolyte medium can determine the potential at which the redox processes occur and hence the operational voltage range of the switch. Therefore, this work clearly elucidates the challenges for achieving long-term stable molecular multistate switches by employing multiple redox-active centres covalently linked to a gold surface.

3.4.2 Monocomponent tetrathiafulvalene SAMs with multiple accessible redox states[3]

3.4.2.1 Preparation and characterization of TTF-SAMs on Au

The TTF derivative used in this work (Figure 3.52) was synthesised by S. Maglione following the methodologies reported in the literature.[84,85] This molecule bears a disulfide group that can react with gold surfaces in order to form a covalent bonded SAM.

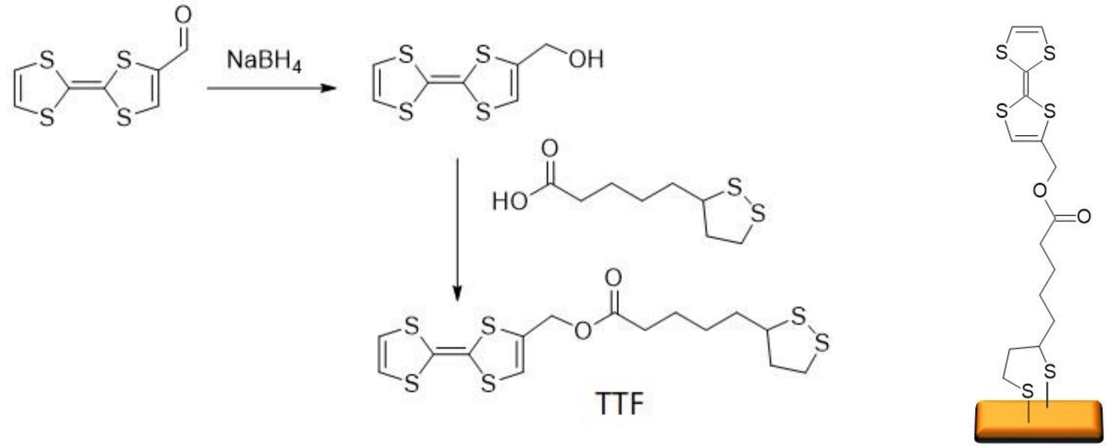

Figure 3.52 Synthesis of TTF derivative and scheme of its corresponding SAM on gold.

The SAMs were prepared by immersion of the freshly cleaned substrates in a 1 mM solution of the synthesized TTF in dry THF under an inert atmosphere and room temperature for 72 h. Subsequently, the functionalized samples were rinsed carefully with THF and dried under a stream of nitrogen giving the target TTF-SAM (Figure 3.52).

The SAMs were successfully characterised by XPS and ToF-SIMS. In Table 3.8 are summarized the binding energies observed in the high-resolution XPS characterization of the TTF-SAM. In the ToF-SIMs spectra (Figure 3.53), it can be appreciated a peak at m/z = 422, corresponding to the TTF molecular ion, and also, different peaks that can be related with possible TTF fragments.

---

[3] This work has been published in *RSC Adv.* 7 (**2017**) 5636 – 5641.

Binding energy (eV)	Atom	Type of bond
532.2	O1s	C-O
333.3	O1s	C=O
284.8	C1s	C-C
285.7	C1s	C=C
288.9	C1s	O-C=O
161.9	S2p$_{3/2}$	S-Au
163.1	S2p$_{1/2}$	S-Au
163.6	S2p$_{3/2}$	C-S-C
164.7	S2p$_{1/2}$	C-S-C

Table 3.8 XPS binding energies for TTF-SAM.

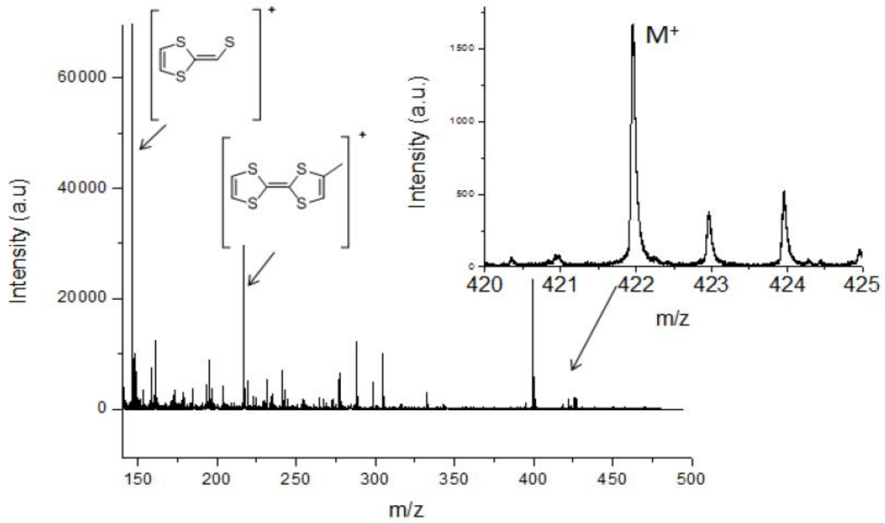

Figure 3.53 ToF-SIMS spectra for TTF-SAM.

3.4.2.2 Electrochemical characterization of TTF-SAM on Au

The confinement of the TTF core on the electrode surface provides an electrochemical interface with three stable redox states, i.e., the neutral, the radical cation and the dication forms of TTF. The TTF-Au modified electrodes were characterized then using electrochemical techniques. Figure 3.54 shows the voltammetric response of the TTF-modified Au surface at different potential scan rates (ν) measured using a solution of $LiClO_4$ 0.1 M in acetonitrile as electrolyte, the functionalized surface as working electrode and platinum and silver wires as counter and pseudo-reference electrodes, respectively. Expectedly, two reversible one-electron processes corresponding to the TTF/TTF$^{\bullet+}$ and TTF$^{\bullet+}$/TTF^{2+} redox couples were observed at the formal potentials $E_1^{1/2}$ = 0.26 V and $E_2^{1/2}$ = 0.63 $V_{vs.\ Ag(s)}$ (at a scan rate of 100 mV s^{-1}), respectively.

The linear relationship between $I_{p,a}$ (i.e., the anodic peak current intensity) and ν is in agreement with the presence of surface-confined redox-active molecules (see Figure 3.55), along with the small peak-to-peak separations (ΔE) observed at low scan rates for the two redox processes, ΔE_1 = 27 mV and ΔE_2 = 19 mV.[86] The full width at half maximum (ΔE_{FWHM}) in a theoretical case, where an ideal Nernstian reaction under the Langmuir isotherm conditions (i.e., all adsorption sites are equivalents and there are no interactions between immobilized electroactive centers) occurs at 25° C, is ca. 90 mV.[19] As previously mentioned, the deviations from the theoretical ΔE_{FWHM} value gives hence information about the redox centers, especially related to the intermolecular interactions.[87] In this case, the ΔE_{FWHM} value of the first redox peak of the TTF-SAMs was larger than 90 mV (i.e., 143 mV), whereas for the second redox peak was slightly lower than the theoretical value (i.e., 79 mV). This type of CV shape has been commonly observed in other TTF-SAMs.[75,88,89]

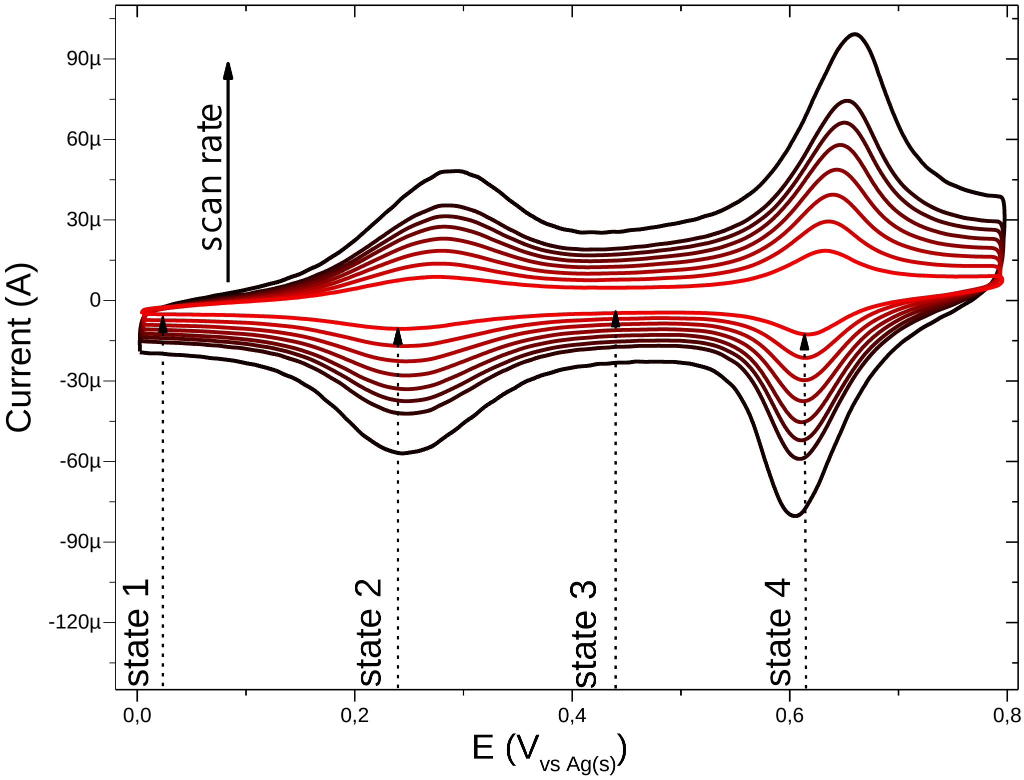

Figure 3.54 CV of TTF-SAM in $LiClO_4$ 0.1 M in ACN at scan rates 0.1, 0.2, 0.3, 0.4, 0.5, 0.6, 0.7 and 1 V s^{-1}

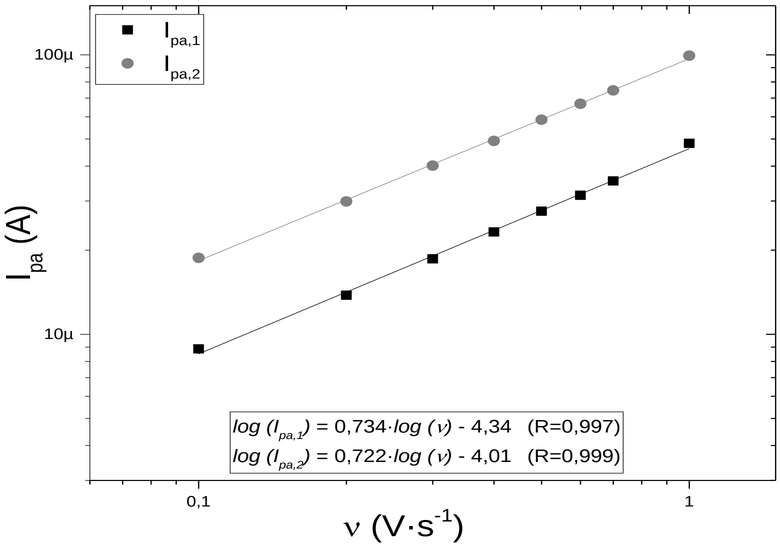

Figure 3.55 Linear relationship of the current peak ($I_{p,a}$) vs the scan rate (ν) for the two redox processes observed in the TTF-SAM on Au.

From the area under the cyclic voltammetry peak, the TTF surface coverage was estimated to be 2.2 10^{-10} mol·cm^{-2} (at scan rate 100 mV·s^{-1}). Repeated electrochemical cycling demonstrated that the SAM was stable and only a significant reduction in the intensity of the peaks was detected when the potential was scanned beyond the first redox process (Figure 3.56).

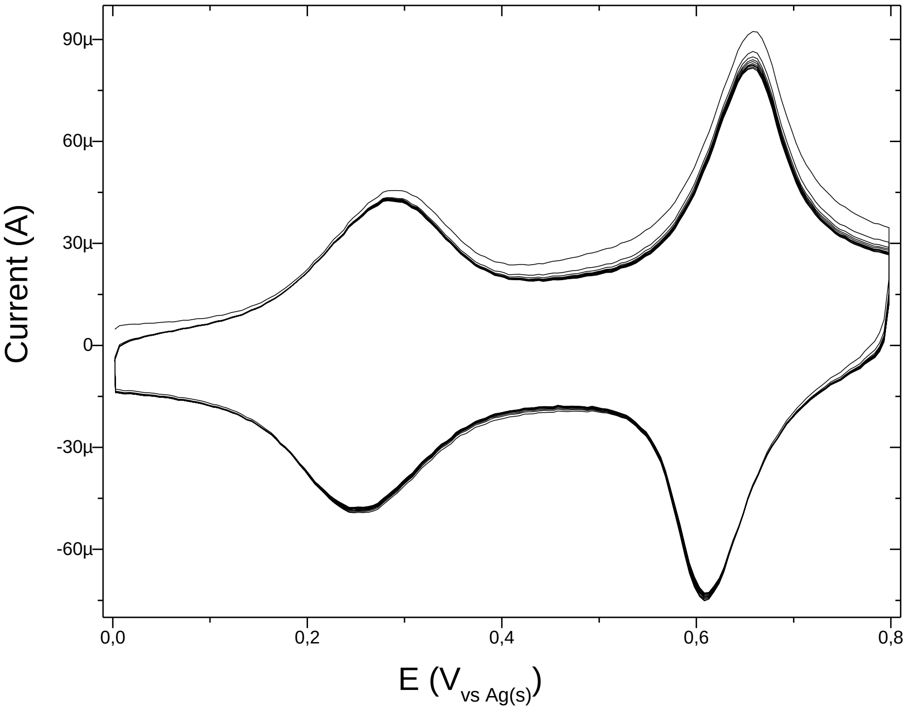

Figure 3.56 CV of the TTF-SAM in $LiClO_4$ 0.1M in acetonitrile, at 1V·s^{-1}, during 10 cycles.

3.4.2.3 Impedance characterization of TTF-SAMs on Au

To characterise the TTF-SAM, impedance spectra were collected, in the same conditions as the ones used in the CV experiments, between 200 kHz and 500 mHz with an AC amplitude of 5 mV (peak to peak) at three different voltages: before the redox process (10 mV), at the first redox peak potential (250 mV), and at the second redox peak potential (620 mV). Nyquist and Bode plots are shown in Figure 3.57.a and b, respectively. In cases where a DC-current can be established, such as when an ion pair is present in the electrolyte solution, Nyquist plots typically display one or more semicircles.[90] Nevertheless, in the case of surface confined molecules under an inert electrolyte, a DC-current cannot be established, and the system shows capacitor behaviour. Accordingly, the Nyquist plots of the TTF-SAM look like straight vertical lines parallel to the y axis (Figure 3.57.a).[57,58,91–93]

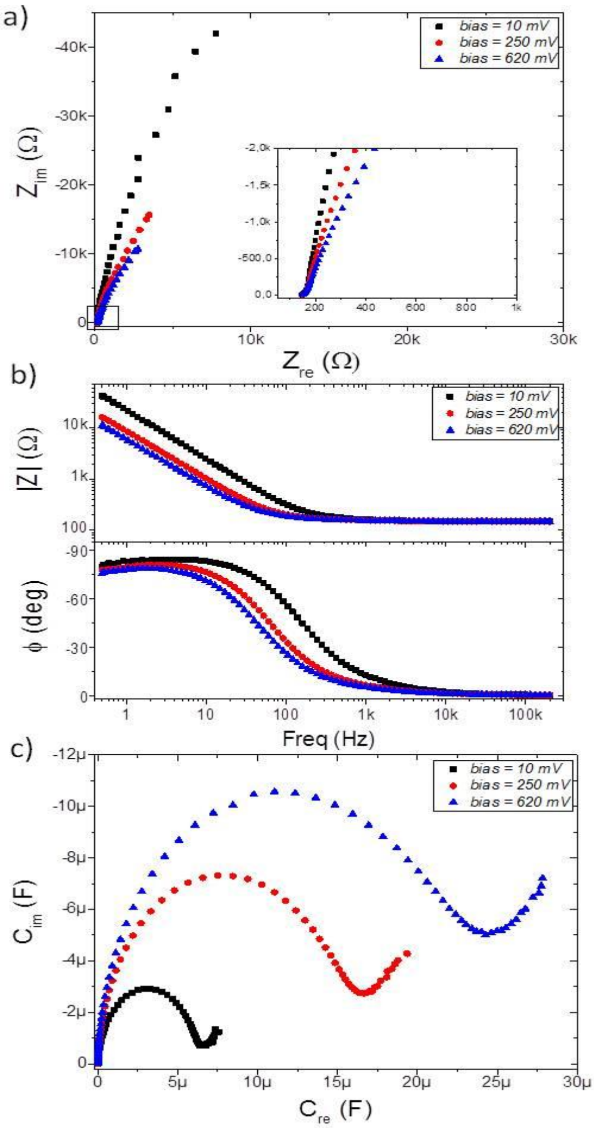

Figure 3.57 EIS of TTF-SAM at 3 different bias voltages: 10 mV (■), 250 mV (●), and 620 mV $_{\text{vs Ag(s)}}$ (▲). a) Nyquist plot, b) Bode plot, and c) Cole-Cole Plot.

The Bode magnitude plots (impedance modulus (|Z|) vs. frequency) at the low frequency region consist of straight lines with slopes close to 1, while the phase angles (ϕ) approach -90°. This behaviour is in agreement with a capacitor-like system,[94] where the gold metal surface acts as one of the capacitor plate and the physisorbed ions at the SAM/electrolyte interface act as the other capacitor plate.[62] At higher frequencies (freq > 10 kHz), the frequency-independent impedance and phase angle close to zero indicate that the system behaves as a resistor, that is, the total impedance is dominated by the solution resistance.[62] This is due to the fact that at high frequencies, the capacitor behaves as a short-circuit element since there is no time to be charged, allowing the AC current to pass.

Noticeable, a significant modulation in |Z| is observed at the low frequency region depending on the DC voltage applied (i.e., on the SAM redox state), indicating that the performed impedance measurements could be successfully used as a readout of the molecular switch. Alternatively, the data have been analysed by means of capacitance Bode plots by using the Equation 3.10.[20,26,58] In fact, capacitance Cole–Cole plots, where the imaginary (C_{im}) versus the real (C_{re}) part of the capacitance are represented, provide very useful information for surface confined redox species.[25–27,57,58,91–93] Figure 3.57.c clearly illustrates that different processes with different time constants are occurring depending on the applied DC potential. The small semicircle recorded at a voltage outside the redox process (i.e., 10 mV) comes from the non-faradaic terms dominated by the resistance of the electrolyte (R_{sol}) and the double layer capacitance (C_{dl}). In the redox window potentials faradaic contributions are also present (i.e., a pseudo-capacitance for charging the monolayer and a resistance for the electron transfer).

Noteworthy, the influence of applied potential on the capacitance spectra of bare Au was much smaller than when the gold is functionalised with the TTF electroactive monolayer, indicating that the observed effect is not simply due to the polarisation of the metal but to the redox processes involved (Figure 3.58).

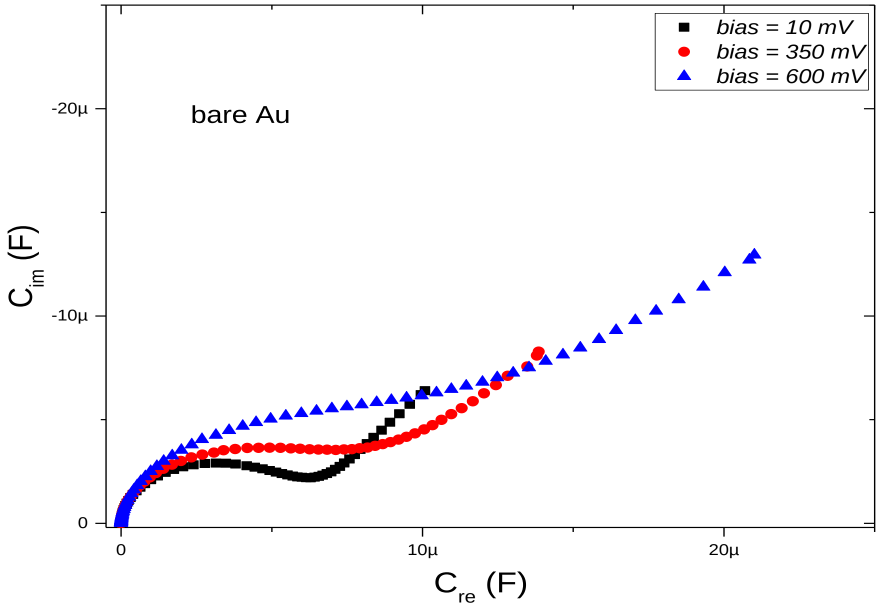

Figure 3.58 Capacitance Cole-Cole plot of the unmodified Au substrate in $LiClO_4$ 0.1 M in acetonitrile at three DC voltages (10 mV, 350 mV and 600 mV).

Further, the C_{re} vs. frequency plot is illustrated in Figure 3.59. We found that at medium/high frequency range, the measured capacitance corresponds to the bulk capacitance, whereas at low frequency values a plateau is reached reflecting the interfacial double-layer capacitance.[95] Consequently, at this low frequency the capacitance is clearly dependant on the redox state of the molecule and, thus, on the applied DC voltage.

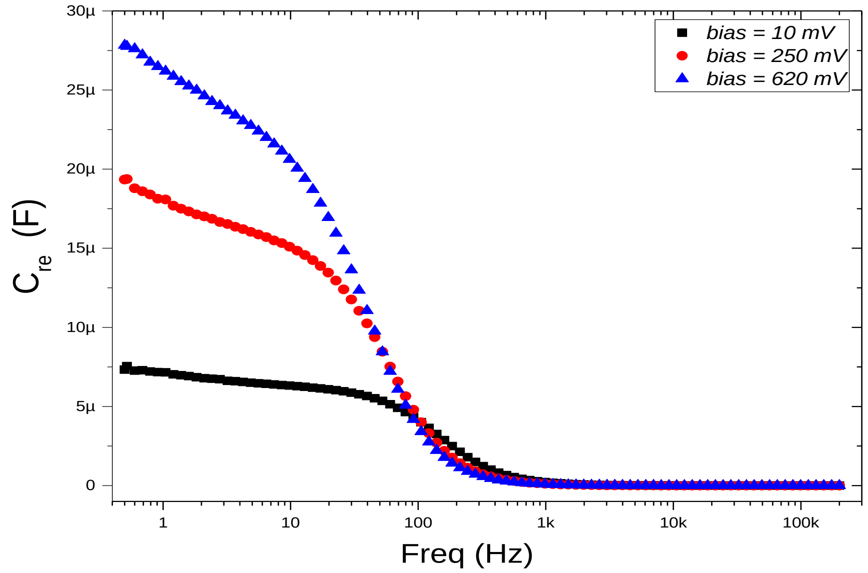

Figure 3.59 C_{re} vs. freq plot of TTF-SAMs at 3 bias voltages: 10 mV (■), 250 mV (●), and 620 mV $_{\text{vs Ag(s)}}$ (▲).

Therefore, this result prompted us to investigate the capacitance response in the electrochemical switchable TTF-SAM at low frequency. Taking into account the initial CV, four different voltage inputs were selected: 10, 250, 450 and 620 mV $_{\text{vs. Ag(s)}}$, respectively (see Figure 3.54). Such voltages correspond, respectively, to a state where the TTF molecule is in neutral state (state 1), where the first oxidation process occurs (state 2), where all the TTF surface-confined molecules should exist as $TTF^{\bullet +}$ radical-cation (state 3) and the last one where the second oxidation process takes place (state 4). A schematic representation of the different TTF-SAM redox states can be found in Figure 3.60.

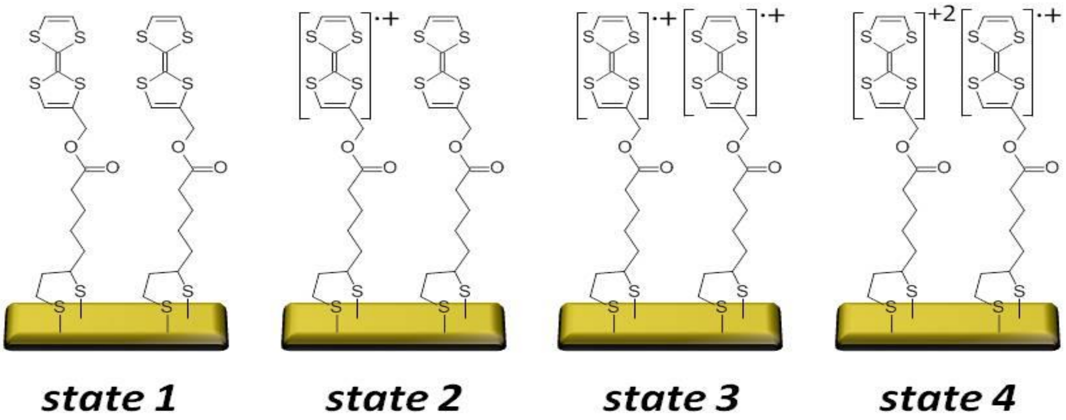

Figure 3.60 Scheme of the TTF-SAM states at the four different DC bias applied: 10 mV (state 1), 250 mV (state 2), 450 mV (state 3), and 620 mV (state 4).

Hence EIS measurements were performed at 1 Hz at the selected DC potentials. In Figure 3.61, the evolution of C_{re} in the four states is shown when 20 cycles were applied to the TTF functionalised gold substrate. Capacitance values discernible and specific for each state with significant on/off ratios were found, validating the feasibility of using the SAM capacitance as output of the electrochemical switch. A perceptible decrease of the initial capacitance value of 3, 15, 2 and 30% for states 1–4, respectively, after 20 cycles, was found. As the values indicate, such variation is more pronounced at the states corresponding to the potential of the redox process. This is attributed to some molecular desorption caused by the bias stress. This is also in accordance to the changes observed in the CV of the SAM before and after the impedance switching experiments (Figure 3.62).

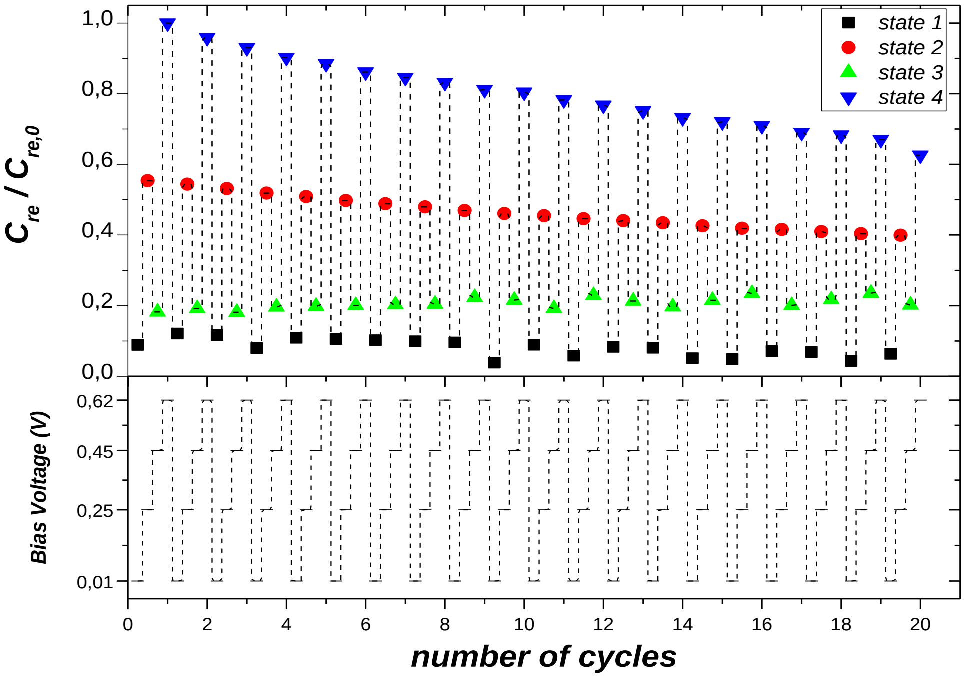

Figure 3.61 Four-state switching of TTF-SAM: at the bottom, applied bias voltage profile; at the top, $C_{re}/C_{re,0}$ (at 1Hz) output at the corresponding states: state 1 (10 mV), state 2 (250 mV), state 3 (450 mV) and state 4 (620 mV).

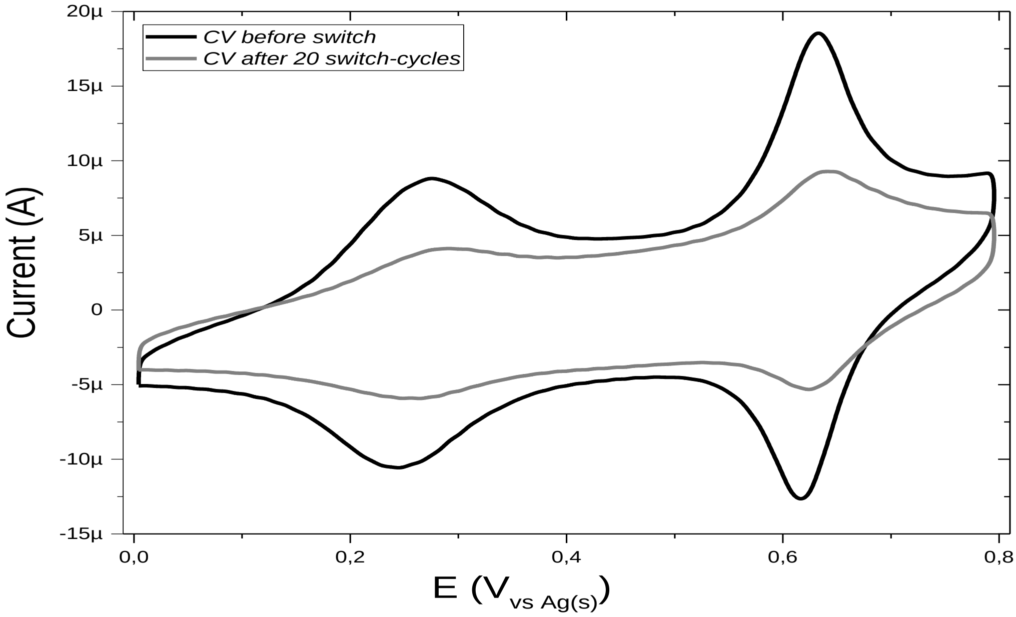

Figure 3.62 CV of the TTF-SAM in $LiClO_4$ 0.1 M in ACN before and after the 20 EIS switching cycles.

The switching response was studied in different samples after the application of 50 cycles achieving similar results (Figure 3.63).

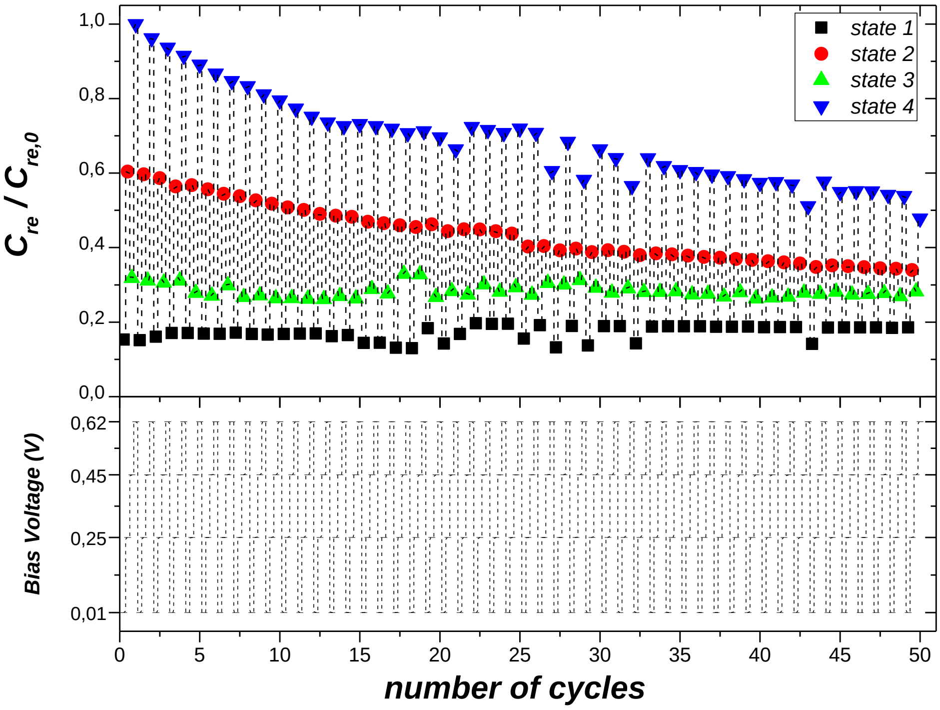

Figure 3.63 Relative capacitance values ($C_{re}/C_{re,0}$) of a TTF-SAM during 50 switching cycles.

Therefore, it has been successfully achieved a surface confined molecular switch operating with both and electric input and output signals by making use of the SAM capacitance. It should be highlighted though that the robustness of the system is limited to the electrochemical stability of the sulphur–gold covalent bond which could probably be improved by avoiding extremely traces of humidity and oxygen. It could be anticipated that other SAMs such as silane derivatives on ITO would be more durable.[75,78]

3.4.2.4 Summary

In summary, a functionalised gold surface with a TTF derivative was prepared in order to realise a surface with multiple accessible redox states. Such hybrid material was investigated as a four-state surface-immobilized switch by taking advantage of the different capacitance response under the application of external electric fields. Importantly, the number of states of the switch was not limited to the number of redox states of the molecule but instead it was determined by the output of the system at defined DC applied potentials. It should be also noticed that quaternary logic storage platforms can easily match the present binary system as they can be decoded directly into two binary-digit equivalents.[96–98] Thus, the results here reported might encourage the development of this type of electrochemical molecular switches for the future implementation in devices.

3.5 References

1 B. L. Feringa, *Molecular Switches*, Wiley-VCH Verlag GmbH, Weinheim, FRG, 2001, vol. 3.

2 J. F. Stoddart, *Acc. Chem. Res.*, 2001, **34**, 410–411.

3 S. Erbas-Cakmak, D. A. Leigh, C. T. McTernan and A. L. Nussbaumer, *Chem. Rev.*, 2015, **115**, 10081–10206.

4 J. F. Callan, A. P. de Silva, N. D. McClenaghan, S. V. Luis, E. Garcia-Espana, S. Quici and L. Prodi, *Chem. Commun.*, 2004, **81**, 2048–2049.

5 A. P. de Silva, H. Q. N. Gunaratne, C. P. McCoy, D. Gosztola, G. L. Graines, M. R. Wasielewski, K. R. A. S. Sandanayake, L. de Cola and L. Flamigni, *Chem. Commun.*, 1996, **257**, 2399–2400.

6 M. Irie, *Chem. Rev.*, 2000, **100**, 1685–1716.

7 R. Langer and D. A. Tirrell, *Nature*, 2004, **428**, 487–492.

8 G. London, G. T. Carroll, T. Fernández Landaluce, M. M. Pollard, P. Rudolf and B. L. Feringa, *Chem. Commun.*, 2009, 1712–1714.

9 R. G. Nuzzo and D. L. Allara, *J. Am. Chem. Soc.*, 1983, **105**, 4481–4483.

10 P. E. Laibinis and G. M. Whitesides, *J. Am. Chem. Soc.*, 1992, **114**, 1990–1995.

11 A. Ulman, in *An Introduction to Ultrathin Organic Films*, Elsevier, 1991, pp. 101–236.

12 H. A. Biebuyck, C. D. Bain and G. M. Whitesides, *Langmuir*, 1989, **5**, 723–727.

13 H. O. Finklea, D. A. Snider, J. Fedyk, E. Sabatani, Y. Gafni and I. Rubinstein, *Langmuir*, 1993, **9**, 3660–3667.

14 I. Alcón, M. Gonidec, M. R. Ajayakumar, M. Mas-Torrent and J. Veciana, *Chem. Sci.*, 2016, **7**, 4940–4944.

15 C. Simão, M. Mas-Torrent, N. Crivillers, V. Lloveras, J. M. Artés, P. Gorostiza, J. Veciana and C. Rovira, *Nat. Chem.*, 2011, **3**, 359–364.

16 G. De Ruiter, L. Motiei, J. Choudhury, N. Oded and M. E. Van Der Boom, *Angew. Chemie Int. Ed.*, 2010, **49**, 4780–4783.

17 C. G. Zoski, *Handbook of Electrochemistry*, Elsevier, 2007.

18 D. A. C. Brownson and C. E. Banks, *The handbook of Graphene Electrochemistry*, Springer London, London, 2014.

19 A. J. Bard and L. R. Faulkner, *Electrochemical Methods: Fundamentals and Applications*, John Wiley & Sons, Inc., New York, NY, 2nd ed., 2001.

20 J. R. Macdonald and W. B. Johnson, *Fundamentals of Impedance Spectroscopy*, 2005.

21 D. R. Franceschetti and J. R. Macdonald, *J. Electroanal. Chem. Interfacial Electrochem.*, 1977, **82**, 271–301.

22 J. R. Macdonald, *J. Electroanal. Chem.*, 1987, **223**, 25–50.

23 A. L. Eckermann, D. J. Feld, J. A. Shaw and T. J. Meade, *Coord. Chem. Rev.*, 2010, **254**, 1769–1802.

24 S. E. Creager and T. T. Wooster, *Anal. Chem.*, 1998, **70**, 4257–4263.

25 P. R. Bueno, F. Fabregat-Santiago and J. J. Davis, *Anal. Chem.*, 2013, **85**, 411–417.

26 P. R. Bueno, G. Mizzon and J. J. Davis, *J. Phys. Chem. B*, 2012, **116**, 8822–8829.

27 M. S. Góes, H. Rahman, J. Ryall, J. J. Davis and P. R. Bueno, *Langmuir*, 2012, **28**, 9689–9699.

28 D. Orbakh, *Nonaqueous electrochemistry*, CRC Press, 1999.

29 W. A. Henderson, *Electrochemistry in Nonaqueous Solutions*, Wiley-VCH Verlag GmbH & Co. KGaA, Weinheim, FRG, 2009.

30 A. Shariati, S. S. Ashrafmansouri, M. H. Osbuei and B. Hooshdaran, *Korean J. Chem. Eng.*, 2013, **30**, 187–193.

31 M. D. Joshi and J. L. Anderson, *RSC Adv.*, 2012, **2**, 5470-5484.

32 M. Freemantle, *Chem. Eng. News*, 2000, **78**, 37–50.

33 T. Katase, R. Kurosaki, K. Murase, T. Hirato and Y. Awakura, *Electrochem. Solid-State Lett.*, 2006, **9**, C69-C72.

34 K. Murase, R. Kurosaki, T. Katase, H. Sugimura, T. Hirato and Y. Awakura, *J. Electrochem. Soc.*, 2007, **154**, D612-D616.

35 T. Welton, *Chem. Rev.*, 1999, **99**, 2071–2083.

36 P. Wasserscheid and T. Welton, *Ionic Liquids in Synthesis: Second Edition*, Wiley-VCH Verlag GmbH & Co. KGaA, Weinheim, Germany, 2008, vol. 1.

37 T. Welton, *Coord. Chem. Rev.*, 2004, **248**, 2459–2477.

38 Z. Conrad Zhang, *Adv. Catal.*, 2006, **49**, 153–237.

39 G.-T. Wei, Z. Yang and C.-J. Chen, *Anal. Chim. Acta*, 2003, **488**, 183–192.

40 D. Oyamatsu, T. Fujita, S. Arimoto, H. Munakata, H. Matsumoto and S. Kuwabata, *J. Electroanal. Chem.*, 2008, **615**, 110–116.

41 J. Le Bideau, L. Viau and A. Vioux, *Chem. Soc. Rev.*, 2011, **40**, 907–925.

42 P. G. Bruce, Ed., *Solid state electrochemistry*, Cambridge University Press, Cambridge, 1994.

43 B. V. Ratnakumar and S. R. Narayanan, in *Handbook of Solid State Batteries and Capacitors*, World Scientific, 1995, pp. 1–40.

44 H. Ohno, *Electrochemical Aspects of Ionic Liquids*, John Wiley & Sons, Inc., Hoboken, NJ, USA, 2005.

45 J. Y. Song, Y. Y. Wang and C. C. Wan, *J. Power Sources*, 1999, **77**, 183–197.

46 V. Aravindan and P. Vickraman, *Eur. Polym. J.*, 2007, **43**, 5121–5127.

47 R. Miao, B. Liu, Z. Zhu, Y. Liu, J. Li, X. Wang and Q. Li, *J. Power Sources*, 2008, **184**, 420–426.

48 A. M. Stephan, S. G. Kumar, N. G. Renganathan and M. A. Kulandainathan, *Eur. Polym. J.*, 2005, **41**, 15–21.

49 S. Ramesh and S.-C. Lu, *J. Mol. Struct.*, 2011, **994**, 403–409.

50 C. G. Wu, M. I. Lu and H. J. Chuang, *Polymer*, 2005, **46**, 5929–5938.

51 E. Marchante, N. Crivillers, M. Buhl, J. Veciana and M. Mas-Torrent, *Angew. Chem. Int. Ed.*, 2016, **55**, 368–372.

52 S. K. Dey, Y.-T. Long, S. Chowdhury, T. C. Sutherland, H. S. Mandal and H.-B. Kraatz, *Langmuir*, 2007, **23**, 6475–6477.

53 Y.-P. Kim, E. Oh, Y.-H. Oh, D. W. Moon, T. G. Lee and H.-S. Kim, *Angew. Chem. Int. Ed.*, 2007, **46**, 6816–6819.

54 Q. W. Sun, K. Murase, T. Ichii and H. Sugimura, *J. Electroanal. Chem.*, 2010, **643**, 58–66.

55 A. Bard and I. Rubinstein, in *Electroanalytical chemistry*, eds. A. J. Bard and I. Rubinstein, Marcel Dekker, Inc, New York, NY, 1976, p. 277.

56 C. A. Nijhuis, W. F. Reus and G. M. Whitesides, *J. Am. Chem. Soc.*, 2009, **131**, 17814–17827.

57 E. Katz, O. Lioubashevsky and I. Willner, *J. Am. Chem. Soc.*, 2004, **126**, 15520–32.

58 T. M. Nahir and E. F. Bowden, *Langmuir*, 2002, **18**, 5283–5286.

59 C. R. Mariappan, T. P. Heins and B. Roling, *Solid State Ionics*, 2010, **181**, 859–863.

60 T. Pajkossy, *J. Electroanal. Chem.*, 1994, **364**, 111–125.

61 E. Boubour and R. B. Lennox, *J. Phys. Chem. B*, 2000, **104**, 9004–9010.

62 E. Boubour and R. B. Lennox, *Langmuir*, 2000, **16**, 4222–4228.

63 K. H. Lee, M. S. Kang, S. Zhang, Y. Gu, T. P. Lodge and C. D. Frisbie, *Adv. Mater.*, 2012, **24**, 4457–4462.

64 T. Moumene, E. H. Belarbi, B. Haddad, D. Villemin, O. Abbas, B. Khelifa and S. Bresson, *J. Mol. Struct.*, 2014, **1065–1066**, 86–92.

65 X. Tian and X. Jiang, *J. Hazard. Mater.*, 2008, **153**, 128–135.

66 Shalu, S. K. Chaurasia, R. K. Singh and S. Chandra, *J. Phys. Chem. B*, 2013, **117**, 897–906.

67 K. H. Lee, S. Zhang, T. P. Lodge and C. D. Frisbie, *J. Phys. Chem. B*, 2011, **115**, 3315–3321.

68 S. Zhang, K. H. Lee, C. D. Frisbie and T. P. Lodge, *Macromolecules*, 2011, **44**, 940–949.

69 J. R. Heath, J. F. Stoddart and R. S. Williams, *Science*, 2004, **303**, 1136a–1136.

70 N. Fuentes, A. Martín-Lasanta, L. Álvarez de Cienfuegos, M. Ribagorda, A. Parra and J. M. Cuerva, *Nanoscale*, 2011, **3**, 4003-4014.

71 F. Meng, Y.-M. Hervault, Q. Shao, B. Hu, L. Norel, S. Rigaut and X. Chen, *Nat. Commun.*, 2014, **5**, 3023-3031.

72 M. Mas-Torrent, C. Rovira and J. Veciana, *Adv. Mater.*, 2013, **25**, 462–468.

73 J. Casado-Montenegro, M. Mas-Torrent, F. Otón, N. Crivillers, J. Veciana and C. Rovira, *Chem. Commun.*, 2013, **49**, 8084–8086.

74 K. M. Roth, J. S. Lindsey, D. F. Bocian and W. G. Kuhr, *Langmuir*, 2002, **18**, 4030–4040.

75 C. Simão, M. Mas-Torrent, J. Casado-Montenegro, F. Otón, J. Veciana and C. Rovira, *J. Am. Chem. Soc.*, 2011, **133**, 13256–13259.

76 L. Wei, K. Padmaja, W. J. Youngblood, A. B. Lysenko, J. S. Lindsey and D. F. Bocian, *J. Org. Chem.*, 2004, **69**, 1461–1469.

77 P. S. Guin, S. Das and P. C. Mandal, *Int. J. Electrochem. Sci.*, 2008, **3**, 1016–1028.

78 J. Casado-Montenegro, E. Marchante, N. Crivillers, C. Rovira and M. Mas-Torrent, *ChemPhysChem*, 2016, **17**, 1810–1814.

79 C. A. Hacker, J. D. Batteas, J. C. Garno, M. Marquez, C. A. Richter, L. J. Richter, R. D. van Zee and C. D. Zangmeister, *Langmuir*, 2004, **20**, 6195–6205.

80 M. Nagata, M. Kondo, Y. Suemori, T. Ochiai, T. Dewa, T. Ohtsuka and M. Nango, *Colloids Surfaces B Biointerfaces*, 2008, **64**, 16–21.

81 S. Ernst, L. Aldous and R. G. Compton, *Chem. Phys. Lett.*, 2011, **511**, 461–465.

82 V. A. Nikitina, R. R. Nazmutdinov and G. A. Tsirlina, *J. Phys. Chem. B*, 2011, **115**, 668–677.

83 C. M. Woodbridge, D. L. Pugmire, R. C. Johnson, N. M. Boag and M. A. Langell, *J. Phys. Chem. B*, 2000, **104**, 3085–3093.

84 G. Cooke, F. M. . Duclairoir, V. M. Rotello and J. F. Stoddart, *Tetrahedron Lett.*, 2000, **41**, 8163–8166.

85 M. Á. Herranz, L. Yu, N. Martín and L. Echegoyen, *J. Org. Chem.*, 2003, **68**, 8379–8385.

86 P. Daum and R. W. Murray, *J. Electroanal. Chem. Interfacial Electrochem.*, 1979, **103**, 289–294.

87 M. Lyons, in *Electroanalytical Chemistry*, eds. A. J. Bard and I. Rubisnstein, Marcel Dekker, Inc, New York, NY, 2014, p. 110.

88 Y. Yokota, A. Miyazaki, K. I. Fukui, T. Enoki, K. Tamada and M. Hara, *J. Phys. Chem. B*, 2006, **110**, 20401–20408.

89 P.-Y. Blanchard, O. Alévêque, S. Boisard, C. Gautier, A. El-Ghayoury, F. Le Derf, T. Breton and E. Levillain, *Phys. Chem. Chem. Phys.*, 2011, **13**, 2118–2120.

90 E. Barsoukov and J. R. Macdonald, *Impedance Spectroscopy: Theory, Experiment, and Applications*, Wiley-Interscience, New Jersey, 2005.

91 Y. Guo, J. Zhao, X. Yin, X. Gao and Y. Tian, *J. Phys. Chem. C*, 2008, **112**, 6013–6021.

92 R. E. Ruther, Q. Cui and R. J. Hamers, *J. Am. Chem. Soc.*, 2013, **135**, 5751–5761.

93 M. Drüschler, N. Borisenko, J. Wallauer, C. Winter, B. Huber, F. Endres and B. Roling, *Phys. Chem. Chem. Phys.*, 2012, **14**, 5090-5099.

94 Z. Kerner and T. Pajkossy, *Electrochim. Acta*, 2000, **46**, 207–211.

95 V. F.Lvovich, *Impedance spectroscopy application to electrochemical and dielectric phenomena*, Wiley, 2012.

96 M.-J. Lee, C. B. Lee, D. Lee, S. R. Lee, M. Chang, J. H. Hur, Y.-B. Kim, C.-J. Kim, D. H. Seo, S. Seo, U.-I. Chung, I.-K. Yoo and K. Kim, *Nat. Mater.*, 2011, **10**, 625–630.

97 R. Waser, R. Dittmann, C. Staikov and K. Szot, *Adv. Mater.*, 2009, **21**, 2632–2663.

98 T. Chattopadhyay, J. N. Roy and A. K. Chakraborty, *Opt. Commun.*, 2009, **282**, 1287–1293.

Chapter 4

Electron transfer constant rates in PTM_n-SAMs determined by Electrochemical Impedance Spectroscopy (EIS)

CHAPTER 4. Electron transfer constant rates in PTM$_n$-SAMs determined by electrochemical impedance spectroscopy (EIS)

4.1 Introduction

Nowadays, the design of molecular systems for Molecular Electronics requires a fundamental understanding in important topics, including the mechanism of charge transfer from the electrodes to the molecules, the transport through the molecules, and the influence of the nature of molecule-electrode contact. Electron transfer (ET) occurs when an electron relocates from an atom or molecule to another such chemical entity.[1] ET is a mechanistic description of a redox reaction, wherein the oxidation state of reactant and product changes. There are several classes of electron transfer, depending on whether the reduction/oxidation is operated by a chemical agent or by an electrode:[2]

- <u>Homogeneous electron transfer</u>: the electron transfer event takes place through a reducing/oxidising agent (redox reaction in a homogeneous phase).
- <u>Heterogeneous electron transfer</u>: an electron moves between chemical species and solid-state electrodes (redox reaction in a heterogeneous phase). Theories addressing heterogeneous electron transfer have applications in electrochemistry and the design of solar cells.

Commonly, oxidation-reduction reactions in a homogenous phase are classified as:

- <u>Inner-sphere electron transfer</u>:[3] the ET proceeds via a covalent linkage between the oxidant and reductant reactants. A ligand bridges the two redox centers during the ET event.

Inner-sphere ET is usually used to describe reactions involving transition metal complexes, and examples of common bridging ligands are halides and pseudohalides such as hydroxide and thiocyanate. Prior to ET, the bridged complex must form, and such processes are often highly reversible. ET occurs through the bridge once it is established (Figure 4.1.left). This bridge can be permanent, and in this case the electron transfer event is termed intramolecular electron transfer. More commonly, however, the covalent linkage is transitory, forming just prior to the

ET and then disconnecting following the ET event. In such cases, the electron transfer is termed intermolecular electron transfer.

- Outer-sphere electron transfer:[4] the ET event occurs between chemical species that remain separate and intact before, during and after the ET event. Because the participating redox centers are not linked via any bridge during the ET process, the electron "hops" through space from the reducing center to the acceptor (Figure 4.1.right). Outer sphere electron transfer can occur between different chemical species (also considered as homogeneous electron transfer) or between identical chemical species that differ only in their oxidation state. The later process is termed self-exchange.

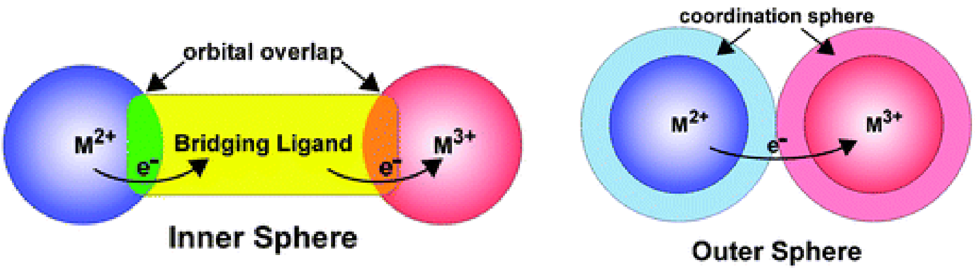

Figure 4.1 Mechanisms of electron transfer in molecular systems.[5]

The first generally accepted theory of ET was developed by Rudolph A. Marcus to explain the rate at which an electron can move or jump from one electron donor to another electron acceptor.[6] It was originally formulated outer-sphere electron transfer reactions, in which the two chemical species only change in their charge with an electron jumping, but do not undergo large structural changes. Later, it was extended to include inner-sphere electron transfer contributions, in which a change of distances or geometry in the solvation or coordination shells of the two chemical species is taken into account.[7]

The original classical Marcus theory for outer-sphere electron transfer reactions demonstrates the importance of the solvent and leads the way to the calculation of the Gibbs free energy of activation, using the polarization properties of the solvent, the size of the reactants, the transfer distance and the Gibbs free energy (ΔG_0) of the redox reaction. The most startling result of Marcus theory was the "inverted region": whereas the reaction rates usually become higher with increasing exergonicity of the reaction, electron transfer should become slower in the very negative ΔG_0 domain (Figure 4.2).

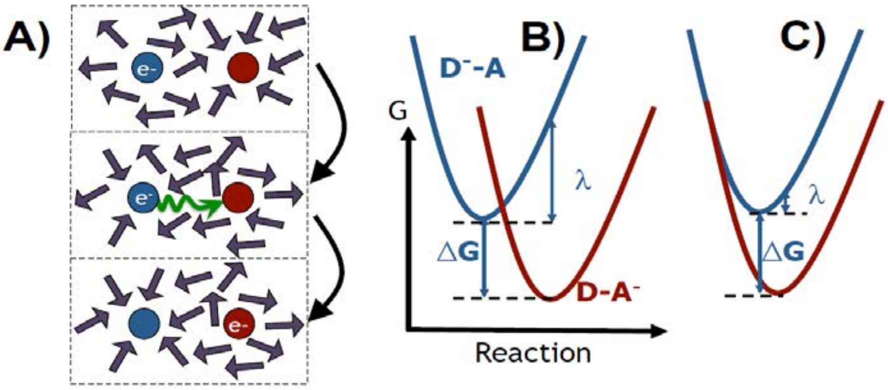

Figure 4.2 A) In solution, the electron transfer reaction is dominated by solvent reorganization. The free energy landscape can be characterized by the driving force (ΔG), measuring the energy released, and reorganization energy (λ), measuring the structural relaxation energy. B) If $\Delta G < \lambda$ the reaction is in the normal regime and the rate increases with ΔG, but C) if $\Delta G > \lambda$ the reaction is inverted and the rate decreases with increasing ΔG.[8]

ET within and between molecules, such as donor-acceptor (D-A) molecules and biological reaction centers, has been a very active research topic for many years. However, the interest has recently been more focused in studying the molecular conductance in the solid phase. Therefore, single molecule junctions, which are considered model interfaces between single organic molecules connected to macroscopic metallic electrodes, have been used as platforms for developing the fundamental understanding needed in this topic. Since the mid-nineties, molecular junctions made from either single molecules or a collection of parallel, oriented molecules (i.e., SAMs) have shown rectification,[9] negative differential resistance,[10] conductance switching,[11] and bistable memory behavior.[12]

4.1.1 Correlation between electrical properties and chemical structure

An approach to understanding the mechanism of electron transfer through organic compounds is to correlate the ET rates with the molecular structure of the matter through which the electrons move. Investigations of ET processes have largely focused on the rates of transfer in solution between donor and acceptor species, either as separated entities or as separate sites of larger molecules.[13,14]

The most extensively used experimental approach for chemists are those that have examined the rates of electron transfer using molecular systems in solution, Donor–Bridge–Acceptor systems, where the donor (D) and acceptor (A) are covalently linked through a molecular bridge (B). Figure 4.3.a sketches a D–B–A system. The processes of electron transfer from the donor to the acceptor site across the molecular bridge can be monitored in solution by time-resolved photophysical techniques and have provided a substantial body of information about the relation between rates of electron transfer and molecular structure. In particular, it has underlined the role of the chemical structure of the bridge in facilitating electron transfer from D to A.

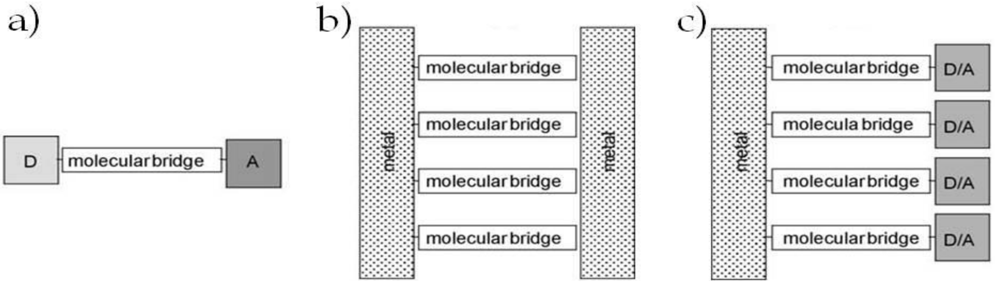

Figure 4.3 Different experimental approaches used to measure and compare electron transfer rates.[15]

Figure 4.3.b represents a solid state metal–SAM–metal junction schematically. A molecular junction can be interpreted as a logical extension of D-B-A molecules, in which both D and A are conductors, usually metals. In this system, an array of molecules bridges two metal surfaces, and the rates of electron transfer are measured as current density vs the applied potential, also considering the thickness of organic layers sandwiched between the electrodes of the junction.[16] The metal–molecule–metal junctions offer the advantage that it is, in principle, possible to bring the energy of the Fermi levels of the electrodes in resonance with the energy of the LUMO - lowest unoccupied molecular orbital (or HOMO - highest occupied molecular orbital) of the molecule by simply increasing the voltage applied to the electrodes.

The incorporation of redox sites in molecular bridges is particularly suitable for studying this kind of effects. This system, represented in Figure 4.3.c, is made of a molecular bridge, appropriately anchored to the metal surface, terminating with an electroactive group (D/A). Because of their well-defined, easy to reach, tuneable energy states, redox centers have been extensively used for designing molecular systems mimicking electronic functions and for basic electron transfer studies. In such an arrangement, the use of fast electrochemical techniques can lead to the determination of heterogeneous electron transfer rates from/to the metal surface to/from the electroactive group across the molecular wire.

The extensive literature describing the D-B-A systems in solution (Figure 4.3.a)[17–20] indicates that the rate of electron transfer (k_{ET}) generally depends exponentially on the distance between D and A, according to the following expression:

$$k_{ET} = k_0 \cdot exp(-\beta d) \qquad \text{(Eq. 4.1)}$$

in which k_0 is a pre-exponential factor, and β is a structure-dependent attenuation factor that describes the decay of electronic coupling between D and A as the distance separating them, d (the length of the bridge), increases. The value of the attenuation factor, β, depends strongly on the electronic structure of the molecule.

SAMs on metal surfaces provide a different approach to the measurements of rates of electron transfer as a function of distance. A redox active center tethered to the SAMs can be separated from the surface of the electrode by increasing distances using organic synthesis and self-assembly. Rates of electron transfer measured by this approach also follow the above relation. Values of β determined by this approach have been reported for alkanethiols,[21-23] and for phenylene–ethynylene oligomers[24] and other conjugated molecules.[25]

4.1.2 Charge Transfer (CT) mechanisms in self-assembled monolayers (SAMs)

According to contemporary theoretical models[26-30] and experimental studies,[31-37] heterogeneous charge transfer mechanism may display two different intrinsic mechanisms: adiabatic (solvent friction) – at short distances, and non-adiabatic (tunnelling) – at long distances, as well as intermediate regimes. In all cases the unimolecular rate constant (k_{ET}) of charge transfer processes can be presented by the following expression:[38]

$$k_{ET} = \frac{(H_{if})^2}{\hbar}\frac{\rho_m}{1+g}\left(\frac{\pi^3 RT}{\lambda}\right)^{1/2} exp\left(-\frac{\Delta G_a}{RT}\right) \qquad \text{(Eq. 4.2)}$$

where H_{if} is electronic coupling matrix element between the electrode and redox couple, ρ_m is the density of electronic states in the metal (electrode), λ is the reorganization free energy, ΔG_a is the activation free energy, R is the gas constant and T the absolute temperature. Here g is adiabaticity criterion which acts as a control parameter for the realization of either adiabatic (g >> 1), or non-adiabatic (g << 1) charge transfer mechanisms and turnover between them.

The adiabaticity criterion, g, is given by the following expression:[27,30,38,39]

$$g = \frac{\pi^3 RT\left(H_{if}\right)^2 \rho_m}{\hbar v_{eff} \lambda} \qquad \text{(Eq. 4.3)}$$

where the effective frequency ν_{eff} is related to a single or several relaxation processes in the vicinity of the reaction zone that are intrinsically coupled to electron transfer. As one can see from the expression above, realization and turnover between two extreme charge transfer mechanisms depends on the interplay between the values of H_{if} and λ. Consequently, at $g << 1$ and $g >> 1$ one arrives to the different expressions for the intrinsic rate constant, with the following phenomenological extensions. The non-adiabatic (tunnelling) charge transfer mechanism[40,41] predicts the exponential decay of the charge-transfer rate constant with the electron-transfer distance d_e:

$$k_{et} \propto exp\left(-\beta\left(d_e - d_0\right)\right) \qquad \text{(Eq. 4.4)}$$

where d_0 is a minimal electron donor-acceptor distance and β is a decay parameter (similar to the attenuation factor presented in D-B-A solution systems) whose value depends on the intervening atomic and molecular structure.[42] The observation of an exponential distance dependence for a given reaction series provides strong evidence for the non-adiabatic (tunnelling) mechanism.

An alternative description of the k_{ET} is required when the electronic interaction between the electron donor and electron acceptor is large enough and is referred to as the adiabatic limit. In this limit, the rate constant is no longer controlled by the magnitude of the electronic coupling but rather by the frictional coupling between the changing charge distribution of the reactants and the polarization of the surrounding medium. This frictional coupling is most often characterized by a characteristic relaxation time of the medium τ_L or the viscosity η of the medium. Phenomenological and theoretical models, based on the Kramers' treatment,[43] have been used to treat k_{ET} in this limit. When the frictional coupling to the medium is very strong, the rate constant decreases as $1/\tau_L$ or $1/\eta$. Empirically, a power law form is often found to describe the friction dependence of the rate constant; for example: $k_{et} \propto \eta^{-\delta}$, where δ is an "empirical" parameter with typical values within the range $0 < \delta \leq 1$.[31] Moreover, this dependence is stronger for faster reactions.[44] For other couples the solvent affects only the activation barrier[45–47] and the rate constant is proportional to the Pekar factor $\gamma = [(1/\varepsilon_{op}) - (1/\varepsilon_s)]$ where ε_{op} and ε_s are the optical and static electrical permittivity of a solvent, respectively.

A simplistic determination of the influence of the solvent dynamics involves plotting the logarithm of the heterogeneous electron transfer rate constant measured typically at the formal potential of the redox molecule, ln (k_{ET}) vs. ln (τ_L^{-1}), for a series of solvents. This approach to determine whether solvent dynamics are important for a particular electron transfer reaction suffers from several shortcomings.[48] The method does not account for the other ways the solvent can influence the observed electron transfer rate. A change in the solvent can affect both the transmission coefficient as well as the partition coefficient by changing the distance of closest approach of the solvated redox center to the electrode surface. The double-layer structure of the electrode and the extent of ion pairing within the solution can also be a function of the solvent. Each of these effects can induce changes in the measured heterogeneous electron transfer rates as the solvent is changed. These artefacts can be minimized by selecting redox molecules with sufficient electronic coupling to the electrode to ensure an adiabatic electron transfer in all the solvents studied. Ideally, the redox molecule should be initially neutral to minimize the effect of changes in the electrode double layer.[48] Changes in the ion pairing of the redox site can be minimized by employing low concentrations of the electrolyte.

Experimentally, adiabatic and non-adiabatic charge transfer mechanisms, and gradual turnover between them, were demonstrated by Khoshtariya et al.[31,32] using nanodevices made of electrode-deposited self-assembled monolayer films of variable thickness and the negatively charged model marker $[Fe(CN)_6]^{3-/4-}$, as well as for a biological molecule–protein cytochrome c.[33,38,49–51]

4.1.3 Electrochemical techniques to obtain k_{ET} in SAM/electrolyte interfaces

Because electron transfer occurring at electrode surfaces share many of the same characteristics of homogeneous electron transfers, electrochemical techniques can play an important role in the validation of electron transfer theories in the kinetic characterization of redox active molecules. Electrochemical techniques are particularly well suited to study long-range electronic coupling and electron transfer between metal electrodes and attached redox molecules.[52]

Redox SAMs have been extensively analysed by time-resolved techniques, such as cyclic voltammetry (CV), chronoamperometry (CA), and indirect laser-induced temperature jump (ILIT), and also frequency-resolved techniques, for instance alternating cyclic voltammetry (ACV) and electrochemical impedance spectroscopy (EIS). The time-resolved ones are well understood and applied to kinetic determinations despite the fact that the effects of SAMs polarization and iR drop contribute in an unknown and distorting manner.

CV has become a very popular method for studying electrochemical reactions. CV measurements over a number of scan rates yield data for electron transfer rate (k_{ET}) analysis of species adsorbed to an electrode using the Laviron's method.[53] However, it is subject to constraints that limit its application (i.e., for high scan rates, where the redox process becomes irreversible, and (E_a–E_c) ≥ 200/n mV). In general, Laviron's method consists on the application of the following equation to estimate α and k_{ET}:

$$E_p = E^0 + \left(\frac{RT}{\alpha nF}\right)\left[ln\left(\frac{RTk_{ET}}{\alpha nF}\right) - \ln v\right] \qquad \text{(Eq. 4.9)}$$

where α is the electron transfer coefficient, ν is the scan rate, n is the number of electrons transferred and E^0 is the formal potential. k_{ET} and α values can be obtained from the intercept and slope of the linear plot of E_p with respect to ln ν, if the value of E^0 is known. One example of the Laviron's method application is represented in Figure 4.4.a.

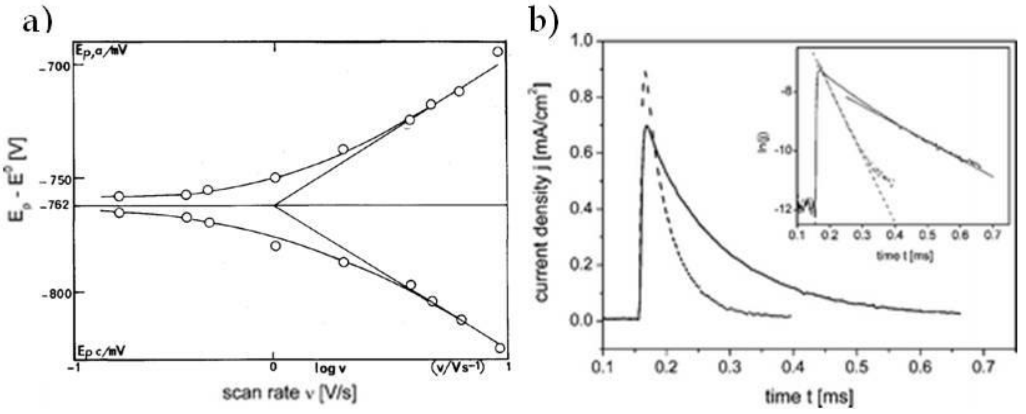

Figure 4.4 a) Peak separation ΔE_p vs. scan rate v (in log scale) for benzo(c)cinnoline.[53] b) Chronoamperometric data for a cobalt complex monolayer. Inset: logarithmic plot including linear fit curves.[54]

CA is another method commonly used to study electrochemical reactions. In a double step experiment, the potential is applied symmetrically around the formal potential of the redox center in small increments. The electron-transfer rate constants, k, can be estimated using the equation:

$$I(t) = I^0 exp(-k \cdot t) \qquad \text{(Eq. 4.10)}$$

First-order rate constants can be extracted from the slopes of the plots of ln I vs t, as it is shown in Figure 4.4.b. The k values increased with the magnitude of the overpotential. The intersection of the linear sections of the cathodic and anodic regions of the log k vs overpotential plots yields the standard electron transfer rate constant (k_{ET}) in the absence of overpotential effects.[55] This method eliminates the background currents generated by the double layer of ions that typically form during CV measurements. CV and CA are generally considered to be limited to measuring rates that are $< 10^4$ s^{-1}. An indirect laser-induced temperature jump (ILIT) technique was developed to measure rates for short bridge lengths.[56] A short (ns) laser pulse impinges onto the backside of a thin gold film electrode. The absorbed laser energy is rapidly (< 1 ps) diffused as heat throughout the gold causing a small change (2 – 4° C) in the temperature on the other side of the gold film, at the SAM/electrolyte solution interface. The interfacial equilibrium is altered and the open circuit potential of the electrode changes. However, this method requires highly specialized equipment and is not readily available.

ACV is similar to CV in that it is a potential sweep method but with an additional small perturbation of the AC signal superimposed on the potential waveform (Figure 4.5). The resulting alternating current is recorded, and the electrochemical response appears as a single peak. Using this method,[57] k_{ET} can be determined by collecting a series of AC voltammetries for a range of AC frequencies, where the ratio of the peak current (i_p) to the background current (i_b) is determined for each frequency. The values of (i_p/i_b) are plotted vs. log f, and the fitting to a Randles-like circuit model provides the double-layer capacitance (C_{dl}) and charge transfer resistance (R_{ct}), both of them needed for the determination of k_{ET}. One advantage of ACV is that very low surface coverages can be probed due to the sensitivity of the method. The disadvantages of this approach are, however, related to frequency dependent fitting inaccuracies[58] and that it does not provide information on reorganization energy or electronic coupling.

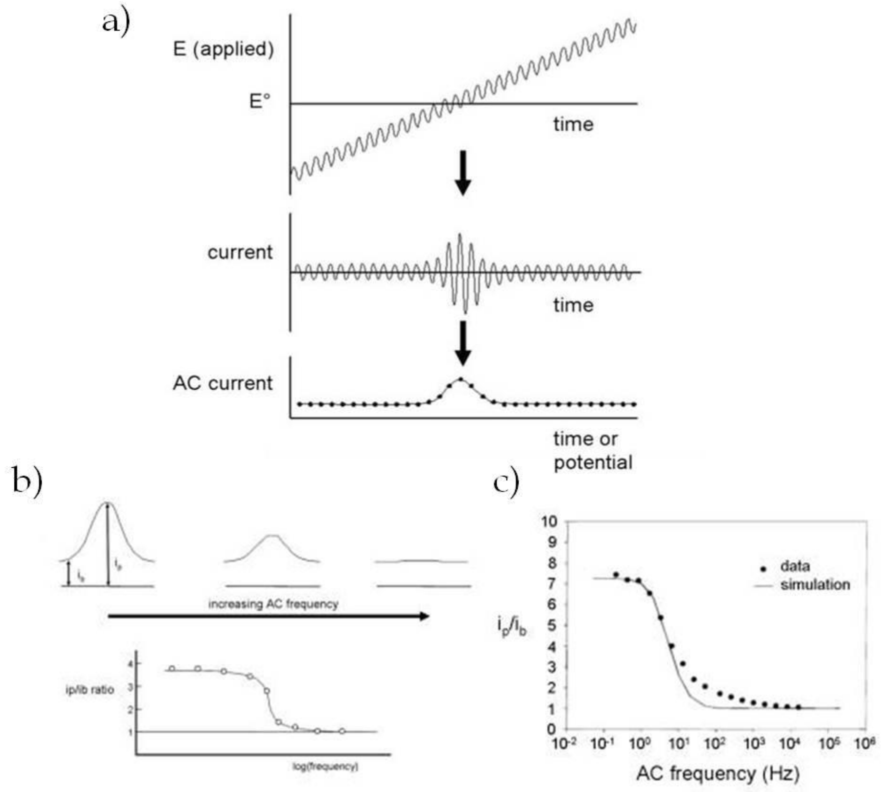

Figure 4.5 a) ACV showing E vs. time, the measured current signal vs. time, and AC current vs. potential. (b) The peak current i_p and the background current i_b are measured for a series of frequencies. The ratio i_p/i_b vs log frequency is plotted. (c) ACV data plot of i_p/i_b vs. frequency.[57]

EIS is a frequency-resolved and steady-state technique, where the frequency response of a system is sampled by measuring the impedance function, Z. The advantage of using an EIS approach is that many parameters can be measured in one experiment. Problems may arise due to the non-ideal behaviour of resistances (charge transfer) and capacitances (double layer) of the system under study or by the limitations imposed through the use of a Randles-like equivalent circuit, effects which can significantly distort derived parameter values in subsequent modelling.

Recently, Bueno et al.[59] have developed a new methodology, based on Electroactive Monolayer Capacitance Spectroscopy (EMCS), as a convenient way to represent EIS data for surface confined redox species (Figure 4.6). This method allows a clear segregation of the faradaic response of the monolayer from the capacitive background. Basically, a peak in the imaginary part of the complex capacitance (after background corrections), allows the EMCS to define electron transfer rates of the processes. This is a simple way to obtain the k_{ET}, without the need of a model fitting or any other additional correction procedure, since the background correction eliminates all the fake contribution, for instance, iR drop and double layer or monolayer polarization contributions.

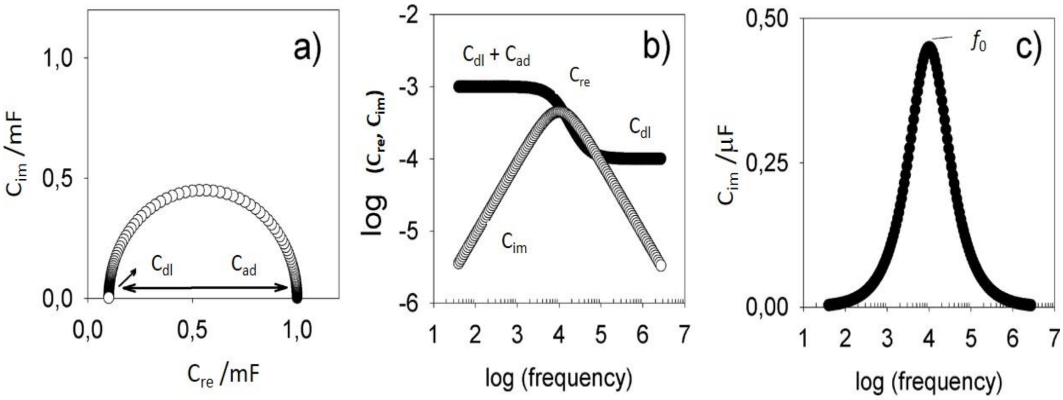

Figure 4.6 (a) Nyquist complex capacitance and (b) Bode capacitive diagrams of an ideal redox SAM process. (c) Bode capacitive plot of the imaginary component only, where the value of f_0 and k_{ET} can be obtained.[60]

The EMCS method, as mentioned in chapter 3, section 3.1.3, is based in the conversion of the complex impedance function, $Z^*(f)$, into complex capacitance $C^*(f)$ through the physical definition $Z^*(f) = 1/\ [j\cdot(2\pi f)\ C^*(f)]$ in which f is the frequency. Before this conversion, the solution resistance (R_e) is here subtracted from the spectrum by means of $Z_{re}\ (f) - R_e$.[59] Note that R_e can be clearly visualized from the beginning of the real part of Z_{re} at high frequency in Nyquist plots and can be thereafter subtracted. This is equivalent to the iR drop correction in transient techniques. A subtraction of the R_e contribution leads to a clean resolution of the R_{ct} and C_{SAM} contributions as theoretically predicted. After the iR drop correction and consecutively calculation of $C^*(f)$, it is possible to observe the faradaic response in the capacitive domain affected only by double layer and monolayer capacitance in parallel to the monolayer dielectric polarization process. The removal of SAM polarization contributions consists in the subtraction of the non-faradaic C_{im}^{corr} from the faradaic one, as is represented in Figure 4.7. The subtraction of these two responses gives a capacitive spectrum in which the influence of SAM dielectric polarization (and double layer) is accounted for and then subtracted.

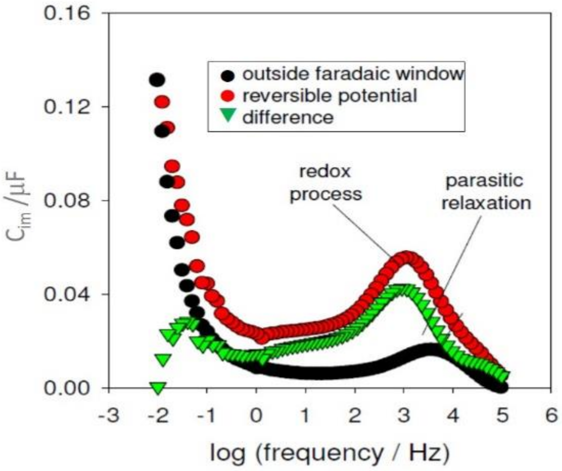

Figure 4.7 Comparison of the imaginary part of complex capacitance of a redox active film after iR drop correction. After subtraction of the black curve (the response of the film outside redox window where only the parasitic terms contribute) from the red curve, the green curve is obtained.[59]

4.2 Precedents

A family of polychlorotriphenylmethyl (PTM) radical derivatives of different molecular lengths (represented in Figure 4.8) have been recently synthesised and characterised in our group.[61] Specifically, the bridging ligand between the PTM radical and the electrode contains 8, 10 and 12 carbon atoms, in this chapter denoted as PTM_8, PTM_{10} and PTM_{12}, respectively. In collaboration with Prof. Christian A. Nijhuis (from Singapore University) this family of molecules were integrated in large area junctions formed by a SAM of the PTM molecules on gold end top contacted with a drop of a liquid metal (EGaIn). The purpose of this work was to study the temperature and chain length influence on their transport properties.

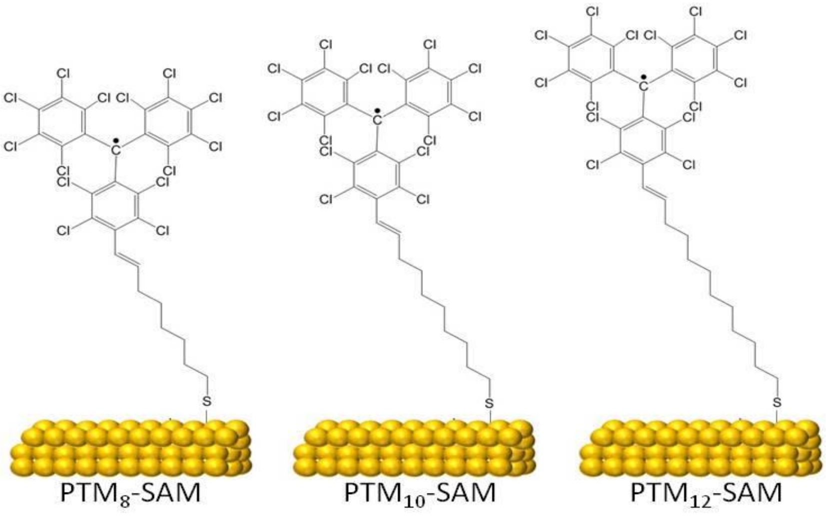

Figure 4.8 Schematic representation of radical PTM_n-SAMs with different length of alkyl chain bridge (spacer with 8, 10 and 12 carbon atoms, respectively).

In that work, the charge transport rate across PTM_n radical SAMs and EGaIn junctions was investigated (Figure 4.9.a), obtaining a length-dependent decay parameter, β, of approximately 0.89 ± 0.01 n^{-1} for PTM radical molecules (Figure 4.9.b). Such exponentially increase of the resistance with length obtained indicate a direct tunnelling across the junctions as charge transport mechanism. The same behaviour was found in their non-radical analogues.

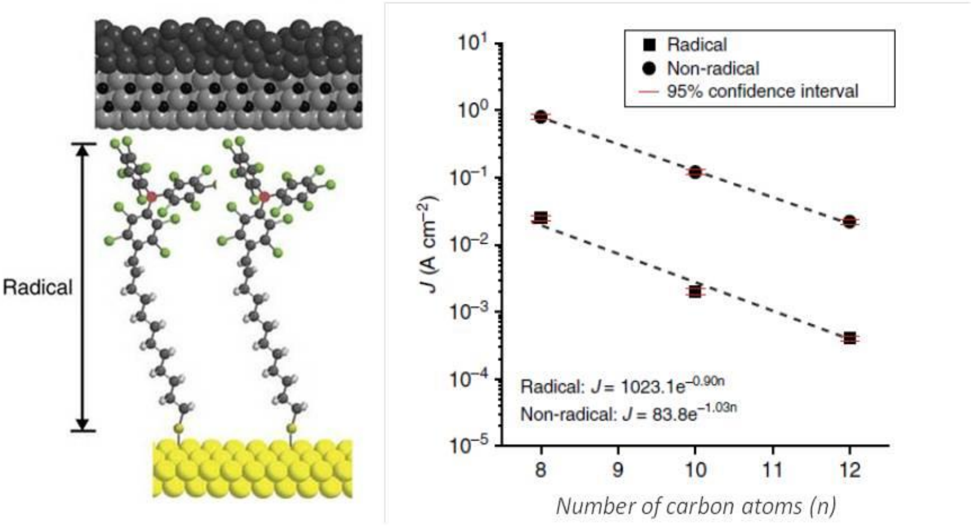

Figure 4.9 Schematic illustration of the Au-PTM-EGaIn junction and dependence of the current density measured across the junction as a function of the alkyl chain length fitted with a tunnelling model.[61]

4.3 Objectives

The aim of this chapter is to explore the transfer rates of the PTM family of molecules previously studied in molecular junctions (i.e., PTM_8, PTM_{10} and PTM_{12}) employing electrochemistry means. The electron transfer reaction involves the $PTM^{\bullet}/PTM^{-}$ redox process within monolayers of PTM radical molecules attached to gold electrode surfaces via alkanethiol bridges of variable length.

Our main interest is placed on the electrochemical response of these systems as a function of the solvent (by using different organic electrolytic environments) and the electron transfer distance (via the alkanethiol bridges of different length, schematically represented in Figure 4.10). Electroactive Monolayer Capacitance Spectroscopy (EMCS) has been selected as the tool to determine the transfer rate constants.

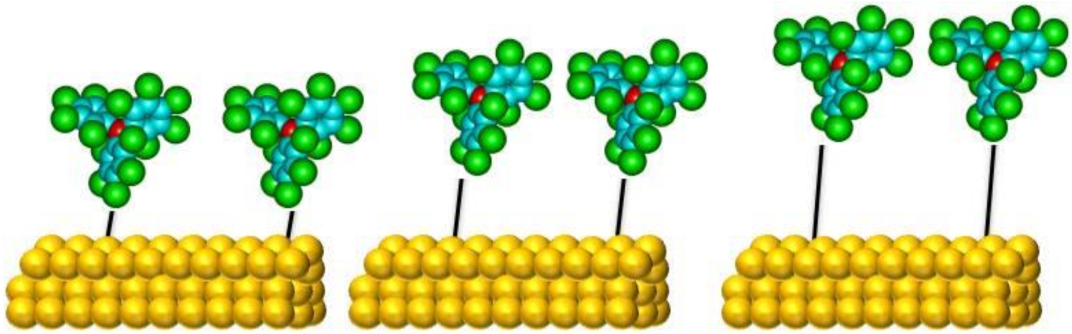

Figure 4.10 Schematic representation of a radical PTM_n-SAMs with different length, n, of alkyl chain bridge (n = 8, 10 and 12 carbon atoms of the alkyl chain bridge).

The second goal described in this chapter is to explore the impact of the electrode coverage and the intermolecular interactions between redox centers on the kinetics of the electron transfer. For that, the surface coverage has been controlled by the preparation of diluted SAMs based on the previous PTM_n radical derivatives, as electroactive compounds, and different alkanethiols, as non-electroactive molecules.

4.4 Preparation of PTM_n-SAMs and electrochemical characterization

Gold (111) substrates consisting of 300 nm Au on mica were used for the preparation of the PTM_n-SAMs. Once the substrates were cleaned (specific details explained in chapter 6, section 6.4.1), they were immersed in 1 mM solution of the perchlorotriphenylmethyl radical derivative in toluene at 40 °C for 24 h, and after that, the solutions were left at room temperature for 24 h more. SAM formation was carried out under light exclusion and under N_2 atmosphere during the total formation process. The samples were then removed from the solution and rinsed with large amounts of toluene to remove weakly adsorbed molecules and any physisorbed material and finally dried with N_2.

Solutions of 0.1 M Bu_4NPF_6 in four different organic solvents, acetonitrile (ACN), dichloromethane (DCM), tetrahydrofuran (THF) and benzonitrile (BzN), were used as supporting electrolytes. In Table 4.1 are collected their main solvent properties.

Solvent	***τ_L (ps)***	***Viscosity (cP)***	***Pekar Factor γ***	***Dipole moment D***	***Dielectric constant ε***	***polarity***
Acetonitrile	0.2	0.38	0.529	3.2	37.5	0.460
Benzonitrile	5.8	1.27	0.390	4.1	25.2	0.333
Dichloromethane	0.9	0.44	0.382	1.8	9.1	0.309
Tetrahydrofuran	1.7	0.55	0.388	1.75	7.6	0.207

Table 4.1 Properties of the solvents used in this study.[62]

The electrolytes were deoxygenated by bubbling argon for 20 min before the measurements. All electrochemical experiments were performed using the 3rd setup described in chapter 2, section 2.2, figure 2.3. The modified Au electrode substrates have been used as working electrodes and Ag and Pt wires as reference and counter electrodes, respectively.

The different PTM$_n$–SAM monolayers have been systematically studied by cyclic voltammetry (CV) and after that, by electrochemical impedance spectroscopy (EIS), using the following procedure:

1st CVs at different scan rates to determine the potential window, the formal redox potential ($E^{1/2}$), check the stability of the SAM and select the DC potentials (from the CV performed at 100 mV/s of scan rate) to apply the EIS measurements.

2nd EIS at two different DC potentials, before and in the formal redox peak potential ($E^{1/2}$), were an AC potential signal of ±5 mV (V_{rms}) is superimposed to the DC bias. The current response is recorded in the frequency range between 200 KHz and 500 mHz.

3rd Treatment of the experimental data to obtain k_{ET}. The data treatment consists of:

  a. Determination of the solution resistance (R_e): obtained from the beginning of the real part of Z_{re} at high frequency in the Nyquist plots.

  b. Correction of iR drop contributions by extracting the solution resistance from the real part of the impedance (Z_{re}^{corr}):

$$Z_{re}^{corr}(f) = Z_{re}(f) - R_e \qquad \text{(Eq. 4.11)}$$

  c. Calculation of $C_{im}^{corr}(f)$ at each applied bias potential, with the corrected impedance data ($Z_{re,c}$):

$$C_{im}^{corr}(f) = \frac{1}{2\pi f} \cdot \frac{Z_{re,c}}{(Z_{re,c}^2 + Z_{im}^2)} \cdot \frac{1}{A} \qquad \text{(Eq. 4.12)}$$

d. Removal of SAM polarization contributions: subtraction of the non-faradaic C_{im} contribution (C_{im} at 0.2 $V_{vs\ Ag(s)}$) from the faradaic one (C_{im} at redox formal potential, $E^{1/2}$):

$$C_{im,f}(f) = C^{corr}_{im,E^{1/2}}(f) - C^{corr}_{im,non-Far}(f) \qquad \text{(Eq. 4.13)}$$

4th From the plot of $C_{im,f}$ vs frequency, it can be directly extracted the frequency at which $C_{im,f}$ reaches its maximum value. This frequency value, f_0, is used to calculate the electron transfer constant rate following the expression:

$$k_{ET} = \pi \cdot f_0 \qquad \text{(Eq. 4.14)}$$

The results obtained for the PTM_8-SAMs are plotted and shown below. The plots corresponding to PTM_{10}-SAMs and PTM_{12}-SAMs are presented as supplementary information in Appendix A.

The confinement of the PTM_8 core on the electrode surface provides an electrochemical interface with two stable redox states, i.e., the radical PTM and the anion form ($PTM^•$ and PTM^-, respectively). Figure 4.11 shows the voltammetric response of the PTM_8-SAMs at different potential scan rates (ν) using a solution of Bu_4NPF_6 0.1 M in acetonitrile (Figure 4.11.a), dichloromethane (Figure 4.11.b), tetrahydrofuran (Figure 4.11.c), and benzonitrile (Figure 4.11.d).

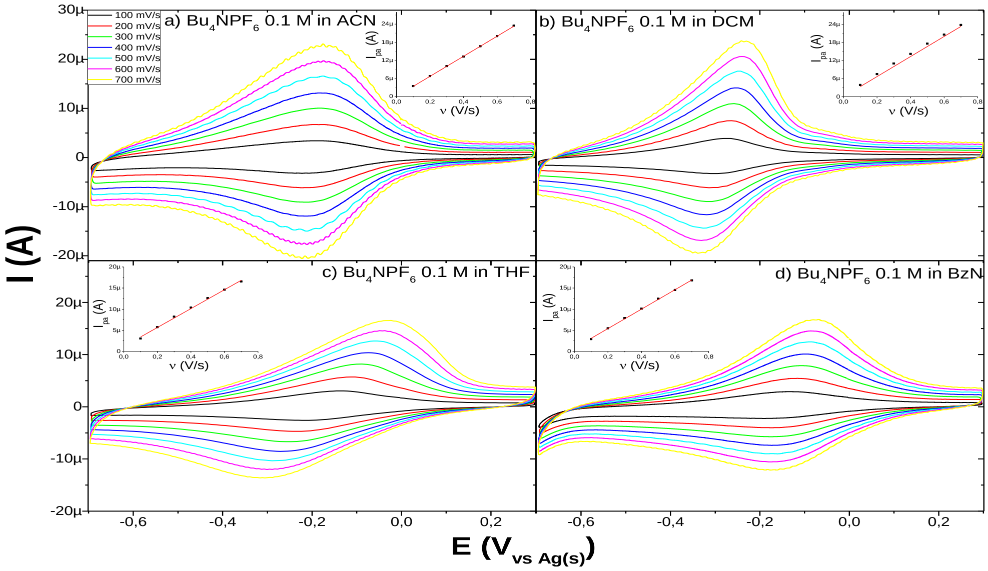

Figure 4.11 CVs at different scan rates (ν varies from 100 to 700 mV/s) for the PTM_8-SAM using Bu_4NPF_6 0.1 M as electrolyte salt in: a) acetonitrile, b) dichloromethane, c) tetrahydrofuran, and d) benzonitrile. Inset figures represent the linear variation of the anodic current peak with the scan rate ($I_{p,a}$ vs ν) for the corresponding electrolytes studied.

Expectedly, one reversible redox process corresponding to the PTM•/ PTM$^-$ is observed. The formal potentials extracted at the scan rate of 100 mV/s are $E^{1/2}$ = -0.2 V, -0.3V, -0.18 and -0.15V vs. $Ag_{(s)}$ in ACN, DCM, THF and BzN, respectively (Figure 4.12). The linear relationship observed in all the cases between $I_{p,a}$ and ν is in agreement with the presence of surface-confined redox-active molecules (see inset plots in Figure 4.11), along with the small peak-to-peak separations ($\Delta E_p = E_{anodic}-E_{cathodic}$) observed at low scan rates, $\Delta E_{p,ACN}$ = 5.4 mV, $\Delta E_{p,DCM}$ = 13.8 mV, $\Delta E_{p,THF}$ = 61.1 mV, and $\Delta E_{p,BzN}$ = 13.0 mV.[63] Only for the THF based electrolyte, ΔE_p separation is larger than expected, and this result is related to a slower electron transfer process, as it will be demonstrated below, by the EIS measurements.

The full width at half maximum (ΔE_{FWHM}) of the PTM_8-SAMs was larger than the theoretical value, that is, ΔE_{FWHM} > 90 mV (i.e., 326, 217, 274 and 283 mV, for ACN, DCM, THF and BzN, respectively). The high ΔE_{FWHM} values indicate the presence of a distribution of redox potentials, although the contribution of other factors cannot be discarded (i.e., repulsive interactions between electroactive centers[64] and double-layer effects[65]).

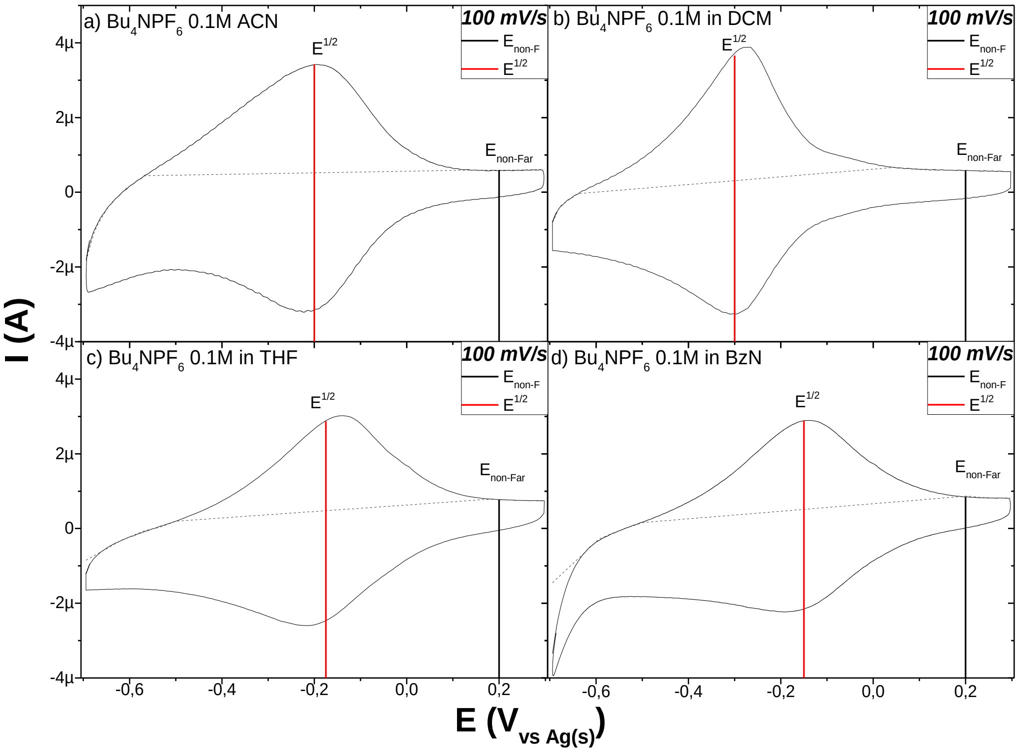

Figure 4.12 CVs of PTM_8-SAM at 100 mV/s in Bu_4NPF_6 0.1 M in: a) ACN, b) DCM, c) THF and d) BzN. Vertical lines indicate the DC bias potentials applied for the impedance experiments.

From the area under the redox peak (Figure 4.12), the PTM_8 surface coverage were estimated to be 2.0, 1.9, 1.5 and 1.5 x 10^{-10} mol·cm^{-2} in ACN, DCM, THF and BzN respectively (at 100 mV·s^{-1} of scan rate). Considering that each PTM molecule would occupy a projected area of approximately 0.67 nm^2,[66] the samples prepared give electrochemically coverages in the range of the 60 - 80% Γ_{max}.

To characterise the PTM_8–SAMs, impedance spectra were also collected, in the same experimental conditions as the ones used in the CV experiments, between 200 kHz and 500 mHz with an AC amplitude of 5 mV (peak to peak) at two different voltages: before the redox process ($E_{non\text{-}F}$, at 0.2 $V_{vs.\ Ag(s)}$), and at the redox peak potential ($E^{1/2}$) in each solvent electrolyte. The DC bias voltages selected are the ones indicated in Figure 4.12 by black and red vertical lines.

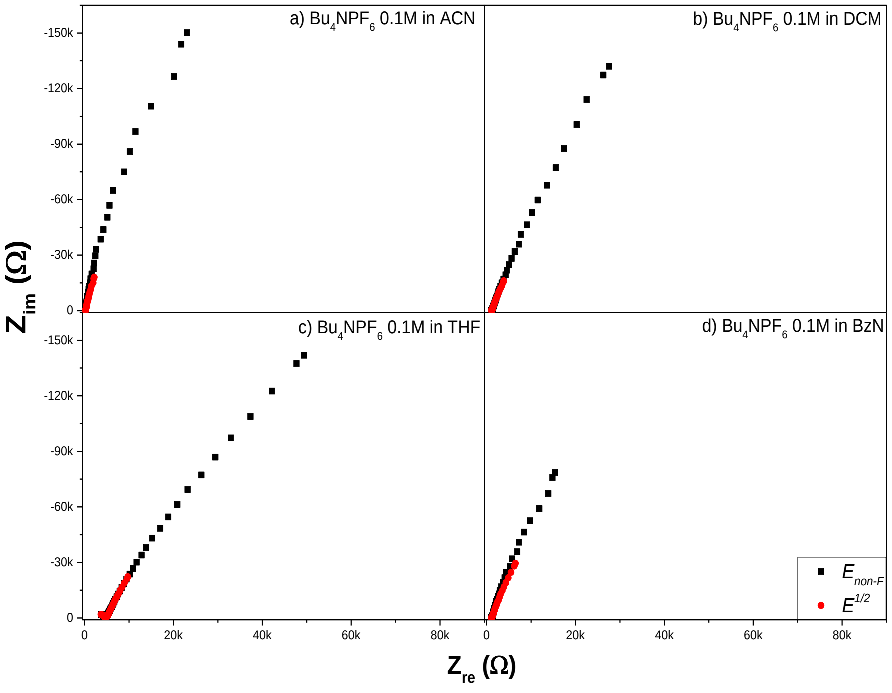

Figure 4.13 Nyquist plots for the EIS characterization of PTM_8-SAMs at two different DC bias voltages, in the non-faradaic current response (■), and at the formal redox potential (●),in Bu_4NPF_6 0.1 M in: a) acetonitrile, b) dichloromethane, c) tetrahydrofuran, and d) benzonitrile.

Nyquist and Bode plots for PTM_8-SAMs, shown in Figure 4.13 and Figure 4.14, respectively, are the standard diagrams to represent EIS measurements.[67–69] The plots corresponding to the characterization of PTM_{10}–SAM and PTM_{12}–SAM are shown in the Appendix A. In the case of surface confined molecules under an inert electrolyte, the system shows capacitor behaviour. Accordingly, the Nyquist plots of the PTM_8–SAMs are close to vertical lines parallel to the *y*-axis, with a partial deviation from theoretically ideal system (Figure 4.13).[70–74]

Similar to what it was observed with Fc-SAMs (chapter 3), the Bode magnitude plots (Figure 4.14) at the low frequency region are straight lines with slopes close to -1, and the phase angles (φ) approach -90º.[75] Generally, at higher frequencies (f>10 KHz), the phase angle is expected to be close to zero, corresponding to a resistor behaviour, as the solution resistance is controlling the process in this range.[76] However, in the present case it can be observed a slightly higher values of the phase angle, beside the variation of the impedance module plateau, that is only due to the impedance response of the reference electrode.[77]

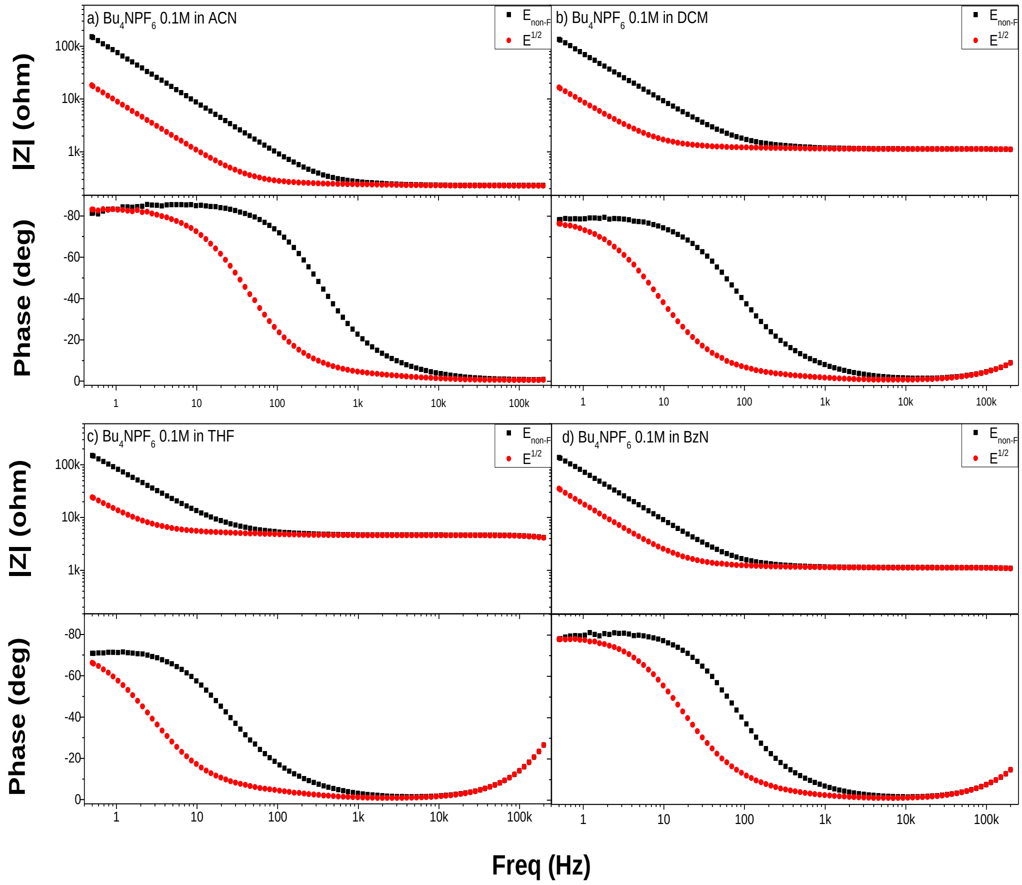

Figure 4.14 Impedance Bode plots for the EIS characterization of PTM_8-SAMs at two different DC bias voltages, in the non-faradaic current response (■), and at the formal redox potential (●),in Bu_4NPF_6 0.1 M in: a) acetonitrile, b) dichloromethane, c) tetrahydrofuran, and d) benzonitrile.

Alternatively, the data can be analysed by means of capacitance Bode plots. In fact, capacitance Cole−Cole plots, where the imaginary (C_{im}) versus the real (C_{re}) part of the capacitance are represented, provide very useful information for surface confined redox species.[70-72] Figure 4.15 clearly illustrates that different processes with different time constants are occurring depending on the applied DC potential. The small semicircle recorded at a voltage outside the redox process (i.e., 0.2 $V_{vs.\ Ag(s)}$) comes from the non-faradaic terms dominated by the resistance of the electrolyte (R_e) and the double layer capacitance (C_{dl}). In the redox window potentials faradaic contributions are also present (i.e., a pseudo-capacitance for charging the monolayer and a resistance for the electron transfer).

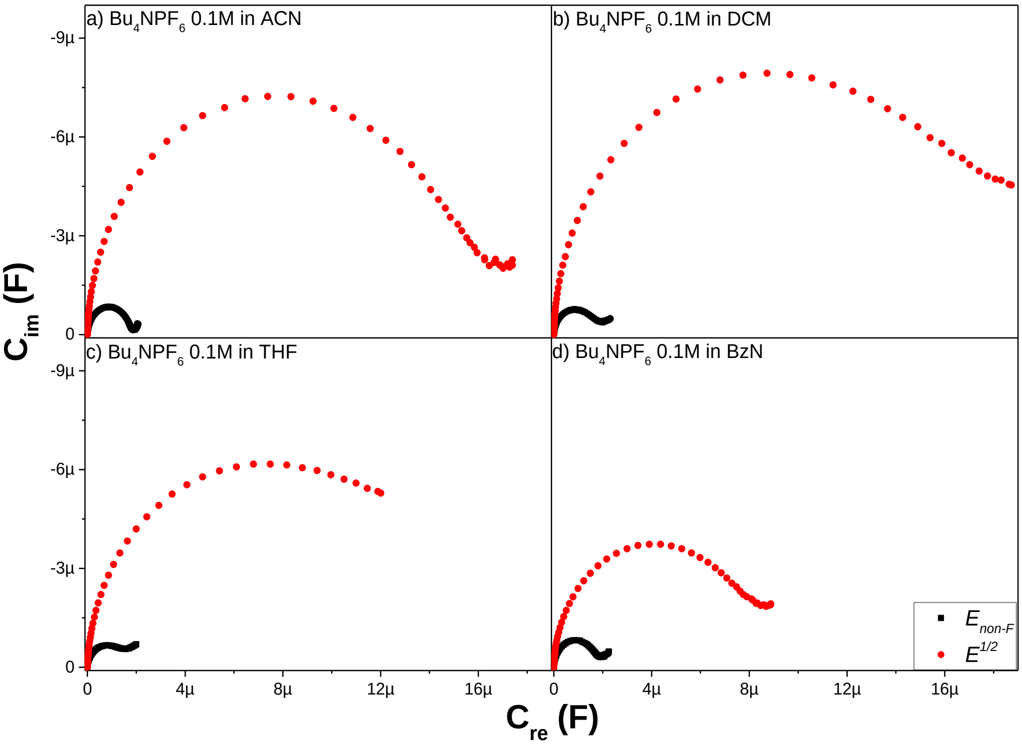

Figure 4.15 Cole-Cole plots for the EIS characterization of PTM$_8$-SAMs at non-faradaic voltage (■), and at the formal redox potential (●), in Bu$_4$NPF$_6$ 0.1 M in: a) acetonitrile, b) dichloromethane, c) tetrahydrofuran, and d) benzonitrile.

The imaginary part of the capacitance for the prepared PTM$_8$-SAMs is plotted against frequency at both DC bias voltages (non-faradaic and formal redox potential, respectively), as shown in Figure 4.16. From this data, it is possible to extract information about the kinetic parameters of the redox transfer.[59,73,74] However, first it is necessary to treat the data (as previously explained, in page 131). In this way, we can gain information exclusively on the redox processes, free of parasitic signals. Figure 4.17 shows the final response of the $C_{im,f}$. From these graphs, the rate constant for the electron transfer process (k_{ET}) have been estimated from the frequency (f_0) at the highest ordinate point using the Eq. 4.14: $k_{ET} = \pi \cdot f_0$.

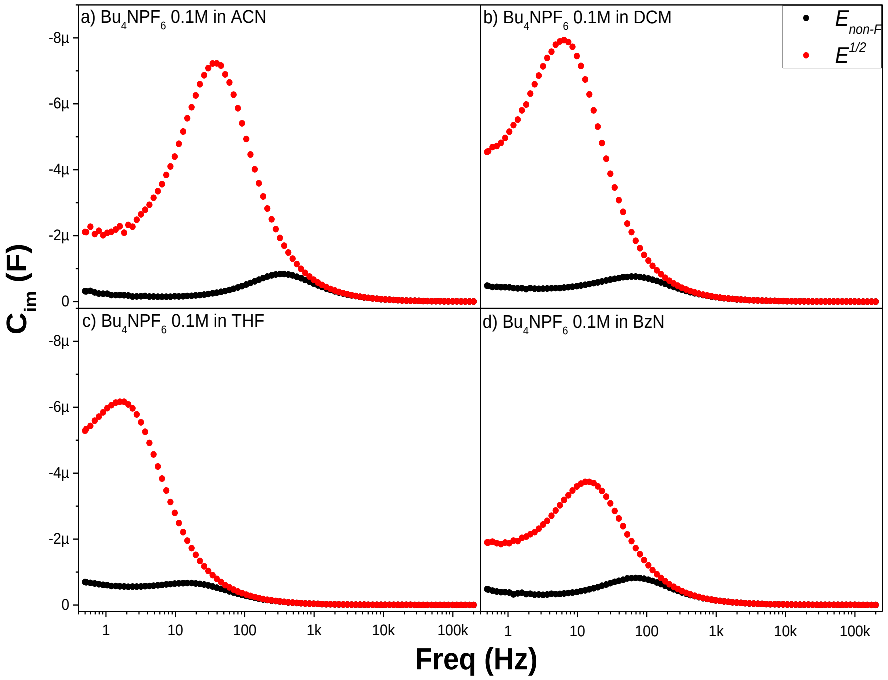

Figure 4.16 Experimental data of the imaginary part of the capacitance vs. frequency, for PTM$_8$-SAMs at two different bias voltage: non-faradaic voltage (■), and at the formal redox potential (●), in Bu$_4$NPF$_6$ 0.1 M in: a) acetonitrile, b) dichloromethane, c) tetrahydrofuran, and d) benzonitrile.

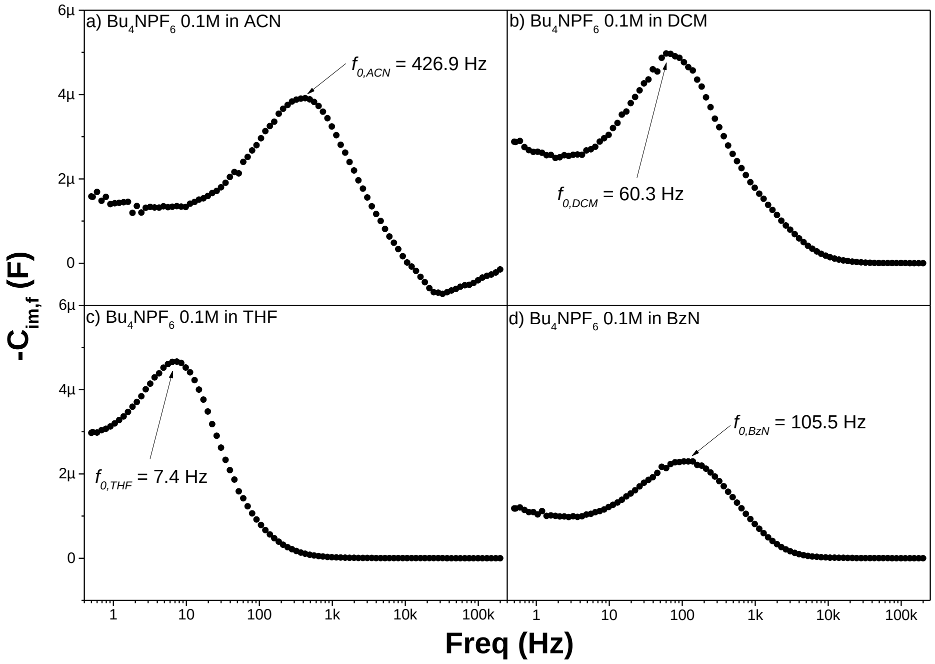

Figure 4.17 Imaginary part of the capacitance vs. frequency, for PTM$_8$-SAMs, after subtraction of the non-faradaic response, in Bu$_4$NPF$_6$ 0.1 M in: a) ACN, b) DCM, c) THF and d) BzN.

The same experiments have been repeated for an average number of 4 samples in each electrolyte system, and for each PTM molecule under study: PTM_8, PTM_{10} and PTM_{12} (see Appendix A). The average of the calculated electrochemical parameters for PTM_8, PTM_{10} and PTM_{12}, extracted from CV and EIS measurements, are shown in Table 4.2.

	Solvent	**$E^{1/2}$ ($V_{vs\ Ag(s)}$)** $\nu = 100mV/s$	**ΔE (mV)** $\nu = 100mV/s$	**ΔE_{FWHM} (V)** $\nu = 100mV/s$	**Γ (mol $\cdot$cm^{-2})**	**$^{(*)}k_{ET} = \pi f_0 (s^{-1})$**
PTM_8	ACN	-0.20	5.4	0.326	$2.0 \cdot 10^{-10}$	1674.2 (±301.0)
	BzN	-0.15	13.0	0.283	$1.5 \cdot 10^{-10}$	366.9 (±197.5)
	DCM	-0.29	13.8	0.217	$1.9 \cdot 10^{-10}$	238.9 (±69.9)
	THF	-0.17	61.1	0.274	$1.5 \cdot 10^{-10}$	24.7 (±10.1)
PTM_{10}	ACN	-0.12	20.9	0.216	$1.4 \cdot 10^{-10}$	1068.8 (±377.0)
	BzN	-0.07	4.7	0.208	$8.8 \cdot 10^{-11}$	319.6 (±93.3)
	DCM	-0.12	20.9	0.216	$1.4 \cdot 10^{-10}$	190.0 (±74.1)
	THF	-0.09	20.8	0.194	$2.9 \cdot 10^{-11}$	27.5 (±6.3)
PTM_{12}	ACN	-0.18	17.8	0.273	$2.2 \cdot 10^{-10}$	1375.3 (±423.7)
	BzN	-0.36	49.4	0.297	$9.0 \cdot 10^{-11}$	66.7 (±6.6)
	DCM	-0.25	8.3	0.169	$1.5 \cdot 10^{-10}$	285.5 (±165.7)
	THF	-0.12	26.7	0.266	$1.1 \cdot 10^{-10}$	47.4 (±15.1)

Table 4.2 Electrochemical parameters obtained from CV and EIS measurements for PTM_8-SAMs, PTM_{10}-SAMs, and PTM_{12}-SAMs. (*) Average value of k_{ET} and error for 4 samples analysed.

4.4.1 Impact of static and dynamic solvent electrolyte properties on k_{ET}

Generally, solvent molecules within a monolayer can alter the thermodynamics of electron transfer in two distinct ways: i) by the intercalation between redox centers that can insulate them from adjacent repulsive electrostatic charges, and ii) can influence the extent of ion pairing. The effect of ion pairing is closely related to the supporting electrolyte concentration. In a previous study performed by Forster and Faulkner[78] in $[Os(bpy)_2Cl(pNp)]^+$ adsorbed monolayers, they determined that k_{ET} was independent of the supporting electrolyte concentration over the range 0.1 to 1.0 M, suggesting that ion pairing is an equilibrium reaction that either precedes or follows electron transfer. Therefore, as the present study has been established at a fixed supporting electrolyte concentration of 0.1 M, the ion pairing effect can be not taken into account.

As previously mentioned, the electrochemical solvent can influence the electron transfer rate through either its static or dynamic properties because of the non-instantaneous rearrangement of the solvent dipole that may precede or follow the electron transfer process.[78] Static properties, such as dielectric constants, can alter the activation barrier for electron transfer, while the dynamic ones, such as a relaxation time, can affect the relative motion of the reactant along the reaction coordinate near the transition state.

In terms of static solvent properties, a solvent of high polarity will favour electron transfer and, generally, the rate of the electron transfer reaction is controlled by the polarity and dielectric constant of the solvent.[79,80] In this study, the k_{ET} associated with PTM_n radical SAMs have been obtained from $C_{im,f}$ vs. frequency plots, as shown in Figure 4.17. The kinetic change with polarity and dielectric constant reflects its sensitivity to the environment, as it can be observed in Figure 4.18 and Figure 4.19, respectively. The variation of k_{ET} for PTM_8, PTM_{10} and PTM_{12}, in the different solvents, follow the tendency $k_{ET,ACN} > k_{ET,BzN} > k_{ET,DCM} > k_{ET,THF}$ (see Table 4.2). Only the result extracted for PTM_{12} in benzonitrile seems to deviate from this trend. In general, the highest value of k_{ET} is obtained in ACN, as it has the highest values of polarity and dielectric constant compared to the rest of solvents used in this study (Table 4.1). The dependence of k_{ET} as a function of both static solvent properties is in agreement to the theory developed by Marcus and others.[81]

As mentioned above, in the case of PTM_{12} in benzonitrile, these behaviour is not strictly followed. It can be related to many different factors, such as the aromatic character of the solvent that might cause the high degree of reorganization.

These PTM surface confined systems are sensitive to the order or defects of the monolayer and the environmentally solvent, so it can be expected different kinetic responses in each film in a specific medium, creating specific localized dielectric polarization effects.[80,82]

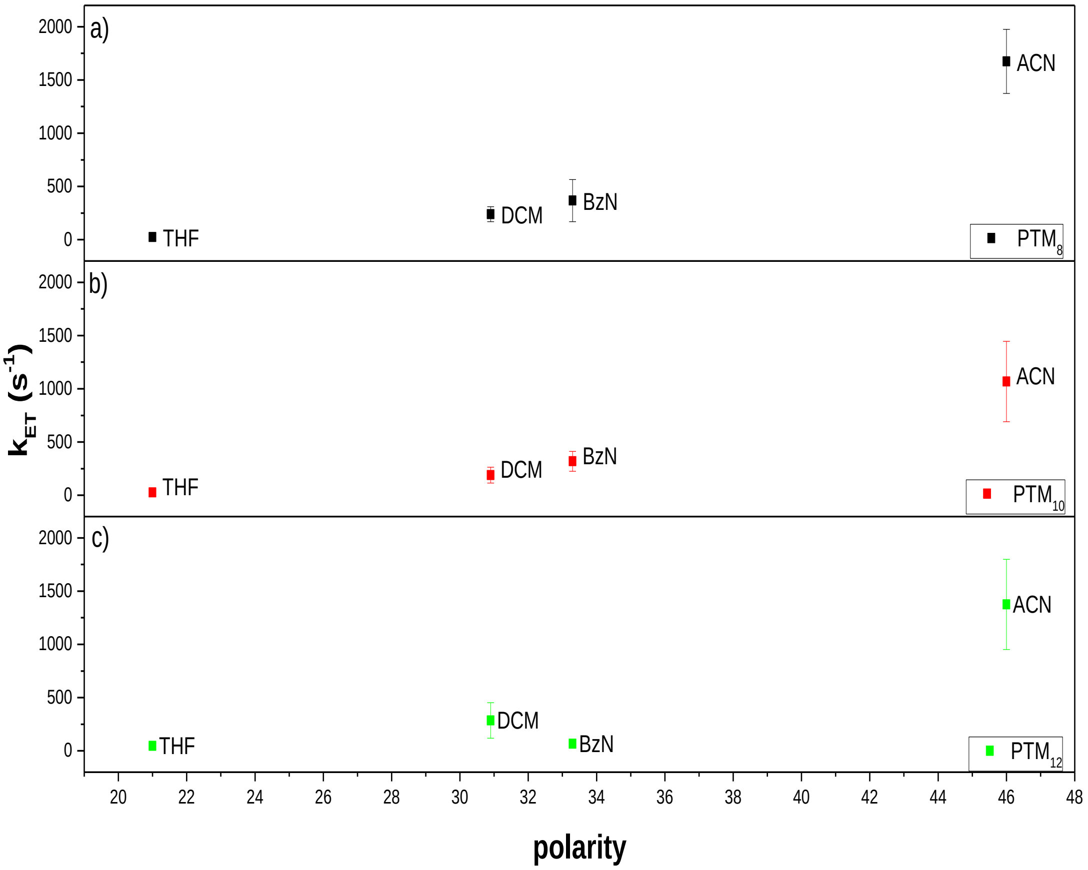

Figure 4.18 Dependence of k_{ET} for PTM_8-SAM (a), PTM_{10}-SAM (b), and PTM_{12}-SAM (c), on the polarity of the solvent.

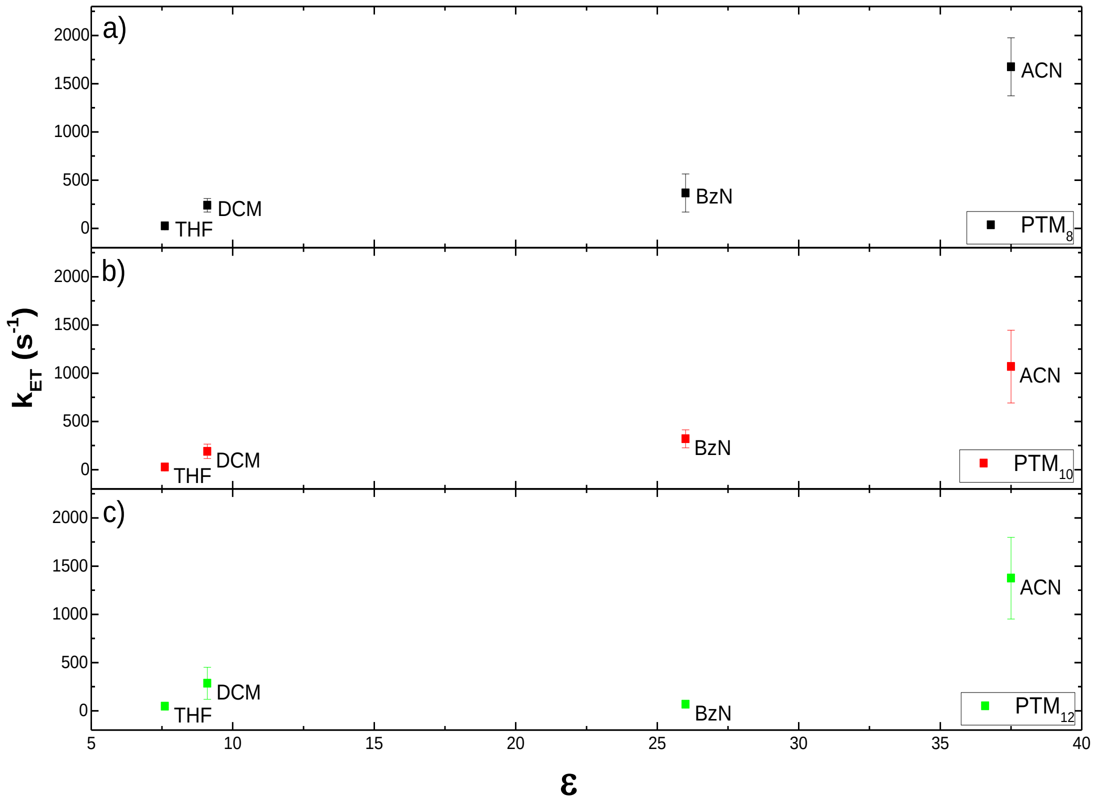

Figure 4.19 Dependence of k_{ET} for PTM$_8$-SAM (a), PTM$_{10}$-SAM (b), and PTM$_{12}$-SAM (c), on the dielectric constant (ε) of the solvent.

In terms of dynamic solvent properties, and according to the modern theory of charge-transfer processes,[28,29] in the case of strong friction coupling between the electron donor and acceptor sites, the rate constant of the intrinsic electron-transfer step could be presented as:

$$k_{et} = \frac{1}{\tau_L}\left(\frac{\Delta G_a}{4\pi RT}\right)^{1/2} exp\left(-\frac{\Delta G_a}{RT}\right) \qquad \text{(Eq. 4.15)}$$

where the parameters of the expression where defined previously (see section 4.1.2, page 121). In the simplest case, τ_L is connected with the solution viscosity by the following equation:[83]

$$\tau_L = \frac{3 \cdot V_m \cdot \eta}{RT} \qquad \text{(Eq.4.16)}$$

where V_m is the molar volume.

The results of k_{ET} vs ($1/\tau_L$), obtained for PTM$_8$, PTM$_{10}$ and PTM$_{12}$ in the four different electrolyte solvents are presented in Figure 4.20. This plot represents only a very rough guide to the role of overdamped solvent dynamics on the electron transfer process, since it neglects any solvent dependence of the activation barrier.

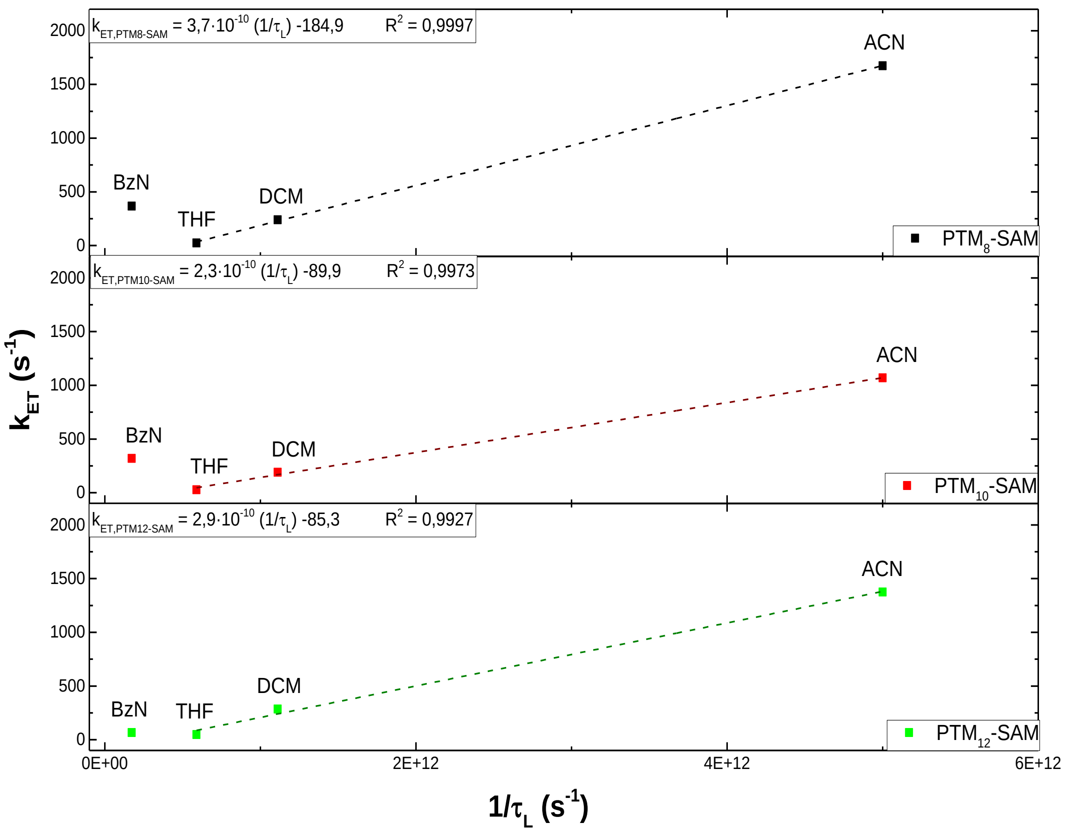

Figure 4.20 Dependence of k_{ET} for PTM_8-SAM (a), PTM_{10}-SAM (b), and PTM_{12}-SAM (c), on the longitudinal relaxation time (τ_L) of the solvent.

These results, except for the benzonitrile solvent, are in agreement with the ascription of the solvent friction mechanism. This suggests that the intrinsic electron-transfer step is strongly coupled with the relaxational motion of the environment,[28,29] being the electron transfer process sensitive to the solvent's ability to relax dynamically to accommodate the new charge placed on the redox center.[35,36] In agreement and following this dynamic solvent properties, it can be seen in Figure 4.21 the linearly correlation of k_{ET} with the inverse of the solvent viscosity, again without considering the benzonitrile results.

Therefore, in this section it can be concluded that the correlation of the rate constant with the viscosity and τ_L, for ACN, DCM and THF, is a signature for an apparent adiabatic ET (frictionally controlled) mechanism. However, when benzonitrile is used as a solvent, this tendency is not followed any more. The aromaticity of the solvent might play a crucial role on the solvatation of the molecules and, in turn, on their reorganisation. The activation barrier could be reduced in this solvent or also other transport mechanism could prevail.

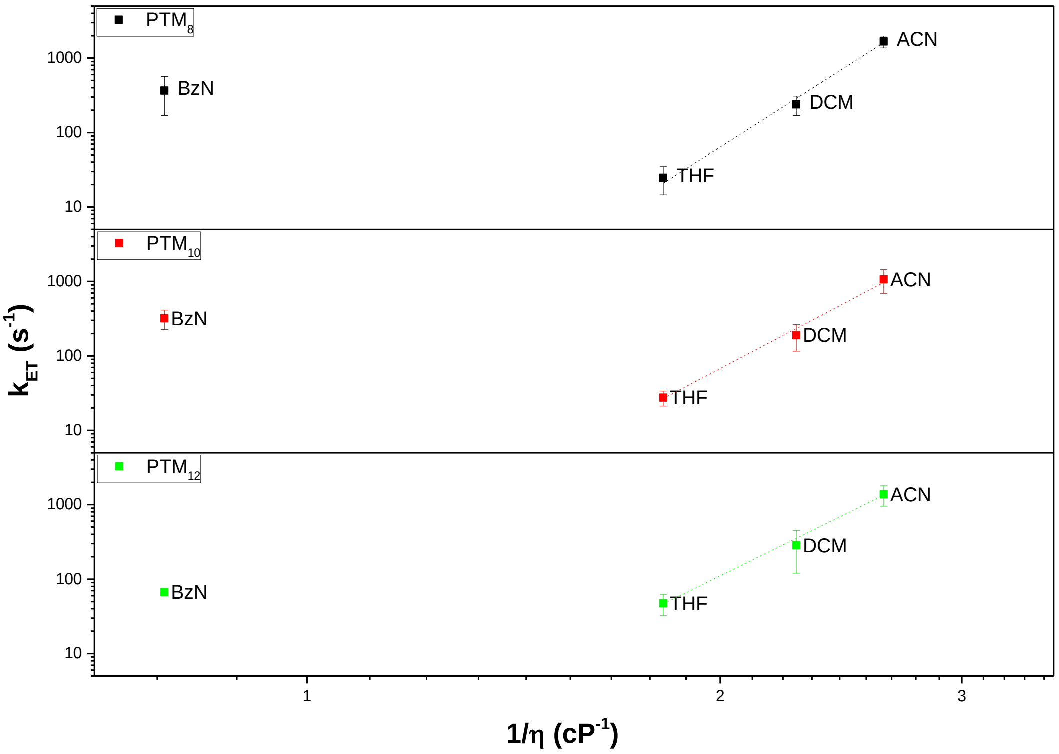

Figure 4.21 Dependence of k_{ET} for PTM$_8$-SAM (a), PTM$_{10}$-SAM (b), and PTM$_{12}$-SAM (c), on viscosity (η) of the solvent (ACN = acetonitrile, DCM = dichloromethane, THF = tetrahydrofuran, and BzN = benzonitrile)

4.4.2 Impact of the distance length (d) on k_{ET}

In the case of PTM$_n$-SAMs, the electroactive group and the electrode are considered as the donor and the acceptor group, and the length of the alkyl chain bridge as the donor-acceptor distance. The electron transfer distances explored here are approximately 12.7, 15.2 and 17.7 Å for the PTM$_8$, PTM$_{10}$ and PTM$_{12}$ monolayers, respectively. These length values are taken from the terminal sulphur atom at the gold electrode to the final bridge carbon attached to the PTM radical molecule. Thus, the distance is taken along the main axis of the bridge, without considering any tilt in the adsorbate layer.

Due to their low mass, electrons can tunnel over long distances (> 15 Å),[84,85] governed by the intervening medium as well as the nature of the donor and the acceptor.[85,86] Therefore, for the range of distances studied in this work, it was initially expected that this family of PTM radical molecules behaved following the non-adiabatic (tunnelling) charge transfer mechanism.

Figure 4.22 shows the representation of the k_{ET} values collected in Table 4.2 as a function of the chain length.

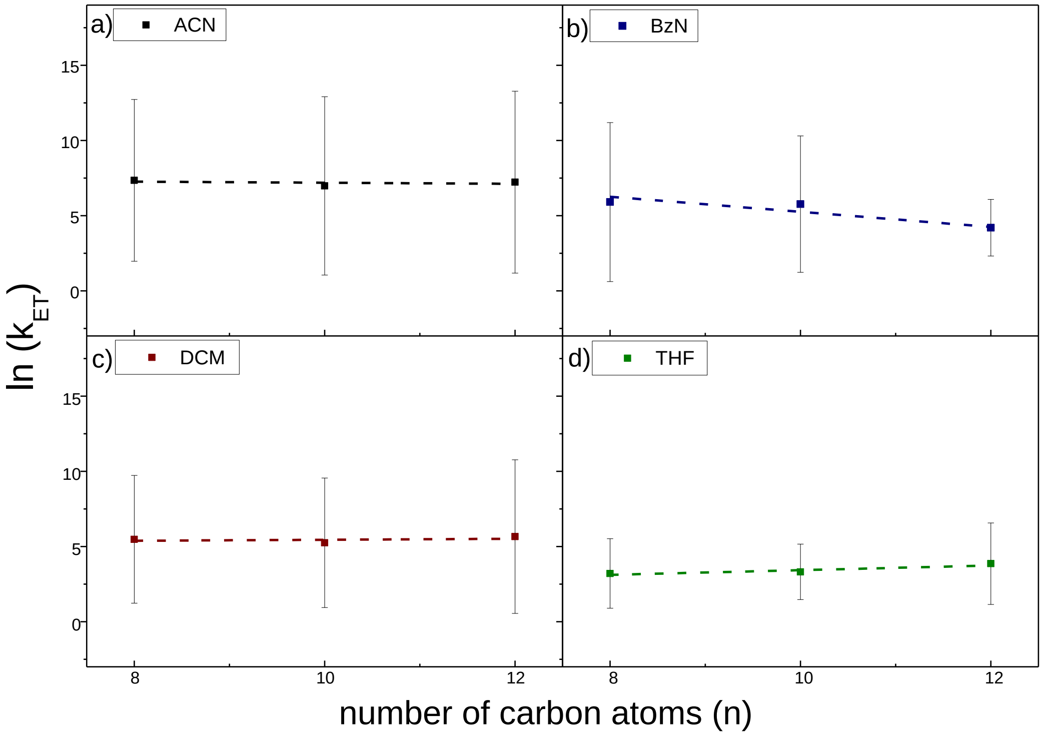

Figure 4.22 ln (k_{ET}) vs number of carbon atoms of the alkyl chain bridge, for the different solvents studied as electrolytes: acetonitrile (a), benzonitrile (b), dichloromethane (c), and tetrahydrofuran (d).

In theory, when the electron transfer process is controlled by the electronic coupling, it is expected the exponentially decay of its strength with the D-A distance, by the Eq. 4.1. A value for the tunnelling coefficient, β, can be obtained by plotting k_{ET} as a function of the length of the alkyl chain. However, the experimental values of k_{ET} obtained seem to be not highly affected by the distance. The dependence of k_{ET} in dichloromethane and acetonitrile environments are not following a constant tendency and, in tetrahydrofuran electrolyte, a modest increase of k_{ET} with the length of the alkyl chain is observed, contrary to the theoretically expected. Only in the systems analysed in benzonitrile electrolyte solvent (Figure 4.22.b), it is observed that k_{ET} slightly decreases from PTM_8 to PTM_{10}, and the diminution is more pronounced from PTM_{10} to PTM_{12}.

Comparing these results, and in concordance with the effect of the solvent properties on k_{ET} obtained before, it could be supposed that the PTM_n-SAMs are in an adiabatic regime (solvent friction coupling) for the electron transfer processes that take place in acetonitrile, dichloromethane and tetrahydrofuran electrolyte solvents and consequently, the variation of ln (k_{ET}) does not show a linear decrease with the distance. Again the exception is found when benzonitrile is used as a solvent. Here, ET process could be in line with a non-adiabatic regime (tunnelling), where the decrease of k_{ET} with the donor-acceptor distance is in agreement with a strong electronic coupling.

Comparing these results with the precedent ones obtained in molecular junctions with the absence of the solvent,[61] it can be clearly observed that the solvent environment have an important influence on the electron transfer processes, and can even modify the prevailing transport mechanisms. However, it should be also kept in mind that the SAMs in our experiments are not completely packed and they are in an electrolyte solution. Thus, the molecules can reorganise or tilt in this environment, which can be realised differently depending on the chain length of the molecule. Such effects lead to clear uncertainties on the study of the influence of k_{ET} on the distance which are not present in the solid-state devices where the molecules are less mobile.

4.5 Preparation and characterization of diluted PTM_n/C_nSH-SAMs

The structure of the PTM_n monolayers can promote lateral interactions between redox centers, which plays an important role in the electron transfer reactions. In this section, diluted SAMs of different PTM derivative molecules (PTM_n) with unsubstituted alkanethiols have been studied intensively to avoid the influence of intermolecular interactions between the electroactive molecules in the electron transfer process.

For the preparation of bi-component SAMs, the alkanethiol selected presents the same alkyl chain length as the corresponding PTM derivative molecule. That is, for the PTM_8, the binary SAMs have been prepared with CH_3-$(CH_2)_7$-SH (from now on C_8SH). Therefore, CH_3-$(CH_2)_9$-SH ($C_{10}SH$) and CH_3-$(CH_2)_{11}$-SH ($C_{12}SH$) have been employed with PTM_{10} and PTM_{12}, respectively.

The PTM/alkanethiol-SAMs were prepared from a mixed component solution (one-step) of 1 mM total thiol concentration of PTM_n and C_nSH in different ratios: 1:1, 1:2 and 1:5, respectively. The details of the PTM/alkanethiol-SAMs preparation are fully described in chapter 6, section 6.4.7. The control of the real composition was done by the estimation of the surface coverage by CV experiments through the integration of the area under the redox peak.

In this part, only solutions of 0.1 M Bu_4NPF_6 in tetrahydrofuran (THF) were used as electrolytes, which were deoxygenated with bubbling argon for 20 min before the measurements. All electrochemical experiments were performed in the 3rd setup and using the same configuration as it was previously performed with PTM_n-SAMs. The diluted PTM_n-SAMs were systematically studied by CV and EIS, using the procedure explained before (see section 4.4, page 130).

The results obtained for PTM_8/C_8SH-SAMs are plotted and shown below. The plots corresponding to $PTM_{10}/C_{10}SH$-SAMs and $PTM_{12}/C_{12}SH$-SAMs are presented as supplementary information in Appendix A. The mixed PTM_8/C_8SH-SAMs on Au substrates were initially characterised using CV techniques. Figure 4.23 shows the voltammetric response of C_8SH/PTM_8-SAMs (prepared in different molar ratio concentrations), at different scan rates (ν).

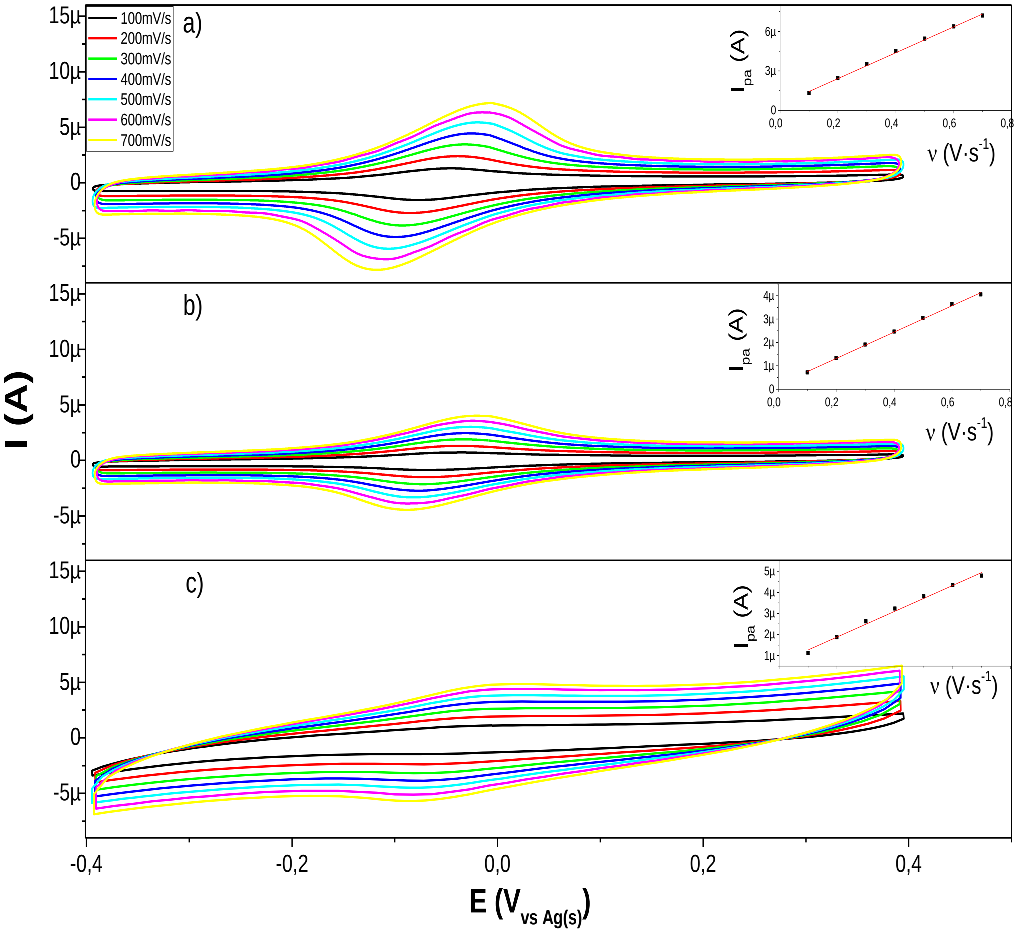

Figure 4.23 CVs in Bu_4NPF_6 0.1 M in THF at different scan rates (ν varies from 100 to 700 mV/s) for the PTM_8/C_8SH-SAMs prepared at different molar concentration ratios: a) 1:1, b) 1:2, and c) 1:5. Inset figures represent the linear variation of the anodic current peak with the scan rate ($I_{p,a}$ vs ν).

As previously observed in mono-component PTM_n-SAMs, the $PTM^{\bullet}$/ PTM^{-} reversible redox process is observed at the formal potentials $E^{1/2} \approx -0.06$ V vs. $Ag_{(s)}$ (values extracted at a scan rate of 100 mV s^{-1}, plotted separately in Figure 4.24). The linear relationship between $I_{p,a}$ and ν, besides the small values of ΔE_p are in concordance to redox processes of surface-confined electroactive molecules (see inset plot in Figure 4.23).[63]

The full width at half maximum (ΔE_{FWHM}) obtained (see Table 4.3) for the PTM_8/C_8SH-SAMs are lower than purely PTM_n films, confirming that the higher values previously obtained are related to the interactions between PTM centers in highly dense-packed SAMs.[64]

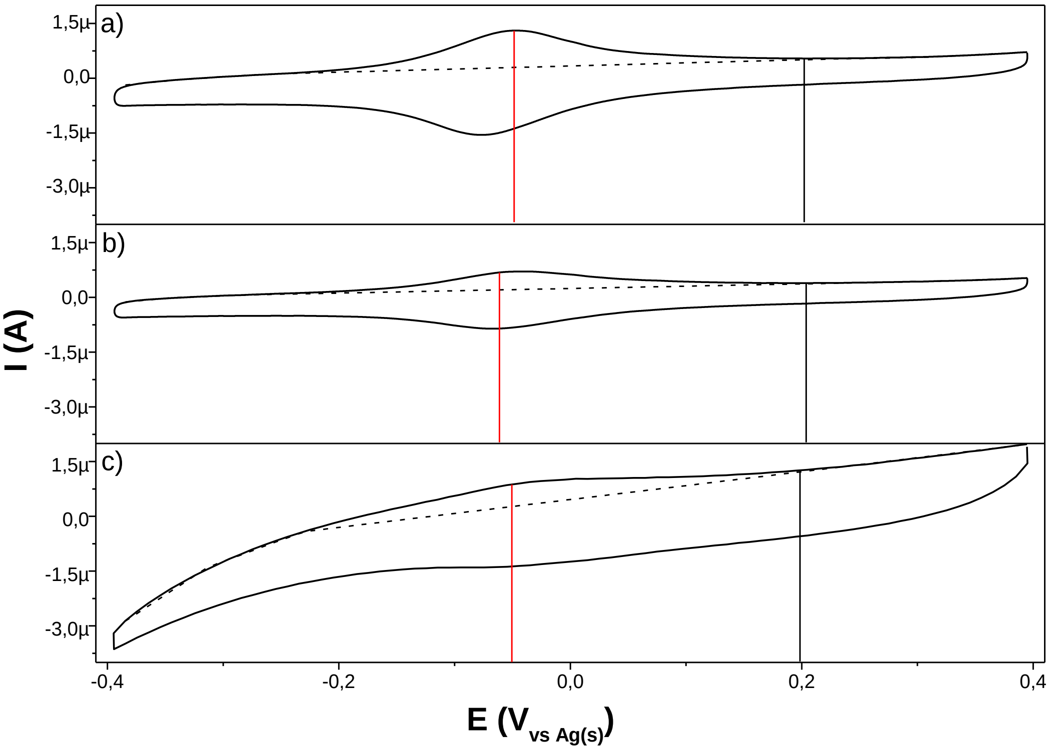

Figure 4.24 CVs at 100 mV/s in Bu_4NPF_6 0.1 M in THF of PTM_8/C_8SH-SAMs prepared at different molar concentration ratios: a) 1:1, b) 1:2, and c) 1:5. Vertical lines indicate the DC bias potentials applied for the impedance experiments.

From the area under the CV peak (Figure 4.24), the PTM_8 surface coverage were estimated to be 3.4, 1.9, 1.3 x 10^{-11} mol·cm^{-2} in 1:1, 1:2 and 1:5 ratios concentrations, respectively (at 100 mV·s^{-1} of scan rate). From these results it can be seen that the final ratio of adsorbates constituting the SAM does not necessarily correspond to the initial composition of the preparation solution.[87] This is related to the assembly process, as it is a dynamic equilibrium that favours formation of the most energetically stable SAM. That is, the composition of the SAM can deviate from the initial ratio of components established by the stoichiometry of the precursors to favour one component over another. Another factor is the reorganization of the surface during and after formation of the monolayer, which complicates the placement of the components in the film, suggesting the possibility of heterogeneous distribution in the monolayer due to rearrangement of molecules forming small islands. Despite the fact that PTM_n coverage monolayers do not follow a linear correlation with the initial ratio of the preparation solution, it can be clearly observed that the PTM_n surface coverage is, in all these diluted SAMs, one order of magnitude lower than the corresponding PTM_n-SAMs.

Continuing with the electrochemical characterization, the impedance analysis has been performed in the same way as the PTM_n-SAMs, where the two different DC bias voltages applied are indicated in Figure 4.24. The experimental results obtained are presented in Figure 4.25 in the form of capacitance bode plots, where the imaginary part of the capacitance (C_{im}) for the PTM_8/C_8SH-SAMs is plotted against frequency at both DC bias voltages (non-faradaic and formal redox potential, respectively). After the data treatment, the final response of the $C_{im,f}$ is shown in Figure 4.26, and k_{ET} have been estimated from the frequency (f_0) at the highest ordinate point.

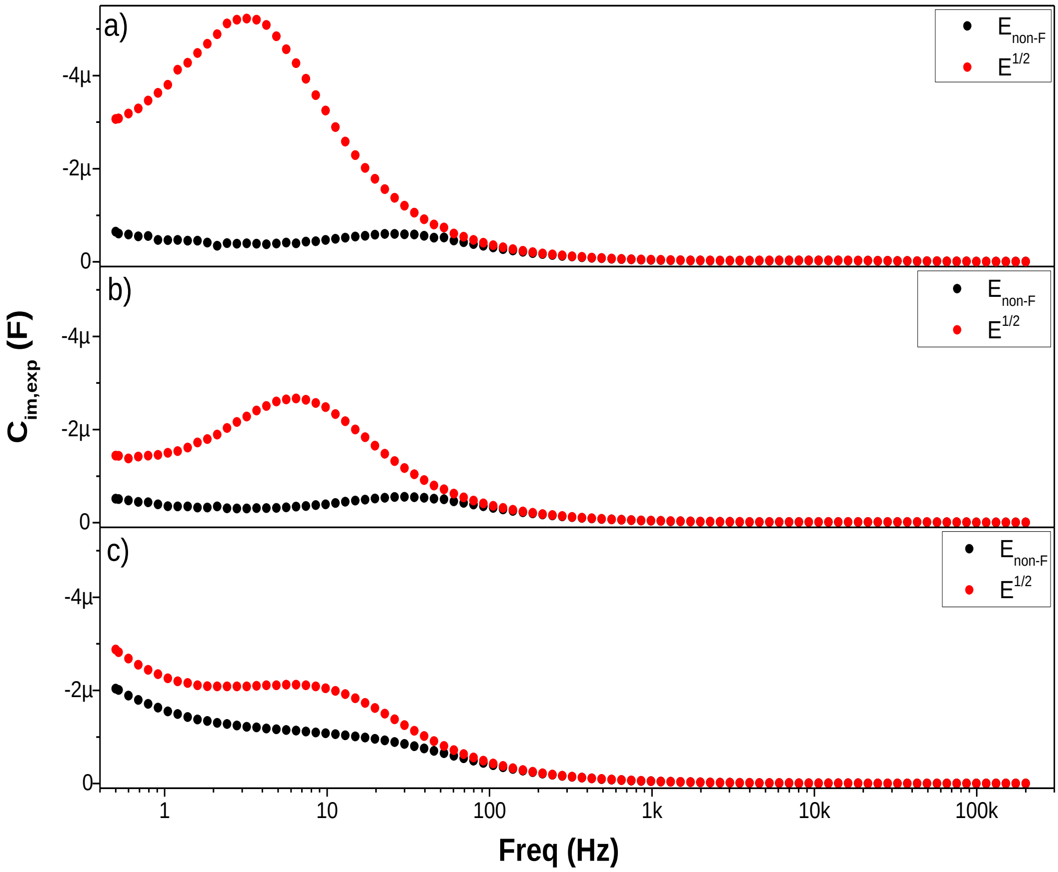

Figure 4.25 Experimental data of C_{im} vs. frequency at two different bias voltage: non-faradaic voltage (●), and at the formal redox potential (●), for PTM_8/C_8SH-SAMs prepared at different molar concentration ratios: a) 1:1, b) 1:2, and c) 1:5.

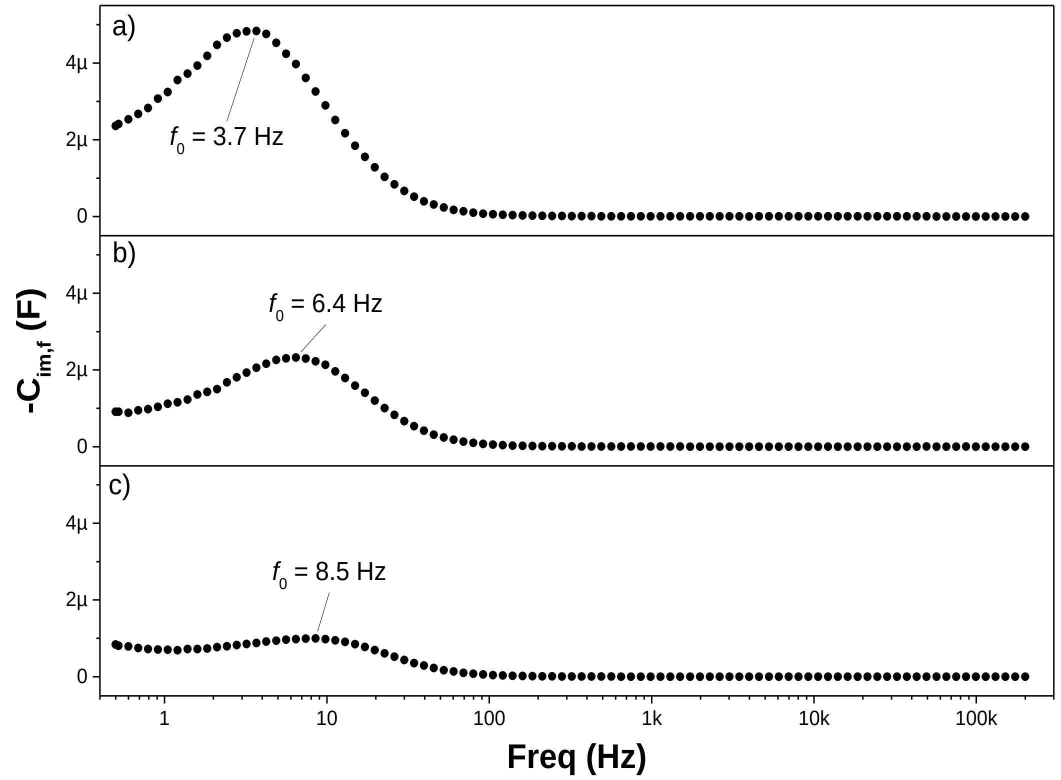

Figure 4.26 $C_{im,f}$ vs. frequency, after subtraction of the non-faradaic response, for PTM$_8$/C$_8$SH-SAMs prepared at different molar concentration ratios: a) 1:1, b) 1:2, and c) 1:5.

The electrochemical parameters extracted from CV and EIS measurements are presented in Table 4.3, for PTM$_8$/C$_8$SH-SAMs, PTM$_{10}$/C$_{10}$SH-SAMs and PTM$_{12}$/C$_{12}$SH-SAMs.

	Ratio	**$E^{1/2}$ ($V_{vs\ Ag(s)}$)** *v = 100mV/s*	**ΔE (mV)** *v = 100mV/s*	**ΔE_{FWHM} (V)** *v = 100mV/s*	**Γ (mol·cm^{-2})**	**$k_{ET} = \pi f_0 (s^{-1})$**
PTM$_8$/C$_8$SH	1:1	-0.07	19.5	0.130	3.4·10^{-11}	11.6
	1:2	-0.06	9.5	0.158	1.9·10^{-11}	20.3
	1:5	-0.07	29.4	0.118	1.3·10^{-11}	26.8
PTM$_{10}$/C$_{10}$SH	1:1	-0.02	14.8	0.169	8.0·10^{-12}	53.9
	1:2	-0.08	9.4	0.155	3.2·10^{-11}	35.4
	1:5	0.05	59.8	0.090	2.3·10^{-12}	124.6
PTM$_{12}$/C$_{12}$SH	1:1	-0.03	0.53	0.133	8.4·10^{-12}	164.8
	1:2	-0.03	0.3	0.194	2.0·10^{-11}	124.6
	1:5	-0.05	29.3	0.173	3.2·10^{-11}	20.3

Table 4.3 Electrochemical parameters obtained from CV and EIS measurements for PTM$_8$/C$_8$SH-SAMs, PTM$_{10}$/C$_{10}$SH-SAMs and PTM$_{12}$/C$_{12}$SH-SAMs.

4.5.1 Impact of the PTM surface coverage (Γ) on k_{ET}

The preparation of diluted SAMs by immersion conditions of the electrode substrates in a mixed solution is highly dependent of specific experimental parameters that influence on the monolayer formation, structure, packing, orientation and stability. Therefore, in this study, the experimental PTM surface coverage has been selected as main parameter to compare the kinetic variations between prepared samples.

The variation of k_{ET} as a function of PTM coverage is shown in Figure 4.27. The important feature to note is the significant decrease of k_{ET} as the PTM coverage increases. The surface coverage and k_{ET} for the non-diluted SAMs is also included in the graph.

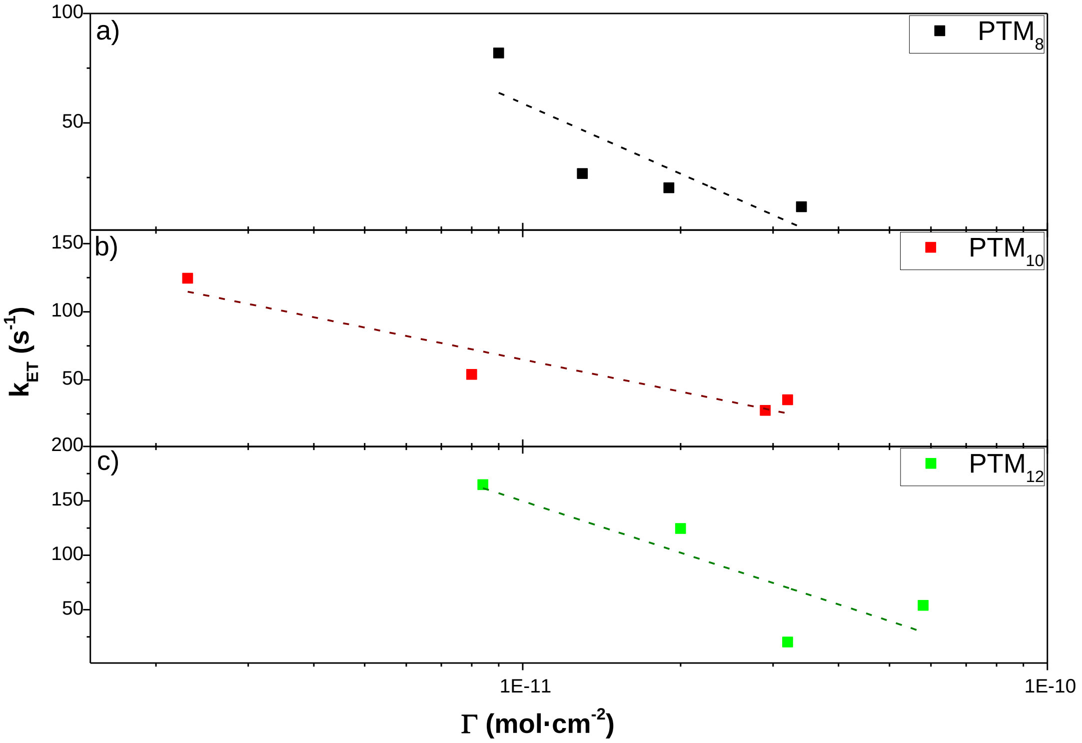

Figure 4.27 Semi-logarithmic plot of k_{ET} vs. surface coverage (Γ).Values extracted from the CV at 100 mV/s of scan rate.

This result can be related to lateral interactions between electroactive centers, where, for highly dense-packed SAMs (in the case presented in this chapter corresponds to mono-component PTM_n-SAMs), intermolecular electronic coupling between neighbouring PTMs can exist, maybe due to repulsion effects,[64] and consequently, giving a lower global value of k_{ET}. Thus, intermolecular interactions between electroactive PTM centers play an important role in the electron transfer process.

4.6 Summary

In this chapter, PTM radical derivative SAMs have provided a solid-state platform for investigating electron transfer kinetics. The analysis of electron transfer characteristics in PTM_n-SAMs is motivated by the removal of the limiting diffusing effects present in solution-phase studies and has laid important foundations relevant to the progression of fundamental electron transfer principals and molecular electronics.

Standard impedance/capacitance methodologies have been used to determine electron transfer kinetics in PTM radical electroactive self-assembled monolayers. Three systems varying the spacer length between 8 and 12 carbon atoms were studied, corresponding to estimated electron-transfer distances between 12.7 and 17.7 Å.

The analysis of the kinetic results presented here indicates the relevant importance of the environment for the electron transfer reactions, which can be a determining factor in the adiabaticity character of the redox processes. Thus generally, in the PTM_n-SAMs, the higher solvent polarity and lower viscosity, the higher k_{ET} is observed. The same tendency is observed with the longitudinal relaxation time of the solvent. However, when benzonitrile is used as a solvent, this trend is not observed, probably due to the aromatic nature of the solvent that modifies the activation energy barrier or the ET process or the SAM organization.

When exploring the effect of the distance of the PTM to the electrode on k_{ET}, a non-clear tendency was found, observing a small influence of this parameter. Only in the case of benzonitrile, k_{ET} was slightly diminishing with the distance as it could be expected for a tunnelling transport. The lack of well-ordered SAMs and degrees of freedom of movement due to the surrounding solvent could play an important role in the interpretation of these results.

Furthermore, it has also been observed the impact of the surface coverage of the PTM_n-SAMs on k_{ET}, showing that the intermolecular electronic coupling between PTM neighbouring centers diminishes k_{ET}.

4.7 References

1 P. Muller, *Pure and Applied Chemistry*,1994, **66**, 1077-1184.

2 M. Nič, J. Jirát, B. Košata, A. Jenkins and A. McNaught, Eds., *IUPAC Compendium of Chemical Terminology*, IUPAC, Research Triagle Park, NC, 2009.

3 J. Verhoeven, *Pure and Applied Chemistry*,1996, **68**, 2223-2286

4 *IUPAC Compendium of Chemical Terminology*, IUPAC, Research Triagle Park, NC.

5 B. J. Holliday and T. M. Swager, *Chem. Commun.*, 2005, 23-26.

6 R. A. Marcus, *J. Chem. Phys.*, 1956, **24**, 966–978.

7 N. S. Hush, *Trans. Faraday Soc.*, 1961, **57**, 557-580.

8 T. Van Voorhis, T. Kowalczyk, B. Kaduk, L.-P. Wang, C.-L. Cheng and Q. Wu, *Annu. Rev. Phys. Chem.*, 2010, **61**, 149–170.

9 R. McCreery, J. Dieringer, A. O. Solak, B. Snyder, A. M. Nowak, W. R. McGovern and S. DuVall, *J. Am. Chem. Soc.*, 2003, **125**, 10748–10758.

10 J. Chen and and J. M. T. J. Chen, M. A. Reed, A. M. Rawlett, *Science*, 1999, **286**, 1550–1552.

11 Y. Luo, C. P. Collier, J. O. Jeppesen, K. A. Nielsen, E. DeIonno, G. Ho, J. Perkins, H.-R. Tseng, T. Yamamoto, J. F. Stoddart and J. R. Heath, *ChemPhysChem*, 2002, **3**, 519–525.

12 K. M. Roth, A. A. Yasseri, Z. Liu, R. B. Dabke, V. Malinovskii, K. H. Schweikart, L. Yu, H. Tiznado, F. Zaera, J. S. Lindsey, W. G. Kuhr and D. F. Bocian, *J. Am. Chem. Soc.*, 2003, **125**, 505–517.

13 V. Balzani, Ed., *Electron Transfer in Chemistry*, Wiley-VCH Verlag GmbH, Weinheim, Germany, 2001.

14 D. M. Adams, L. Brus, C. E. D. Chidsey, S. Creager, C. Creutz, C. R. Kagan, P. V. Kamat, M. Lieberman, S. Lindsay, R. A. Marcus, R. M. Metzger, M. E. Michel-Beyerle, J. R. Miller, M. D. Newton, D. R. Rolison, O. Sankey, K. S. Schanze, J. Yardley and X. Zhu, *J. Phys. Chem. B*, 2003, **107**, 6668–6697.

15 M. A. Rampi and G. M. Whitesides, *Chem. Phys.*, 2002, **281**, 373–391.

16 B. Mann and H. Kuhn, *J. Appl. Phys.*, 1971, **42**, 4398–4405.

17 M. A. Fox, *Acc. Chem. Res.*, 1999, **32**, 201–207.

18 M. N. Paddon-Row, *Acc. Chem. Res.*, 1994, **27**, 18–25.

19 D. B. MacQueen and K. S. Schanze, *J. Am. Chem. Soc.*, 1991, **113**, 7470–7479.

20 G. L. CLOSS and J. R. MILLER, *Science*, 1988, **240**, 440–447.

21 K. Slowinski, R. V. Chamberlain, C. J. Miller and M. Majda, *J. Am. Chem. Soc.*, 1997, **119**, 11910–11919.

22 K. Weber, L. Hockett and S. Creager, *J. Phys. Chem. B*, 1997, **101**, 8286–8291.

23 H. O. Finklea and D. D. Hanshaw, *J. Am. Chem. Soc.*, 1992, **114**, 3173–3179.

24 S. Creager, C. J. Yu, C. Bamdad, S. O'Connor, T. MacLean, E. Lam, Y. Chong, G. T. Olsen, J. Luo, M. Gozin and J. F. Kayyem, *J. Am. Chem. Soc.*, 1999, **121**, 1059–1064.

25 E. P. A. M. Bakkers, A. L. Roest, A. W. Marsman, L. W. Jenneskens, L. I. de Jong-van Steensel, J. J. Kelly and D. Vanmaekelbergh, *J. Phys. Chem. B*, 2000, **104**, 7266–7272.

26 S. W. Feldberg and N. Sutin, *Chem. Phys.*, 2006, **324**, 216–225.

27 L. D. Zusman, *Chem. Phys.*, 1987, **112**, 53–59.

28 D. F. Calef and P. G. Wolynes, *J. Phys. Chem.*, 1983, **87**, 3387–3400.

29 J. T. Hynes, *J. Phys. Chem.*, 1986, **90**, 3701–3706.

30 M. Bixon and J. Jortner, in *Advances in Chemical Physics: Electron Transfer - from Isolated Molecules to Biomolecules.*, 1999, pp. 35–202.

31 D. E. Khoshtariya, T. D. Dolidze, D. Krulic, N. Fatouros and D. Devilliers, *J. Phys. Chem. B*, 1998, **102**, 7800–7806.

32 D. E. Khoshtariya, T. D. Dolidze, L. D. Zusman and D. H. Waldeck, *J. Phys. Chem. A*, 2001, **105**, 1818–1829.

33 D. E. Khoshtariya, T. D. Dolidze, D. Sarauli and R. van Eldik, *Angew. Chem. Int. Ed.*, 2006, **45**, 277–281.

34 C. Miller, P. Cuendet and M. Graetzel, *J. Phys. Chem.*, 1991, **95**, 877–886.

35 X. Zhang, J. Leddy and A. J. Bard, *J. Am. Chem. Soc.*, 1985, **107**, 3719–3721.

36 X. Zhang, H. Yang and A. J. Bard, *J. Am. Chem. Soc.*, 1987, **109**, 1916–1920.

37 T. D. Dolidze, D. E. Khoshtariya, P. Illner, L. Kulisiewicz, A. Delgado and R. van Eldik, *J. Phys. Chem. B*, 2008, **112**, 3085–3100.

38 D. E. Khoshtariya, J. Wei, H. Liu, H. Yue and D. H. Waldeck, *J. Am. Chem. Soc.*, 2003, **125**, 7704–7714.

39 D. N. Beratan and J. N. Onuchic, *J. Chem. Phys.*, 1988, **89**, 6195–6203.

40 P. F. Barbara, T. J. Meyer and M. A. Ratner, *J. Phys. Chem.*, 1996, **100**, 13148–13168.

41 W. B. Curry, M. D. Grabe, I. V. Kurnikov, S. S. Skourtis, D. N. Beratan, J. J. Regan, A. J. A. Aquino, P. Beroza and J. N. Onuchic, *J. Bioenerg. Biomembr.*, 1995, **27**, 285–293.

42 D. Beratan, J. Betts and J. Onuchic, *Science*, 1991, **252**, 1285–1288.

43 H. A. Kramers, *Physica*, 1940, **7**, 284–304.

44 W. R. Fawcett and M. Opallo, *J. Electroanal. Chem.*, 1993, **349**, 273–284.

45 A. Kapturkiewicz and W. Jaenicke, *J. Chem. Soc. Faraday Trans. 1 Phys. Chem. Condens. Phases*, 1987, **83**, 2727.

46 M. J. Weaver, D. K. Phelps, R. M. Nielson, M. N. Golovin and G. E. McManis, *J. Phys. Chem.*, 1990, **94**, 2949–2954.

47 G. E. McManis, R. M. Nielson, A. Gochev and M. J. Weaver, *J. Am. Chem. Soc.*, 1989, **111**, 5533–5541.

48 I. Rubinstein, *Physical electrochemistry : principles, methods, and applications*, M. Dekker, 1995.

49 T. D. Dolidze, D. E. Khoshtariya, D. H. Waldeck, J. Macyk and R. van Eldik, *J. Phys. Chem. B*, 2003, **107**, 7172–7179.

50 J. Wei, H. Liu, D. E. Khoshtariya, H. Yamamoto, A. Dick and D. H. Waldeck, *Angew. Chem. Int. Ed.*, 2002, **41**, 4700–4703.

51 T. D. Dolidze, S. Rondinini, A. Vertova, D. H. Waldeck and D. E. Khoshtariya, *Biopolymers*, 2007, **87**, 68–73.

52 A. J. Bard, H. D. Abruna, C. E. Chidsey, L. R. Faulkner, S. W. Feldberg, K. Itaya, M. Majda, O. Melroy and R. W. Murray, *J. Phys. Chem.*, 1993, **97**, 7147–7173.

53 E. Laviron, *J. Electroanal. Chem. Interfacial Electrochem.*, 1979, **101**, 19–28.

54 T. Albrecht, K. Moth-Poulsen, J. B. Christensen, A. Guckian, T. Bjørnholm, J. G. Vos, J. Ulstrup, A. M. Rawlett, J. M. Tour, A. J. Bard and D. C. Ralph, *Faraday Discuss.*, 2006, **131**, 265–279.

55 C. P. Chen, W. R. Luo, C. N. Chen, S. M. Wu, S. Hsieh, C. M. Chiang and T. Y. Dong, *Langmuir*,

2013, **29**, 3106–3115.

56 J. F. Smalley, S. W. Feldberg, C. E. D. Chidsey, M. R. Linford, M. D. Newton and Y.-P. Liu, *J. Phys. Chem.*, 1995, **99**, 13141–13149.

57 S. E. Creager and T. T. Wooster, *Anal. Chem.*, 1998, **70**, 4257–4263.

58 J. Li, K. Schuler and S. E. Creager, *J. Electrochem. Soc.*, 2000, **147**, 4584.

59 P. R. Bueno, G. Mizzon and J. J. Davis, *J. Phys. Chem. B*, 2012, **116**, 8822–8829.

60 M. S. Góes, H. Rahman, J. Ryall, J. J. Davis and P. R. Bueno, *Langmuir*, 2012, **28**, 9689–9699.

61 L. Yuan, C. Franco, N. Crivillers, M. Mas-Torrent, L. Cao, C. S. S. Sangeeth, C. Rovira, J. Veciana and C. A. Nijhuis, *Nat. Commun.*, 2016, **7**, 12066–12075.

62 J. Comyn, *Int. J. Adhes. Adhes.*, 1997, **17**, 177.

63 P. Daum and R. W. Murray, *Chemically modified electrodes*, Wiley-VCH Verlag GmbH & Co. KGaA, Weinheim, Germany, 2009, vol. 103.

64 M. Lyons, in *Electroanalytical Chemistry*, eds. A. J. Bard and I. Rubisnstein, Marcel Dekker, Inc, New York, NY, 2014, p. 110.

65 C. P. Smith and H. S. White, *Anal. Chem.*, 1992, **64**, 2398–2405.

66 N. Crivillers, M. Mas-Torrent, J. Vidal-Gancedo, J. Veciana and C. Rovira, *J. Am. Chem. Soc.*, 2008, **130**, 5499–5506.

67 J. N. Murray, *Prog. Org. Coatings*, 1997, **31**, 375–391.

68 L. V. S. Philippe, G. W. Walter and S. B. Lyon, *J. Electrochem. Soc.*, 2003, **150**, B111–B119.

69 J. R. Macdonald and W. B. Johnson, *Fundamentals of Impedance Spectroscopy*, John Wiley & Sons, Inc., New Jersey,2nd ed., 2005.

70 T. M. Nahir and E. F. Bowden, *Langmuir*, 2002, **18**, 5283–5286.

71 E. Katz, O. Lioubashevsky and I. Willner, *J. Am. Chem. Soc.*, 2004, **126**, 15520–32.

72 Y. Guo, J. Zhao, X. Yin, X. Gao and Y. Tian, *J. Phys. Chem. C*, 2008, **112**, 6013–6021.

73 R. E. Ruther, Q. Cui and R. J. Hamers, *J. Am. Chem. Soc.*, 2013, **135**, 5751–5761.

74 M. Drüschler, N. Borisenko, J. Wallauer, C. Winter, B. Huber, F. Endres and B. Roling, *Phys. Chem. Chem. Phys.*, 2012, **14**, 5090-5099.

75 Z. Kerner and T. Pajkossy, *Electrochim. Acta*, 2000, **46**, 207–211.

76 E. Boubour and R. B. Lennox, *Langmuir*, 2000, **16**, 4222–4228.

77 C. G. Zoski, *Handbook of Electrochemistry*, Elsevier, 2007.

78 R. J. Forster and L. R. Faulkner, *J. Am. Chem. Soc.*, 1994, **116**, 5444–5452.

79 N. K. Bhatti, M. S. Subhani, A. Y. Khan, R. Qureshi and A. Rahman, *Turkish J. Chem.*, 2006, **30**, 165–180.

80 P. R. Bueno and J. J. Davis, *Anal. Chem.*, 2014, **86**, 1337–1341.

81 R. A. A. Marcus and N. Sutin, 1985, **811**, 265–322.

82 P. R. Bueno and J. J. Davis, *Anal. Chem.*, 2014, **86**, 1997–2004.

83 P. Debye, *Polar molecules*, Dover Publications, New York, NY, 1945.

84 D. De Vault and B. Chance, *Biophys. J.*, 1966, **6**, 825–847.

85 J. R. Winkler and H. B. Gray, *J. Am. Chem. Soc.*, 2014, **136**, 2930–2939.

86 B. Albinsson, M. P. Eng, K. Pettersson and M. U. Winters, *Phys. Chem. Chem. Phys.*, 2007, **9**, 5847-5864.

87 K. Heister, D. L. Allara, K. Bahnck, S. Frey, M. Zharnikov and M. Grunze, *Langmuir*, 1999, **15**, 5440–5443.

Chapter 5

Application of ion gels as dielectrics in Organic Field-Effect Transistors (OFETs)

CHAPTER 5. Application of Ion gels as dielectrics in Organic Field-Effect Transistors

5.1 Introduction

Organic electronics is a rapidly growing interdisciplinary field, which started by the discovery of conductive polymers by Heeger, MacDiarmid and Shirakawa et al. in 1977.[1] The advantages of organic electronic devices compared to traditional inorganic electronics lie in their low cost, tunability (by changes in chemical structure) and facile deposition (i.e. printing). Although organic devices cannot replace inorganic-based ones in most applications, they open up new possibilities for flexible and large-area electronics. Interesting organic electronics devices include light-emitting diodes,[2] solar cells,[3] diodes,[4] and organic field-effect transistors (OFETs).[5]

OFETs have the same basic structure as inorganic thin-film transistors used commonly in displays. The defining characteristic of OFETs is that the active layer, semiconductor, is an organic material; it is either a polymer or a small organic molecule. The electrodes and the insulator layer may be organic or inorganic. Major possible applications for OFETs include active matrix displays,[6-8] RF-ID tags,[9] and sensors.[10,11]

In many applications for OFETs, such as thin-film batteries or external RF-fields,[12] low voltages are desired. However, OFETs usually need voltages of over 20 V. This is mainly related to the specific capacitance of the gate dielectrics, which determines the induced charge in the semiconductor channel for the applied gate voltage. Low capacitances are translated into low induced charge densities, since the gate dielectric layers have to be made thick in order to avoid leakage current through it.[13]

Large specific capacitances have been achieved using solution processible ferroelectric polymers[14,15] and ultrathin self-assembled monolayers.[13,16,17] An interesting approach is using a dielectric containing mobile ions, where the ions form electric double layers at the gate electrode and semiconductor surface, decreasing the effective thickness of the dielectric layer and facilitating a large charge carrier concentration to accumulate to the semiconductor. The different methods for utilizing ion-based based gate dielectrics include anionic polymers,[18] ion-conducting membranes[19] and an ion gels.[20] Generally, these ion gels consist of an ionic liquid and a block copolymer, which form a physically cross- linked gel. The ions of the liquid are able to move inside the gel, enabling the formation of the electric double layers, and allowing the device to be operated at voltages below 2 V. Despite the low voltage operation of these transistors, they present some drawbacks, such as slow switching (caused by the limiting ion mobility in the gel), and leakage through the insulator (due to electrochemical reactions).

5.1.1 OFET device configurations

The main components of an OFET are: source and drain electrodes of width W (channel width) and separated by a distance L (channel length), an organic semiconductor thin film as active layer, which is separated from a gate electrode by the insulating dielectric (Figure 5.1).

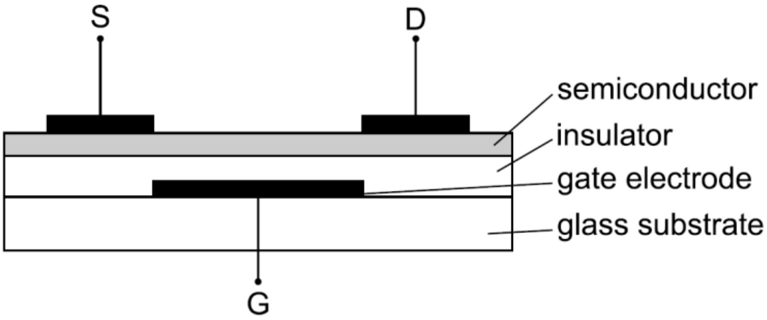

Figure 5.1 Schematic configuration of a field-effect transistor where S, D, and G correspond to source, drain and gate electrodes, respectively.

Voltage is usually applied to the gate electrode (V_g) and the drain electrode (V_{ds}). The source electrode is normally grounded, and the other voltages are given relative to this. Applying a gate voltage (V_g) results in accumulation of charge carriers at the organic semiconductor/gate insulator interface (illustrated in Figure 5.2). This voltage, V_g, controls the current between the source and drain electrodes when there is a supply voltage between the source and the drain, which is also used to turn the device from the off to the on state. The term field-effect originates from the electric field induced by the gate, which controls the formation of a conducting semiconductor channel between the other two terminals.[21]

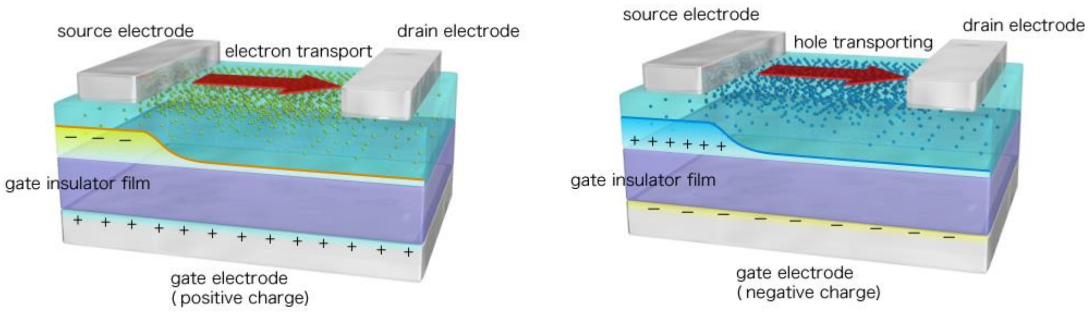

Figure 5.2 Illustration of the current flowing between source and drain electrodes modulated by the gate voltage.[22]

The basic operations of FETs are amplification and switching. Amplification means that a small variation in the input voltage, i.e. the gate voltage, induces a large variation in output currents between the source and the drain. Switching means that the device can be turned on and off by changing the gate voltage: the off state means that the current between the source and the drain is zero. Switching is generally used in digital circuits.[21]

Different configurations of OFETs are shown in Figure 5.3. The choice of the device structure is done according to what is convenient for the materials and deposition methods used. The gate electrode can be either on top or on the bottom of the device; this determines the mutual order of the semiconductor and dielectric layers. The source and drain electrodes can be deposited before or after the semiconductor layer; this results in bottom and top contact configurations, respectively.

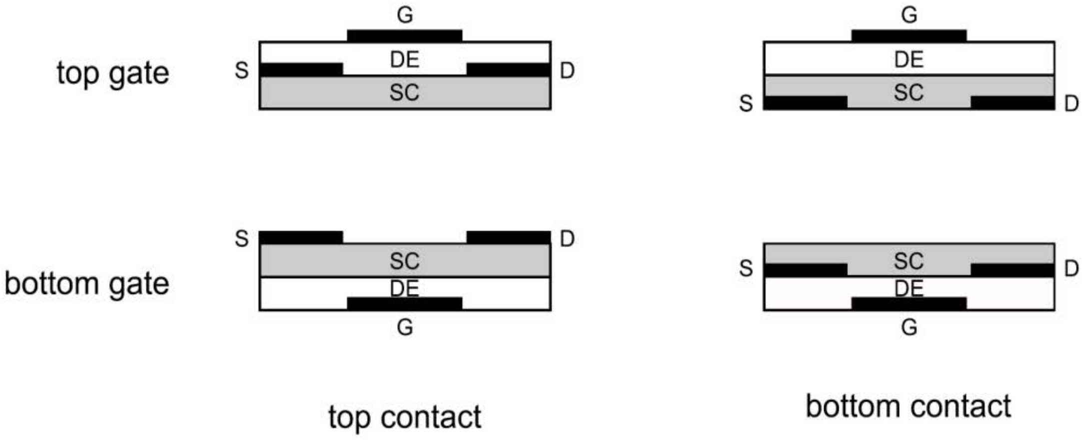

Figure 5.3 Different OFET configurations commonly employed. “DE” denotes the dielectric, “SC” the semiconductor and S,D and G, the source, drain and gate contacts, respectively.[23]

If the substrate is a doped silicon wafer, it can serve as the bottom gate electrode.[24] Top-gate structures have the advantage of the dielectric layer acting also as a passivation layer for the semiconductor, since many organic semiconductors degrade when exposed to ambient air. When the electrodes are metal, top-contact geometry has been found to offer a lower contact resistance between the semiconductor and the source and drain electrodes. This is because during the deposition the metal penetrates into and mixes with the semiconductor.[23]

The device geometry with a top-contact and bottom-gate or bottom-contact and top-gate configuration is called a staggered geometry. In this structure, the semiconductor-electrode contacts are on the opposite side of the semiconductor layer than the conducting channel. This introduces an additional resistance called access resistance between the electrode and the channel, since the semiconductor is very poorly conducting where there is no field-induced charge.[23]

Interface smoothness is important to the function of the OFET, especially in the interface between the semiconductor and dielectric layers. When fabricating solution-processed semiconductor and dielectric layers, the dissolution of the bottom layer when depositing the top layer may result in interface mixing and increased roughness. This impairs the charge transport of the semiconductor, which happens at the interface to the dielectric. Therefore it is critical to plan the device fabrication in such a way that the solvent of the top layer does not dissolve the bottom layer.[25]

5.1.1.1 Operating regimes of Organic Field-Effect Transistors (OFETs)

When an applied gate voltage induces charges in the semiconductor layer, initially most of them fill the many localized states in the band gap. Only at sufficiently high gate voltages electrons begin to fill the conduction band (for p-type semiconductors, holes begin to fill the valence band). This gives an important characteristic: the charge carrier mobility measured by using the field-effect is not constant but a function of the gate voltage.[26]

When no source-drain bias is applied, the charge carrier concentration in the transistor channel is uniform. A linear gradient of charge density from the carrier injecting source to the extracting drain forms when a small source-drain voltage is applied ($V_{ds} << V_g$). This is the linear regime, in which the current flowing through the channel is directly proportional to V_{ds}. The threshold voltage of a field-effect transistor, V_{Th}, is the minimum gate-to-source voltage differential that is needed to create a conducting path between source and drain terminals.

When the source-drain voltage is further increased, a point $V_{ds} = V_g - V_{Th}$ is reached, at which the channel is pinched off. A space-charge-limited saturation current $I_{ds,sat}$ can flow across this narrow depletion zone as carriers are swept from the pinch-off point to the drain by the comparatively high electric field in the depletion region. Further increasing the source-drain voltage will not substantially increase the current but leads to an expansion of the depletion region and thus a slight shortening of the channel. Since the potential at the pinch-off point remains $V_g - V_{Th}$ and thus the potential drop between that point and the source electrode stays approximately the same, the current saturates at a level $I_{ds,sat}$.

The equations describing the current-voltage characteristics in the linear region, with $V_{ds} << V_g$ (because there is no depletion region), can be simplified to:

$$I_{ds} = \frac{W}{L}\mu_{lin}C_i(V_g - V_{Th})V_{ds} \quad \text{(Eq. 5.1)}$$

In this equation, W and L are the width and length of the channel, respectively, and C_i is the specific capacitance of the insulator. The drain current (I_{ds}) is proportional to the gate voltage (V_g), and the field-effect mobility in the linear regime (μ_{lin}) can thus be extracted from the gradient of I_{ds} vs V_g at a constant V_{ds}:

$$\mu_{lin} = \frac{\delta I_{ds}}{\delta V_g}\frac{L}{WC_iV_{ds}} \quad \text{(Eq. 5.2)}$$

In the saturation regime, the channel is pinched off when $V_{ds} = V_g - V_{Th}$ and the current cannot increase substantially anymore and saturates ($I_{ds,sat}$). Then, the drain current is given by:[24]

$$I_{ds,sat} = \frac{W}{2L}\mu_{sat}C_i(V_g - V_{Th})^2 \quad \text{(Eq. 5.3)}$$

In the saturation regime, the square root of the saturation current is directly proportional to the gate voltage, being the mobility independent to the gate voltage. If this is not the case, gate voltage dependent saturation mobility (μ_{sat}) can be extracted using:

$$\mu_{sat}(V_g) = \frac{\delta I_{ds,sat}}{\delta V_g}\frac{L}{WC_i}\frac{1}{(V_g - V_{Th})} \quad \text{(Eq. 5.4)}$$

In addition to the field-effect mobility, another important parameter that determines the OFET performance is the on-off ratio (I_{ON}/I_{OFF}), which is the ratio of the drain current in the on-state at a particular gate voltage and the drain current in the off-state. For clean switching behaviour of the transistor, this value should be as large as possible. In situations where contact resistance effects at the source-drain electrodes can be neglected, the on-current mainly depends on the mobility of the semiconductor and the capacitance of the gate dielectric. In OFETs, the off state simply does not have an accumulation of charges in the channel, and the low conductivity of the semiconductor itself ensures that a very low current flows between the source and drain electrodes. If there is a substantial leakage current in the off state, the on-off ratio is small.

Field-effect mobilities of the order 1–5 $cm^2/(V \cdot s)$ have been achieved with solution processed organic semiconductors.[23,25,27] This compares favourably with a-Si TFTs which have mobilities of similar magnitude. OFETs have the advantage of room-temperature processing which makes them compatible with flexible substrates.

5.1.1.2 Output characteristics of OFETs

Transistor output characteristics can be analysed by applying a constant gate voltage V_g, sweeping the drain-source voltage, V_{ds}, and measuring the drain current I_{ds}. A representative set of output curves with different gate voltages is given in Figure 5.4. Initially the current varies linearly with V_{ds}, but after a certain voltage levels off to a saturation value. The saturation current is larger the more positive the gate voltage is (for an n type semiconductor).[21] From the output characteristics, the linear regime at low V_{ds} and the saturation regime at high V_{ds} are evident.

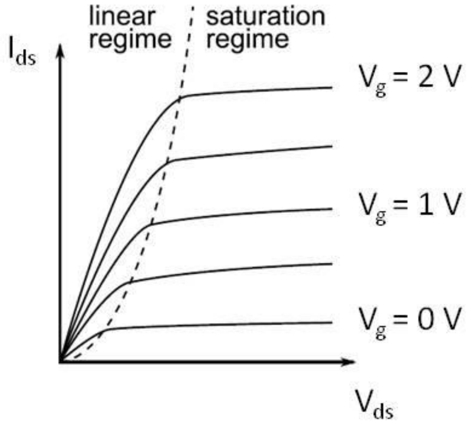

Figure 5.4 Example of output curves for different gate voltages.[21]

5.1.1.3 Transfer characteristics of OFETs

In addition to output characteristics another important way to examine transistor function is to measure the drain current while sweeping the gate voltage and keeping the drain voltage constant. The result is called a transfer curve. According to Eq. 5.1, the drain current should increase linearly with the gate voltage in the linear region, i.e. when the drain current is low. In the saturation region, the drain current depends on the gate voltage quadratically as in Eq. 5.3. Therefore it is useful to plot the square root of the saturation drain current as a function of the gate voltage:

$$\sqrt{I_{ds,sat}} = \sqrt{\frac{W\mu C_i}{2L}}\left(V_g - V_{th}\right) \tag{Eq. 5.5}$$

A representative plot of Eq. 5.5 is given in Figure 5.5.a. Fitting a straight line to the curve gives the threshold voltage V_{Th} as the V_g axis intercept, and the charge carrier mobility can be calculated from the slope k of the line:

$$\mu = \frac{2Lk^2}{WC_i} \tag{Eq. 5.6}$$

It is important to note that this equation describes the mobility in the saturation regime.

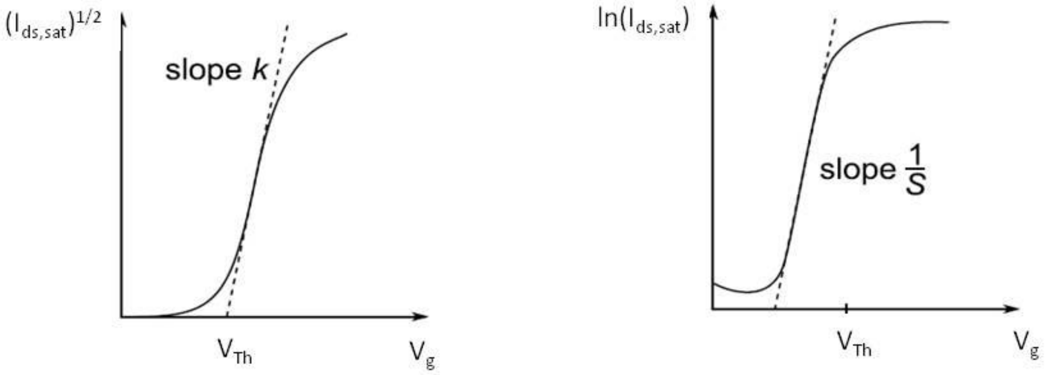

Figure 5.5 Two ways of plotting the transfer characteristics of OFETs: a) the square root of the transfer curve in the saturation region, i.e. large V_{ds}, b) the subthreshold slope of a transfer curve.[21]

When the gate voltage is below threshold, the drain current is not zero, but depends exponentially on V_g. If the natural logarithm of the drain current is plotted against V_g, the result is a straight line below V_{th}. The reciprocal of the slope of this line is called the subthreshold slope, S, and it is usually given in units of V/decade. The smaller the value of S, the more sharply the transistor turns on.[21]

5.1.2 Organic semiconductors

Organic semiconductors are solids whose building blocks are π-bonded molecules or polymers made up by carbon and hydrogen atoms and – at times – heteroatoms such nitrogen, sulphur and oxygen. They exist in form of molecular crystals or amorphous or crystalline thin films. In general, they are electrical insulators but become semiconducting when charges are either injected from appropriate electrodes, upon doping or by photoexcitation.

Organic materials that have semiconducting or conducting properties are essential to the field of organic, flexible and printed electronics. Their structure is very different from inorganic semiconductors, which consist of a closely spaced and highly ordered lattice of atoms. Organic semiconductors are molecular or polymeric materials, which are held together mainly by weak van der Waals forces.

Semiconducting polymers have a variety of different structures, but they all have one thing in common: a conjugation of alternating double and single bonds along the polymer backbone.[28] Small conjugated organic molecules such as pentacene and rubrene are also semiconducting and have been widely studied as materials in organic electronics (Figure 5.6).[29]

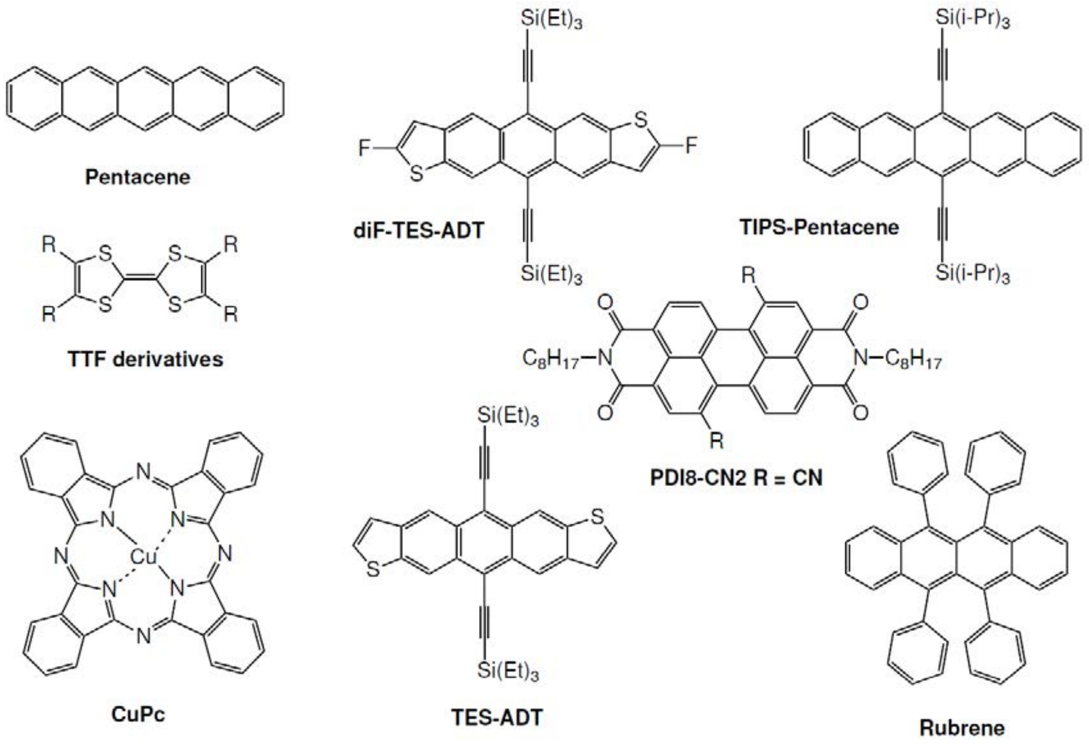

Figure 5.6 Some common small conjugated molecules used in organic electronics applications.[30]

Organic semiconductors are usually divided into hole-(p) and electron-(n) transporting materials. This division is however very different from inorganic p- and n-type semiconductors, where the charge carrier type is determined by doping impurities. With organic semiconductors the classification is made simply by which type the material performs better with in devices. This in turn is mostly determined by the efficiency of charge injection at electrodes, and not by the actual mobility of the charge in the material. Generally, materials with high-lying HOMO levels are hole-transporting, and materials with low LUMO levels are electron-transporting. There are also compounds which are ambipolar, i.e. they can transport both electrons and holes well.[28,31]

Small molecules had been commonly deposited employing vacuum deposition techniques due to their lower solubility in organic solvents, and can form films with a variety of crystallinity degrees.[32] The technologies applied to grow organic single crystals are based on solution (such as recrystallization,[33] solvent exchange[34] and dropcasting[35]) and vapour deposition techniques (like the physical vapour transport method[36]).

In principle, small molecules could potentially give rise to more highly crystalline films than polymers leading to higher mobilities, but it is imperative to find low cost and scalable routes to process them. Important advances have been realized in the synthesis of novel semiconductors, improving the solubility of the small molecules and making them compatible with recently described low-cost and large-scale fabrication techniques based on printing technologies.[37] The technique of blending organic semiconductors with polymers either insulating or semiconducting for tuning the solution processability and thin film properties, is now commonly employed in organic electronics and thin film transistors.[38] For instance, blends of organic semiconductors with polystyrene (PS) have led to thin films with an enhanced crystallinity and environmental stability.[39–41]

5.1.3 Insulator materials

Initially OFETs were fabricated with the bottom gate structure using a single-crystal silicon wafer as both the substrate and the gate electrode. In this case the dielectric was thermally grown SiO_2. This fabrication method was convenient due to the well-established methods of silicon microelectronic technology. More recently focus has shifted towards organic dielectric materials which, like organic semiconductors, offer the advantage of low-cost, large-area processing.[23]

The capacitance of the dielectric is the most important property of the dielectric layer. The larger the capacitance, the more charges are induced in the semiconductor channel at a given gate voltage. The capacitance is:

$$C = \frac{\varepsilon_0 \varepsilon_r A}{d} \qquad \text{(Eq.5.7)}$$

where ε_0 is the vacuum dielectric constant, ε_r is the insulator dielectric constant, A the electrode surface area and d the thickness of the dielectric. The specific capacitance, C_i, in the equations describing transistor current-voltage characteristics is C/A. High capacitance is beneficial, because it allows larger currents with lower operating voltages.[42] The route to higher capacitance dielectrics can be achieved in two ways: increasing the dielectric constant or decreasing the thickness.[23] As device dimensions such as the channel length L are reduced, the dielectric layer needs to be made thinner as well; the ratio d/L should be less than 0.1 for acceptable on-off characteristics.[43]

It is well established that charge transport in the semiconductor occurs only in the first few molecular layers of the semiconductor at the dielectric interface. Therefore the properties of the dielectric at the interface are important. If the interface is rough, there are valleys in the semiconductor that can act as charge traps. In bottom-gate devices, a rough interface can also prevent the formation of large crystal domains in the semiconductor. This is of course not relevant in amorphous semiconductors. The interface roughness between two polymers is determined by a balance between the entropy which favours a large surface area and the unfavourable energy of interaction between the materials.[25]

Especially with inorganic dielectrics such as SiO_2 the surface of the semiconductor is often modified with a self-assembled monolayer (SAM). SAMs are formed spontaneously through chemisorption, where one end of the active molecule has a strong interaction with the surface of the substrate. As a result, the surface is covered with molecules that have the same orientation. For example, alkyltrichlorosilanes self-assemble readily on hydroxylated surfaces such as glass and SiO_2. In the interface between the dielectric and the semiconductor, the SAM can induce a dipole moment depending on the terminal group of the molecule. For an electron-rich terminal group that is directed towards the semiconductor, the threshold voltage is shifted to more positive voltages in p-type transport. Similarly, for an electron-withdrawing terminal group, the threshold voltage shifts to a more negative value.[42,44]

Self-assembled monolayers or multilayers can also be used as dielectric layers themselves, which is a route to achieving very thin dielectric layers.[25] Solution-processed polymer dielectric layers can be made as thin as 50 nm by spin-coating.[43] A challenge especially in very thin layers is that there should be no leakage current from the gate electrode through the dielectric. This means that the dielectric should withstand high voltages over it without breaking down, and that there should not be pinholes or other defects which allow current to pass through it.[25,42]

The other route to achieve a high capacitance, the use of high dielectric constant insulators (high ε_r), has also been investigated, but they too have some drawbacks. High ε_r dielectrics usually contain polar groups that are susceptible to ionic impurities. These can drift in the electric field induced by the gate, creating a hysteresis in the transistor curves. Even without impurities, the randomly oriented dipoles of the dielectric at the semiconductor interface cause energetic disorder, which hinders charge transport. Within the hopping model of transport, where the density of states is usually simplified to a Gaussian distribution, the added disorder broadens the density of states. This is illustrated in Figure 5.7. The energetic disorder is especially detrimental to amorphous semiconductors that already have a high degree of disorder in their structure.[25,42]

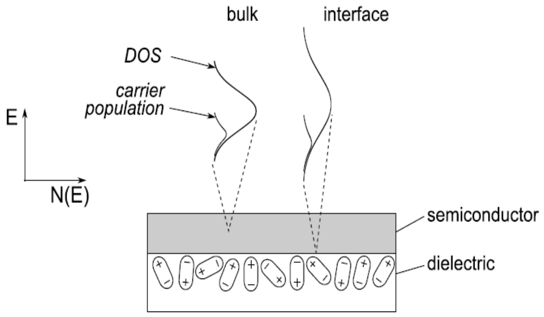

Figure 5.7 In the Gaussian hopping model, the density of states, N(E), is broadened due to the polar disorder in the dielectric at the interface.[42]

Polar and ionic groups in the dielectric interface may also act as traps to charge carriers. Such trapping has been found to be one cause for the scarcity of electron-transporting OFET materials: groups with a higher electron affinity than the semiconductor readily trap electrons. Many studies of semiconducting materials have been and still are conducted with SiO_2 as the gate dielectric. The SiO_2 surface contains many Si−OH groups, which are electron-trapping. Many semiconductors do show n-type transport in other applications than OFETs, such as light-emitting diodes. One way to reduce the trapping is to use a thin buffer layer such as a SAM between the dielectric and semiconductor.[25]

Examples of frequently used high ε_r polymer dielectrics include poly(4-vinylphenol) (PVP) and poly(methyl methacrylate) (PMMA), which have dielectric constants 4.5 and 3.5, respectively. Inorganic dielectrics generally have high dielectric constants: for example in SiO_2 $\varepsilon_r = 3.9$, in Al_2O_3 $\varepsilon_r = 8.4$ and in TiO_2 ε_r is as high as 41. Examples of low ε_r dielectrics are poly(perfluoroethylene-co-butenyl vinyl ether) with $\varepsilon_r = 2.1$ and poly(propylene-co-(1-butene)) with $\varepsilon_r = 2.3$. The choice of dielectric is often a trade-off between the high capacitance that polar, high ε_r dielectrics offer and the trap-free conduction in devices with a low ε_r dielectric.[42,45]

5.1.4 Ion gels as dielectric in OFETs

Ion gels were first demonstrated as gate insulators in organic field-effect transistors in 2007 by the Frisbie group.[46] Solid polymer electrolytes were studied before as gate dielectrics in OFETs, but the switching speeds of these transistors are restricted to only a few hertz.[47] This is due to the low mobility of the salt ions within the solid polymer matrix. Ion gels consist of a polymer matrix swollen with an ionic liquid. The polymer concentration of the gel can be as low as 5 % by weight, allowing the ions to move relatively freely inside the gel.

When an external voltage is applied to the ion gel, electric double layers form rapidly at the electrodes due to the high ionic mobility and relatively low polymer content. They form very thin electric double layers giving rise to a high specific capacitance, which enables transistor function at low voltages. The specific capacitances of ion gels usually range from 1 to 40 $\mu F/cm^2$.[20,46,48,49] This compares favourably with the specific capacitances of more conventional dielectrics: devices fabricated with SiO_2 and polyimide display specific capacitances of 10 nF/cm^2 [50] and 20 nF/cm^2,[51] respectively. Capacitances this low requires high operating voltages, which is not feasible in many applications.

The high capacitance of ion gels enables high induced charge densities in ion gel gated organic field-effect transistors at low voltages. When the semiconductor is p-type, applying a negative gate voltage creates electric double layers at the gel- electrode and gel-semiconductor interfaces as depicted in Figure 5.8. The negative ions in the gel accumulating on the semiconductor interface induce positive charges, holes, in the semiconductor channel. The channel becomes conductive and current flows between the source and drain electrodes.

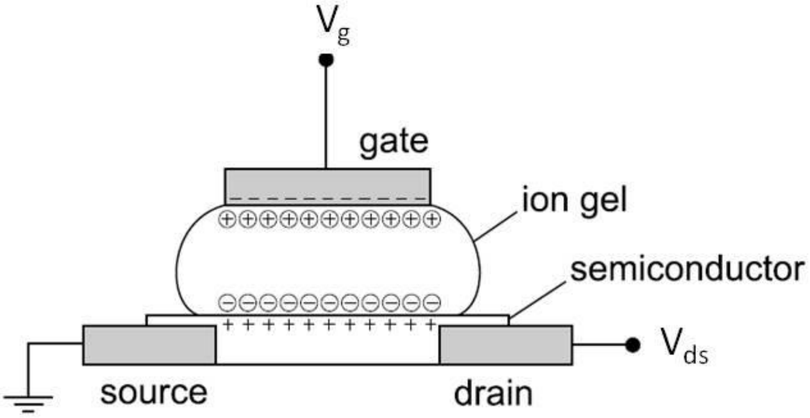

Figure 5.8 A top-gate OFET with an ion gel dielectric layer.[52]

The doping mechanism in electrolyte-gated OFETs is not necessarily purely field-effect: the anions may be able to penetrate into the semiconductor layer resulting in electrochemical doping. This has been studied with ATR-IR experiments and the mathematical modelling of ion diffusion, where the findings were that at high frequencies (> 1 kHz) the mechanism is primarily electrostatic i.e. field-effect, whereas electrochemical doping comes into play at low frequencies. The limiting factor is the ion diffusion speed into the semiconductor. The equations describing the current-voltage characteristics of OFETs (section 5.1.1.1) are valid also for electrochemical transistor operation.[20]

The large capacitance of the ion gel offers many advantages. The large charge density induced in the channel can potentially give rise to higher charge carrier mobilities due to increased trap-filling in the semiconductor.[49] Because the capacitance stems from the electric double layers, the thickness of the gel layer itself doesn't significantly affect the capacitance.[12] This makes layer deposition easier, since the thickness does not need to be controlled closely. The gate electrode doesn't even need to be exactly on top of the channel: the high polarizability of the gel makes it possible to fabricate transistors where the gate is offset from the channel by as much as 60 μm.[47,49] Again this eases the device fabrication.

A major drawback of ion gel gated transistors is their slow polarization time: the switching speed is limited by the ion movement through the gel.[49] Ion gel dielectrics are however better than previous solid polymer electrolytes, where the maximum switching speed has been estimated to be a few hundred hertz.[47] The maximum switching speed for ion gel transistors is approximately 1 MHz, when the minimum time for electric double layer formation is estimated as 1 μs.[12]

The aim of organic and printed electronics to produce low-cost flexible components presents another challenge when studying ion gels as dielectrics: electropositive metals such as copper can easily oxidize when in contact with an electrolyte at positive biases. Therefore only expensive noble metals such as gold, platinum or palladium can be used as metal electrodes.[12] This can be circumvented by using conductive polymers[49] or certain carbon-based conductors[12] as electrode materials. Organic semiconductors on the other hand are usually stable towards electrolytes.[12]

Ion gel gated transistors have another potential disadvantage concerning power consumption: in addition to their high on currents, they usually also have large off currents due to both static and dynamic leakage. One important source of static leakage current is water (as well as other impurities), which can cause electrochemical reactions at the electrodes. Dynamic leakage currents derive from the large capacitance of the ion gel which leads to large displacement currents when the transistor is switched. This can be addressed by decreasing the device size.[12,49]

5.2 Precedents

Previously in the group the use of different organic semiconductors, blended with polystyrene (PS), for the fabrication of OFETs have been reported. It was demonstrated that the application of the same printing formulation and experimental conditions gave rise highly reproducible and uniform crystalline films with high OFET performance.[39,40]

The deposition of the organic semiconductor blend solutions was performed by using the bar-assisted meniscus shearing technique (BAMS). This technique results in crystalline and uniform thin films of organic semiconductors onto rigid and flexible substrates with low material utilization. Further, BAMS is compatible with scalable roll-to-roll manufacturing processes for large-area and low-cost electronics.[39,40,53]

BAMS consists in pouring the organic semiconductor blend solution between a heated substrate and a smooth cylindrical bar positioned at a controlled distance forming a confined meniscus (schematically represented in Figure 5.9). Afterwards the bar is displaced along the whole extension of the substrate of interest yielding instantaneously a crystalline and uniform thin film due to the fast solvent evaporation.[39,40]

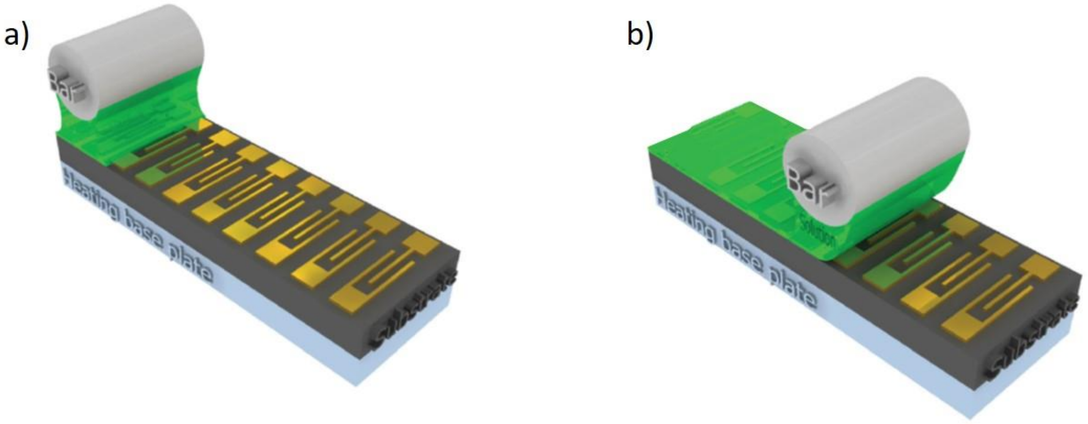

Figure 5.9 Representative sketch of BAMS method: a) formation of meniscus between the bar and the substrate, b) the bar is dragged along the substrate for the thin film deposition.[39]

5.3 Objectives

In the previous OFETs fabricated in the group by BAMS, SiO_2 was used as dielectric and, thus, gate voltages > 20 V were required to operate the devices. The goal of this chapter is to implement in such OFETs an ion gel formed by EMIM-TFSI ionic liquid and PVDF-HFP copolymer as gate dielectric. The high specific capacitance of the ion gel would lead to transistors with an operating voltage as low as 2 V. Furthermore, the processability of the ion gel solutions makes them compatible with low-cost and scalable fabrication techniques, as well as suitable to their application on flexible substrates.

For this purpose, three different OFET configurations were selected: bottom-gate, top-gate and side-gate geometry (Figure 5.10). In the first one it has been used Si/SiO_2 as reference system, while in the second one the ion gel was sandwiched between the gate electrode and the substrate with the semiconductor channel. Finally, in the side gate configuration, the ion gel is on top of the semiconductor layer and the source, drain and gate electrodes.

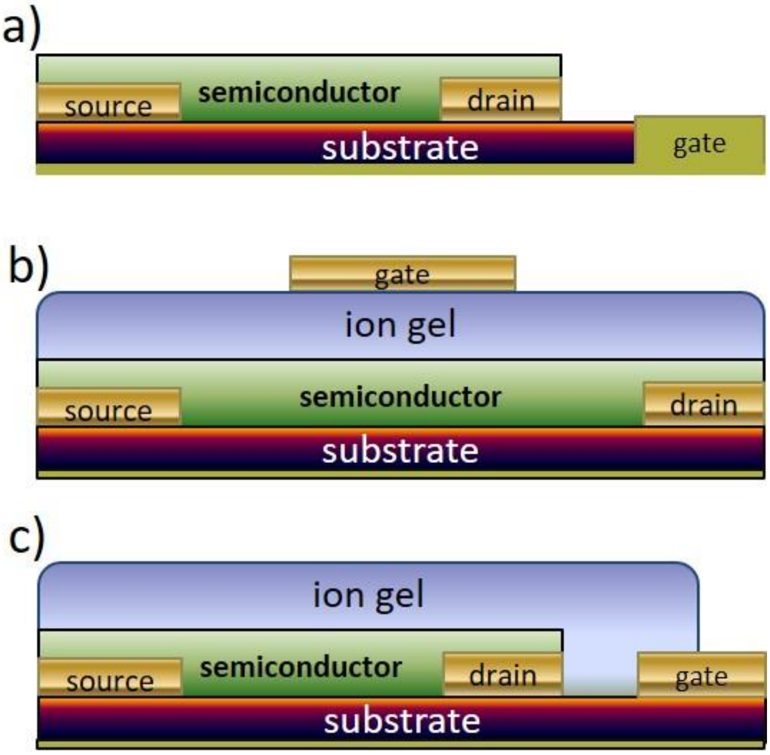

Figure 5.10. Cross sectional schematic of an OFET: a) Bottom gate bottom contact configuration, b) top ion gel gated with bottom contact, and c) side ion gel gated with bottom contact configuration.

The p-type semiconductor used in this work was 2,8-difluoro-5,11-bis(triethylsilylethynyl) anthradithiophene (diF-TES-ADT or also called herein diF), blended with polystyrene (PS) and deposited by bar-assisted meniscus shearing (BAMS) (represented in Figure 5.11). This semiconductor blend has already been processed by BAMS, gibing high-crystalline thin films in one single fabrication step and high field-effect mobility (~ 1 cm^2·V^{-1}·s^{-1}).[39,40,53]

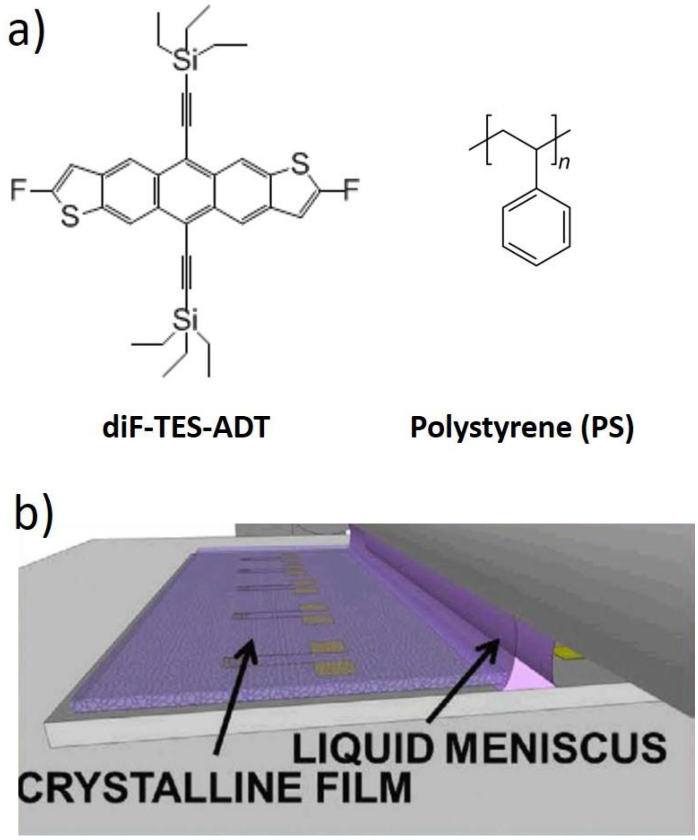

Figure 5.11 a) Chemical structures of diF-TES-ADT and PS, b) schematic representation of BAMS setup.[54]

5.4 Frequency dependence of the ion gel capacitance

Prior to the fabrication and electrical characterization of ion gel based devices, the ion gel solution was prepared following the same procedure as described in chapter 3, section 3.3.1. The ion gel solution was drop-casted onto a glass slide, and after evaporation of the solvent at room conditions, a clear 100 μm thick gel was obtained. For the determination of the specific capacitance of the ion gel, it was sandwiched between two planar gold disc electrodes of different diameter (10 and 20 mm), and the specific capacitance was measured as a function of frequency ($C = -1/(2\pi f \cdot Z_{im})$), where Z_{im} is the imaginary impedance and f is frequency). The results are displayed in Figure 5.12, where the measured capacitance is as large as 9.7 μF·cm^{-2} at low frequency (~1 Hz), in concordance with previous results performed by Lee et al.[55], and it is comparable to those of softer ion gels based on poly(styrene-b-methyl methacrylate-b-styrene) (SMS) triblock copolymers.[56]

Capacitance values decrease with increasing frequency, also known as capacitance dispersion. This has been attributed to the interaction between electrical charges on the electrode and counterions in the electrolyte, and is typical for electrolytes in contact with solid electrodes.[57,58]

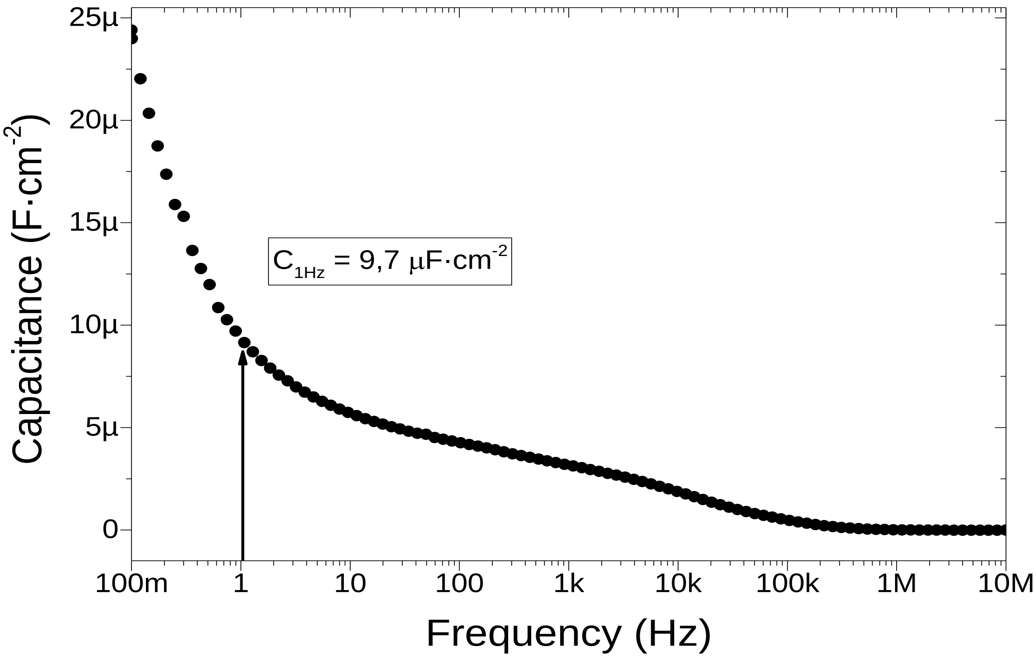

Figure 5.12 Frequency dependence of specific capacitance for a 100 μm thick free-standing ion gel based on PVDF-HFP copolymer and EMIM-TFSI ionic liquid.

5.5 Fabrication of OFET devices

A heavily doped n-type silicon wafer featuring thermal Si/SiO$_2$ (200 nm thick) was used as substrate for the devices. Source, drain and side-gate electrodes were defined by photolithography. The photolithography is divided into six different sub-processes, as it is depicted in Figure 5.13.

Initially it is important to clean the wafer with a flux of nitrogen to remove any possible dust particle. Then, the wafer is covered with a layer of pure hexamethyldisilazane (HMDS) and is spun coated at 5000 rpm with an acceleration of 4000 rpm/s during 25 seconds. After that, the photoresist (i.e. S1813) is carefully poured on the substrate at room temperature in order to evade bubble formation, and spin-coated at the same previously mentioned conditions. The photoresist-coated wafer is then prebaked to remove solvent excess, at 95 °C for 45 seconds on a hotplate.

After that, the photoresist is exposed to a pattern of intense UV light. In this step, the light source must be high energy sufficient to break the long-chain of resist polymer into shorter length such that they easily dissolve in the developer solution. Hence, UV light is directly applied above the mask onto the e-beam resist layer. The mask consists of interdigitated structures which are described by the channel length (L) and the channel width (W).

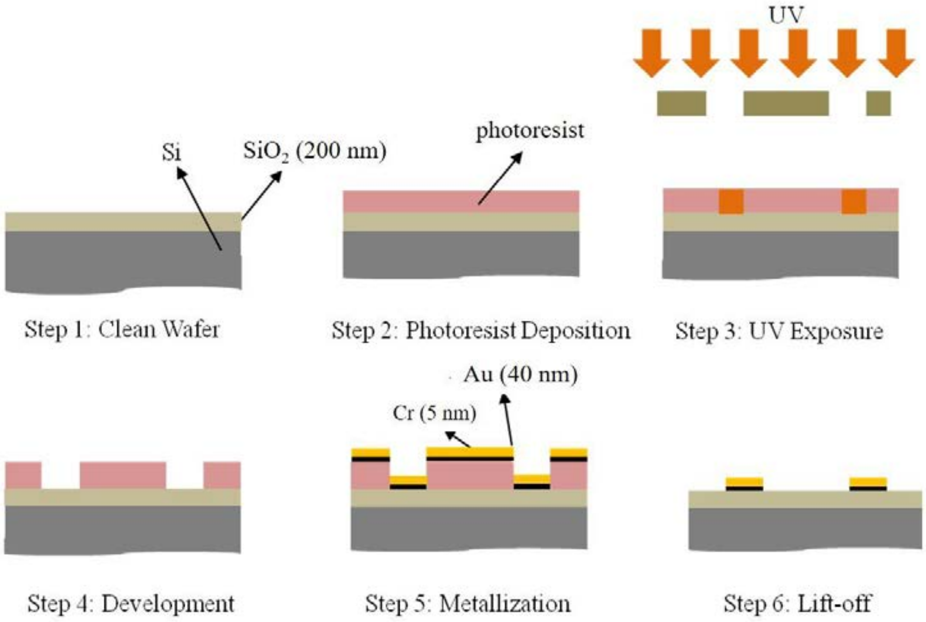

Figure 5.13 Schematic diagram depicting six major steps in the photolithography process for electrode fabrication.[59]

When the UV irradiation is finished, the wafer is immersed in a developer solution (i.e. MF-319) for at least 5 minutes in order to remove the exposed UV region, and cleaned with distilled water. The dried developed sample is then fed into the metallization chamber (e-beam evaporation) and a very thin layer of Cr/Au (5 nm/40 nm) is thermally evaporated on the sample. Chromium acts as the adhesion layer between gold (Au) and the silicon dioxide. After metallization, the substrates were immersed in acetone to remove the photoresist, taking the film with it, and leaving only the film which was deposited directly on the substrate (Figure 5.14). The channel width (W) and length (L) were 20700 µm and 30 µm, respectively (namely having a geometrical ratio W/L = 690).

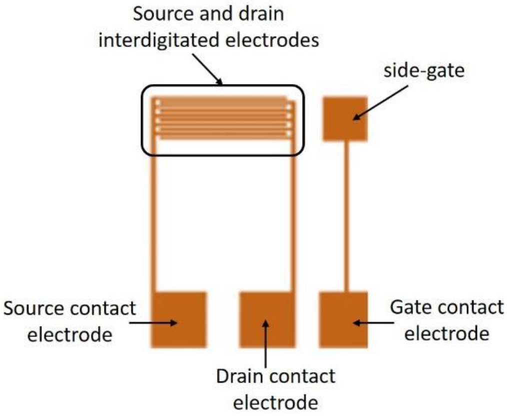

Figure 5.14 Schematic top-view of the OFET patterning with the interdigitated and side-gate electrodes indicated.

Prior to the deposition of the organic semiconductor solution, the substrates were cleaned in ultrasonic bath with acetone and isopropanol for 15 min respectively and afterwards ozone-treated for 25 min (for further experimental details, see chapter 6). A polyvinylpyrrolidone (PVP) water solution was deposited on top of the substrates, leaving the interdigitated area without covering. In this way, the organic semiconductor film will be directly deposited by BAMS on this uncovered region, and the rest of the semiconductor material will be easily removed with the PVP layer just by cleaning the substrates with milliQ-Q water.

As previously mentioned, diF-TES-ADT was selected as active material. The blend solution was prepared as previously reported by mixing diF-TES-ADT with polystyrene in a 4:1 ratio, and then dissolved in chlorobenzene reaching a final concentration of 2 wt%.[40] The blend solution was kept on a hot-plate at 105 °C for 1 h to ensure the complete dissolution of the two components. The blend coating was realized in ambient conditions through a home-adapted bar coater and keeping the substrate temperature at 105 °C. About 20 µL of the blend solution heated at the same temperature as the bed coater were deposited between the substrate and the bar, and immediately after that, the bar was sheared at a speed of 1 cm s^{-1}.

Firstly, it was checked the domain size of diF-TES-ADT films blended with PS (diF:PS, from now on) by using the polarized optical microscope (see Figure 5.15). The crystals of the semiconducting thin film do not show any dependency with respect to the bar-shearing direction because of the high deposition speed (i.e. 1 cm s^{-1}),[40] even though it is not observed uniform crystalline domains as previously described. This could be drive to the fact that, opposite to the reported work, there the electrodes were not functionalised with a pentafluorobenzenethiol (PFBT) SAM which enhances the semiconductor crystallisation. In any case, it was decided to perform this preliminary studies with these samples.

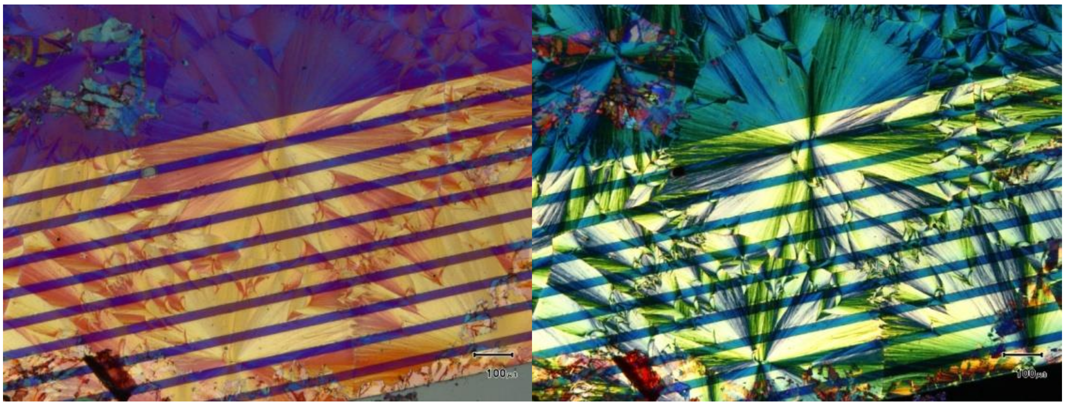

Figure 5.15 Optical microscopy images of diF:PS, acquired with a cross polarizer. On the left, polarizer/analyser = 0°. On the right, polarizer/analyser = 90°.

5.6 Electrical OFET characterization

A) Si/SiO2 back gate dielectric OFET characterization

To compare the ion gel properties with a more conventional dielectric, a reference transistor has been studied. For that, and since our substrate of choice is Si/SiO_2, the organic semiconductor diF:PS has been systematically characterized by using a bottom-gate bottom-contact configuration, as it was previously mentioned. The devices were electrically measured under ambient conditions and the corresponding results are presented in Figure 5.16 and Figure 5.17. This electrical cross-check along with the optical one allowed us to verify systematically the quality of our blend coating.

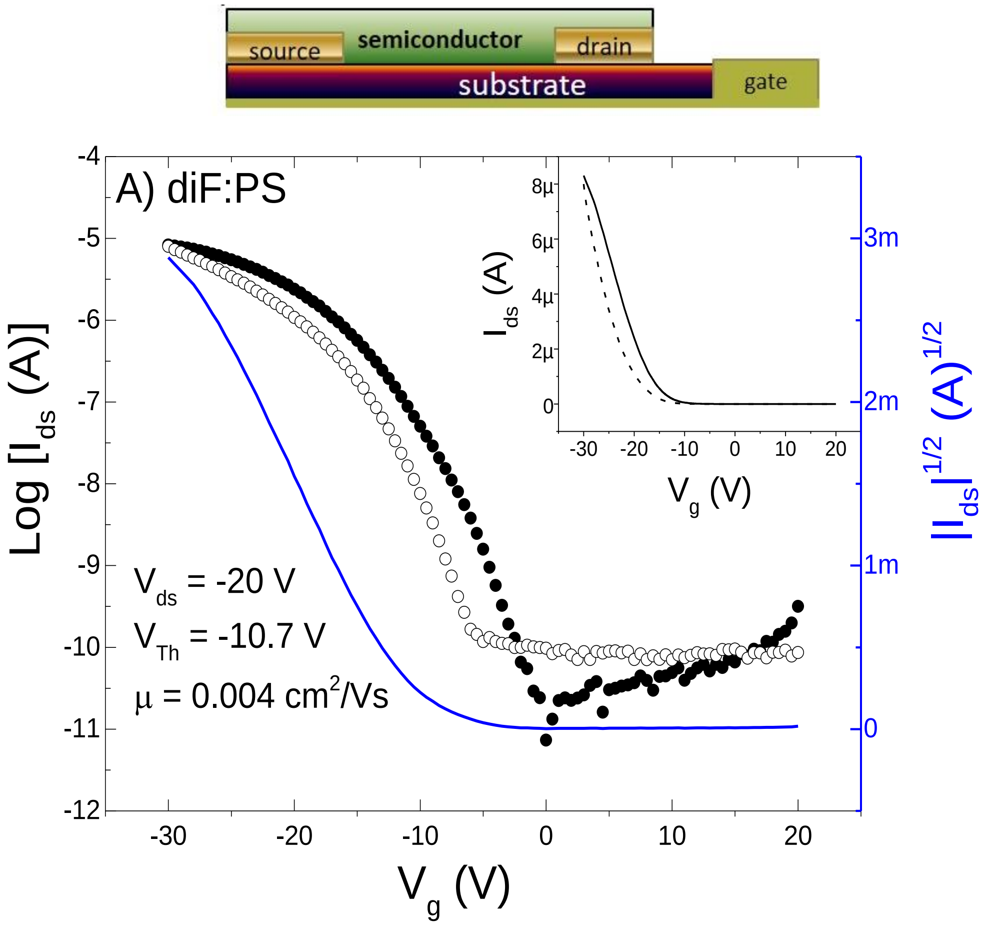

Figure 5.16 Log-Lin plot of the transfer characteristics of diF:PS devices in bottom-gate bottom-contact configuration. The inset is the corresponding Lin-Lin plot. Closed symbols correspond to forward, while open symbols correspond to reverse sweeps.

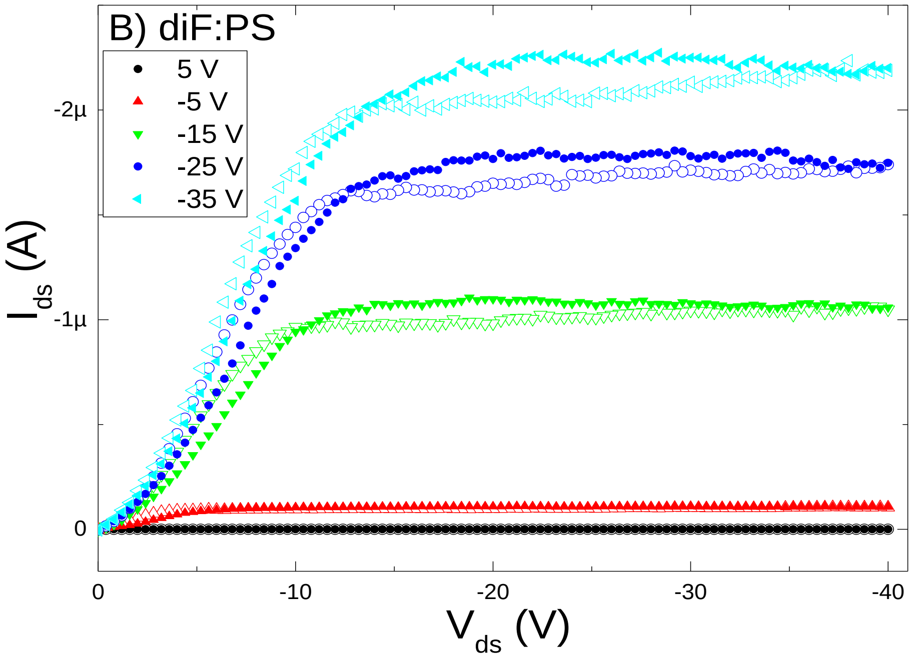

Figure 5.17. I-V output characteristics of diF:PS devices in bottom-gate bottom-contact configuration, with V_g spanning from +5 to -35 V with pace of 10 V. Closed symbols correspond to forward, while open symbols correspond to reverse sweeps.

The transfer characteristics sweeping the gate voltage were measured (Figure 5.16). The threshold voltage obtained was $V_{Th} = -10.7$ V. To obtain an estimate of the mobility, a straight line was fitted to the square root of the transfer curves. The mobility was calculated using Eq. 5.6, obtaining a mobility of ~0.004 $cm^2 \cdot V^{-1} \cdot s^{-1}$. In comparison with previously reported results in the group (around 1 $cm^2 \cdot V^{-1} \cdot s^{-1}$),[40] here it has been obtained lower values of mobilities, and this difference can be related to the non-homogeneous crystal domains of the semiconductor layer, promoting a decrease on the charge mobility.

As mentioned, one approach to improve the electrical performance of the devices consists in the pre-treatment of the source and drain electrodes, resulting in a better fine tuning of charge-injection and morphological homogeneity of the active material coating.[60] However, in this case, the functionalization of the source and drain interdigitated electrodes was not possible to perform without the modification of the side gate electrode, due to the solubility of the PVP film to the ethanolic solution of the functional group (e.g. PBFT) required for the surface modification.

The hysteresis observed in the electrical measurements is usually ascribed to the charge storage, the slow polarization of dielectric and/or charge trapping in the dielectric/ semiconductor interface. The device studied here, based on diF:PS semiconductor, shows an on/off ratio on the order of ~10^5 and subthreshold slope S = 2.8 V/decade.

Figure 5.17 displays the output characteristics of a diF:PS device at different gate voltages (V_g). The output characteristics show an increase in channel conductance with increasing V_g. Also, saturation in the drain current is observed in the high drain voltage regime. The low linearity observed at low V_{ds} voltages are an indication of a high contact resistance.

B) Ion gel top gated OFETs characterization

The first configuration studied for the electrical characterization of ion gel based OFETs had a top-gate bottom-contact structure, as depicted in Figure 5.10.b. The ion gel was placed on top of the channel region and the semiconductor layer, and the top gate contact was prepared by brush-painting silver paint. The output of the ion gel top-gated transistors was measured at different gate voltages and the results are presented in Figure 5.18. The output characteristics of the transistor display saturation behaviour, and the output current, I_{ds}, is greater than 1.0 μA at V_g = -1.3 V and V_{ds} = -0.4 V. Thus, high current is achieved at low operating voltages (~ two orders of magnitude less than when SiO_2 was used).

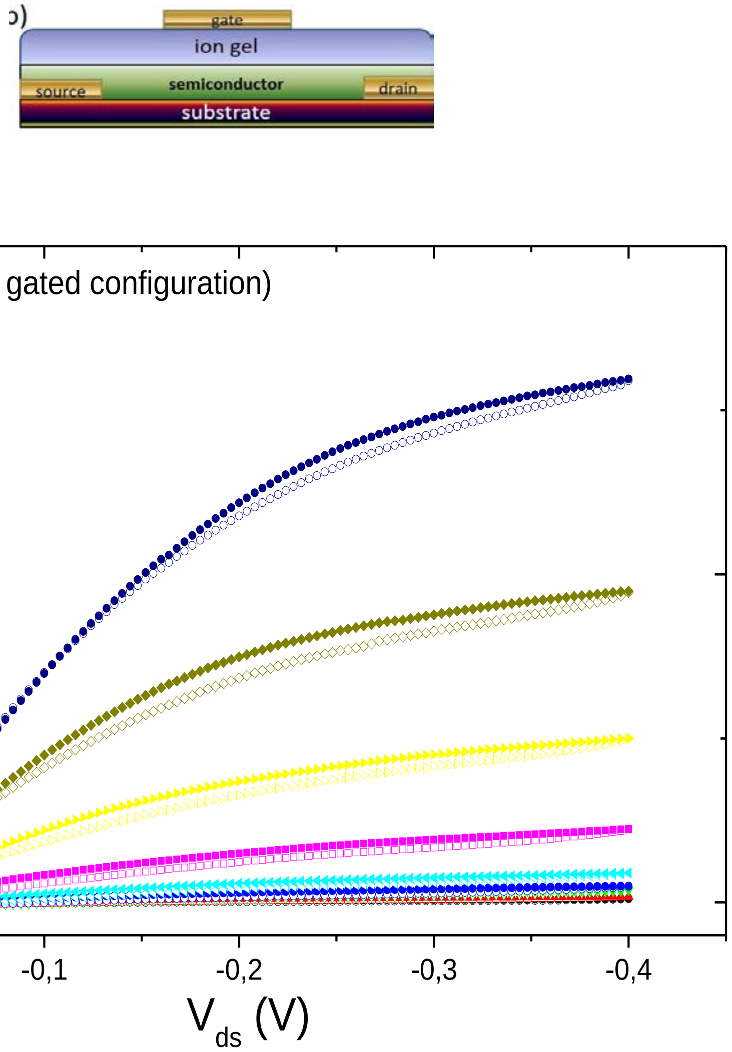

Figure 5.18 Output characteristics of diF:PS top-gate ion gel based OFET, with V_g spanning from -0.5 to -1.3 V with pace of -0.1 V. Closed symbols correspond to forward, while open symbols correspond to reverse sweeps.

The transfer characteristics of the ion gel top-gated OFET was measured for a drain voltage of –0.4 V and the result is presented in Figure 5.19. The square root of the drain current forward sweep is also plotted to extract the field-effect mobility.

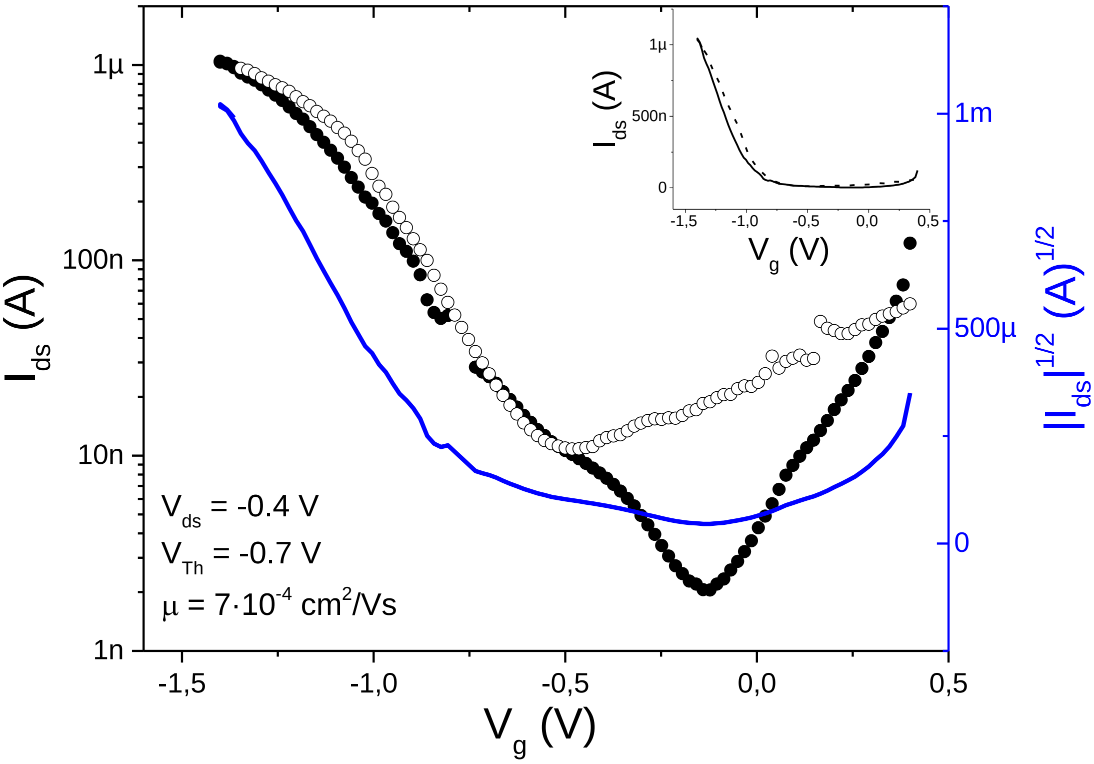

Figure 5.19 Transfer characteristics in the saturation regime and extraction of mobility and threshold voltage of diF:PS ion gel based OFET in top-gate configuration. The inset is the corresponding Lin-Lin plot.

The mobility was calculated using Eq. 5.6, as previously explained, and using the experimental capacitance value obtained (at 1 Hz of frequency) for the ion gel. The mobility calculated from the curve was $7 \cdot 10^{-4}$ $cm^2 \cdot V^{-1} \cdot s^{-1}$. This value is lower than the reference OFET device previously characterized. This can be explained by charge trapping, or other forms of anomalous dispersion, in which charge carriers undergo relaxation, leading to a decrease of mobility.[61] Moreover, on/off ratio is less than 10^3, and the subthreshold slope voltage extracted from the logarithmic plot of the transfer curve is 0.4 V/decade. This large value of the off current can be due to static and dynamic leakage. One important source of static leakage current is water or other impurities, which can cause electrochemical reactions at the electrodes. Dynamic leakage currents can be derived from the large capacitance of the ion gel, which leads to large displacement currents when the transistor is switched.[12,49]

C) Ion gel side gated OFET characterization

In order to improve the results obtained with ion gel top-gated OFETs, an alternative configuration device was proposed, which consists in the use of a side-gate bottom-contact structure, depicted in Figure 5.10.c. Such non-conventional device configuration has the advantage that the device fabrication process is simplified because all electrodes were patterned simultaneously and precise alignment of the gate electrode on the semiconductor channel was not required. The free-standing ion gel was simply laminated over the diF:PS semiconductor layer and the side-gate electrode, and measured under ambient conditions.

In the electrical characterization of these devices, the output response and the transfer characteristics were also measured, which are shown in Figure 5.20 and Figure 5.21, respectively. The output characteristics for the side-gated OFET demonstrate that the free-standing ion gel can modulate the electron current properly.

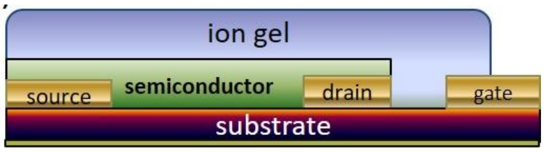

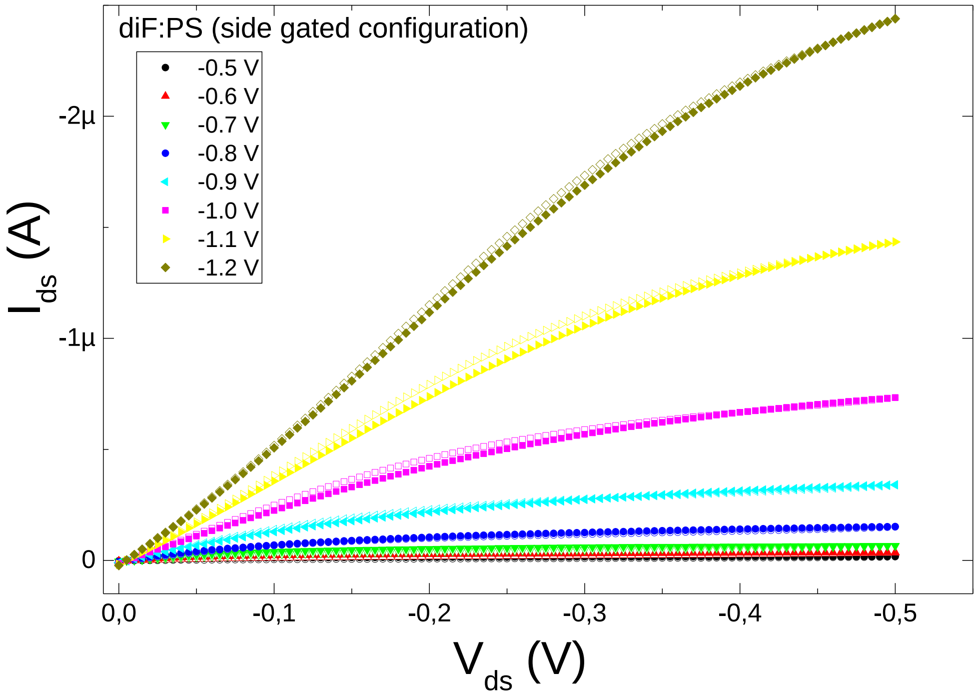

Figure 5.20 Output characteristics of diF:PS ion gel gated OFET, with V_g spanning from -0.5 to -1.2 V with pace of -0.1 V. Closed symbols correspond to forward, while open symbols correspond to reverse sweeps.

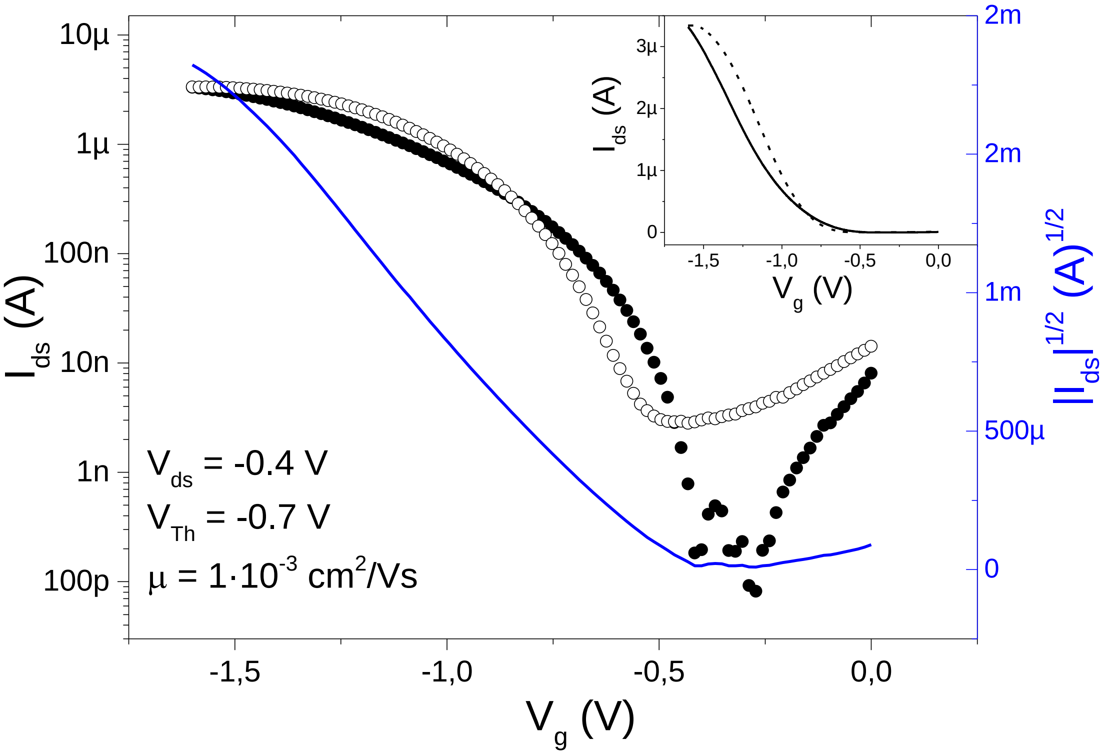

Figure 5.21 Transfer characteristics in the saturation regime and extraction of mobility and threshold voltage of diF:PS ion gel based OFET in side-gate configuration. The inset is the corresponding Lin-Lin plot.

The transfer characteristics of the diF:PS ion gel gated OFET was measured for different drain voltages and the results presented in Figure 5.21 correspond to V_{ds} = –0.4 V, in the saturation regime. The threshold voltage obtained was V_{Th}= -0.7 V, and the subthreshold slope S extracted from the logarithmic plot of the transfer curves was approximately S = 0.2 V/decade. This value is very low compared with conventional OFETs, but is of the order of previous reported ion gel gated transistors (0.1 - 0.2 V/decade, approximately). So that, the value obtained here does agree with the results in the literature. This ion gel based OFET operates at low voltage (below 2 V) and exhibits an on/off current ratio in the range of ~10^4, which is in the same order than other ion gel tri-block polymer based devices.[20] Again, some current hysteresis is observed between forward and reverse sweeps. Besides the previous factors that can generate this hysteresis process, here it can also be related to the ionic liquid used here, EMIM-TFSI. It is known that this ionic liquid is hydrophobic (not miscible with water). But it is also hygroscopic and can absorb a certain amount of water from the air, making the gel susceptible to water impurities. The impurities can cause hysteresis due to electrochemical reactions at the electrodes even at low voltages.

Since the transfer curve is in the saturation region, the square root of the drain current forward sweep is also plotted in Figure 5.21. The mobility in this case was calculated using the value for the capacitance, 9.7 μF/cm^2, obtaining $\mu \approx 0.001$ cm$^2 \cdot$V$^{-1} \cdot$s^{-1}. Comparing this result with the one obtained in the ion gel top-gate configuration, it can be seen that the mobility has increased, being close to the mobilities extracted from the reference OFET device (where SiO_2 was used as dielectric layer).

The lower μ of the ion gel devices can be attributed to the different semiconductor-dielectric interface. Morphological defects, such as the interface roughness, together with the orientation of the molecules, can reduce the performance of the device. Furthermore, there is experimental evidence for a lowering of the mobility with an increasing dielectric constant of the insulating layer.[42,62] Higher dielectric constant of the insulating layer can cause a broader distribution of the electronic states in the organic semiconductor, resulting in the reduced charge carrier mobility.

Finally, in Table 5.1 the results obtained for the three different configuration devices used in this study are presented. Despite the slightly decrease of the field-effect mobility by using the ion gel as dielectric, it has been obtained devices that operate at lower voltages with suitable on/off ratio values.

Gate configuration and dielectric material	**μ (cm$^2 \cdot$V$^{-1} \cdot$s^{-1})**	**V_{Th} (V)**	**S (V/decade)**	**$I_{ON/OFF}$**
Bottom-gated SiO_2	$4 \cdot 10^{-3}$	-10.7	2.8	10^5
Top-gated IG	$7 \cdot 10^{-4}$	-0.7	0.4	$< 10^3$
Side-gated IG	$1 \cdot 10^{-3}$	-0.7	0.2	10^4

Table 5.1 Summary of results obtained for the three different OFET device configurations.

5.7 Summary

In summary, organic field-effect transistor using an ion gel as a high capacitance gate dielectric layer have been fabricated. The specific capacitance was over 10 $\mu F \cdot cm^{-2}$ at low frequency, a value that is comparable to that reported for ion gels based on block copolymers and other conventional electrolytes. It is also important to highlight the compatibility of the ion gel solution with low-cost and scalable processed techniques, also being suitable for their application on flexible substrates.

In this preliminary study, the ion gel was prepared by drop-casting, and after that, was transferred and laminated onto the OFET device using top-gated and side-gated transistor configurations. Herein, the use of ion gels has allowed the development of operating devices within a characteristic narrow operating voltage range of below 2 V and on/off current ratio of $\sim 10^4$.

Despite the lower mobility values, future work in this area will be devoted to improve the performance of the device by:

i) Optimising the fabrication of the semiconductor film
    a. Isolating in a proper way the gate electrode from the interdigitated area before the deposition of the organic semiconductor solution
    b. Using surface pre-treatments of the source and drain electrodes to obtain higher morphological homogeneity of the active material layer

ii) Fabricating the ion gel layer by BAMS, so in this way it can be applied with low cost and scalable preparation processes.

Overall, these results demonstrate that the ion gels are highly appealing as electrolyte dielectrics to be applied in low cost and flexible organic transistors.

5.8 References

1 C. K. Chiang, C. R. Fincher, Y. W. Park, A. J. Heeger, H. Shirakawa, E. J. Louis, S. C. Gau and A. G. MacDiarmid, *Phys. Rev. Lett.*, 1977, **39**, 1098–1101.

2 J. H. Burroughes, D. D. C. Bradley, A. R. Brown, R. N. Marks, K. Mackay, R. H. Friend, P. L. Burns and A. B. Holmes, *Nature*, 1990, **347**, 539–541.

3 H. Hoppe and N. S. Sariciftci, *J. Mater. Res.*, 2004, **19**, 1924–1945.

4 K. E. Lilja, T. G. Bäcklund, D. Lupo, T. Hassinen and T. Joutsenoja, *Org. Electron.*, 2009, **10**, 1011–1014.

5 A. Tsumura, H. Koezuka and T. Ando, *Appl. Phys. Lett.*, 1986, **49**, 1210–1212.

6 T. N. Jackson, Yen-Yi Lin, D. J. Gundlach and H. Klauk, *IEEE J. Sel. Top. Quantum Electron.*, 1998, **4**, 100–104.

7 C. D. Sheraw, L. Zhou, J. R. Huang, D. J. Gundlach, T. N. Jackson, M. G. Kane, I. G. Hill, M. S. Hammond, J. Campi, B. K. Greening, J. Francl and J. West, *Appl. Phys. Lett.*, 2002, **80**, 1088–1090.

8 L. Zhou, A. Wanga, S.-C. Wu, J. Sun, S. Park and T. N. Jackson, *Appl. Phys. Lett.*, 2006, **88**, 083502–083504.

9 E. Cantatore, T. C. T. Geuns, G. H. Gelinck, E. van Veenendaal, A. F. A. Gruijthuijsen, L. Schrijnemakers, S. Drews and D. M. de Leeuw, *IEEE J. Solid-State Circuits*, 2007, **42**, 84–92.

10 M. E. Roberts, S. C. B. Mannsfeld, N. Queraltó, C. Reese, J. Locklin, W. Knoll and Z. Bao, *Proc. Natl. Acad. Sci. U. S. A.*, 2008, **105**, 12134–9.

11 T. Sekitani, T. Yokota, U. Zschieschang, H. Klauk, S. Bauer, K. Takeuchi, M. Takamiya, T. Sakurai and T. Someya, *Science*, 2009, **326**, 1516–1519.

12 Y. Xia, W. Zhang, M. Ha, J. H. Cho, M. J. Renn, C. H. Kim and C. D. Frisbie, *Adv. Funct. Mater.*, 2010, **20**, 587–594.

13 Y. D. Park, D. H. Kim, Y. Jang, M. Hwang, J. A. Lim and K. Cho, *Appl. Phys. Lett.*, 2005, **87**, 243509.

14 R. C. G. Naber, C. Tanase, P. W. M. Blom, G. H. Gelinck, A. W. Marsman, F. J. Touwslager, S. Setayesh and D. M. de Leeuw, *Nat. Mater.*, 2005, **4**, 243–248.

15 C. D. Dimitrakopoulos, *Science (80-.).*, 1999, **283**, 822–824.

16 M. Halik, H. Klauk, U. Zschieschang, G. Schmid, C. Dehm, M. Schütz, S. Maisch, F. Effenberger, M. Brunnbauer and F. Stellacci, *Nature*, 2004, **431**, 963–966.

17 M.-H. Yoon, A. Facchetti and T. J. Marks, *Proc. Natl. Acad. Sci. U. S. A.*, 2005, **102**, 4678–4682.

18 L. Herlogsson, X. Crispin, N. D. Robinson, M. Sandberg, O.-J. Hagel, G. Gustafsson and M. Berggren, *Adv. Mater.*, 2007, **19**, 97–101.

19 N. J. Kaihovirta, C.-J. Wikman, T. Mäkelä, C.-E. Wilén and R. Österbacka, *Adv. Mater.*, 2009, **21**, 2520–2523.

20 J. Lee, L. G. Kaake, J. H. Cho, X.-Y. Zhu, T. P. Lodge and C. D. Frisbie, *J. Phys. Chem. C*, 2009, **113**, 8972–8981.

21 B. G. Streetman and S. Banerjee, *Solid state electronic devices*, Pearson Prentice Hall, San Francisco, 7th ed., 2006.

22 C. A. & H. N. Lab, 2017. Available from: *http://www.cstf.kyushu-u.ac.jp/~adachilab/lab/?page_id=3898*.

23 D. Braga and G. Horowitz, *Adv. Mater.*, 2009, **21**, 1473–1486.

24 G. Horowitz, *Adv. Mater.*, 1998, **10**, 365–377.

25 H. Sirringhaus, *Adv. Mater.*, 2005, **17**, 2411–2425.

26 M. Shur, *Physics of semiconductor devices*, Prentice Hall, 1990.

27 T. Uemura, Y. Hirose, M. Uno, K. Takimiya and J. Takeya, *Appl. Phys. Express*, 2009, **2**, 111501–111503.

28 A. Kraft, in *Organic Molecular Solids*, ed. W. Jones, CRC Press, 1997.

29 A. Facchetti, *Mater. Today*, 2007, **10**, 28–37.

30 F. G. Del Pozo, *Coating Engineering of Composite Materials for Organic Field-Effect Transistors,* PhD. Thesis, Universidad Autònoma de Barcelona, 2014.

31 V. Coropceanu, J. Cornil, D. A. da Silva Filho, Y. Olivier, R. Silbey and J.-L. Brédas, *Chem. Rev.*, 2007, **107**, 926–952.

32 C. D. Dimitrakopoulos and D. J. Mascaro, *IBM J. Res. Dev.*, 2001, **45**, 11–27.

33 A. L. Briseno, S. C. B. Mannsfeld, X. Lu, Y. Xiong, S. A. Jenekhe, Z. Bao and Y. Xia, *Nano Lett.*, 2007, **7**, 668–675.

34 D. H. Kim, D. Y. Lee, H. S. Lee, W. H. Lee, Y. H. Kim, J. I. Han and K. Cho, *Adv. Mater.*, 2007, **19**, 678–682.

35 M. Mas-Torrent, M. Durkut, P. Hadley, X. Ribas and C. Rovira, *J. Am. Chem. Soc.*, 2004, **126**, 984–985.

36 C. Kloc, P. G. Simpkins, T. Siegrist and R. A. Laudise, *J. Cryst. Growth*, 1997, **182**, 416–427.

37 Y. Xu, C. Liu, D. Khim and Y.-Y. Noh, *Phys. Chem. Chem. Phys.*, 2015, **17**, 26553–26574.

38 J. Smith, R. Hamilton, I. McCulloch, N. Stingelin-Stutzmann, M. Heeney, D. D. C. Bradley, T. D. Anthopoulos, J. Rysz, T. D. Anthopoulos, P. Smith, H. Sirringhaus, R. J. Kline, M. D. McGehee, M. F. Toney, B. J. E. v. Rens and D. M. d. Leeuw, *J. Mater. Chem.*, 2010, **20**, 2562-2574.

39 F. G. del Pozo, S. Fabiano, R. Pfattner, S. Georgakopoulos, S. Galindo, X. Liu, S. Braun, M. Fahlman, J. Veciana, C. Rovira, X. Crispin, M. Berggren and M. Mas-Torrent, *Adv. Funct. Mater.*, 2016, **26**, 2379–2386.

40 I. Temiño, F. G. Del Pozo, M. R. Ajayakumar, S. Galindo, J. Puigdollers and M. Mas-Torrent, *Adv. Mater. Technol.*, 2016, **1**, 1600090.

41 M. R. Niazi, R. Li, M. Abdelsamie, K. Zhao, D. H. Anjum, M. M. Payne, J. Anthony, D.-M. Smilgies and A. Amassian, *Adv. Funct. Mater.*, 2016, **26**, 2371–2378.

42 J. Veres, S. Ogier, G. Lloyd and D. de Leeuw, *Chem. Mater.*, 2004, **16**, 4543–4555.

43 L.-L. Chua, P. K. H. Ho, H. Sirringhaus and R. H. Friend, *Appl. Phys. Lett.*, 2004, **84**, 3400–3402.

44 G. Barnes and I. Gentle, *Interfacial science : an introduction*, Oxford University Press, 2011.

45 J. Veres, S. D. S. D. Ogier, S. W. S. W. Leeming, D. C. D. C. Cupertino, S. Mohialdin Khaffaf and S. M. Khaffaf, *Adv. Funct. Mater.*, 2003, **13**, 199–204.

46 J. Lee, M. J. Panzer, Y. He, T. P. Lodge and C. D. Frisbie, *J. Am. Chem. Soc.*, 2007, **129**, 4532–4533.

47 M. J. Panzer and C. D. Frisbie, *J. Am. Chem. Soc.*, 2007, **129**, 6599–6607.

48 J. H. Cho, J. Lee, Y. He, B. Kim, T. P. Lodge and C. D. Frisbie, *Adv. Mater.*, 2008, **20**, 686–690.

49 J. H. Cho, J. Lee, Y. Xia, B. Kim, Y. He, M. J. Renn, T. P. Lodge and C. Daniel Frisbie, *Nat. Mater.*, 2008, **7**, 900–906.

50 Z. Bao, A. Dodabalapur and A. J. Lovinger, *Appl. Phys. Lett.*, 1996, **69**, 4108–4110.

51 Z. Bao, Y. Feng, A. Dodabalapur, V. R. Raju and A. J. Lovinger, *Chem. Mater.*, 1997, **9**, 1299–1301.

52 S. Lehtimäki, *Ion gels as gate dielectrics in Organic Thin-Film Transistors,* Masters Thesis, Tamper University of Technology, 2011.

53 S. Georgakopoulos, F. G. del Pozo and M. Mas-Torrent, *J. Mater. Chem. C*, 2015, **3**, 12199–12202.

54 Q. Zhang, F. Leonardi, S. Casalini, I. Temiño and M. Mas-Torrent, *Sci. Rep.*, 2016, **6**, 39623.

55 K. H. Lee, M. S. Kang, S. Zhang, Y. Gu, T. P. Lodge and C. D. Frisbie, *Adv. Mater.*, 2012, **24**, 4457–4462.

56 K. H. Lee, S. Zhang, T. P. Lodge and C. D. Frisbie, *J. Phys. Chem. B*, 2011, **115**, 3315–3321.

57 Z. Kerner and T. Pajkossy, *Electrochim. Acta*, 2000, **46**, 207–211.

58 T. Pajkossy, *Solid State Ionics*, 2005, **176**, 1997–2003.

59 Dnanotech,2011. Available from: *http://www.dileepnanotech.com*.

60 D. J. Gundlach, J. E. Royer, S. K. Park, S. Subramanian, O. D. Jurchescu, B. H. Hamadani, a J. Moad, R. J. Kline, L. C. Teague, O. Kirillov, C. A. Richter, J. G. Kushmerick, L. J. Richter, S. R. Parkin, T. N. Jackson and J. E. Anthony, *Nat. Mater.*, 2008, **7**, 216–221.

61 J. C. Blakesley, F. A. Castro, W. Kylberg, G. F. A. Dibb, C. Arantes, R. Valaski, M. Cremona, J. S. Kim and J.-S. Kim, *Org. Electron.*, 2014, **15**, 1263–1272.

62 I. N. Hulea, S. Fratini, H. Xie, C. L. Mulder, N. N. Iossad, G. Rastelli, S. Ciuchi and A. F. Morpurgo, *Nat. Mater.*, 2006, **5**, 982–986.

Chapter 6

Experimental part

CHAPTER 6. Experimental Part

6.1 Techniques and instrumentation

6.1.1 Spectroscopy and Spectrometry

- **Fourier Transform Infrared Spectroscopy (FT-IR)**: The spectra of the samples were performed by using the Spectrum One FT-IR Spectrometer from Perkin Elmer with the universal ATR Polarization accessory.

- **Polarization Modulation-Infrared Reflection-Adsorption Spectroscopy (PM-IRRAS)**: Experiments were performed by using the IR-Spectrometer Vertex 70 from Bruker. The experiments were performed in a sample compartment purged with nitrogen to reduce atmospheric interferences (angle of incidence 80°, spectra collection for 5 min).

- **X-ray Photoelectron Spectroscopy (XPS):** X-ray Photoelectron Spectroscopy measurements were performed at the Solid and Surfaces Characterization Services (SACSS) of Extremadura University by Daniel Gamarra, with a K-Alpha from Thermo Scientific in ultra-high vacuum conditions (base pressure $5x10^{-10}$ mbar) with a monochromatic $Al_{K\alpha}$ X-ray source (1486.74 eV). The energy resolution measured by the FWHM of the Ag 3d5/2 peak for a sputtered silver foil was 0.6 eV. The spot size was 3.5 mm by 0.5 mm.

- **Time-of-Flight Secondary Ion Mass Spectrometry (ToF-SIMS):** Time of Flight Secondary Ions Mass Spectrometry measurements were performed at the Solid and Surfaces Characterization Services (SACSS) of Extremadura University by Daniel Gamarra with a TOF-SIMS5 under the following specific conditions of analysis: primary gun energy of 25 KV, extractor energy of 9 KV, emission current 1.05 µA; employing Bi_3^{++} with an intensity of the primary ions of 0.25 pA. The experiments were performed under vacuum at $2.3 \cdot 10^{-9}$ mbar. The spot size was (200 x 200) μm^2 with a resolution of 128 x 128 pixels, collecting above of $1 \cdot 10^{12}$ ions $\cdot cm^{-2}$ of ionic density per spectrum.

6.1.2 Electrochemistry

- **Cyclic Voltammetry (CV):** CV measurements were performed in different homemade electrochemical cells with a potentiostat-galvanostat VersaSTAT3 from Princeton Applied Research, a Bio-Logic VMP3 potentiostat, and a Novocontrol Alpha-AN impedance analyser equipped with a potentiostat POT/GAL 30V/2A electrochemical interface.

- **Electrochemical Impedance Spectroscopy (EIS):** The EIS experiments were recorded by using a Bio-Logic VMP3 potentiostat, and a Novocontrol Alpha-AN impedance analyser equipped with a potentiostat POT/GAL 30V/2A electrochemical interface. The impedance measurements were obtained at different DC potentials, and were superimposed on a sinusoidal potential modulation of ±5 mV (Vrms). The resulting current was recorded over a frequency domain of 100 KHz to 500 mHz. Thirty points, equally spaced on a logarithmic scale, were acquired per decade increment in frequency. All experiments were performed at room temperature.

- **Capacitance switching measurements:** The AC impedance switching process was recorded at 1 Hz using a Novocontrol Alpha-AN impedance analyser equipped with a potentiostat POT/GAL 30V/2A electrochemical interface. A low AC voltage of 5 mV was superimposed at different applied DC bias. These cycling experiments were performed by pre-biasing the sample at the corresponding DC voltage for each state, during 5 seconds in the case of liquid electrolytes, and 15 seconds for the solid ion gels.

- **Organic field-effect transistor (OFET) electrical measurements:** Electrical measurements were acquired at ambient conditions using an Agilent 5100A and Easy Expert software. The samples were contacted with a SÜSS probe station.

6.1.3 Other techniques

- **Scanning Electron Microscopy (SEM):** SEM images were acquired in the scientific and technical services of ICMAB by Dr. Judith Oró in a QUANTA FEI 200 FEG-ESEM in a high vacuum mode (HV). SEM was used to characterize the surface morphology and to obtain the thicknesses of the ion-gel films.

- **Atomic Force Microscopy (AFM):** AFM images were performed in the scientific and technical services of ICMAB by Maite Simón in the dynamic mode using 5500LS SPM system from Agilent Technologies.

- **Contact Angle:** Measurements were carried out using a System DSA 100 from KRÜSS in the clean room facilities. The DSA100 is equipped with software for measuring the contact angle and surface tension of a liquid. Moreover, the contact angle experiments were carried out with 3 μL drops of liquid keeping high reproducibility between the replicas due to the automatic dispenser.

- **Spinner:** Spin-coating films were performed with a spinner equipment from Laurell Technologies model WS-650SZ-6NPP/LITE.

- **Differential Scanning Calorimetry (DSC):** A differential scanning calorimeter analysis was performed in the scientific and technical services of ICMAB by Roberta Ceravola on a Perkin Elmer DSC8500 LAB SYS equipped with a Liquid N_2 controller CRYOFILL. The measurements were conducted with the samples heated from room temperature to 200 °C followed by cooling to -50 °C, and then heating again up to 200 °C at a cooling and heating rate of 10 °C $\cdot$min^{-1}.

- **UV/Ozone cleaner:** JetLight UVO-Cleaner® 42 was used to clean the substrates before the preparation of SAMs or OFET devices. The application of UV-ozone cleaning is highly effective in removing organic contaminants from Au surfaces.

- **Glovebox:** Glove Box GP (Concept)-II-P from JACOMEX, with electrical measurement system and organic evaporator inside. This glove box was used to make processes under restrictive atmosphere to oxygen and water in an environment of nitrogen.

6.2 Reagents and solvents

- **Solvents**: HPLC solvents dichloromethane (DCM), acetone, absolute ethanol (EtOH), isopropanol, acetonitrile (ACN), tetrahydrofuran (THF), toluene (TOL) chlorobenzene (CB) and benzonitrile (BzN) were supplied by Teknokroma and were from the ROMIL-SpS category (Super purity Solvents). Perchloric acid 60% ($HClO_4$) in ACS grade was purchased from Panreac. Water used in electrochemical experiments was purified with a MilliQ ultrapure water filtration system (Merck-Millipore) to a resistivity of at least 18.2 MΩ cm (25°C). Acetone extra dry (99.8%), for the preparation of solid ion gels, was purchased by Acros Organics (Fisher Scientific).

- **Ionic liquids (ILs):** 1-Ethyl-3-methylimidazolium bis(trifluoromethylsulfonyl)imide (EMIM-TFSI), 1-Ethyl-3-methylimidazolium ethyl sulphate (EMIM-$EtSO_4$), 1-Ethyl-3-methylimidazolium tetrafluoroborate (EMIM-BF_4) and 11-Butyl-3-methylimidazolium trifluoromethanesulfonate (BMIM-OTf) were supplied by Aldrich and generally dried under vacuum at 70 °C for 24h prior to their use. In order to remove water contamination from BMIM-OTf, it was dried by sparging nitrogen through the IL while heating at 100°C for 2 hours, and then it was immediately placed over a dry molecular sieves and kept in the glove box under nitrogen.

- **Polymers:** Polystyrene (PS) ($M_w \approx 3000$ g mol^{-1}) and pellets of poly(vinylidene fluoride-co-hexafluoropropylene) (PVdF-HFP) ($M_w \approx 400{,}000$, $M_n \approx 130{,}000$) were purchased from Sigma-Aldrich and used as received.

- **Electrolyte salts**: Tetrabutylammonium hexafluorophosphate (Bu_4NPF_6), ammonium hexafluorophosphate (NH_4PF_6) potassium hexafluorophosphate (KPF_6), and lithium perchlorate ($LiClO_4$) were supplied by Aldrich and used as received.

- **SAM compounds:** 11-(Ferrocenyl) undecanethiol ($FcC_{11}SH$) was purchased from Aldrich and used as received. Anthraquinone derivatives (AQ) were synthesized by Dr. Francisco Javier Casado in NANOMOL group. Tetrathiafulvalene derivatives (TTF) were synthesized by M. Serena Maglione in NANOMOL group. For the TTF derivative synthesis, 2-formyltetrathiafulvalene was purchased from TCI Chemicals, while $NaBH_4$ and thioctic acid were bought from Sigma-Aldrich. All the reagents were used without further purification. Perchlorotriphenylmethyl radical (PTM-$(CH_2)_n$-SH) derivatives were synthesized by Dr. Carlos Franco in NANOMOL group, and the details of the synthesis are described in "Chemical control over the energy-level alignment in a two-terminal junction" *Nature Communications* **2016** (7) 12066-12075.

- **Organic semiconductors:** 2,8-difluoro-5,11-bis(triethylsilylethynyl) anthradithiophene (diF-TES-ADT) was purchased from Lumtec.

- **Substrates for SAMs**: Gold (111) substrates consisting of 300 nm Au on mica were purchased from Georg Albert PVD-Beschichtungen. Commercial Au substrates consisting of 50 nm of Au on glass were purchased from Phasis. Evaporated gold for co-planar electrodes were prepared through a homemade mask by evaporating a Cr/Au layer (15 nm/75 nm) on a glass slide of 1 mm of thickness. A System Auto 306 evaporator from Boc Edwards was used for the thermal evaporation.

- **Electrodes for OFETs**: The devices were fabricated on heavily doped n-type Si wafer (purchased from Si-mat) with a 200 nm thick layer of SiO_2. Before the organic semiconductor coating, source (S) and drain (D) electrodes were patterned using photolithography (MicroWriter MLTM Laser Lithography System) and thermally evaporating a Cr/Au (5 nm/40 nm) layer (system Auto 306 from Boc Edwards). The positive photoresist and developer used in this work were Microposit S1813 and MF-319, respectively. The last step of the electrodes fabrication is the so called "lift-off" that consists in the immersion of the substrates in acetone to remove the photoresist. The channel width (W) and length (L) were 20700 µm and 30 µm, namely having a geometrical ratio W/L = 690.

6.3 Preparation of ion gels

For the preparation of the ion gel, initially, the polymer (PVdF-HFP) is dissolved in acetone in a weight ratio 1:10 of polymer to solvent. The polymer solution is stirred continuously until a homogeneous mixture is achieved. Then the ionic liquid (EMIM-TFSI) is added to the solution in a mass ratio 1:4 of polymer to IL. The solution was prepared at room temperature and argon atmosphere. The drop-casting method is used for the preparation of the ion gels onto the planar home-made electrochemical cell delimiting the area with a silicon mask. The films were prepared inside an argon atmosphere glovebox ([O_2] < 1 ppm; [H_2O] < 1.5 ppm), where the solvent was allowed to evaporate. In the case of ion gels deposited by spin coating, the conditions were fixed at spin speed of 1000 rpm, and spin time of 30s. The thickness of the ion-gel films was varied by changing the volume of solution deposited on the solid substrates.

6.4 Preparation of OFETs

Prior to the deposition of the soluble organic semiconductor layer, the substrates were cleaned in ultrasonic bath with acetone and isopropanol for 15 min each and afterwards ozone-treated for 25 min. The organic semiconductor solution and polymer were mixed in a 4:1 ratio, and then dissolved in chlorobenzene reaching a final concentration of 2 wt%. The blend solution was kept on a hot-plate at 105 °C for 1 h to ensure the complete dissolution of the two components. The blends coating were realized by the bar-assisted meniscus shearing technique (BAMS) at ambient conditions, in which a smooth cylindrical bar was positioned ≈ 300 μm above the cleaned Si/SiO_2 substrates with prefabricated gold electrodes that were heated to 105 °C. About 20 μL of the blend solution was deposited between the bar and the substrate forming a confined meniscus. Immediately, the solution was sheared at a speed of ≈ 1 cm s^{-1}. As the bar moves, the meniscus is displaced and by convective self-assembly (i.e., evaporation-induced self-assembly) a thin film is formed.

6.5 Preparation of self-assembled monolayers (SAMs)

6.5.1 General procedures

All the laboratory glassware employed for the monolayer preparation was firstly cleaned by using a milliQ water solution of Hellmanex (2% v/v). Afterwards the substrates were cleaned several times with distilled water and later dried inside an oven at 60° C.

The different type of gold substrates used in this Thesis were rinsed with different solvents with increasing polarity (dichloromethane, acetone and ethanol) and dried under a nitrogen stream. Then, substrates were exposed to ozone in a UV ozone chamber for 20 minutes and washed for at least 30 minutes in ethanol. Finally the substrates were rinsed with isopropanol and dried under a N_2 stream before immersing them in the solution of the target molecule.

6.5.2 Preparation of Fc-SAMs

The ferrocene SAMs were prepared under light exclusion and under inert atmosphere. The substrates were immersed in a 1 mM solution of 11-(ferrocenyl) undecanethiol ($FcC_{11}SH$) in ethanol at ambient conditions (25 ± 3°C) for 18 h. The samples were then removed from the solution and rinsed with large amounts of ethanol to remove physisorbed material and finally dried with N_2.

For the fabrication of Fc-SAMs on the WE of co-planar substrates, the substrate was placed vertically using a Teflon holder, and only the WE was immersed into the $FcC_{11}SH$ solution, to avoid the surface functionalization of the CE and RE gold electrodes,.

6.5.3 Preparation of AQ-SAMs

The SAMs based on anthraquinone were prepared by immersing a freshly cleaned Au substrate in a 0.5 mM solution of the AQ derivative in THF for 40 h under inert atmosphere at room temperature with exclusion of light. Afterwards, the samples were removed from the solution and rinsed with large amounts of THF and dried with N_2.

6.5.4 Preparation of AQ/Fc-SAMs

The mixed SAM was prepared by two approaches: 1) from a mixed component solution (one-step) and 2) sequential immersion in solutions of each component (two-steps). The optimised conditions for the fabrication of bi-component SAMs was obtained through the 2-step procedure in the following conditions: first, the freshly cleaned gold (on glass) substrate was immersed in a 0.5 mM solution of the AQ derivative in THF for 40 h at room temperature, and then, the modified substrate was rinsed and immersed in a 1 mM solution of $FcC_{11}SH$ in THF at room temperature for 1, 2 and 4 h under argon. Finally, the sample was rinsed with large amount of THF and dried with N_2.

6.5.5 Preparation of TTF-SAMs

Freshly cleaned gold (on mica) substrates were immersed in 1 mM solution of the TTF derivative in THF for 72 h. SAM formation was carried out under light exclusion and under nitrogen atmosphere. Later, the samples were removed from the solution and rinsed with large amounts of THF and dried with N_2.

6.5.6 Preparation of PTM-SAMs

The gold (111) substrates were immersed in the solution of 1 mM of PTM-$(CH_2)_n$-SH in toluene at 40 °C for 24 h, and after that, at room temperature for 24 h more. SAM formation was carried out under light exclusion and under N_2 atmosphere during the total formation process. The samples were then removed from the solution and rinsed with large amounts of toluene to remove weakly adsorbed molecules and any physisorbed material and finally dried with N_2.

6.5.7 Preparation of diluted PTM/Alkanethiols-SAMs

The diluted PTM-SAMs were prepared by dipping the gold (111) substrates in a toluene 1 mM solution (total thiol concentration) of PTM-$(CH_2)_n$-SH and a co-adsorbent $CH_3(CH_2)_{n-1}SH$ in different ratios 1:1, 1:2 and 1:5, respectively, at the same conditions than mono-component PTM-SAMs (24 h at 40 °C, and 24 h more at room temperature). Finally the samples were rinsed with toluene and dried with N_2.

Conclusions

CONCLUSIONS

The work developed in this Thesis has been focused on the preparation of different self-assembled monolayers (SAMs) based on electroactive molecules, such as ferrocene (Fc), anthraquinone (AQ), tetrathiafulvalene (TTF) and polychlorotriphenylmethyl radical (PTM), as active components in electronic switchable devices. With a view to future applications, attention has been paid to understanding the electron transfer (ET) processes that take place in these type of molecular systems and also, the use of ion gels as electrolytes or dielectric layers have been employed to extend their applicability to future entirely solid state devices.

In particular, from the work performed in this Thesis, it can be concluded that:

1) Electrochemical Impedance Spectroscopy is a relative simple and accurate technique that has been successfully implemented to characterise molecular switches based on electroactive SAMs.

2) It has been demonstrated the possibility to write and read electrochemical switches by using an electrical input to control the switch, as well as an electrical output to monitor it, such as the monolayer capacitance.

3) Fully solid state devices have been achieved by using ion gels as electrochemical media to operate molecular switches based on electroactive SAMs, showing higher stability than the same ones operated in liquid environments.

4) Multi-state switchable devices based on bi-component electroactive SAMs with an electron donor and an electron acceptor were successfully prepared, achieving a three-state redox molecular switches in a relatively narrow voltage window in which SAMs are stable.

5) Multi-state switchable devices based on mono-component SAMs have been obtained by functionalising gold surfaces with TTF derivative compounds, obtaining a higher number of states than the redox states of the molecule by using the capacitance output

of the system at defined DC applied potentials. Thus, the states of an electrochemical molecular switch can be fixed at different oxidation (or reduction) degrees of the SAM as long as the output response is distinct and constant.

6) The electron transfer kinetics have been satisfactorily elucidated in a family of PTM radical SAMs by analysing AC impedance responses at DC potentials centered on the reversible half-wave potential of the redox process.

7) The PTM based SAMs under kinetic study revealed the high influence of the liquid electrolytic environment as a determining factor in the adiabaticity character of the redox processes.

8) The electrochemical surface coverage of PTM based SAMs has a notorious relevance to the electron transfer process, showing a significant decrease of k_{ET} in denser SAMs associated to intermolecular electronic coupling between redox neighbouring centers.

9) It has been fabricated an organic field-effect transistor (OFET) using an ion gel as a high capacitance gate dielectric layer, obtaining devices that can operate in a voltage range of below 2 V. Further, the use of ion gels in OFETs provides a simple route to integrate the dielectric layers in the devices which is, in addition, compatible with low-cost solution processing methods and flexible substrates.

In general, it can be concluded that the results obtained in this Thesis represent an important progress in the field of Molecular Electronics. The use of electroactive SAMs together with electrochemical and impedance techniques will favour the integration of molecular based devices in future electronic components. Furthermore, the introduction of ion gels in these devices encourages the development of completely solid state devices for their use in future flexible technologies.

Appendix A

Experimental results of PTM_{10} and PTM_{12} SAMs

Appendix A. Results of PTM$_{10}$ and PTM$_{12}$ SAMs

Experimental results for PTM$_{10}$-SAMs

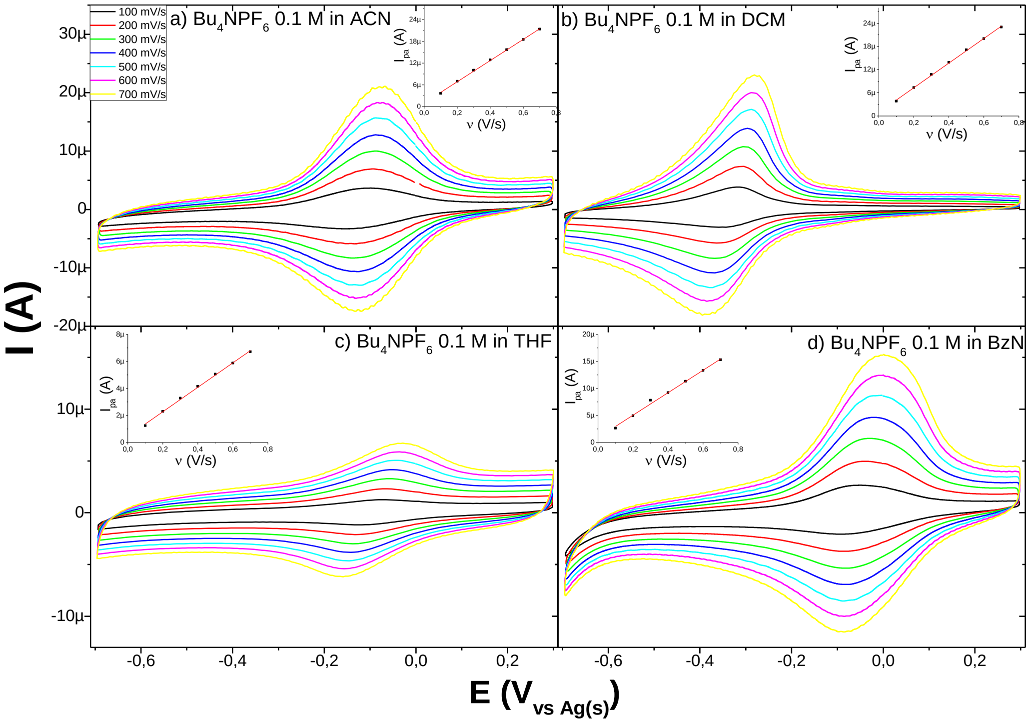

Figure A.1 CVs at different scan rates (ν varies from 100 to 700 mV/s) for the PTM$_{10}$-SAM using Bu$_4$NPF$_6$ 0.1 M as electrolyte salt in: a) acetonitrile, b) dichloromethane, c) tetrahydrofuran, and d) benzonitrile. Inset figures represent the linear variation of the anodic current peak with the scan rate ($I_{p,a}$ vs ν) for the corresponding electrolytes studied.

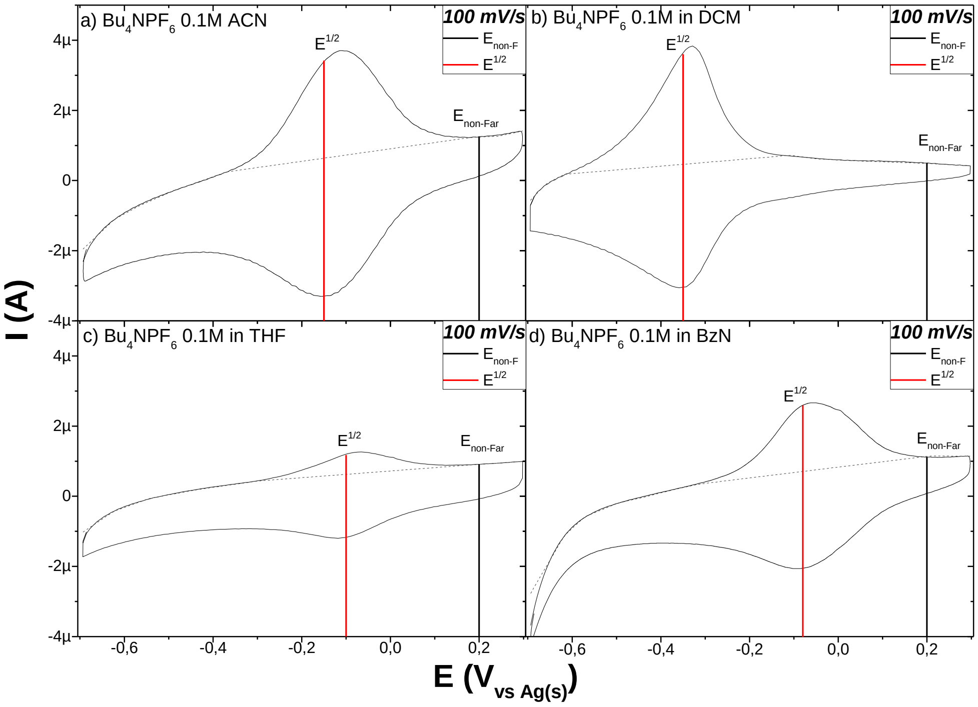

Figure A.2 CVs of PTM$_{10}$-SAM at 100 mV/s in Bu$_4$NPF$_6$ 0.1 M in: a) ACN, b) DCM, c) THF and d) BzN. Vertical lines indicate the DC bias potentials applied for the impedance experiments.

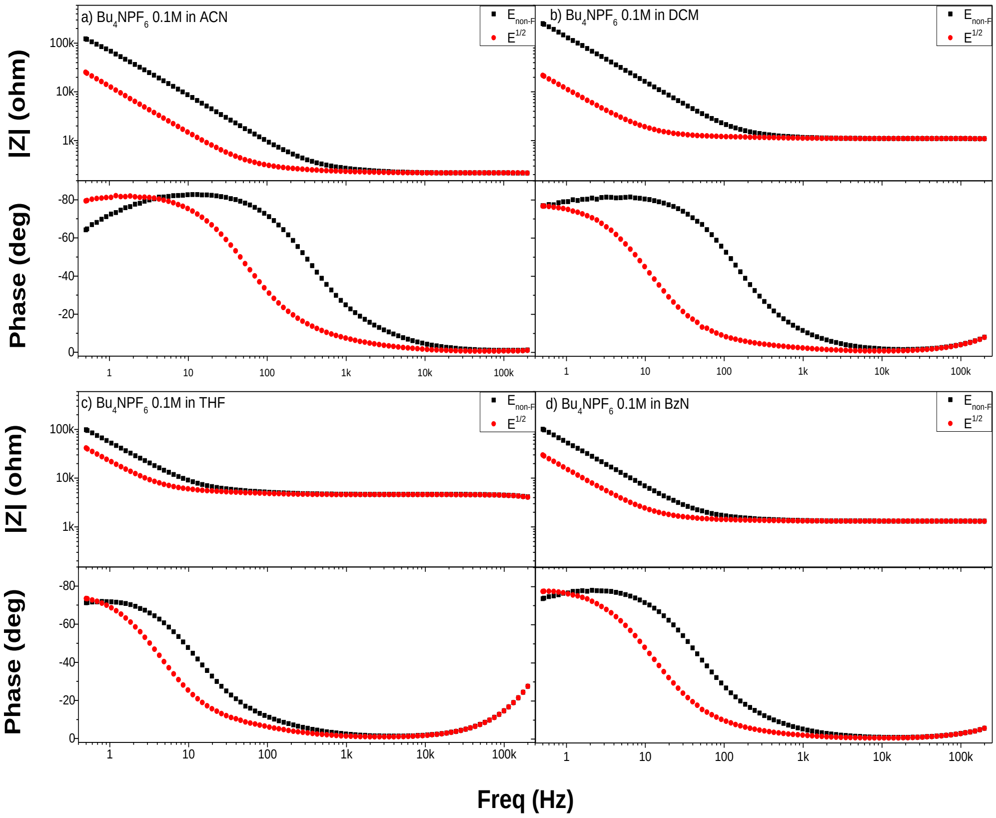

Figure A.3 Impedance Bode plots for the EIS characterization of PTM$_{10}$-SAMs at two different DC bias voltages, in the non-faradaic current response (■), and at the formal redox potential (●),in Bu$_4$NPF$_6$ 0.1 M in: a) ACN, b) DCM, c) THF and d) BzN.

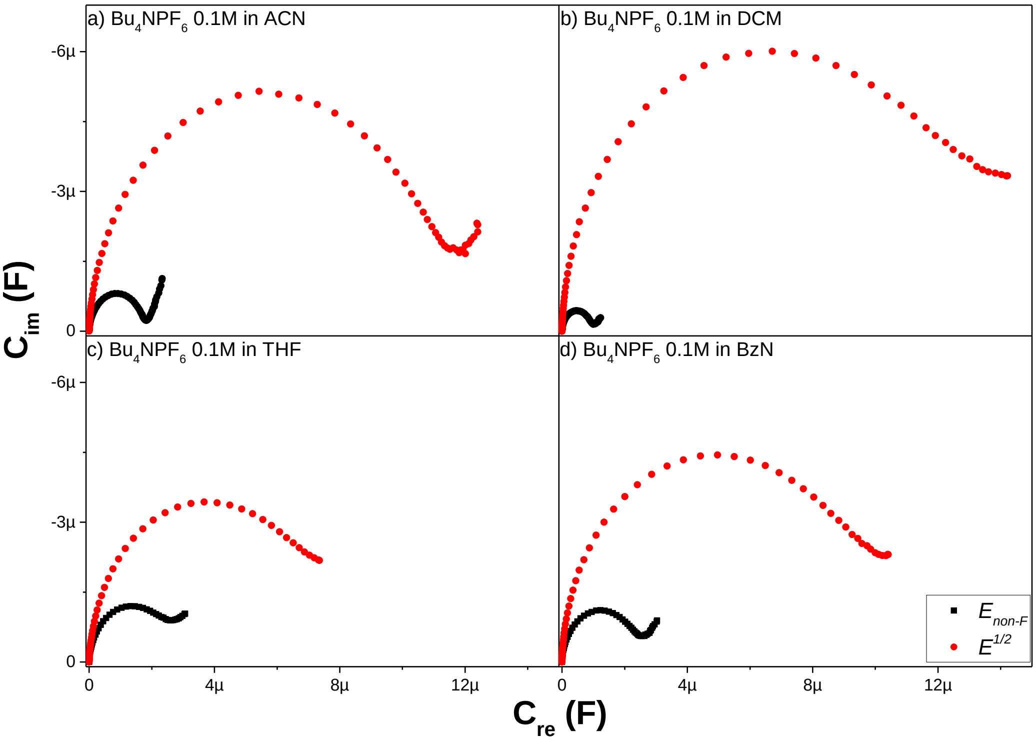

Figure A.4 Cole-Cole plots for the EIS characterization of PTM$_{10}$-SAMs at non-faradaic voltage (■), and at the formal redox potential (●), in Bu$_4$NPF$_6$ 0.1 M in: a) ACN, b) DCM, c) THF and d) BzN.

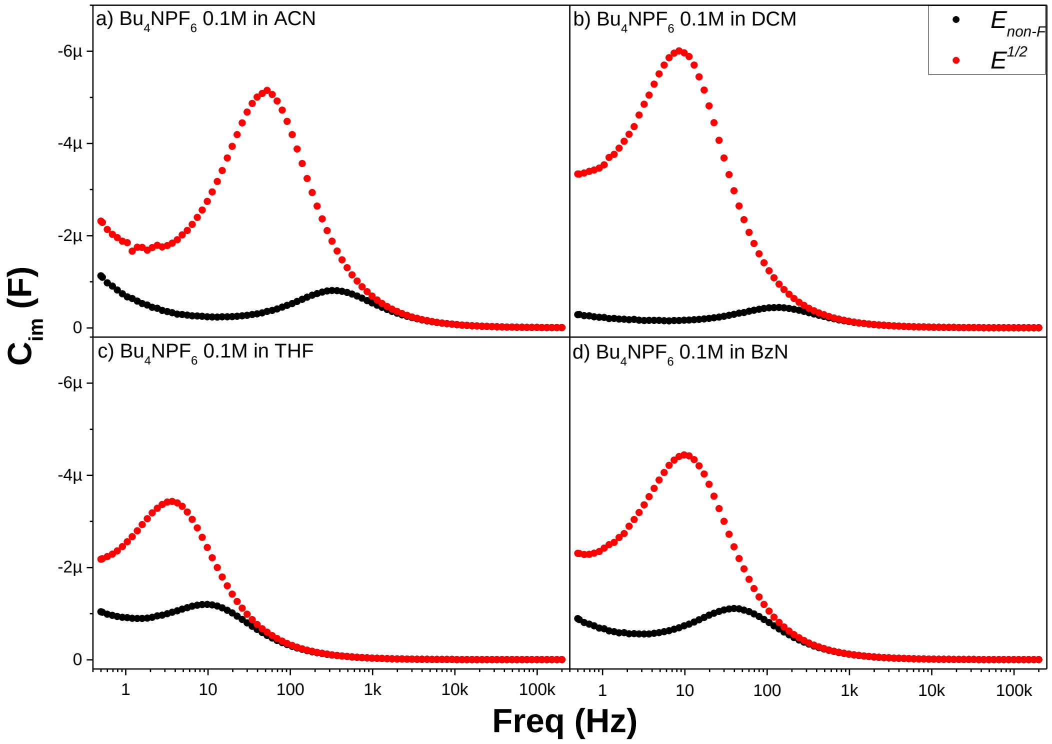

Figure A.5 Experimental data of the imaginary part of the capacitance vs. frequency, for PTM$_{10}$-SAMs at two different bias voltage: non-faradaic voltage (■), and at the formal redox potential (●), in Bu$_4$NPF$_6$ 0.1 M in: a) ACN, b) DCM, c) THF and d) BzN.

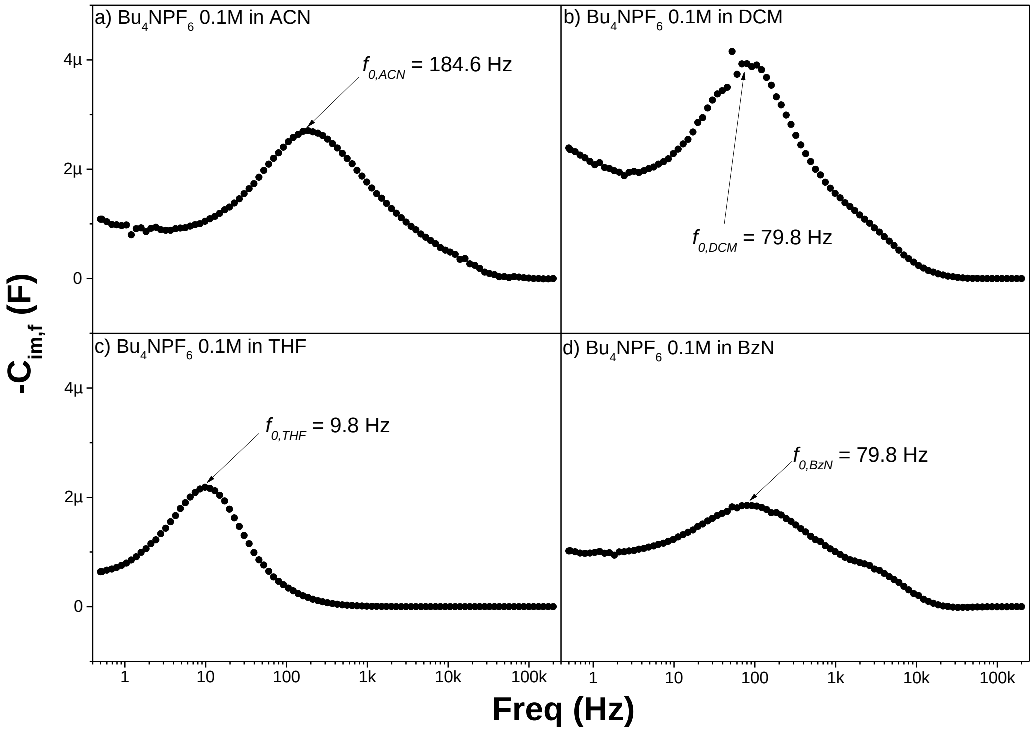

Figure A.6 Imaginary part of the capacitance vs. frequency, for PTM$_{12}$-SAMs, after subtraction of the non-faradaic response, in Bu$_4$NPF$_6$ 0.1 M in: a) ACN, b) DCM, c) THF and d) BzN.

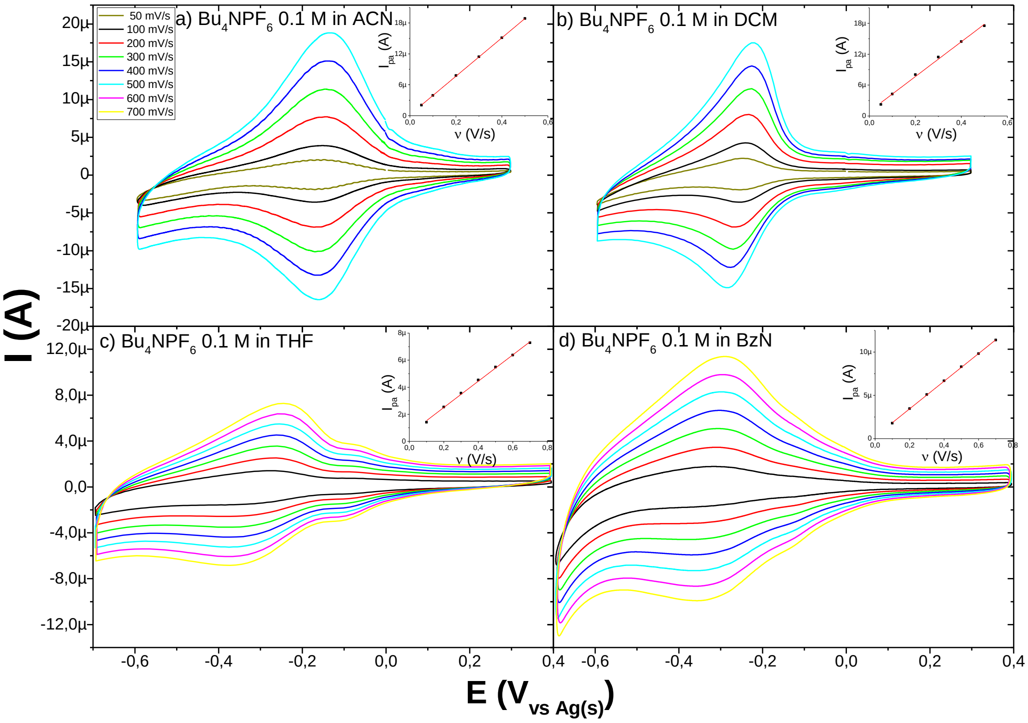

Figure A.7 CVs at different scan rates (ν varies from 50 to 700 mV/s) for the PTM$_{12}$-SAM using Bu$_4$NPF$_6$ 0.1 M as electrolyte salt in: a) acetonitrile, b) dichloromethane, c) tetrahydrofuran, and d) benzonitrile. Inset figures represent the linear variation of the anodic current peak with the scan rate (I$_{p,a}$ vs ν) for the corresponding electrolytes studied.

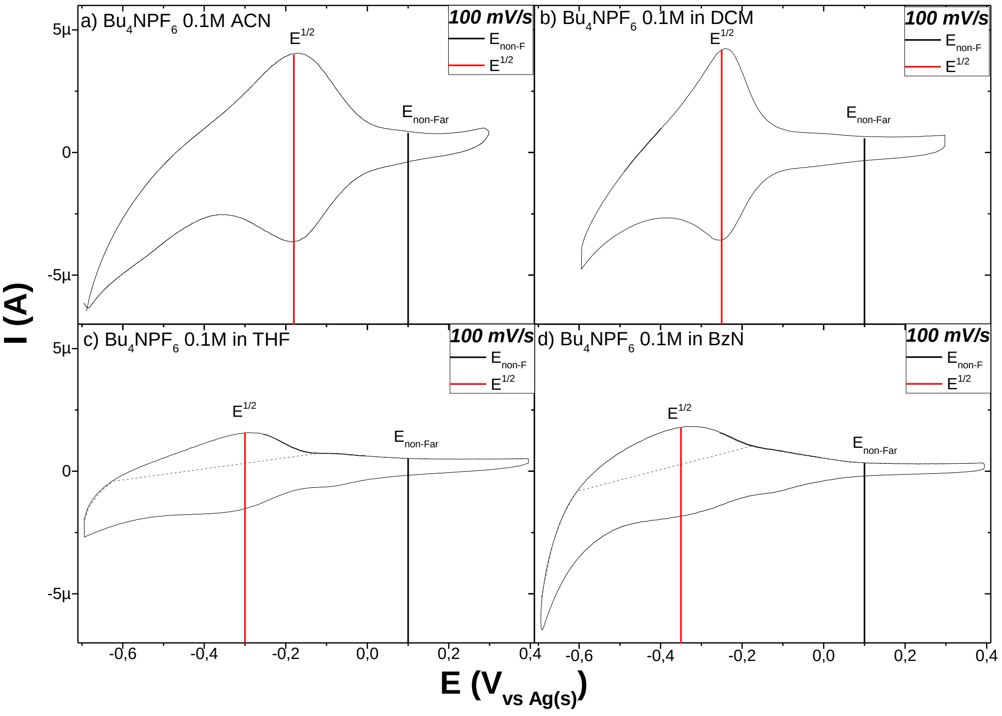

Figure A.8 CVs of PTM$_{12}$-SAM at 100 mV/s in Bu$_4$NPF$_6$ 0.1 M in: a) ACN, b) DCM, c) THF and d) BzN. Vertical lines indicate the DC bias potentials applied for the impedance experiments.

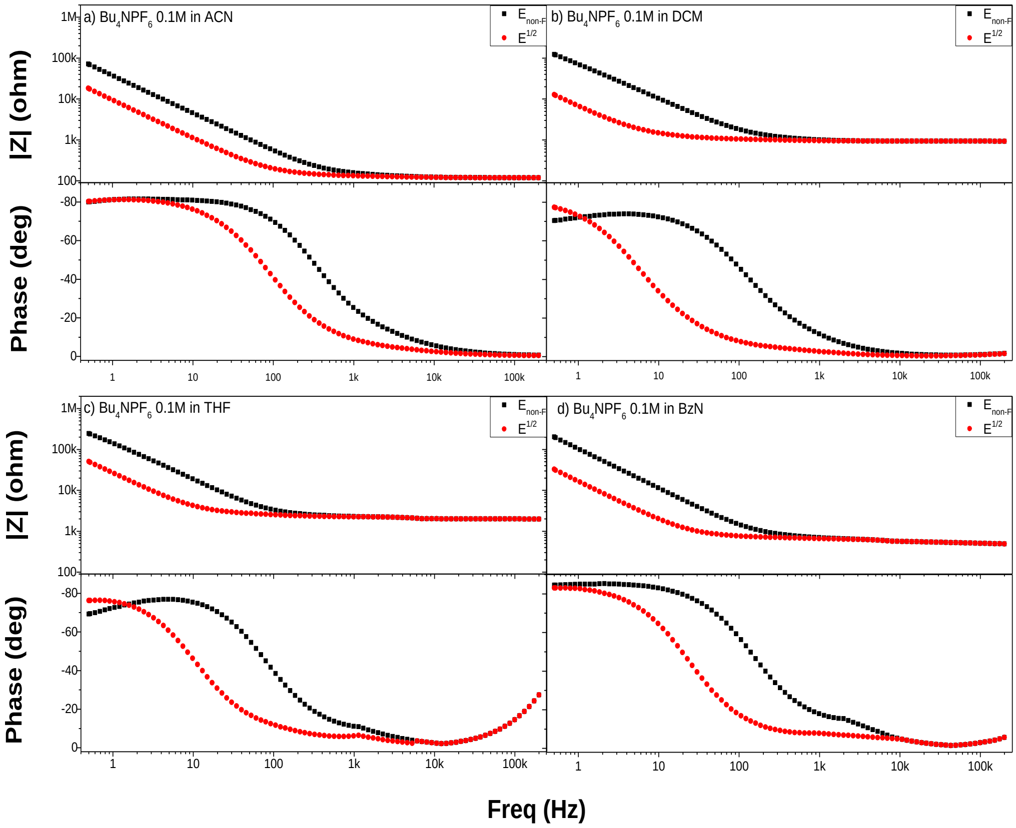

Figure A.9 Impedance Bode plots for the EIS characterization of PTM$_{12}$-SAMs at two different DC bias voltages, in the non-faradaic current response (■), and at the formal redox potential (●),in Bu$_4$NPF$_6$ 0.1 M in: a) ACN, b) DCM, c) THF and d) BzN.

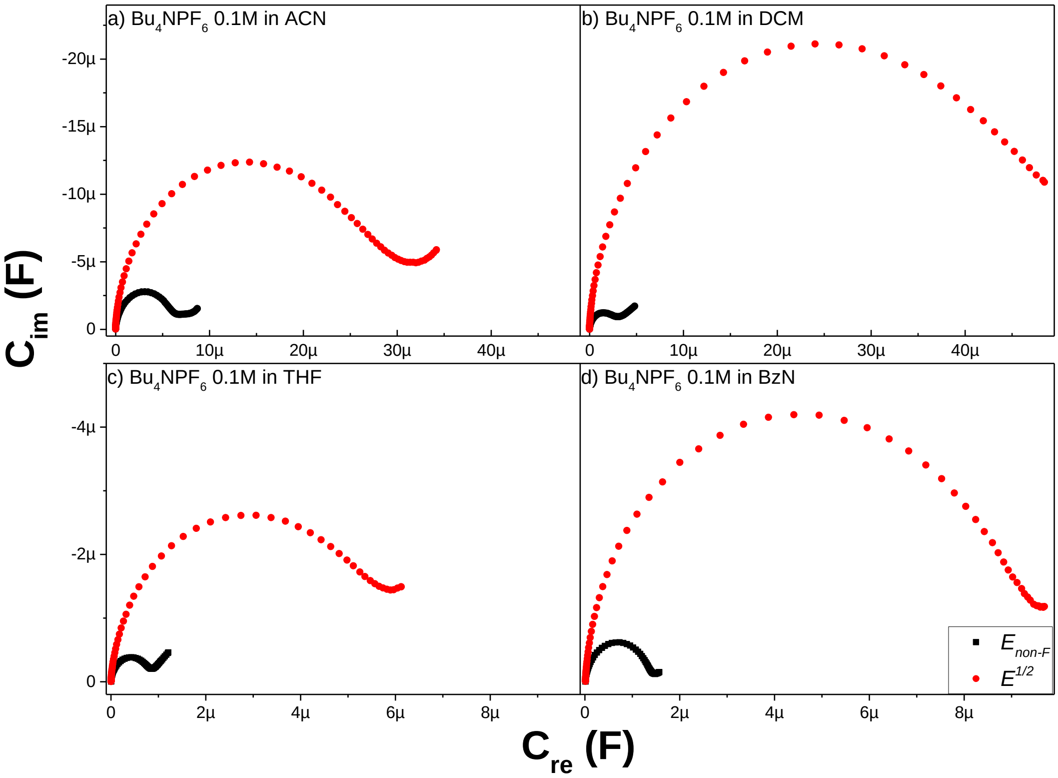

Figure A.10 Cole-Cole plots for the EIS characterization of PTM$_{12}$-SAMs at non-faradaic voltage (■), and at the formal redox potential (●), in Bu$_4$NPF$_6$ 0.1 M in: a) ACN, b) DCM, c) THF and d) BzN.

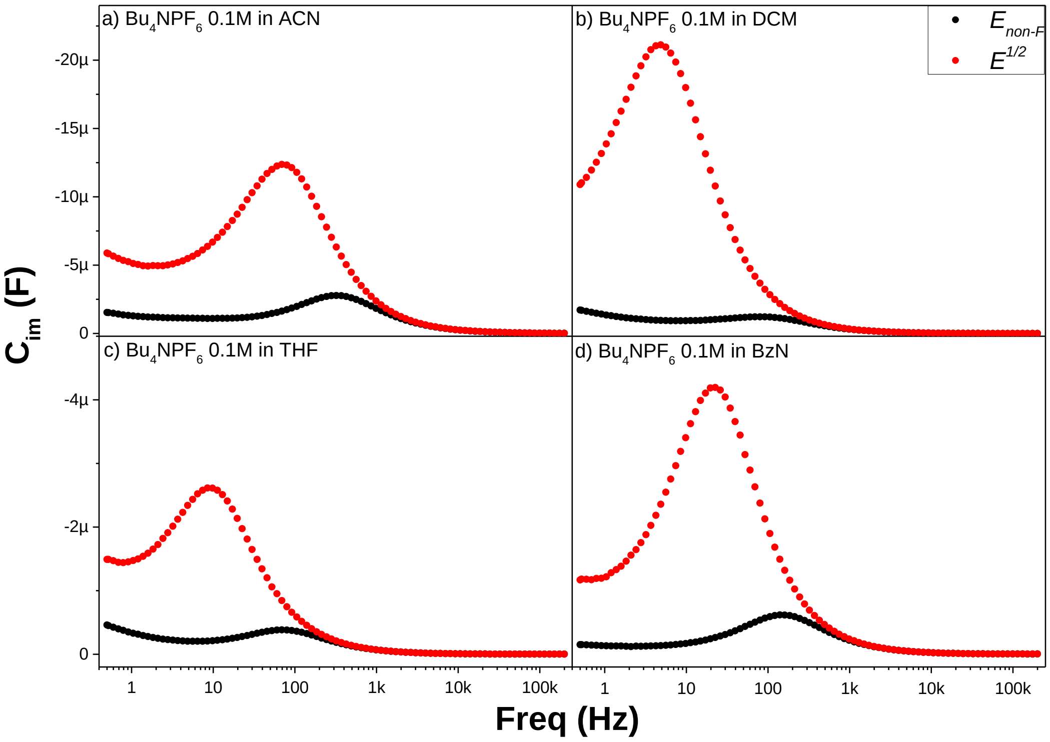

Figure A.11 Experimental data of the imaginary part of the capacitance vs. frequency, for PTM$_{12}$-SAMs at two different bias voltage: non-faradaic voltage (■), and at the formal redox potential (●), in Bu$_4$NPF$_6$ 0.1 M in: a) ACN, b) DCM, c) THF and d) BzN.

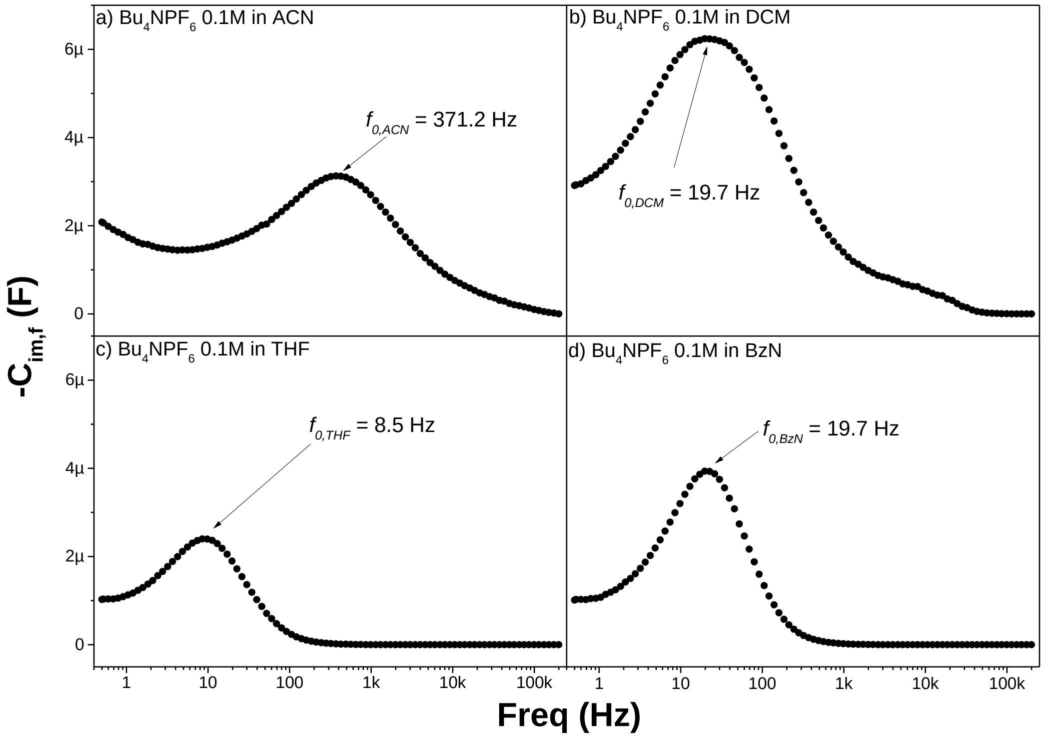

Figure A.12 Imaginary part of the capacitance vs. frequency, for PTM$_{12}$-SAMs, after subtraction of the non-faradaic response, in Bu$_4$NPF$_6$ 0.1 M in: a) ACN, b) DCM, c) THF and d) BzN.

Experimental results for PTM$_{10}$/C$_{10}$SH-SAMs

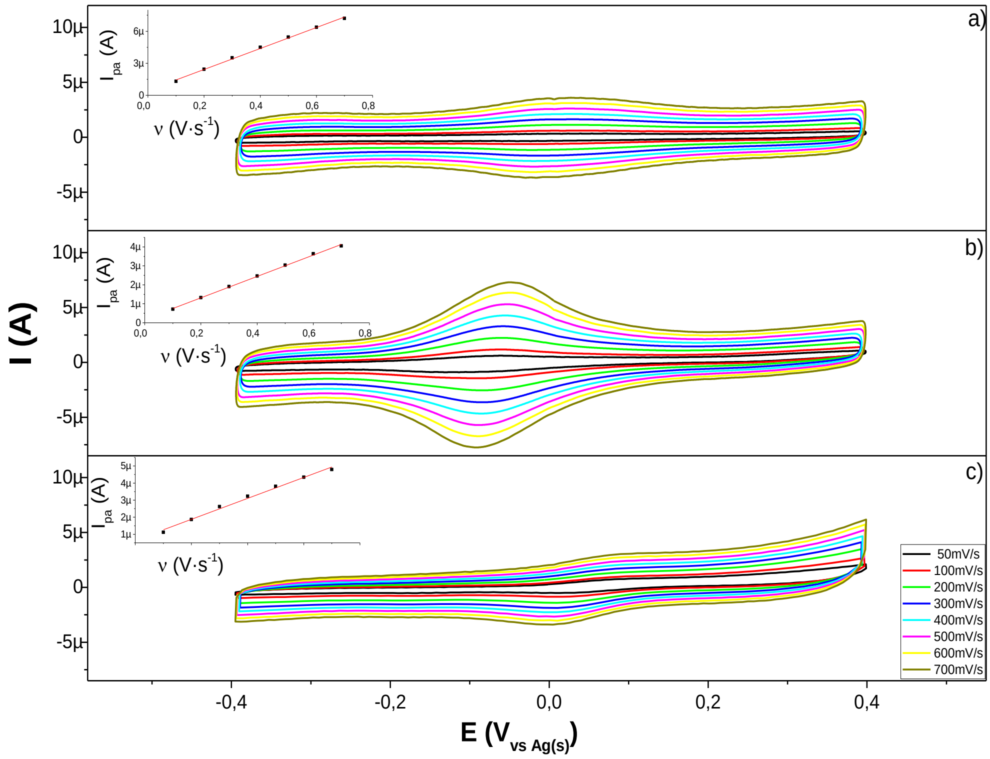

Figure A.13 CVs in Bu$_4$NPF$_6$ 0.1 M in THF at different scan rates (ν varies from 50 to 700 mV/s) for the PTM$_{10}$/C$_{10}$SH-SAMs prepared at different molar concentration ratios: a) 1:1, b) 1:2, and c) 1:5. Inset figures represent the linear variation of the anodic current peak with the scan rate (I$_{p,a}$ vs ν).

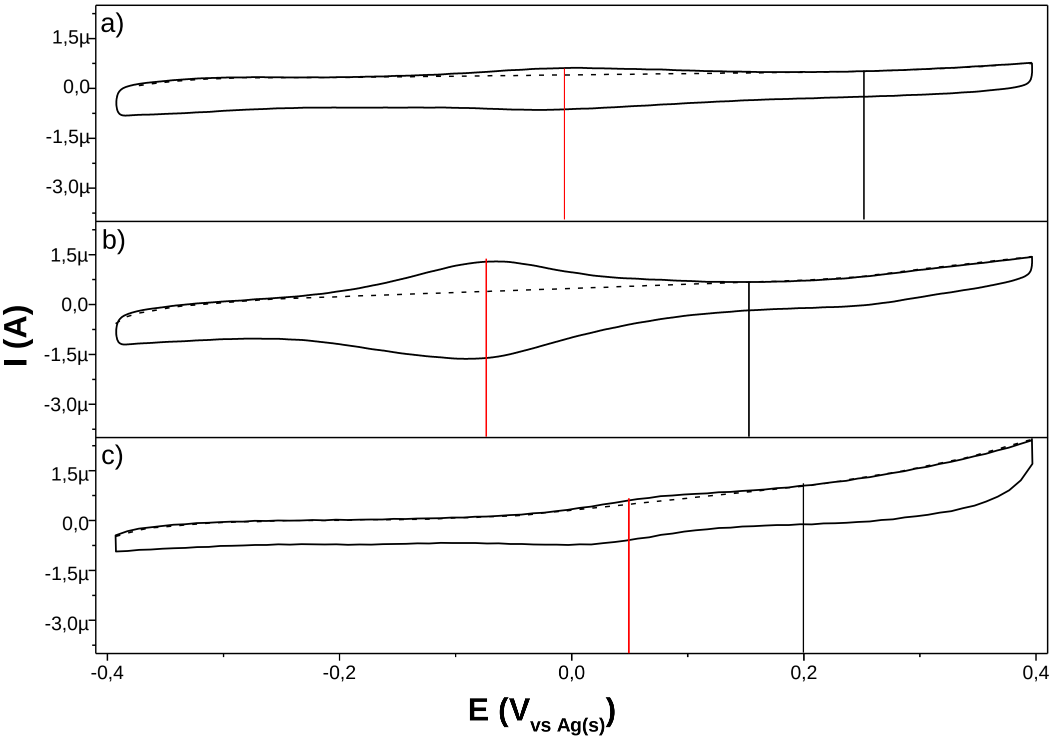

Figure A.14 CVs at 100 mV/s in Bu$_4$NPF$_6$ 0.1 M in THF of PTM$_{10}$/C$_{10}$SH-SAMs prepared at different molar concentration ratios: a) 1:1, b) 1:2, and c) 1:5. Vertical lines indicate the DC bias potentials applied for the impedance experiments.

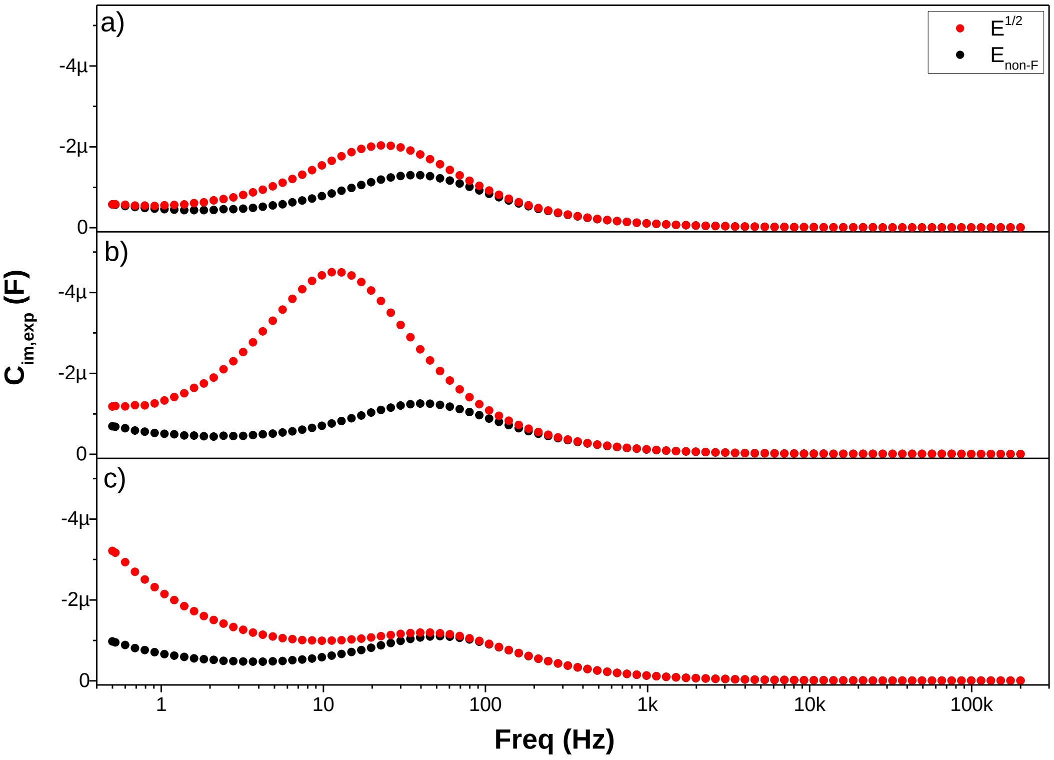

Figure A.15 Experimental data of C_{im} vs. frequency at two different bias voltage: non-faradaic voltage (●), and at the formal redox potential (●), for $PTM_{10}/C_{10}SH$-SAMs prepared at different molar concentration ratios: a) 1:1, b) 1:2, and c) 1:5.

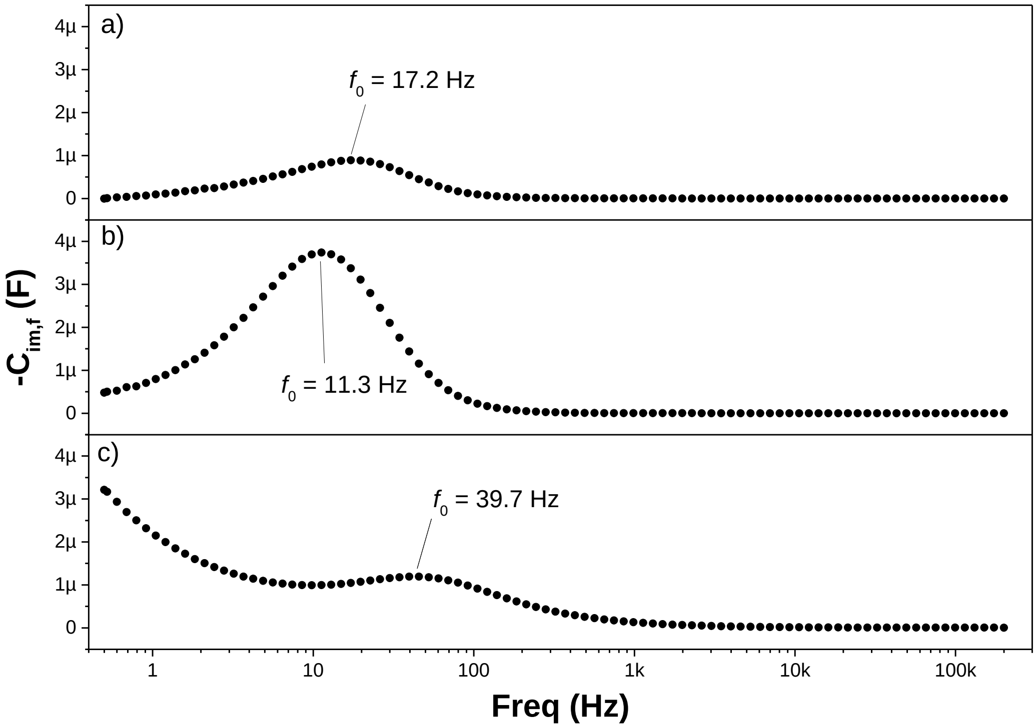

Figure A.16 $C_{im,f}$ vs. frequency, after subtraction of the non-faradaic response, for $PTM_{10}/C_{10}SH$-SAMs prepared at different molar concentration ratios: a) 1:1, b) 1:2, and c) 1:5.

Experimental results for PTM$_{12}$/C$_{12}$SH-SAMs

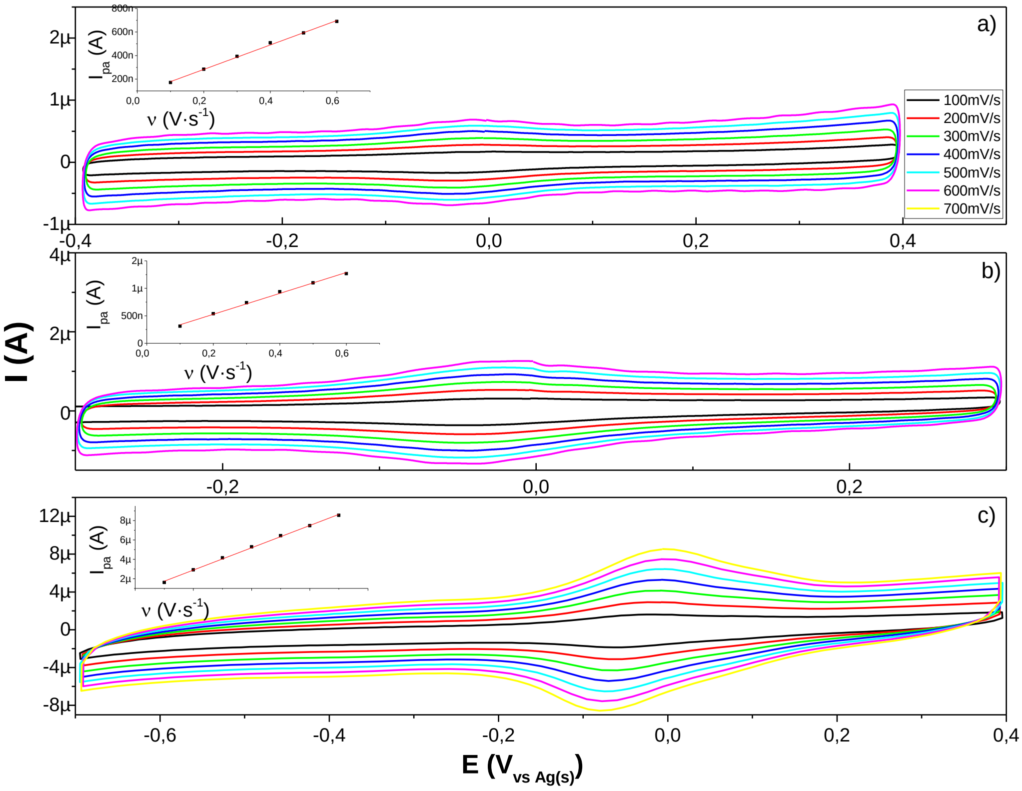

Figure A.17 CVs in Bu$_4$NPF$_6$ 0.1 M in THF at different scan rates (ν varies from 100 to 700 mV/s) for the PTM$_{12}$/C$_{12}$SH-SAMs prepared at different molar concentration ratios: a) 1:1, b) 1:2, and c) 1:5. Inset figures represent the linear variation of the anodic current peak with the scan rate (I$_{p,a}$ vs ν).

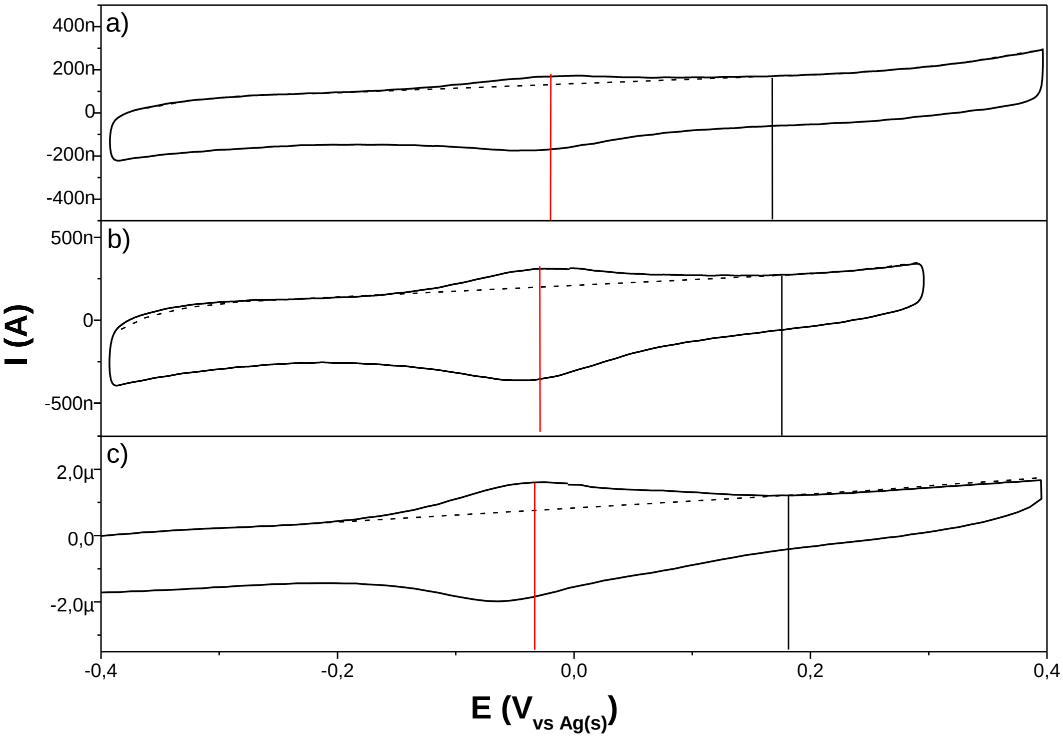

Figure A.18 CVs at 100 mV/s in Bu$_4$NPF$_6$ 0.1 M in THF of PTM$_{12}$/C$_{12}$SH-SAMs prepared at different molar concentration ratios: a) 1:1, b) 1:2, and c) 1:5. Vertical lines indicate the DC bias potentials applied for the impedance experiments.

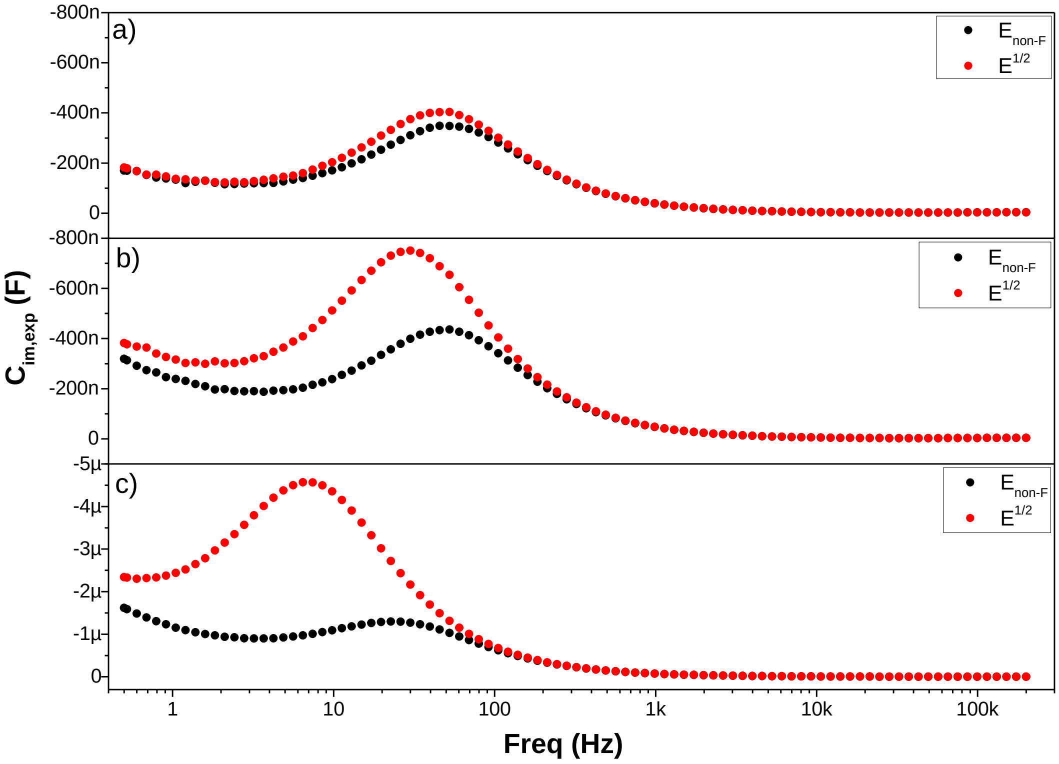

Figure A.19 Experimental data of C_{im} vs. frequency at two different bias voltage: non-faradaic voltage (●), and at the formal redox potential (●), for $PTM_{12}/C_{12}SH$-SAMs prepared at different molar concentration ratios: a) 1:1, b) 1:2, and c) 1:5.

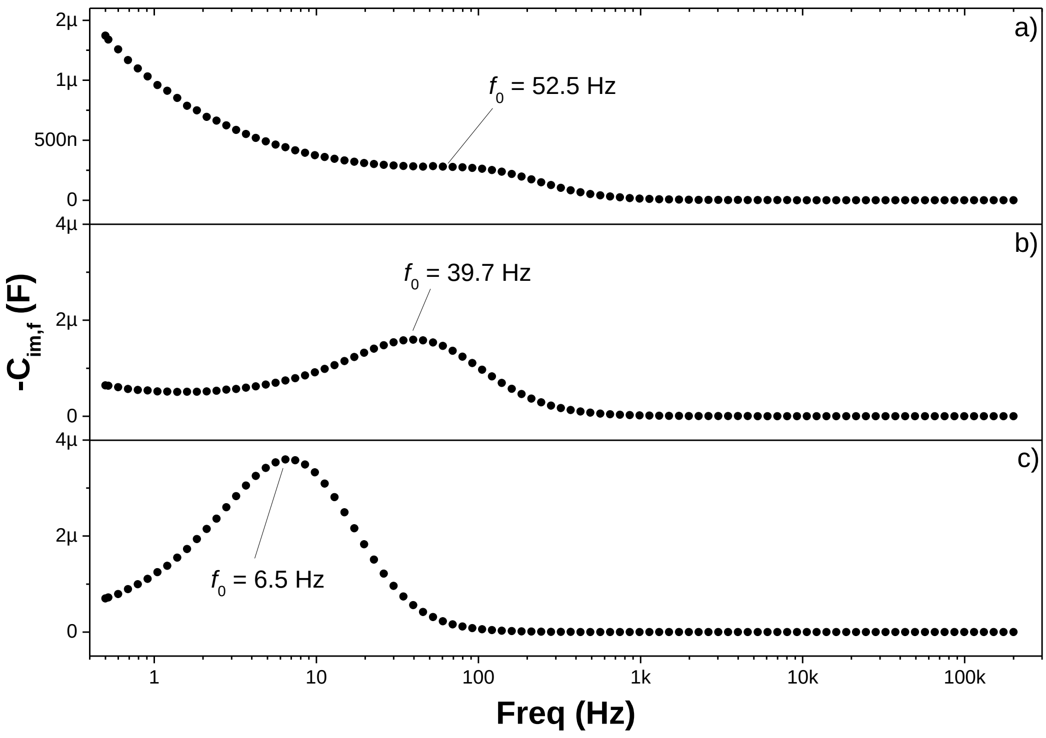

Figure A.20 $C_{im,f}$ vs. frequency, after subtraction of the non-faradaic response, for $PTM_{12}/C_{12}SH$-SAMs prepared at different molar concentration ratios: a) 1:1, b) 1:2, and c) 1:5.

Appendix B

Publications

Appendix B. Publications

I. E. Marchante, N. Crivillers, M. Buhl, J. Veciana and M. Mas-Torrent. *"An Electrically Driven and Readable Molecular Monolayer Switch Based on a Solid Electrolyte" Angewandte Chemie International Edition* **2016**, 55, 368.

II. J. Casado-Montenegro, E. Marchante, N. Crivillers, C. Rovira and M. Mas-Torrent. *"Donor/Acceptor Mixed Self-Assembled Monolayers for Realising a Multi-Redox-State Surface" ChemPhysChem Communications* **2016**, 17, 1810.

III. E. Marchante, M. S. Maglione, N. Crivillers, C. Rovira and M. Mas-Torrent. *"A four-state capacitance molecular switch based on a redox active tetrathiafulvalene self-assembled monolayer" RSC Advances* **2017**, 7, 5636.